# Modelling Ultrafast THz-Induced Antiferromagnetic Magnetisation Dynamics for Next Generation Data Processing

**Joel Hirst**

A thesis submitted in partial fulfilment of the requirements of
Sheffield Hallam University
for the degree of
*Doctor of Philosophy*

November 2023

*To Bronwyn, mum and dad.*

# Abstract

Globally, we are seeing a transition towards cloud-based storage and computing. To meet this ever-increasing demand for data, endeavours should be made to find ways of storing digital information at greater densities and improved efficiencies. At present, cloud-based storage works by storing digital information in large data centres filled with Hard Disk Drives (HDDs). These drives contain platters of ferromagnetic grains, which correspond to 0 and 1 bit states. The most efficient means of reversal is via the resonance mode in ferromagnets, which sits in the GHz range meaning reversal is generally limited to ns timescales. Antiferromagnets are a class of magnetic material where neighbouring atomic magnetic moments are aligned antiparallel, resulting in no net magnetisation. For digital storage applications, antiferromagnets offer high stability and insensitivity to external magnetic fields due to their inherently strong exchange field that arises from the coupling between the two sublattices. This opens the possibility for reduced bit sizes because of the lack of stray fields between grains. The exchange field also gives rise to inherently fast THz magnetisation dynamics, orders of magnitudes faster than the ferromagnets currently found in HDD technology opening the possibility for switching on picosecond, or *ultrafast*, timescales. To better understand the applicability of antiferromagnets for future storage and memory applications, in this thesis we use computational models to study properties and switching dynamics of the antiferromagnet $Mn_2Au$ and toy models of layered materials with antiferromagnetic and ferromagnetic order. A multiscale model of $Mn_2Au$ is presented and verified against previous analytical and theoretical work. The feasibility of switching using THz frequency fields is then investigated using atomistic and micromagnetic models across a range of temperatures. We then present an atomistic model of $Mn_2Au$ coupled ferromagnetically to Permalloy and perform further switching simulations and show that there is a significant speedup in the switching compared to a pure ferromagnetic system while still being able to access the information via conventional readout methods of the ferromagnetic Permalloy layer. Finally, we study toy multilayer and thin film systems and investigate how standing spinwave modes can be used to reduce the minimum field strengths for switching.

*Keywords*: Antiferromagnetism, Ultrafast Magnetism, Atomistic Spin Dynamics, Switching, Spinwaves.

# Declaration

I hereby declare that:

1. I have not been enrolled for another award of the University, or other academic or professional organisation, whilst undertaking my research degree.
2. None of the material contained in the thesis has been used in any other submission for an academic award.
3. I am aware of and understand the University's policy on plagiarism and certify that this thesis is my own work. The use of all published or other sources of material consulted have been properly and fully acknowledged.
4. The work undertaken towards the thesis has been conducted in accordance with the SHU Principles of Integrity in Research and the SHU Research Ethics Policy.
5. The word count of the thesis is 36102.

Name: Joel Hirst
Date: Friday 15th March, 2024
Award: PhD
Director(s) of Studies: Prof. Doug Cleaver
Advisor: Dr. Thomas Ostler
Second Supervisor: Dr. Sergiu Ruta

# Acknowledgements

I would firstly like to thank my supervisor, Dr. Thomas Ostler for his continued support throughout this journey. I am forever in his debt for the opportunities and constant encouragement over the course of the past three years. I'd also like to thank Prof. Doug Cleaver and Dr. Sergiu Ruta for their scientific knowledge and support. Thank you to all people involved in collaborative works. In particular, I'd like to thank Dr. Jerome Jackson, Dr. Unai Atxitia, Dr. Ezio Iacocca.

I'd like to thank my office pals from Sheffield Hallam, Harry, Kris and Raph, who've brought me great happiness over the past few years. Thank you for the gossip, laughs, beers and support in putting together this thesis.

I'd like to thank my family. Mum and Dad, thank you for all the love, support and care. I would not be in this lucky position without your never-ending encouragement. Blythe and Dyl, your humour and stories have been a constant relief. Never change.

Bronwyn, thank you for being you. I could not have gone on this journey without you. Thank you for always being there for me and for your endless kindness and love.

Finally, I'd like to thank my Gran. For the sticker magazines, history books, science books, newspaper cutouts, help with all forms of homework, ribena, and the general nurturing of my worldly curiosity for the first 20 years of my life. Consider this my repayment.

# Publications

## Published

- **Hirst, J.**, Ruta, S., Jackson, J. et al. *Simulations of magnetization reversal in FM/AFM bilayers with THz frequency pulses.* Scientific Reports 13, 12270 (2023).
- **Hirst, J.**, Atxitia, U., Ruta, S., Jackson, J., Petit, L., & Ostler, T. (2022). *Temperature-dependent micromagnetic model of the antiferromagnet $Mn_2Au$: A multiscale approach.* Phys. Rev. B, 106(9), 094402.
- Rana A. , Liao C.T., Iacocca E., Zou J., Pham M. , Lu X., Subramanian E., Yuan H.L, Ryan S.A., Bevis C.S., Karl R. M. , Glaid A.J., Rable J., Mahale P., **Hirst, J.**, Ostler T., Liu W., O'Leary C.M., Y. Young-Sang, Bustillo K., Ohldag H. , Shapiro D.A. , Yazdi S., Mallouk T.E., Osher S.J., Kapteyn H.C. , Crespi V.H., Badding J.V., Tserkovnyak Y., Murnane M.M. & Miao J., *Three-dimensional topological magnetic monopoles and their interactions in a ferromagnetic meta-lattice.* Nat. Nanotechnol. 18, 227–232 (2023).

## In Preparation

- Jackson, J., Ruta, S., **Hirst, J.**, Petit, L., & Ostler, T. Heisenberg Exchange interactions in $Mn_2Au$ and CuMnAs
- Rockwell, K., **Hirst, J.**, Ostler, T., Iacocca E., Soliton nucleation from ultrafast transient grating in a 1D ferromagnetic chain

# Table of Contents

# List of Figures

# List of Tables

# List of Abbreviations

ASD ..... Atomistic Spin Dynamics
AC ..... Alternating Current
BZ ..... Brillioun Zone
DC ..... Direct Current
MFA ..... Mean Field Approximation
SSW ..... Standing Spin-Wave
LLG ..... Landau-Lifshitz-Gilbert
LLB ..... Landau-Lifshitz-Bloch
DFT ..... Density Functional Theory
GPU ..... Graphical Processing Unit
CPU ..... Central Processing Unit
HPC ..... High Performance Computing
LSWT ..... Linear Spinwave Theory
TTM ..... Two Temperature Model
DW ..... Domain Wall
HAMR ..... Heat Assisted Magnetic Recording
HDD ..... Hard Disk Drive
FM ..... Ferromagnet
AFM ..... Antiferromagnet
FiM ..... Ferrimagnet
MOKE ..... Magneto-Optical Kerr Effect
SEMPA ..... Scanning Electron Microscopy with Polarization Analysis
XMLD ..... X-ray Magnetic Linear Dichroism
PEEM ..... Photoelectron Emission Microscopy

# List of Symbols

$A$ ..... Exchange stiffness
$a$ ..... Lattice constant along $x$-axis
$b$ ..... Lattice constant along $y$-axis
$c$ ..... Lattice constant along $z$-axis
$C$ ..... Spin-spin correlation function
$B$ ..... Applied field
$D$ ..... Spinwave stiffness
$\mathbf{D}_{ij}$ ..... Dzyaloshinskii–Moriya interaction energy
$\delta_{ij}$ ..... Kronecker delta function
$h$ ..... Plancks constant
$\hbar$ ..... reduced Plancks constant
$J_{ij}$ ..... Isotropic exchange integral between spins $i$ and $j$
$J_0$ ..... Zero point exchange energy
$J_{0,\nu\nu}$ ..... Intra-sublattice exchange energy
$J_{0,\nu\kappa}$ ..... Inter-sublattice exchange energy
$J_0$ ..... Zero point exchange energy
$J_{\mathbf{k}}$ ..... Fourier transform of exchange energy
$k$ ..... wave vector
$\mathbf{n}$ ..... Neel vector
$n$ ..... Neel vector length
$\mathbf{m}$ ..... reduced magnetisation
$m$ ..... reduced magnetisation length
$m_e$ ..... reduced equilibrium magnetisation
$N$ ..... Number of spins
$k_B$ ..... Boltzmanns Constant
$t$ ..... Time
$\Delta t$ ..... Time-step
$V$ ..... Volume
$d$ ..... Anisotropy constant

# Chapter 1

# Introduction

*The sun did not shine, it was too wet to play, so we sat in the house all that cold, cold wet day. I sat there with Sally. We sat here we two and we said 'How we wish we had something to do.*

– *DR. SEUSS*, The Cat in the Hat.

## 1.1 Motivation

The demand for data has increased hugely in recent years due to the explosion of cloud storage and our ever-increasing online presence. Of course, this data must be stored somewhere, and at present the cheapest and therefore most widely used method of storing data is using Hard Disk Drives (HDDs). HDDs are comprised of two key components, the platter and the read-write head. The platter is made of magnetic domains which, depending on their orientation, correspond to a digital 0 or 1 bit state. The change in bit state from, say, a 0 to 1 is done by applying a magnetic field to the bits to reverse the orientation of the magnetisation. The device used to drive the reversal and read the magnetic data is the read-write head and they can typically transfer data at speeds between 150 and 250 MB/s [1]. Inducing switching costs energy, with a current being passed through the read-write head to generate a magnetic field. As already alluded to, HDDs are the most widely used method of digital data storage, the majority of which are housed in data centres with the sole purpose of managing and storing data for digital applications and cloud services. Globally, data centres currently account for between 0.9 and 1.3% of global electricity demand [2]. Between 2015 and 2021, the workload of data centres increased by 260% with energy usage rising by a comparatively low value of between 10-60% due to technological advances [2]. Despite the improvements in hardware and efficiency, if we as a society are to transition to net zero, this growth in energy consumption cannot be considered sustainable, and other methods of data storage and processing should be the subject of investigation.

## 1.2 Fundamentals of Magnetic Materials

To be able to understand the limitations of current magnetic recording methods and the macroscopic ordering observed in magnetic materials, we must first introduce some of the key quantities, namely the magnetic moment, exchange, and anisotropy. These fundamental quantities provide insights into the behaviour of magnetic materials and govern their properties. The magnetic moment, arising from the intrinsic spin of electrons within atoms, forms the basis of a material's magnetic behaviour. Exchange interac-

tions describe the interplay between neighbouring spins and determines the long-range order of a magnetic material. Finally, anisotropy refers to the directional preference of a magnetic material and influences the size response to any external magnetic fields. By briefly outlining the physics behind these key quantities, we can begin to unravel the intricacies and shortcomings of magnetic recording techniques and begin to understand possible ways to improve data storage efficiency and density.

### 1.2.1 The Magnetic Moment

The idea of a magnetic moment can easily be introduced by considering the Bohr model of the atom, where we have an electron orbiting a stationary nucleus. The electron has speed $v$ and orbits at a radius $R$ meaning the period of rotation is $2\pi R/v$. The current of the loop is therefore $I = -ev/2\pi R$ where $e = -1.6 \times 10^{-19}$ A s is the charge of the electron. The magnetic moment generated from a current in a loop is $\mu = I \int dA$ where $dA$ is the surface element of the loop. The magnetic moment of the circular motion of the electron in orbit is therefore

$$\mu = -\frac{evR}{2} \tag{1.1}$$

The angular momentum of the electron is $L = m_e Rv$ where $m_e$ is the mass of the electron. While this is true for a classical system, quantum mechanics tells us that angular momentum is quantized in units of $\hbar = 1.5054 \times 10^{-34}$ J s. The orbital magnetic moment along a particular direction, in this case $z$, is therefore

$$\mu_z = -\frac{e\hbar}{2m_e} m_l, \quad m_l = 0, \pm 1, \pm 2, ... \tag{1.2}$$

The magnetic moment is therefore quantised in units of $\mu_B = \frac{e\hbar}{2m_e}$, where $\mu_B$ is known as the Bohr magneton. It has a numerical value $\mu_B = 9.2740 \times 10^{-24}$ J T$^{-1}$. It follows that since each electron contributes $\mu_B$, the total magnetic moment of an atom would be an integer multiple of this value. In solids, especially metallic materials, the delocalisation of electrons, and electrostatic interactions means the moment can be much lower and the magnetic moment arises predominantly from the intrinsic spin. Unlike orbital angular momentum from particles moving in space, spin is an inherent

property of particles unrelated to motion. The origin of the intrinsic spin can be shown using relativistic quantum mechanics. The mathematical detials of intrinsic spin do not significantly impact later sections and therefore an in-depth discussion is not required. However, it is worth noting that it contributes strongly to the overall local magnetic moment. The electron intrinsic angular momentum has quantum number $\mathbf{s} = \frac{1}{2}$ and it turns out the magnetic moment that arises from the intrinsic spin of electrons is given by

$$\mu = -\frac{e}{2m_e} g\mathbf{s} \tag{1.3}$$

where $g$ is the electron spin g-factor and takes the value $g = 2.00232$ [3]. The magnetic quantum number, $m_s$, can take values $m_s = \pm\frac{1}{2}$ and so the component projected along a given axis is therefore

$$\mu = -\frac{e}{2m_e} g m_s \hbar, \quad m_s = \pm\frac{1}{2}. \tag{1.4}$$

The classic example often found in textbooks is iron (Fe), which with its 4 unpaired $3d$ electrons should have a magnetic moment of $4\mu_B$. Which is much larger than the experimentally observed non-integer value of $\approx 2.2\mu_B$. In metallic systems such as this, electrons become partially delocalised, meaning the magnetic moment cannot be described by quantised orbitals and a band structure description of the system is required.

### 1.2.2 Exchange Interaction

The Exchange interaction describes the interaction between the spins of electrons in a many-electron system and is responsible for the macroscopic ordering observed in magnetic materials. For many body systems, it cannot be calculated directly from the wave function in a closed-form analytical expression because of the number of electrons involved making it intractable. In such cases, approaches like density functional theory (DFT) can be employed to compute the ground state energy, with the exchange constants subsequently determined by constraining the magnetic moments within a supercell in a spinwave configuration for a given wavevector. Because of its importance to the remainder of this thesis, the quantum mechanical description of the exchange

interaction will be introduced by considering the simple case of a two-electron system, such as the $H_2$ or He atom. In this section, we will follow the approach of Blundell [4], although similar approaches can be found in other magnetism textbooks [5, 6].

Consider two electrons on neighbouring atoms, the total wavefunction, $\Psi(1,2) = \Phi(\mathbf{r}_1, \mathbf{r}_2)\chi(s_1, s_2)$, where $\Phi$ is the total spatial wavefunction, $\chi$ is the total spin wavefunction. Since electrons are fermions, the total wavefunction of the two-electron system must be antisymmetric under the exchange of electrons, meaning

$$\begin{aligned} \Psi(1,2) &= -\Psi(2,1) \\ \Phi(\mathbf{r}_1, \mathbf{r}_2)\chi(1,2) &= -\Phi(\mathbf{r}_2, \mathbf{r}_1)\chi(s_2, s_1) \end{aligned} \tag{1.5}$$

If the above is to be true, either the total spacial wavefunction,$\Phi$, or total spin wavefunction, $\chi$, can be symmetric

$$\Psi(1,2) = \begin{cases} \Phi_{\text{sym}}(\mathbf{r}_1, \mathbf{r}_2)\chi_{\text{anti}}(s_1, s_2) \\ \\ \Phi_{\text{anti}}(\mathbf{r}_1, \mathbf{r}_2)\chi_{\text{sym}}(s_1, s_2) \end{cases} \tag{1.6}$$

where we have two possibilities, either the spin component is in an antisymmetric singlet state $\chi_S$, $(S = 0)$. Or, the case where the spin wavefunction is symmetric, in which case the spin component is in a symmetric triplet state $\chi_T$, $(S = 1)$. The total wavefunctions for each case is given by

$$\Psi_{\text{S}}(1,2) = \frac{1}{\sqrt{2}} \left[\phi_a(\mathbf{r}_1)\phi_b(\mathbf{r}_2) + \phi_a(\mathbf{r}_2)\phi_b(\mathbf{r}_1)\right] \chi_S \tag{1.7}$$

$$\Psi_{\text{T}}(1,2) = \frac{1}{\sqrt{2}} \left[\phi_a(\mathbf{r}_1)\phi_b(\mathbf{r}_2) - \phi_a(\mathbf{r}_2)\phi_b(\mathbf{r}_1)\right] \chi_T \tag{1.8}$$

with $\phi_{a,b}(\mathbf{r}_{1,2})$ being the individual wavefunction of electron 1 or 2 in state $a$ or $b$. The respective energies are

$$E_S = \int \Psi_S^* \mathcal{H} \Psi_S d\mathbf{r}_1 d\mathbf{r}_2 \tag{1.9}$$

$$E_T = \int \Psi_T^* \mathcal{H} \Psi_T d\mathbf{r}_1 d\mathbf{r}_2 \tag{1.10}$$

The difference between the two

$$E_S - E_T = 2 \int \phi_a^* (\mathbf{r}_1) \phi_b^* (\mathbf{r}_2) \mathcal{H} \phi_a (\mathbf{r}_2) \phi_b (\mathbf{r}_1) d\mathbf{r}_1 d\mathbf{r}_2 \tag{1.11}$$

In the above $\mathcal{H}$ is the Hamiltonian of the electron system in a spatially varying potential. For full electronic structure calculations, it contains terms for accounting for the potential arising from external fields, the Coulomb interaction between nuclei and electrons, and the Coulomb interaction between pairs of electrons. In this example we are only interested in the Coulomb interaction between electrons and can therefore safely ignore the other two terms. The singlet state $\mathbf{S}_1 \cdot \mathbf{S}_2 = -\frac{3}{4}$ and for the triplet state $\mathbf{S}_1 \cdot \mathbf{S}_2 = \frac{1}{4}$. The Hamiltonian can be written in terms of a spin-independent, $\mathcal{H}_{\text{rad}}$, and spin-dependent term, $\mathcal{H}_{\text{spin}}$

$$\mathcal{H} = \mathcal{H}_{\text{rad}} + \mathcal{H}_{\text{spin}} = \frac{1}{4} (E_{\text{s}} + 3E_{\text{T}}) - (E_{\text{S}} - E_{\text{T}}) \mathbf{S}_1 \cdot \mathbf{S}_2 \tag{1.12}$$

The exchange integral, or constant, is defined as

$$\mathcal{J} = \frac{E_S - E_T}{2} = \int \phi_a^* (\mathbf{r}_1) \phi_b^* (\mathbf{r}_2) \mathcal{H} \phi_a (\mathbf{r}_2) \phi_b (\mathbf{r}_1) d\mathbf{r}_1 d\mathbf{r}_2 \tag{1.13}$$

hence the spin-dependent term can be written as

$$\mathcal{H}_{\text{spin}} = -2\mathcal{J} \mathbf{S}_1 \cdot \mathbf{S}_2 \tag{1.14}$$

For two electrons, the above derivation was fairly straightforward, however for many-body systems it becomes a non-trivial process and advanced computational methods must be used to determine the exchange constant $\mathcal{J}$. Regardless, Heisenberg showed

in 1928 [7] that the Hamiltonian can be written to describe interactions between any neighbouring atomic spins

$$\mathcal{H}_{\text{spin}} = -\sum_{i,j} J_{ij}\mathbf{S}_i \cdot \mathbf{S}_j \tag{1.15}$$

with $J_{ij}$ denoting the exchange energy between the atomic spins $i$ and $j$ and $\mathbf{S}_i$, $\mathbf{S}_j$ are the atomic spin vectors for each respective site. The above is commonly known as the extended Heisenberg model, and the key assumption in this model is that the electrons are localised to each atomic site.

### 1.2.3 Anisotropy

Magnetocrystalline Anisotropy refers to the preferential orientation of the magnetisation in relation to a specific crystal lattice. Other forms of anisotropy exist, such as shape and surface anisotropies, but these will not be the topic of much discussion in this thesis and the remainder of this section will be devoted to common forms of magnetocrystalline anisotropy. It arises from the spin-orbit interaction [5, 4, 8] and the simplest phenomenological model of magnetocrystalline anisotropy is the lowest order expansion of a *uniaxial* anisotropy [5]

$$E = K_1 \sin^2(\theta) + K_2 \sin^4(\theta) + ... \tag{1.16}$$

where $\theta$ is the angle from the *easy* axis and $K_1$ and $K_2$ are the second and fourth order uniaxial anisotropy constants. It is often the case that the value of $K_2$ is roughly an order of magnitude smaller than $K_1$ and can be ignored [8]. It is also the case that not all materials have a preferential direction along a single axis. Another common example, and one that will be used in several chapters in this thesis, is cubic anisotropy. For a cubic system with easy-axis orientations along either $x$, $y$ or $z$ directions, the anisotropy energy is given by [5]

$$E = K_1^c \left(m_x^2 m_y^2 + m_x^2 m_z^2 + m_y^2 m_z^2\right) + K_2^c m_x^2 m_y^2 m_z^2 ... \tag{1.17}$$

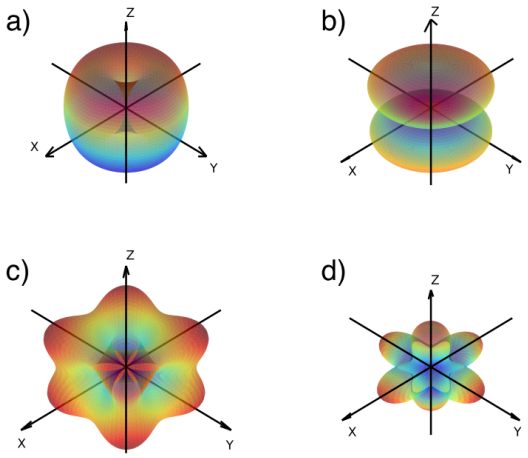


**Figure 1.1:** Anisotropy energy landscapes for (a) uniaxial anisotropy with positive $K_1$, (b) uniaxial anisotropy with negative $K_1$, (c) cubic anisotropy with positive $K_1^c$ and (d) cubic anisotropy with negative $K_2^c$. Taken from Ref. [9].

where we have cubic anisotropy constants $K_1^c$ and $K_2^c$. Like with the uniaxial case, $K_1^c >> K_2^c$ and therefore $K_2^c$ can often be ignored. $m_x$, $m_y$ and $m_z$ are the Cartesian components of the reduced magnetisation. An example of the energy landscapes for uniaxial and cubic anisotropies where the higher order constants have been neglected can be found in Fig. 1.1. For the uniaxial case with positive $K_1$, the energy minimum is along the anisotropy axis. For negative $K_1$, the energy minimum occurs along any orientation in the $xy$ plane. A similar pattern is seen for the cubic case, with positive $K_1^c$ having an energy minimum along either the $x$, $y$, or $z$ axis and negative $K_2^c$ having energy minimum at 45° from each axis.

### 1.2.4 Types of Magnetic Order

Four different types of magnetic ordering will be mentioned throughout this thesis, those are ferromagnetism, antiferromagnetism, ferrimagnetism, and finally paramagnetism. A schematic depiction of each can be found in Fig. 1.2. In ferromagnetic systems, the exchange coupling constant, $J > 0$, is positive, resulting in neighbouring atomic magnetic moments preferentially aligning parallel to one another, yielding a net spontaneous magnetisation. The parallel alignment of the atomic spins leads to a strong magnetisation even in the absence of an external magnetic field, which is a defining characteristic of ferromagnetism. Contrastingly, in antiferromagnetic materi-

als $J < 0$, leading to an antiparallel alignment of adjacent spins and no net moment. The antiparallel configuration of neighbouring atomic spins means antiferromagnets do not exhibit any spontaneous magnetisation. Like with antiferromagnets, ferrimagnetism also possesses negative J, however, the relative concentrations and magnitudes of the magnetic moments allow a net magnetisation to emerge. The uncompensated magnetisation is lower than in ferromagnets due to the opposing antiparallel spins. Finally, paramagnetic systems lack any form of long-range ordering in the absence of an applied field with thermal effects outweighing any exchange interactions. Under the application of a strong magnetic field, a net magnetisation can be observed for paramagnetism as the field partially aligns the randomly oriented atomic moments. Unlike ferromagnetic materials, this induced magnetisation is lost as soon as the external field is removed.

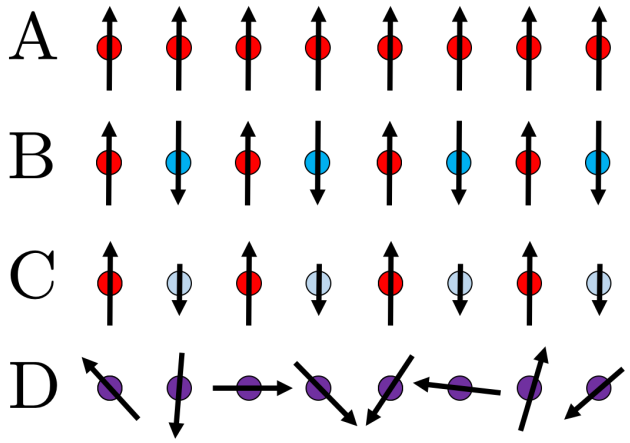


**Figure 1.2:** Schematic representation of the different types of magnetic order. A) Ferromagnetism B) Antiferromagnetism C) Ferrimagnetism D) Paramagnetism.

## 1.3 The Challenges of Recording Media

A brief introduction to magnetic recording was provided in the motivation section, here we will present in greater detail the challenges associated with enhancing the storage density of FM-based HDD technology. As already mentioned, HDD storage devices contain two key components: the platter and the read-write head. The platter consists of ferromagnetic grains which are non-uniformly shaped [10], largely due to the

manufacturing process, with each grain being separated by a non-magnetic material that accumulates at the grain boundaries. This breaks the exchange coupling between neighbouring grains. Typical diameters are between 5 and 10 nm. In an ideal scenario, a single grain would be used to represent a bit state, however in reality a collection of between 10 to 20 grains [11] are grouped together to form the bit state to help with stability. Current methods make use of having the magnetic bits aligned perpendicularly to the thin FM film in what has become known as perpendicular magnetic recording (PMR). Fig. 1.3 shows a schematic of the PMR setup. Panel (a) illustrates the read-write head as it scans the surface of the magnetic recording layer, while panel (b) displays the distinct, non-uniformly shaped grains alongside their associated bit states which are shown as red and blue regions. The materials used for the magnetic recording layer have, for many years, been made of FM CoCr alloys, such as CoCrPt, CoCrTa, and CoCrNb [12] however a transition to FePt layers promises higher areal density [13]. The read-write head is made of two distinct components: The inductive write element, which uses currents pass through a coil to generate a magnetic field, and the read element, which converts the magnetisation orientation of each bit to a digital signal, either using giant magnetoresistance (GMR) or tunnelling magnetoresistance (TMR) - these effects will be discussed in a bit more detail later on. The bit density on conventional PMR-based hard drives is being pushed towards 1.3 $Tb/in^2$ in 2023 with releases such as Western Digital's $2^{nd}$ generation ePMR platform [14]. Further improvements in density and energy efficiency are still needed to cope with the growth in cloud-based storage.

An obvious way to improve processing and storage times would be to decrease the time it takes for the reversal of magnetic bits, reducing the amount of time the write head spends actively generating a magnetic field. Faster reversal can generally be achieved by increasing the strength of the applied field in the write element, which means generating a larger current and an increased loss of energy in the wires in the form of heat. In addition to this, the resonance frequency of FM materials typically sits in the GHz range [16], meaning the switching process is generally restricted to nanosecond (ns)

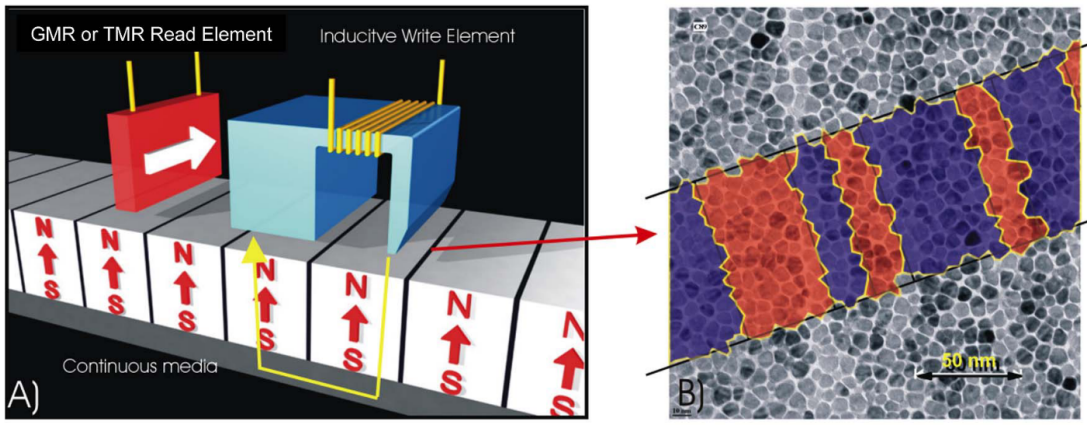


**Figure 1.3:** (a) Schematic diagram of the read-write head passing over the perpendicularly magnetised bits on the platter. (b) TEM micrograph of the magnetic grains on the platter. The magnetisation orientation of the bits is denoted by the red and blue regions. Taken from Ref. [15]. ©2008 IEEE.

timescales. In response to the growing societal need for data, if it is not possible to enhance data processing speeds by reducing the reversal speed to improve efficiency, another approach is to increase bit density by reducing the size of ferromagnetic grains. Shrinking grain size, however, reduces thermal stability, heightening the likelihood of spontaneous bit orientation flips. The probability of a switching event occurring is governed by the Arrhenius-Néel law [17]

$$f = f_0 \exp\left(-\frac{KV}{k_B T}\right) \tag{1.18}$$

where $K$ is the uniaxial anisotropy constant, $V$ is the volume of the grain, $T$ is the temperature, $f_0$ is the attempt frequency (usually ranging from 10s to 100s GHz for ferromagnets) and $k_B = 1.38 \times 10^{-23}$ J K$^{-1}$ is the Boltzmann constant. By decreasing the grain volume, you decrease the magnitude of the exponent in the above, which increases the probability of an individial grain switching. As more grains flip in an idividual bit, the signal to noise ratio (SNR), which is proportional to $\sqrt{N}$ where $N$ is the number of grains in a bit, decreases - making readout of the bit state more difficult. To counteract this, ferromagnets with elevated anisotropy barriers can be used instead. As mentioned in the previous section, the anisotropy keeps the grains pinned along the 1 or 0 directions, with increased anisotropy leading to stronger bit alignment along these orientations. The downside to this is that larger magnetic fields are then required to

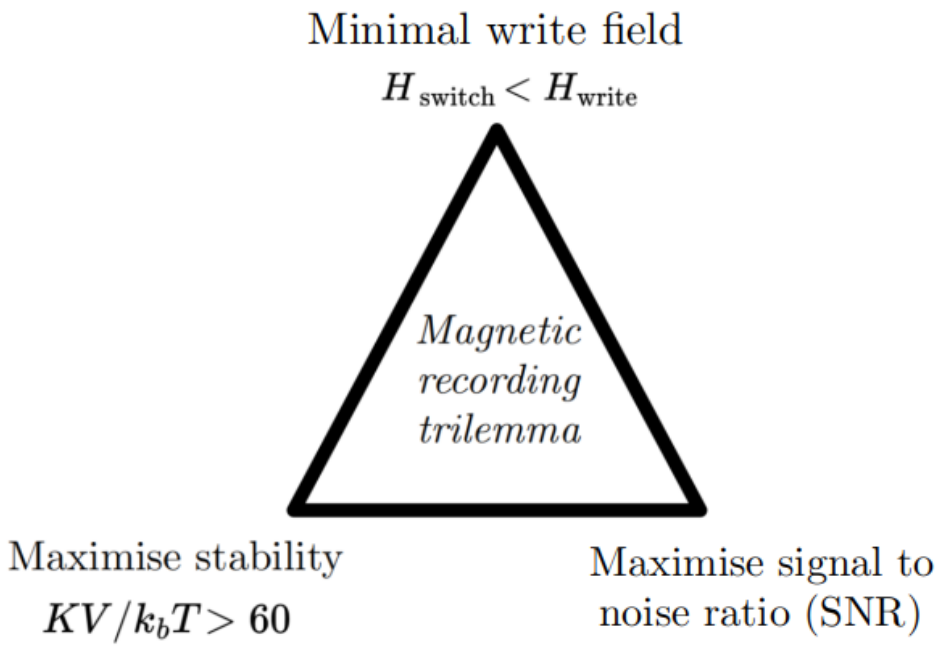


**Figure 1.4:** The magnetic recording trilemma. Adapted from Ref. [18].

push the bits over the increased anisotropy energy barrier. This tradeoff between SNR, stability and field size is known as the *trilemma* of magnetic recording (A schematic of which can be found in Fig. 1.4) and is limiting further development of traditional HDD devices. At the device level, hard disk drives rely on precise electromechanical control to manipulate stored data. Specifically, reading and writing information heavily depends on the rotational speed of the platter, positioning and accuracy of the read/write head, and the switching dynamics of both the ferromagnetic electromagnet in the write heard and free ferromagnetic layer in the GMT/TMR sensing element. Overcoming these limitations is vital for the realisation of AFM based HDD devices, but a detailed analysis of these engineering questions is beyond the focus of the work presented here.

## 1.4 Heat Assisted Magnetic Recording

Heat Assisted Magnetic Recording (HAMR) is a recent advancement in HDD technology that makes use of heating to increase the areal density in ferromagnet HDDs [20–24]. The idea is simple, a near field transducer (NFT) [25] is used to locally heat the FM grains close to the Curie temperature, $T_C$ (the temperature at which the material

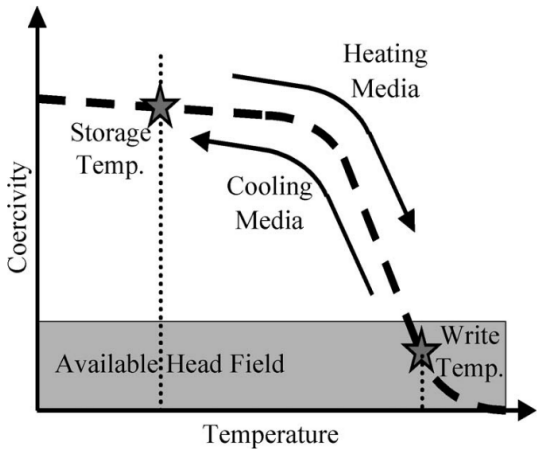


**Figure 1.5:** HAMR schematic. Taken from Ref. [19].

undergoes a phase transition from ferromagnetic to paramagnetic, losing its macroscopic magnetic properties). This large increase in temperature reduces the coercivity, making it easier to switch the grains. A schematic of the process can be found in Fig. 1.5 Because of this reduction in coercivity, materials with a larger anisotropic barrier (such as FePt [13, 26]) can be used with similar fields to those used already in HDD devices when been subject to heating. Because of the higher anisotropy barrier, a higher areal density of grains can be used for HAMR devices. In a review article from 2016 on HAMR technology by Weller *et al.* [27], they expect the areal density to increase from 1 Tb/in$^2$ for conventional HDD to 3-4 Tb/in$^2$ for HAMR devices. HAMR-based HDD enterprise products have recently been announced by Seagate [28] with the release of the Mozaic 3+ platform planned for 2024 [29].

## 1.5 Ultrafast Magnetism

The area of ultrafast magnetism was born in 1996 following the pioneering work of Beaurepaire *et al.* [30] who showed that following the application of a femtosecond (fs) laser pulse to FM Nickel (Ni), the magnetisation would drop significantly within a single picosecond. A figure of the demagnetisation process recorded using time-resolved magneto-optical Kerr effect (MOKE) measurements can be found in Fig. 1.6. It was found that the electron and spin temperatures exhibit different dynamics following the application of the laser, indicating the spin system heats separately from the electronic

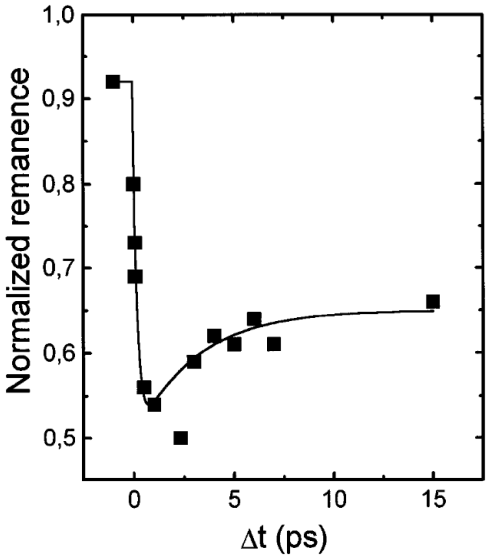


**Figure 1.6:** Transient longitudinal magneto-optical Kerr effect (MOKE) of a Ni(20 nm)/$MgF_2$(100 nm) film for a 7 mJ cm−2 laser pump fluece. Image taken from [**?** ]

system on the picosecond timescale (see Fig. 3 of Ref. [30]). Beaurepaire *et al.* introduced a phenomenological model, known as the three-temperature model (3TM) to describe the demagnetisation process. They attributed it to the laser heating of the electron bath, which is coupled directly to the spin and lattice degrees of freedom. Not long after this initial discovery, picosecond timescale demagnetisation was reported in the other ferromagnetic transition metals (Co, Fe) [31, 32]. The exact mechanisms for ultrafast demagnetisation remains an open topic, although much of the discussion has attributed it to either spin-flip or spin-transport properties, with seminal works supporting both arguments discussed briefly over the next two paragraphs.

In the paper of Koopmans *et al.* [33], they looked to explain the fact that certain elements, such as Gadolinium (Gd), undergo a much slower relaxation, with the demagnetisation taking approximately 100 ps compared to the sub-ps timescales seen for Ni, Fe and Co. They attributed the differing timescales to Elliott-Yafet spin-flip processes, which, without going into much detail, allowed the authors to derive a simple equation for the demagnetisation dynamics that contained an element-specific scaling factor that described the different relaxation times. They determined the scaling factor to be $R \propto a_{\mathrm{sf}} T_C^2/\mu_s$ where $T_C$ is the Curie temperature, $\mu_s$ is the magnetic moment

and $a_{\text{sf}}$ is the probability of a spin flip occurring. In essence, a smaller ratio of $T_C$ to $\mu_s$, which is the case in Gd, leads to much slower relaxation. For a spin-flip induced change in angular momentum to occur, which would be required for this description of ultrafast demagnetisation, there must be a transfer from electronic spin to the lattice subsystem [34, 35], which at the time of publication had not been observed experimentally.

Another mechanism used to explain the ultrafast demagnetisation in the transition metals came from Battiato *et al.* [36], who proposed that demagnetisation arose from superdiffusive spin transport of laser-excited electrons. They developed a semiclassical model of finite elapsed time and transport in space between multiple electronic collisions and numerical results compared well with the experimental data for Ni with roughly a 50% quenching of the magnetisation predicted in the first 200 fs. This prediction challenged the notion that ultrafast angular momentum dissipation was required in any capacity and instead suggested transport effects play a primary role.

Recently, work by Dornes *et al.* [37] demonstrated experimentally using femtosecond time-resolved X-ray diffraction that in ultrafast demagnetisation of thin films of Fe, 80% of the spin angular momentum is transferred to the lattice on a sub-ps timescale. This result showed that interactions between the lattice is essential for fully describing ultrafast demagnetisation in ferromagnetic materials, thus providing strong evidence for a spin-flip mechanism occurring.

### 1.5.1 All Optical Switching (AOS) in Ferri & Ferromagnets

Since the work of Beaurepaire *et al.* [30], much work has gone into the understanding of how optical excitations can be used as a method for ultrafast and efficient magnetic switching. The first observation of all optical switching (AOS) was shown by Stanciu *et al* [38] in 2007, where it was shown in ferrimagnetic GdFeCo that a single 40 fs circularly polarised laser pulse could reverse the magnetic FeCo sublattice within 700 fs. In addition to the heating from the laser, the circular polarisation generates an ef-

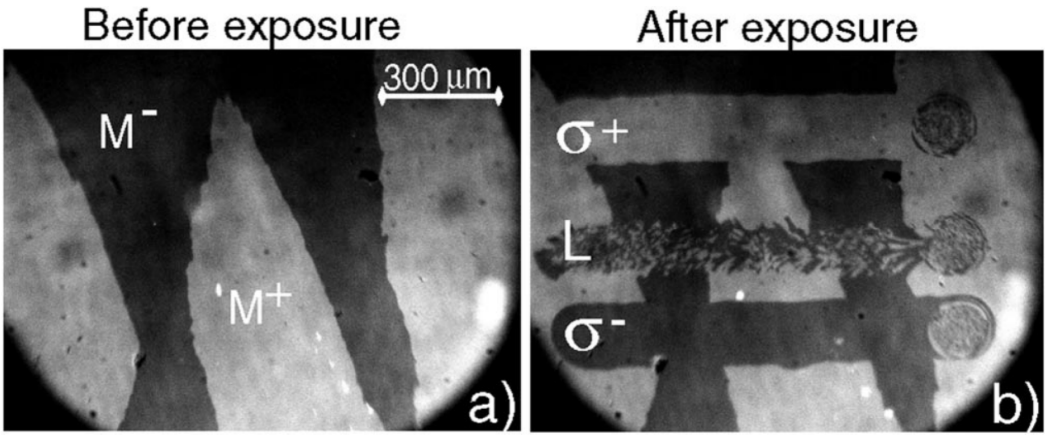


**Figure 1.7:** The effect of ultrashort polarised laser pulses on magnetic domains in $Gd_{22}Fe_{74.6}Co_{3.4}$. (a) Magneto-optical image of the initial magnetic state of the sample before laser exposure. White and black areas correspond to up and down orientations of the magnetisation, respectively. (b) Domain pattern obtained by sweeping at low speed ($\sim 30\mu$m/s) linearly (L) right-handed ($\sigma+$), and left-handed ($\sigma-$) circularly polarised beams across the surface of the sample, with a laser fluence of about 11.4 mJ/cm$^2$. Taken from Ref. [38].

fective magnetic field via the inverse Faraday effect (IFE) with the magnetisation being induced in different directions depending on the helicity of the optical pulse. Fig. 1.8 shows the main result of their work, with the linearly polarised beam generating randomly distributed domains of up and down orientations of the magnetisation in sharp contrast to the left & right-handed helicities, which entirely switch the magnetisation into either an up or down state.

In the experiments of Stanciu *et al.*, the magnetisation dynamics were not measured, and it was not until the experiments of Radu *et al* [39] who revealed that the heating over the compensation point brings the system into what they describe as a non-equilibrium transient ferromagnetic state. The Fe and Gd sublattices exhibit different magnetisation dynamics, as shown in Fig. 1.9, and lose their sublattice magnetisation independently of one another. The ferromagnetic-like state emerges because of the differing speeds in the demagnetisation and reaches a magnitude of 25% of the equilibrium value during the remagnetisation process. The measurements were made with an external field of $\pm 0.5$ T to reinitialise the magnetic order and to allow for independent measurements of the magnetic response of both sublattices. It was believed the external field was essential for triggering switching.

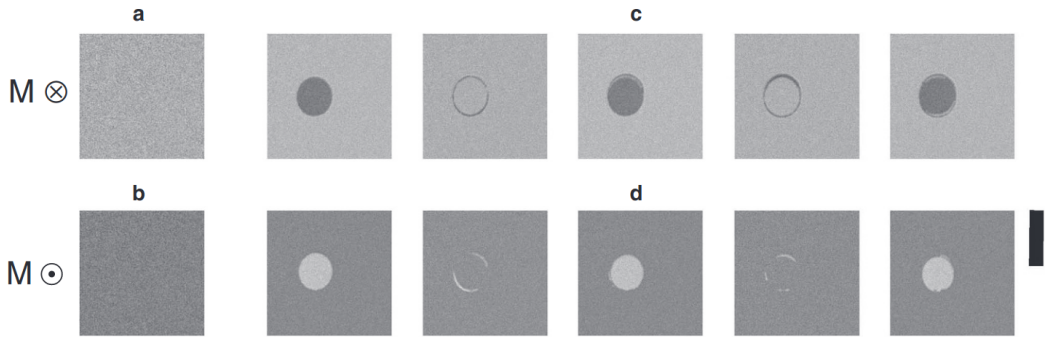


**Figure 1.8:** Panels (a) and (b) show the equilibrium state of a $Gd_{24}Fe_{66.5}Co_{9.5}$. The light and dark grey region represents spin-down and spin-up orientations of the magnetisation. The remaining panels show the film after a 100 fs excitation with N = 1, 2...5 pulses with a fluence of 2.30 mJ/cm$^2$. Each laser pulse excites the same circular region of the film and reverses the magnetisation within it. The scale bar corresponds to 20 $\mu$m. Taken from Ref. [40].

One year later, Ostler *et al.* [40] showed that heating alone can trigger deterministic switching in GdFeCo. Using atomistic simulations following fs laser heating, the net magnetisation could switch due to the transfer of angular momentum between the antiferromagnetically coupled sublattices. Experiments confirmed the result, with single laser pulses reversing the magnetisation regardless of polarisation or initial orientation of the magnetisation. Since then, the interest in deterministic switching using fs lasers in ferrimagnets has grown [41–43], with other systems containing transition and rare-earth metals such as Pt/Co/Gd stacks [44], Tb/Co multilayers [45] and $Mn_2RuGa$ [46] have also been shown to switch following single-shot laser excitation.

Being able to achieve deterministic switching in ferrimagnets using fs laser pulses has been well understood for over a decade now, but it has been only recently that developments in FMs have been made. It has been shown that by combining a FiM with an FM to create a bilayer-type structure, it is possible to induce switching in a FM within 7 ps as a result of the exchange coupling between the two layers [47]. Earlier this year, it was shown that a femtosecond laser pulse can induce switching in layered FM spin valves [48] without the presence of any FiM layers. The reversal in the spin valves has been shown to occur on ps timescales - orders of magnitude faster than the GHz dynamics normally found in ferromagnets. While the mechanism behind switching in

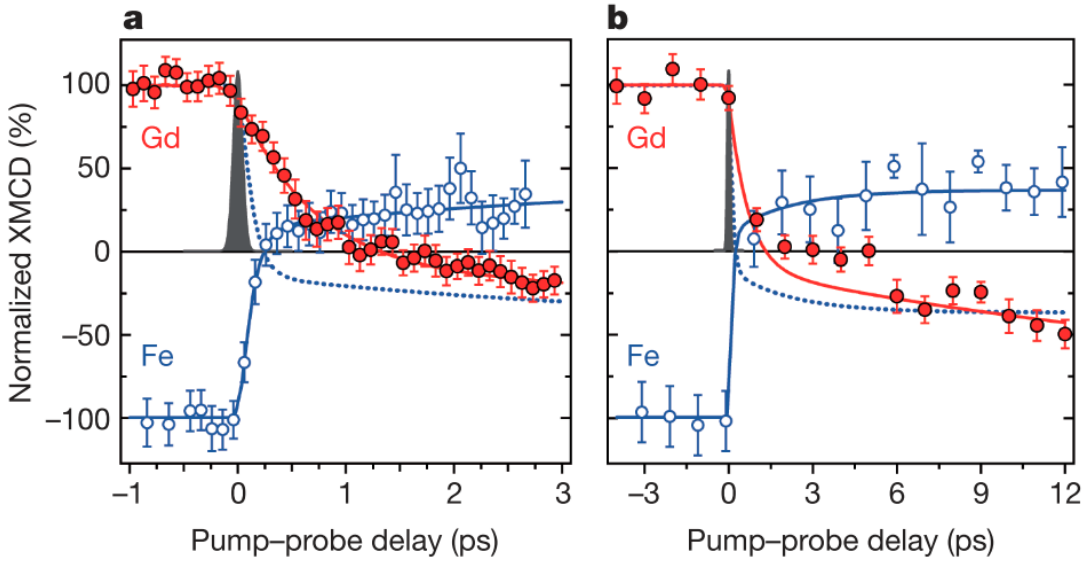


**Figure 1.9:** Time resolved XMCD measurements of Gd and Fe sublattices in the ferrimagnet GdFeCo. Magnetisation dynamics for the first 3 ps following a laser pulse are shown in panel (a) and 12 ps in panel (b). The experiment was performed at a sample temperature of $T = 83$ K for an incident laser fluence of 4.4 mJ cm$^{-2}$. Taken from Ref. [39].

FiMs is well understood, the exact mechanism behind this recent observation is not fully understood.

### 1.5.2 Conventional Applications of Antiferromagnetism

As already mentioned in an earlier section, AFM ordering occurs when the lowest energy state is when neighbouring magnetic moments align antiparallel such that on a macroscopic scale, the net magnetisation of the material is 0. As a result, they react weakly to external magnetic fields and do not produce any stray fields. They were famously described by the discoverer of antiferromagnetism, Louis Néel, in his Nobel Prize winning lecture as "extremely interesting from the theoretical viewpoint, but do not seem to have any practical application" [49]. Since his speech, it has been realised that AFMs do indeed have a role to play in magnetic recording when, in the 1980s, the GMR effect was discovered [50, 51]. What was observed was a change in the electrical resistance in a non-magnetic conductor sandwiched by two ferromagnetic layers depending on the relative orientation of the two surrounding magnetic layers. If the electron spin is misaligned, there is a higher probability of a scattering event occuring when an electron travel from one layer to another. This leads to an increase in the elec-

trical resistance. When the layers are aligned, the electron spin moving through each layer tend to be aligned, resulting in less scattering events. To keep one of the layers fixed while the other is allowed to change orientation, an antiferromagnet is coupled to one of the ferromagnetic layers which pins the magnetisation orientation [52].

GMR heads became the standard method of magnetisation readout in magnetic recording technology up until the industry transitioned to TMR in 2006 [53]. Unlike GMR, TMR works on the principle of quantum tunnelling of electrons from two FM layers (one pinned by an AFM layer) separated by a thin insulator film. Very simply put, if the magnetisation of the two FM are aligned and a current is applied, tunnelling is more likely to occur meaning the system has a lower resistance. The parallel or antiparallel alignment of the layers returns high and low resistance values, which can be used as a binary signal.

### 1.5.3 Néel Spin-Orbit Torques and Switching in Antiferromagnets

Besides their use as pinning layers in read-write heads, the fact AFMs react weakly to external magnetic fields is seen as a potential benefit for use as recording media as it ensures the stability of data well beyond that of ferromagnets, which typically have a retention of $\sim$ 10 years [54]. AFMs also have intrinsically ultrafast dynamics, orders of magnitudes quicker than their ferromagnetic counterparts. The large exchange field that arises as a result of the oppositely aligned sublattices means the resonant frequencies of AFMs is in the THz range [55] compared to GHz for ferromagnets - opening the possibility of magnetic reversal on ultrafast timescales and for uses in THz emitters [56–59] and magnonics [60].

The immunity of AFMs to external applied magnetic fields (the conventional way of generating reversal in FMs) is a barrier holding back the development of AFM devices for spintronic applications. However, recent developments have shown that electrical

switching is possible using current-induced Néel spin-orbit torques (NSOTs). In systems with broken inversion symmetry the spin-orbit coupling leads to carriers with opposite momentum having opposite spin polarization. For example, an electron moving from left to right will have the opposite spin compared to an electron moving from right to left. When a current is applied to a material with broken inversion symmetry and strong Spin-orbit coupling will leads to a non-equilibrium spin polarisation which induces a torque on local magnetic moments [61]. AFMs such as CuMnAs and $Mn_2Au$ have locally broken inversion symmetry (inversion symmetry is preserved over the overall crystal structure, but broken locally due to the ordering at specific lattice sites) meaning an electrical current can induce a spin polarisation local to each sublattice with the resultant torque having an alternate sign for each sublattice. The magnetic moments undergo a rotation in opposite directions while keeping the AFM order.

Switching in AFMs has already been achieved using this technique. In metallic CuMnAs, reversal of the Néel vector ($\mathbf{n} = \mathbf{m_1} - \mathbf{m_2}$ where $\mathbf{m_1}$ and $\mathbf{m_2}$ are the reduced magnetisations of each sublattice) was first observed in the work of Wadley et al. [62] who used electrical currents to generate spin-orbit-torques (SOTs) which induce switching. Similar results have been observed experimentally in $Mn_2Au$ [63–66] and NiO [67]. While switching in AFMs in possible, it has not yet been done on ultrafast timescales, with reversal being attributed to domain propagation processes rather than coherent rotation of the Néel vector. The closest the community has come to experimentally achieving coherent switching is the recent work of Behovits *et al.*, who achieved a deflection of 30° of the Néel vector in $Mn_2Au$ on picosecond timescales following the application of a THz electric field. Much of this thesis will be spent investigating conditions for ultrafast switching in $Mn_2Au$ using computational modelling techniques.

The benefits of AFMs are clear, however, the control of the Néel vector is a problem due to the lack of macroscopic magnetisation, and sophisticated techniques are required to access information on the magnetic order. Computationally, this is not a

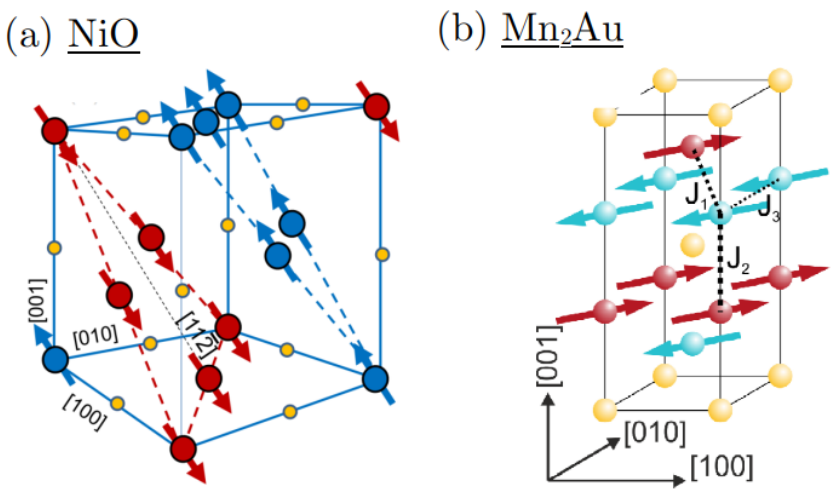


**Figure 1.10:** Unit cell configuration of two AFM materials that are drawing interest for switching applications. (a) NiO, with the Ni sublattices shown in blue/red and the O atoms shown in gold.(b) $Mn_2Au$, with the Mn sublattices shown in blue/red with the Au atoms shown in gold. Images taken from [68] (NiO) and [69] $Mn_2Au$.

problem. Several studies have shown it is possible to induce a reversal in antiferromagnetic NiO [70] and $Mn_2Au$ [71, 72]. In the case of NiO, it was shown that switching using incredibly large square field pulses, with strengths upwards of 15 Tesla, is possible. A comparison of the two crystal structures can be found in Fig. 1.10 While the switching was shown to be on picosecond timescales, being able to generate fields of this size experimentally requires energy-intensive setups. For $Mn_2Au$ it was shown that using staggered fields (i.e. each sublattice receives an equal but opposite magnetic field) that arise from electric field-induced SOTs can lead to picosecond reversal. Much remains unexplored regarding switching in $Mn_2Au$, with open questions regarding simple access to the magnetic order and the effects of pumping at the intrinsic resonant frequencies.

## 1.6 Thesis Outline

The next chapter will detail of the modelling techniques employed within this research project. This is the first multiscale model of an AFM that combines DFT, atomistic and LLB modelling methods. Tests are performed validating the newly developed AFM-LLB in a range of scenarios such as the transverse & longitudinal dynamics,

antiferromagnetic resonance, and thermally induced domain wall motion. Chapter 4 investigates switching in $Mn_2Au$ with the emphasis on driving Néel vector reversal using THz frequency pulses using atomistic spin dynamics with comparisons being made to analytical and additional LLB modelling. Chapter 5 investigates magnetisation reversal in Py/$Mn_2Au$ bilayers as a possible route to overcome the difficulties in read-out of the antiferromagnetic order vector while only observing a moderate slowdown in the THz dynamics as a result of coupling to an FM. Chapter 6 is the final results chapter, and delves into the properties of hypothetical multilayer and thin-films materials further and the possibility of using naturally occurring standing spinwaves as a mediator for more efficient magnetic switching. Concluding remarks and a discussion of possible future work are presented in chapter 7.

# Chapter 2

# Modelling Methods

*We're building something, here, detective, we're building it from scratch.*
*All the pieces matter.*

– *DET. LESTER FREAMON*, The Wire. Created by David Simon.

## 2.1 Introduction

The choice of modelling method generally depends on the length, timescales and type of processes under investigation. On the smallest time and length scales are *ab initio* methods, such as Density Functional Theory (DFT), which is able to describe the behaviour over distances of several unit cells, typically in the Å to nm range. Ideally, the electronic structure and inter-atomic interactions would be solved using the many-body Schrödinger equation for the electron system, but this is computationally impossible due to what is essentially an infinite number of electrons in solids. Calculations of electronic structure using DFT is based on the Hohenberg-Kohn theorems [73], which state that; (i) the ground state electron density is uniquely determined by the external static potential between electrons and nuclei and (ii) the electron density that minimises the total energy gives the ground state electron density and energy. Computationally, working with the electron density is more tractable than the full many-body wave function, thus making calculations of electronic structure for many-electron systems possible. For magnetic systems, DFT is capable of determining exchange interactions, atomic magnetic moments and magnetocrystalline anisotropy. Time-dependent DFT (TD-DFT) can be used to describe some dynamic processes, but the timescale is generally on the order of femtoseconds, making simulations of switching on ps and ns timescales unfeasible. There are a wide range of DFT software packages that have been widely used for electronic structure calculations of magnetic materials, such as QuantumEspresso [74], SPRKKR [75], VASP [76] to name just a few. While no DFT calculations were performed by the author, results from DFT calculations were used as input parameters to modelling work completed as part hence the inclusion of the above short description.

In cases where the dynamics of atomic spins occur over a much longer timescale than the motion of electrons, alternative methods such as Ising models or Atomistic Spin dynamics (ASD) can be used in place of DFT. These models are capable of describing the magnetisation dynamics of discretised atomic spins localised to specific lattice sites using a classical Heisenberg Hamiltonian. Because of these simplifications, simulation timescales can range from fs to ns, making it an ideal modelling technique for applica-

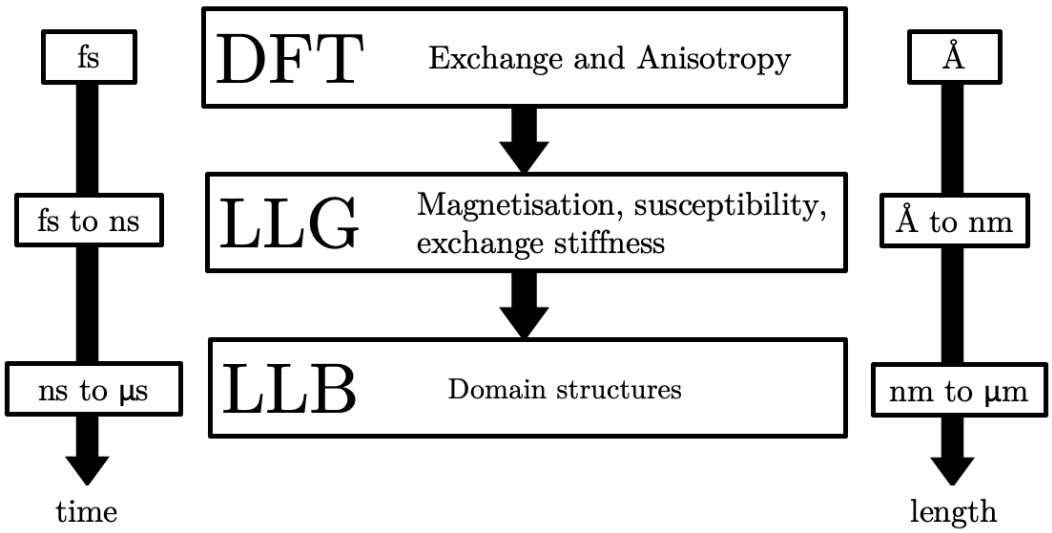


**Figure 2.1:** Schematic showing the differing length and time scales for the magnetic modelling methods in this PhD. By linking the stages together, magnetic processes on µs timescales and µm lengthscales can be investigated with only the unit cell configuration used as an initial input in the DFT stage. This process of linking together different modelling techniques across multiple scales is known as multiscale modelling.

tions from ultrafast switching to domain wall dynamics and will be the main modelling method used as part of this thesis. A short discussion of the Ising model and mean-field approximations (MFA) will be presented in section 2.2 while a more detailed description of ASD, including the Heisenberg Hamiltonian and computational implementation will be given in section 2.3 because of its use throughout all results chapters.

The final modelling method that will be seen in this thesis is micromagnetics. In conventional micromagnetics using the LLG equation, the magnetisation vector is treated as a continuous vector field with the anisotropy and exchange energies being coarse-grained on nm lengthscales. This form of micromagnetics is formulated on the assumption that the strength of the magnetisation remains constant limiting it to simulations at static temperature. Several codes are available with a plethora of features and are implemented with various parallelisation capabilities. These micromagnetic models are particularly useful when attempting to model scenarios in which the dynamics occur across $\mu$m distances and where high frequency spinwaves do not contribute to the dynamics, for example, when modelling domain structures or vortex core dynamics. Some of the more notable software packages for LLG-based micromagnetics are Mu-

max [77] and OOMMF [78], which, according to Google Scholar, have 2856 and 2214 citations respectively as of 27/09/23. Another micromagnetic option is the use of the Landau-Lifshitz-Bloch (LLB) equation which has an intrinsic temperature dependence and describes a collection of atomistic spins, using what is known as a macrospin, which typically has dimensions between 10-100 nm. The substitution of usually $10^4$ to $10^5$ atomistic spins with a single macrospin allows for simulations with dynamics variations in temperature on time and lengthscales that are not achievable using atomistic models. Using the LLB model, it is possible to replicate atomistic simulations with a fraction of the computational cost and also simulate up to µs with µm system sizes. A more detailed introduction and mathematical description of the LLB model will be presented in section 2.4.

It is possible to link together the different modelling processes in what has become multiscale modelling. The input parameters in DFT are the crystal structure and ground state magnetic configuration. The outputs are the atomic magnetic moments, exchange, and anisotropy constants. These are then used as inputs into the atomistic model, which is able to calculate the temperature dependence of the magnetisation, anisotropy and exchange that can then be used as input into an LLB model to describe processes on $\mu$m and $\mu$s length and timescales without having to use any experimental results.

## 2.2 Ising and Mean Field Models

In cases where the precessional dynamics of the magnetisation are not important, it is possible to calculate equilibrium properties using static models. The first of which to be discussed briefly in this section is the atomistic Ising model [79, 80]. This model only includes spin-up and spin-down states, meaning the anisotropy energy is, in essence, infinite as the spin orientation cannot deviate from the anisotropy axis. The Hamiltonian

for the Ising model is given by

$$\mathcal{H} = -\sum_{i \neq j} J_{ij} s_i s_j - \mu_o \mu_B \sum_i H_i s_i \tag{2.1}$$

where spin $i$ is $s_i = \pm 1$ and $J_{ij}$ is the exchange energy between spin $i$ and spin $j$. The most common solver for the Ising model is the metropolis algorithm [81]. The steps are simple: (i) randomly select a spin in the lattice, (ii) flip it, (iii) calculate the change in energy $\Delta\mathcal{H}$ using Eq. 2.1, (iv) if $\Delta\mathcal{H} < 0$, accept the change, (v) if $\Delta\mathcal{H} < 0$, the change can be accepted with probability $e^{-\Delta\mathcal{H}/k_B T}$.

Instead of using Monte-Carlo algorithms, Mean Field Approximations (MFA) can be used to describe magnetic systems by reasoning that a magnetic spin experiences an average exchange field arising from the neighbouring spins. This effective field is assumed to be equal for all atomic spins. This approach was first proposed by Weiss in the early 20th century [82] who stated that the effective field is directly proportional to the magnetisation $H_{\text{eff}} = k\langle s \rangle$ where $k$ is the molecular field constant. For a lattice with $z$ nearest neighbours with interacting with exchange $J_{ij}$ subject to a magnetic field $H$ incorporated into a mean-field approach, Eq. 2.1 becomes

$$\mathcal{H} = -\sum_i s_i \left( z J_{ij} \langle s \rangle - \mu_o \mu_B H \right) \tag{2.2}$$

where we have effective field $H_{\text{eff}} = z J_{ij} \langle s \rangle - \mu_o \mu_B H$. It can be shown [5] that the magnetisation is given by the equation

$$\langle s \rangle = \tanh \frac{\mu_o \mu_B H + z J_{ij} \langle s \rangle}{k_B T} \tag{2.3}$$

Other mean-field quantities will be introduced as and when needed for the remainder of the thesis, but the magnetisation was provided here as an example of how the simplicity of these approximations allows for first approximation to the static properties of a magnetic system and a fast comparison to experiment. The downside to the above approximations is that magnetic materials cannot always be accurately described with

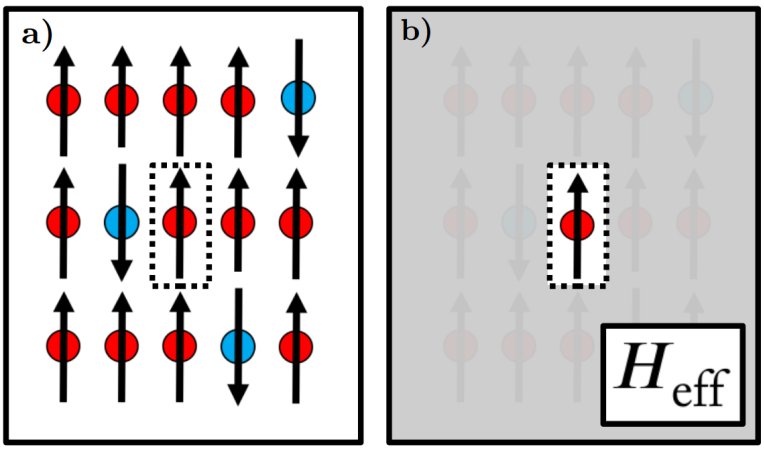


**Figure 2.2:** (a) The Ising model with $s_i = \pm 1$ and (b) the mean field approximation where the spins experience an effective field which contains contributions from the exchange and any externally applied fields.

a simple nearest-neighbour exchange approach as the exchange constants can vary greatly along different directions in real-space. Mean field approximations also fail to account for the propagation of spin deviations (spinwaves) at low temperatures - leading to an overestimation of the magnetisation. At high temperatures, long-range thermodynamic fluctuations govern the magnetisation, and therefore a local exchange field gives a poor approximation and again underestimates the true value. For a more accurate description, dynamical equations of motion that treat spin as a quantity that can vary in 3D can be used.

## 2.3 Atomistic Spin Dynamics

Atomistic Spin dynamics will be the most used modelling method used in this thesis. Like with the Ising model, the magnetic moment is treated as localised to each atomic site however the moment is not restricted to up or down states, but instead can orientate itself along any direction on a unit sphere. The dynamic evolution of the magnetisation undergoes a damped precession in the presence of a magnetic field and it was Landau and Lifshitz in the 1930's that first derived an equation of motion that described the equation of motion [83]

$$\frac{\partial \mathbf{M}}{\partial t} = -\gamma(\mathbf{M} \times \mathbf{B}) - \frac{\gamma\alpha}{M}\mathbf{M} \times (\mathbf{M} \times \mathbf{B}) \tag{2.4}$$

Where $\mathbf{M}$ is the magnetisation, $\mathbf{B}$ is an external magnetic field and $\gamma = 1.76 \times 10^{11}$ $\mathrm{T}^{-1}$ $\mathrm{s}^{-1}$ is the gyromagnetic ratio of the electron. The first term in the above is the precession of the magnetisation around the magnetic field axis, and the second term describes the damping towards the field direction. A schematic of the two terms can be found in Fig. 2.3. The damping parameter, $\alpha$, determines the relaxation rate towards the direction of the effective field. Gilbert later derived an equation that accounted for damping effects on the precession of the magnetisation and this form of the equation became the preferred choice in micromagnetic and atomistic simulation methods [84]. The LLG equation in its implicit form as derived by Gilbert was given by

$$\frac{\partial \mathbf{M}}{\partial t} = -\gamma \mathbf{M} \times \mathbf{H} + \frac{\lambda}{M} \mathbf{M} \times \frac{\partial \mathbf{M}}{\partial t} \tag{2.5}$$

where $\lambda$ is the Gilbert damping parameter. The above is difficult to solve numerically due to the differential being present on both sides of the equation and it can be shown that in the case of isotropic damping, i.e the damping is equal for all magnetisation directions, the LL and LLG equations take identical forms (see Appendix A for a derivation) with the damping parameters for the LL and LLG equation being related with the expression $\alpha = \gamma\lambda/(1+\lambda^2)$. For the modelling of atomic spin moments, the preferred form of the Landau-Lifshitz-Gilbert equation is given as [85]

$$\frac{\partial \mathbf{S}_i}{\partial t} = -\frac{\gamma_i}{(1+\lambda_i^2)\,\mu_i} \left( \mathbf{S}_i \times \mathbf{H}_i + \lambda_i \mathbf{S}_i \times \mathbf{S}_i \times \mathbf{H}_i \right) \tag{2.6}$$

where, instead of $\mathbf{M}$, we have $\mathbf{S}_i$ which is the unit vector orientation of a spin at lattice site $i$ with magnetic moment $\mu_i$, and $\mathbf{H}_i$ is the effective field. The exact form and contributing terms to the effective field in an atomistic framework will be discussed shortly. The macroscopic magnetisation can be related to $\mathbf{S}_i$ via

$$\mathbf{m} = \frac{1}{N} \sum_{i}^{N} \mathbf{S}_i \tag{2.7}$$

where $N$ is the total number of atoms in the system. Much of this thesis will be on the discussion of AFMs. For AFMs with two opposing sublattices, the above will always

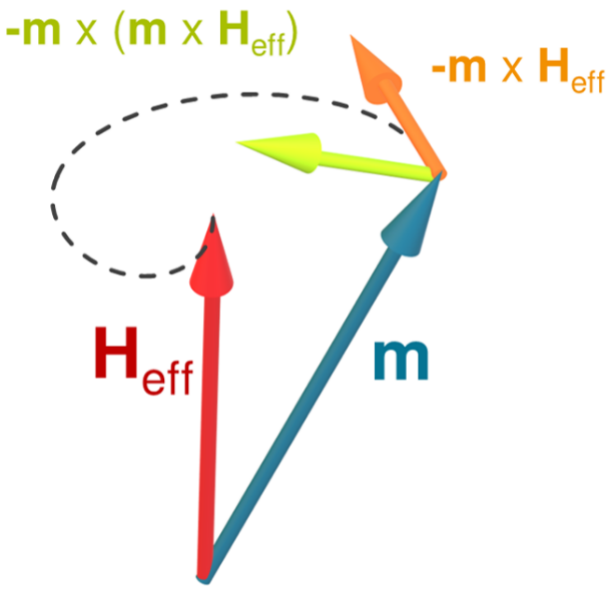


**Figure 2.3:** LLG schematic. Image taken from Ref. [86].

be zero and it is therefore useful to describe the order vector in AFMs (known as the Néel vector) as

$$\mathbf{n} = \frac{1}{N_\kappa}\sum_{i}^{N_\kappa}\mathbf{S}_i - \frac{1}{N_\nu}\sum_{i}^{N_\nu}\mathbf{S}_i \tag{2.8}$$

where $n$ denotes the Néel vector, and $\kappa$ and $\nu$ denote the two different sublattices. ASD as a modelling tool has proved incredibly useful for the magnetism community.

### 2.3.1 Generalised Heisenberg Hamiltonian

An atomistic system has a spin Hamiltonian that combines all magnetic interactions into a single equation. Perhaps the most common form of spin Hamiltonian that contains the three most common terms found in atomistic modelling of magnetic materials: the exchange energy, anisotropy energy and Zeeman energy, is written as

$$\mathcal{H} = \underbrace{-\sum_{\langle ij\rangle} J_{ij}\mathbf{S}_i\cdot\mathbf{S}_j}_{\text{exchange}} \underbrace{- d_z\sum_i \left(S_i^z\right)^2}_{\text{uniaxial anisotropy}} \underbrace{-\mu_s\mathbf{B}\cdot\sum_i\mathbf{S}_i}_{\text{magnetic field}} \tag{2.9}$$

The constant $J_{ij}$ is the exchange coupling constant between site $i$ and site $j$. The second term describes the uniaxial anisotropy with constant $d_z$ acting on site $i$ along the $z$-axis. The final term is the Zeeman energy, which describes the interaction between

the atomistic spins and any applied fields. The Zeeman energy is at a minimum when the spins are in alignment with the magnetic field. There exists some cases where the exchange is anisotropic, such as FePt [87] where the exchange can be written as a 3x3 tensor $\underline{\underline{\mathrm{J_{ij}}}}$. For isotropic systems, which will be the case for all results chapters, the isotropic exchange constant can be related to the extended 3x3 tensor through the relation $J_{ij} = \frac{1}{3}\,\mathrm{Tr}\left\{\underline{\underline{\mathrm{J_{ij}}}}\right\}$.

Many additional terms have not been included here as they will not feature for the remainder of this thesis, but they do deserve a mention because of their importance in different atomistic studies. For example, there exists other forms of exchange, such as the Dzyaloshinskii–Moriya interaction (DMI) [88, 89], $\mathcal{H}_{i,j}^{\mathrm{DMI}} = \mathbf{D}_{ij} \cdot \left(\mathbf{S}_i \times \mathbf{S}_j\right)$, which competes with the Heisenberg exchange seen above and leads to non-collinear alignment of neighbouring atomic spins giving rise to structures such as skyrmions [90], spin spirals [91] and vortices [92]. The existence of DMI was first proposed and observed in non-centrosymmetric crystals [88, 93]. Tunable DMI was shown to exist in at the interface between ferromagnetic and heavy metals with a large spin-orbit coupling [94, 95]. The majority of this thesis will be focused on collinear AFMs, and therefore the inclusion of antisymmetric exchange terms in the atomistic Hamiltonian have been neglected.

Contributions from the dipolar interactions, which gives rise to a demagnetising field, have also been ignored. The demagnetising field that arises from dipole-dipole interactions is generally much weaker on the length scales usually considered in atomistic modelling and, in the particular case of AFMs, the antiparallel alignment of neighbouring moments cancels out any macroscopic magnetisation, and thus, there is no net magnetisation to generate the demagnetization field. For this thesis, it will be neglected because of the focuse on AFMs, and the $\mu$m (typical distances for continuum based micromagnetics) lengthscales at which it plays an important role compared to mostly nm sized systems that will be simulated as part of this thesis. The Hamiltonian is

related to the effective field found in the LLG equation through the relation

$$\mathbf{H}^i_{\text{eff}} = -\frac{\partial \mathcal{H}}{\partial \mathbf{S}_i} + \mathbf{H}^i_{\text{th}} \tag{2.10}$$

where $\mathbf{H}^i_{\text{th}}$ describes the thermal effects, which will be discussed in the next section.

### 2.3.2 Langevin Dynamics

The addition of a thermal contribution was first proposed by Brown in the 60s [96]. It is described by a Gaussian white noise process with the spin fluctuations from the thermal fields being of a much higher frequency than the spin precession [97]. Throughout this thesis, the noise in the atomistic spin model will remain uncorrelated on all time-scales, although coloured noise processes have been investigated as an alternative to frequency-independent noise processes [98, 99]. The stochastic Gaussian white noise process is described by the following set of equations [100]

$$\begin{aligned} \langle \xi_{i\alpha}(t) \rangle &= 0 \\ \left\langle \xi_{i\alpha}(t) \xi_{j\beta}\left(t'\right) \right\rangle &= \frac{2\lambda k_B T}{\gamma \mu_s} \delta_{ij} \delta_{\alpha\beta} \delta\left(t - t'\right) \end{aligned} \tag{2.11}$$

where $\langle ... \rangle$ denotes the average, $i, j$ are atom locations, $\alpha, \beta = x, y, z$ are the Cartesian coordinates, $\delta_{ij}$ is the Kronecker delta function and the prefactor $2\lambda k_B T/\gamma\mu_s$ is the strength of the fluctuations. The Kronecker deltas state that the Cartesian components of $\xi_i$ are uncorrelated, and the random thermal fields acting on different magnetic moments are independent [101]. The term $\mathbf{H}^i_{\text{th}}$ in Eq. 2.10 is given by [102]

$$\mathbf{H}^i_{\text{Th}} = \xi(t) \sqrt{\frac{2\lambda k_B T}{\gamma \mu_s \Delta t}}, \tag{2.12}$$

where $T$ is the temperature of the simulation, $\Delta t$ is the size of the timestep, $k_B$ is the Boltzmann constant and $\xi(t)$ is a Gaussian distribution with a mean of zero.

### 2.3.3 Implementation

Several open-source software packages exist each with a wide large range of features and parallelisation capabilities. Some of the more notable ones are VAMPIRE [85] originating from the University of York, UPPASD [101] from Uppsala University in Sweden, and Spirit [103] from the universities of Iceland and Aachen. While a number of atomistic packages are available, all the atomistic modelling as part of this work has been completed using a code that has been developed entirely as part of this PhD. The reason for this is two-fold; firstly, some of the modelling methods and analysis techniques required as part of this PhD are simply not available in other packages. And secondly, it is a good exercise in enhancing understanding the key physics in ASD, as well as a knowledge of high-performance and parallel scientific computing software development. The atomistic code built as part of this PhD has been written with C++ for the serial CPU implementation and CUDA for the parallelised GPU implementation. The next three sections will cover some of the key components of the package, including the integration method, GPU parallelisation and calculation of the exchange field, which is the main overhead in the integration process.

#### Heun Integration

The choice of numerical integration method for the LLG equation is a trade-off between speed and stability of the numerical solution. The LLG equation can be solved using implicit schemes which generally allows for greater numerical stability for larger timesteps. These schemes usually involve solving a set of linear equations, which for ASD systems with atomic moments numbering in the range $10^5$-$10^6$ for a typical system, is not a computationally viable option. For ASD it is therefore necessary to use explicit and semi-implicit solvers. Some of the more notable methods include the Depondt-Mertens [104] scheme and Mentinks semi-implicit scheme [105]. By far the the most common integration method for ASD is the Heun scheme [102], which will be used for all ASD and micromagnetic LLB simulations in the thesis. This method makes use of a predictor and corrector Euler steps, from which the average gives the result of the spin orientation at the next time step. A schematic of the method can be

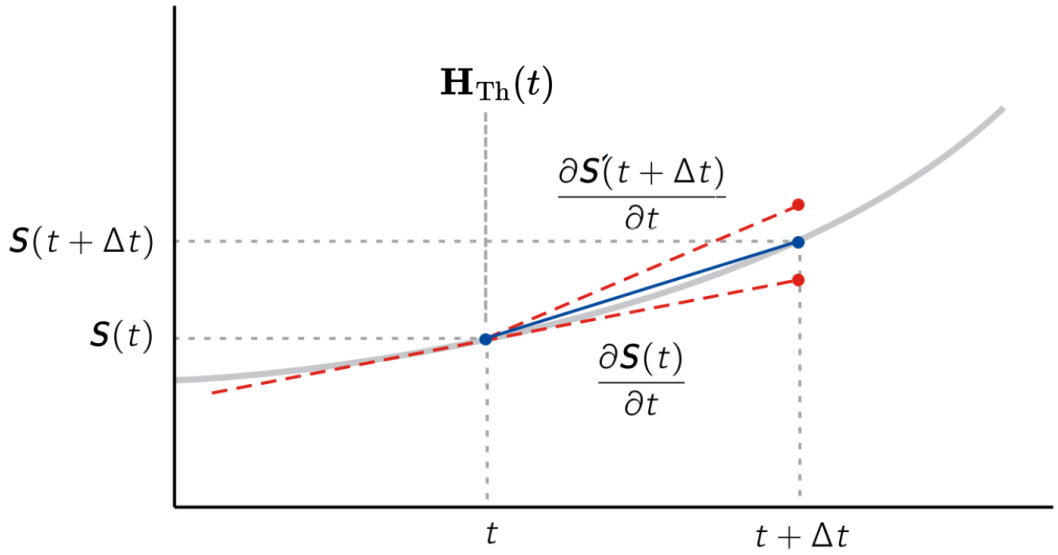


**Figure 2.4:** Heun schematic. Adapted from Ref. [106].

found in Fig. 2.4. The *predictor* is a straightforward Euler step. For the LLG equation, this would be

$$\mathbf{S}'(t+\Delta t) = \mathbf{S}(t) + \Delta t \frac{\partial \mathbf{S}(t)}{\partial t} \tag{2.13}$$

the predictor step is used in the corrector step to calculate the final spin position

$$\mathbf{S}(t+\Delta t) = \mathbf{S}(t) + \frac{1}{2}\left[\frac{\partial \mathbf{S}(t)}{\partial t} + \frac{\partial \mathbf{S}'(t+\Delta t)}{\partial t}\right]\Delta t \tag{2.14}$$

the length of the spin vector is not preserved after the predictor and corrector and therefore must be renormalised to ensure stability. The other important point is that the effective field must also be updated for both corrector and predictor steps. The stochastic term remains the same between the two.

### Calculation of the Exchange Interaction

The exchange interaction is usually the main cause of computational expense. If we imagine an atomistic system whereby each spin interacts with all others, the integration time scales quadratically process, $O(N^2)$, making simulations using single CPU cores increasingly difficult with increasing system size. It is often the case that long-range interaction can be neglected while still accurately capturing the relevant magnetisation dynamics. However, in cases such as FePt [107], the interactions are usually taken

into account up to 5 unit cells away meaning the calculation of the exchange field at site $i$ involves the summation of upwards of 1000 neighbours. To ease the workload it is possible to perform the summation over the neighbouring spins as a convolution in systems where there exists a translationally invariant lattice. By transforming the spin and exchange matrices into Fourier space via a fast-Fourier transform, performing a straightforward multiplication of the two transformed matrices, then converting back to real space. The integration time reduces to $O(N \log N)$ [108]. In real space the exchange field for site $i$ is given by the equation

$$H_{\text{ex}}^{i} = \sum_{\langle ij \rangle} J_{ij} \mathbf{S}_{j} \tag{2.15}$$

After applying a Fourier transform of the spin lattice and exchange matrix. The field in Fourier space becomes

$$H_{\text{ex}}^{k} = J_{k} \mathbf{S}_{k} \tag{2.16}$$

The Fourier transform of the exchange matrix has to be performed only once prior to any integration of the LLG equation. Once the above element-wise multiplication has been completed in Fourier space, the result is inverse Fourier transformed to give the updated exchange field.

### GPU parallelisation

Graphical Processing Units are pieces of computer hardware that have seen a tremendous amount of development over the course of the 21st century due to the growing popularity in video games, and, more recently, the birth of cryptocurrency, which relies on GPUs for the verification of transactions. GPUs contain a larger number of processing cores connected to the global memory of the card. Because the integration of the LLG equation depends only on the effective field at the previous timestep, the memory requirements are generally pretty low, with 5-10s GB needed for say a simple cubic system with nearest neighbour exchange containing upwards of $10^6$ atomic spins. The entire spin system can be passed to a single GPU without having to transfer data back and forth from the GPU to CPU for a single integration step. The integration

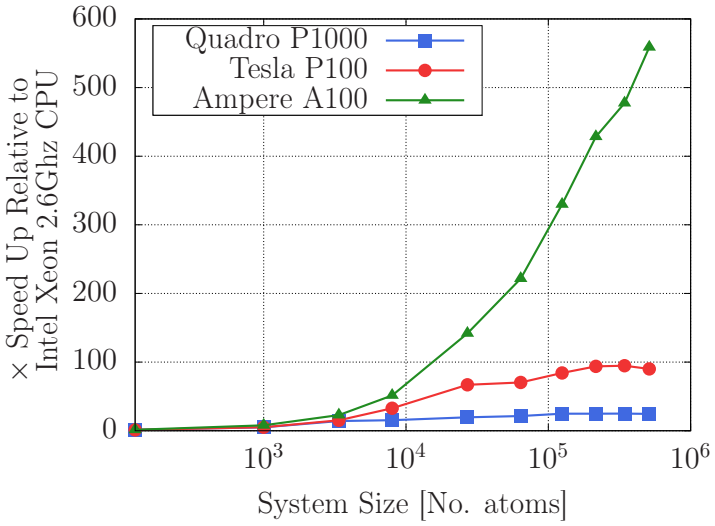


**Figure 2.5:** The relative speed-up of using GPU hardware compared to the single core of an Intel Xeon 2.6 GHz CPU. The neighbouring exchange interactions were calculated using the real space method which is a $O(N^2)$ process for single CPU core computation.

of the spin system can be passed to separate GPU cores which can be completed independently of one another and then transferred back to the CPU for analysis and producing outputs. The increase in performance can be significant and a comparison of the relative speedup for three GPUs against a single core of an Intel Xeon 2.6GHz CPU can be found in Fig. 2.5. The three GPUs differ greatly in performance, with the Quadro P1000 (blue squares) being a small form factor card, the Tesla P100 (red circles) being found in some older generation HPC facilities, and the A100 (green triangles) representing the state of the art in GPU units. Most large-scale tier-1 and tier-2 HPC facilities are in the process of transitioning to GPU nodes with A100, which can cost upwards of £5000 in today's market. The Intel Xeon is a relatively low performance CPU by today's standards with much higher performing units being available on the market. Its selection rests on the fact it is the most widely used CPU on the Sheffield Hallam HPC cluster.

## 2.4 The Landau-Lifshitz-Bloch Equation

In a classical micromagnetic framework, the length of the magnetisation vector, $\mathbf{M}$, cannot vary and therefore simulations with transient changes in temperature are not

possible. In the case of Atomistic Spin Dynamics (ASD), the change in magnetisation length arises from the increased magnitude of the noise processes and when averaged over every spin, there is a reduction in the magnetisation length. In the 1990s, Garanin [109] derived a macroscopic equation specifically for FMs that could account for dynamic changes in magnetisation length known as the Landau-Lifshitz-Bloch (LLB) equation. Instead of atomistic spins localised to lattice sites, we simulate a collection of spins, known as a macrospin, using a single equation of motion. A schematic representation can be found in Fig. 2.6. The number of spins that can be approximated using a single macrospin generally depends on the process under investigation. For cases where the magnetisation varies coherently at all points in space, a single macrospin would be sufficient to accurately describe the dynamics of the system. For systems with spatial variation in the magnetisation, such as domain walls, the size of the macrospin depends on the exchange length. For simple uniaxial anisotropy can be calculate via $\sqrt{A/K}$ where $A$ is the exchange stiffness and $K$ is the uniaxail anisotropy constant. For soft materials where $K$ is small, the exchange length is often 10s nm thus allowing for larger cell sizes while ensuring an accurate numerical solution. For hard magnets such as FePt, the exchange length can be around 1 nm, meaning small cell sizes are essential to ensure stability [5]. It is common to determine the optimal cell size through a convergence study, where the relative energy error of the domain wall compared to an analytical expression for a domain wall is calculated as a function of micromagnetic cell size.

Unlike the atomistic model where the input parameters are material constants, the inputs into the LLB model are rather temperature-dependent functions, namely: (i) the magnetisation, $m(t)$, which describes how the magnetisation reduces as a function of temperature. (ii) the susceptibility, $\tilde{\chi}(T)$, which refers to the response of a system to a magnetic field, $\partial m/\partial B$, and (iii) the exchange stiffness, $A(T)$, which quantifies the resistance to changes in the magnetisation orientation of neighbouring spins. These values can either be taken from experimental measurements, analytical approximations, or, taken from simulation results from atomistic models as part of a multiscale

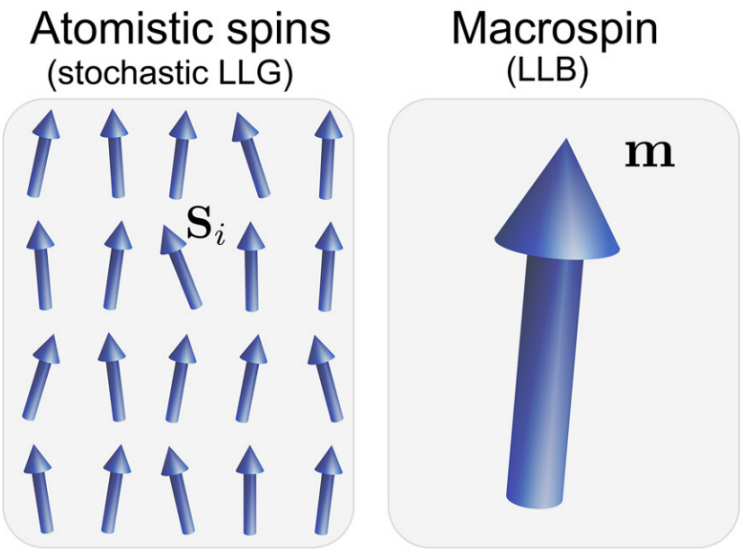


**Figure 2.6:** Schematic representation of the LLG and LLB models for a ferromagnet. In an atomistic model, the dynamics are calculated for every spin $\mathbf{S}_i$ using the stochastic LLG equation. The macrospin model described the dynamics of the average magnetisation of a collection of spins $\mathbf{m} = \sum_i \langle \mathbf{S}_i \rangle / N$, where $N$ is the number of spins in the macrospin, using the LLB equation. Image taken from Ref. [110].

modelling approach. The LLB model was later extended for ferrimagnets with magnetisation below the critical temperature [111]. Extensive work already exists using the LLB formalism for ferro and ferrimagnets, some of the more notable works include multiscale modelling and simulations of ferromagnetic resonance [26, 112] in FePt, ultrafast magnetisation dynamics in ferromagnetic alloys [113], and ultrafast switching in ferrimagnetic TbFeCo [114]. The general LLB equation excluding any stochastic noise is given by [109]

$$\frac{1}{\gamma}\frac{d\mathbf{m}_\nu}{dt} = -\left[\mathbf{m}_\nu \times \mathbf{H}_{\text{eff},\nu}\right] + \alpha_\parallel^\nu \frac{\mathbf{m}_\nu \cdot \mathbf{H}_{\text{eff},\nu}}{m_\nu^2}\mathbf{m}_\nu - \alpha_\perp^\nu \frac{\left[\mathbf{m}_\nu \times \left[\mathbf{m}_\nu \times \mathbf{H}_{\text{eff},\nu}\right]\right]}{m_\nu^2} \tag{2.17}$$

As with the LLG equation seen previously, the LLB equation contains a precessional (term one) and damping term (term three) but it also contains a term that accounts for the changes in the magnetisation length (term two). The subscript $\nu$ denotes the sublattice. For ferromagnets, there is just one sublattice. For collinear antiferromagnets, there is two. For complex ferrimagnets and non-collinear antiferromagnets it can take a range of values. Instead of the Gilbert damping, $\lambda$, we now have two effective damping parameters $\alpha_\perp$ and $\alpha_\parallel$ which define the transverse and longitudinal relaxation

rates. The dimensionless transverse effective damping parameter is defined differently above and below the critical temperature for ferromagnets. It is given by:

$$\alpha_{\perp} = \begin{cases} \lambda\left(1 - \frac{T}{3T_C}\right), & T < T_C \\ \lambda\frac{2T}{3T_C}, & T > T_C \end{cases} \tag{2.18}$$

There exists no LLB equation capable of describing the above critical temperature in ferrimagnets but the above holds for $T > T_C$ for collinear AFMs. The longitudinal damping parameter is defined for all temperatures as:

$$\alpha_{\parallel}^{\mathrm{FM}} = \lambda\frac{2T}{3T_C}. \tag{2.19}$$

The effective field for the ferromagnetic LLB is given by:

$$\mathbf{H}_{\text{eff}} = \mathbf{B} + \mathbf{H}_a + \mathbf{H}_{ex} + \mathbf{H}_{\parallel} \tag{2.20}$$

Where $\mathbf{B}$ is any externally applied magnetic fields, $\mathbf{H}_a$ is the anisotropy field, $\mathbf{H}_{ex}$ is the exchange field between neighbouring macrospins. It is important to note that the exchange term, $\mathbf{H}_{ex}$, term describes the exchange between ferromagnetically coupled macrospins, not the exchange coupled sublattices. The final term, $\mathbf{H}_{\parallel}$, is the longitudinal field. As with the transverse damping parameter, the longitudinal field is defined differently above and below the critical temperature

$$\mathbf{H}_{\text{eff}}^{\parallel} = \begin{cases} \frac{1}{2\tilde{\chi}_{\parallel}}\left(1 - \frac{m^2}{m_e^2}\right)\mathbf{m}, & T \lesssim T_C \\ \\ -\frac{1}{\tilde{\chi}_{\parallel}}\left(1 + \frac{3}{5}\frac{T_N}{T - T_N}m^2\right)\mathbf{m}, & T \gtrsim T_C \end{cases}, \tag{2.21}$$

where $\tilde{\chi}$ and $m_e$ are temperature-dependant quantities, namely the parallel susceptibility and equilibrium magnetisation respectively. As already mentioned the LLB model has already been utilised using a multiscale approach for ferro and ferrimagnets. The first multiscale description of an AFM using the LLB model will be presented in chapter 3.

## 2.5 Spinwaves

Just as phonons are quantised excitations of the crystal lattice, magnons are quantised excitations in spin dynamics. The propagation of the magnon leads to a periodic change in the spin across the lattice, known as a spin-wave [115]. In atomistic spin dynamics, we take the classical limit and the quantisation of spin is replaced by a continuous deviation on the unit sphere. A classical spin-wave is therefore a spatially periodic variation in the spin orientation [106]. A schematic can be found in Fig. 2.7. The spin-wave dispersion relation, i.e. the spinwave frequencies as a function of the wavevector, $\omega(k)$, can be calculated theoretically using both atomistic spin dynamics and linear spinwave theory (LSWT). A brief mathematical description of dispersion relation calculations using ASD and LSWT will be given over the next couple of sections. Experimentally, the spinwave dispersion can be determined from neutron scattering experiments because of the coupling of neutron spin to the electronic spin [116]. The first measurement of the SW dispersion using neutron scattering was reported by Elliott and Lowde [117] in the 1950s who measured a quadratic scaling with $\omega \propto k^2$ for low values of $k$ in FM Fe. The first measurement of the linear scaling of the dispersion for low values of $k$ predicted for AFMs was first seen in hematite in 1960 by Goedkoop and Riste [118]. Since then the interest in spinwaves has grown significantly culminating in the formation of a research area known as magnonics, which explores the idea of using spinwaves instead of electrical currents as carriers of digital information [119, 120, 60, 121]. The main advantage behind using spinwaves to transmit information is that it promises lower energy dissipation than traditional electronics, where large amounts of energy is lost as heat. In multiscale modelling of magnetic materials, the dispersion relation is an important validation of the magnetic parameters calculated using *ab-initio* methods, especially in the case of systems with antiferromagnetic, DMI or other non-trivial magnetic ordering, where the atomistic system cannot be approximated by simply using a nearest-neighbour model. Modelling methods can be used to predict the microscopic properties such as the exchange constants and anisotropy, with neutron scattering experiments providing independent experimental confirmation.

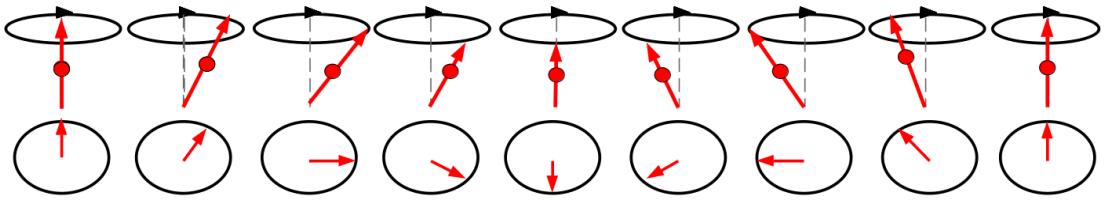

**Figure 2.7:** Schematic of a spinwave propagation along a ferromagnetic 1D spin chain. The apparent change in length in the top pane is due to the visualisation angle, not as a result of physical changes in the spin length. Bottom pane shows a top-down view of the spin orientation.

### 2.5.1 Linear Spin Wave Theory

Linear Spin Wave Theory (LSWT) is an analytical approach that can be applied at low temperatures to calculate the spinwave dispersion. It assumes small fluctuations in the spin orientation and overall long-range order from mean-field theory. Its success in describing results from neutron scattering experiments has resulted in the creation of dedicated software packages for LSWT calculations [122, 123]. A simple derivation of the dispersion relation for a system with a single atom in the unit cell can be found in section 4.2 of Ref. [106], but will be included here as the equations will be frequently referenced. Beginning with the LLG equation and neglecting the damping term and constants in Eq. 2.6 and also assuming our Heisenberg Hamiltonian only contains exchange interaction leaves

$$\frac{\partial \mathbf{S}_i}{\partial t} = \sum_j J_{ij} \left( \mathbf{S}_i \times \mathbf{S}_j \right) \tag{2.22}$$

Assuming the spins are the mean value plus some small deviation from the ground state, i.e

$$\mathbf{S}_i = \langle \mathbf{S} \rangle + \delta \mathbf{S}_i \tag{2.23}$$

The equation of motion becomes:

$$\begin{aligned} \frac{\partial}{\partial t} \left( \langle \mathbf{S} \rangle + \delta \mathbf{S}_i \right) &= \left( \langle \mathbf{S} \rangle + \delta \mathbf{S}_i \right) \times \sum_j J_{ij} \left( \langle \mathbf{S} \rangle + \delta \mathbf{S}_j \right) \\ \frac{\partial}{\partial t} \delta \mathbf{S}_i &= \sum_j J_{ij} \langle \mathbf{S} \rangle \times \delta \mathbf{S}_i - \langle \mathbf{S} \rangle \times \sum_j J_{ij} \delta \mathbf{S}_j \end{aligned} \tag{2.24}$$

given that $\langle \mathbf{S} \rangle$ is a constant and taking a Fourier transform:

$$\begin{aligned} \frac{\partial}{\partial t}\delta\mathbf{S}_k &= \sum_j J_{ij} \langle \mathbf{S} \rangle \times \delta\mathbf{S}_\mathbf{k} - \langle \mathbf{S} \rangle \times J_\mathbf{k}\delta\mathbf{S}_\mathbf{k} \\ \frac{\partial}{\partial t}\delta\mathbf{S}_k &= (J_0 - J_\mathbf{k}) \langle \mathbf{S} \rangle \times \delta\mathbf{S}_\mathbf{k} \end{aligned} \tag{2.25}$$

where $J_0$ is just the sum over the exchange interactions and the Fourier transform of $\sum_j J_{ij}\delta\mathbf{S}_j$ is the same as the convolution taken between Eqs. (2.15) and (2.16). If we assume the magnetisation is along the $z$-axis ($\langle \mathbf{S} \rangle = (0, 0, \langle S \rangle)$) and and assume wave like solutions

$$\begin{aligned} \delta S^x_\mathbf{k}(t) &= \delta S_\mathbf{k}(0) \mathrm{e}^{+\mathrm{i}\omega t} \\ \delta S^y_\mathbf{k}(t) &= \delta S_\mathbf{k}(0) \mathrm{e}^{-\mathrm{i}\omega t} \\ \delta S^z_\mathbf{k}(t) &= 0 \end{aligned} \tag{2.26}$$

the equation of motion becomes

$$\begin{pmatrix} \delta S^x_\mathbf{k} \\ \delta S^y_\mathbf{k} \\ \delta S^z_\mathbf{k} \end{pmatrix} = -\mathrm{i} \left(J_0 - J_\mathbf{k}\right) \langle S \rangle \begin{pmatrix} -\mathrm{i}\omega_\mathbf{k} & 0 & 0 \\ 0 & \mathrm{i}\omega_\mathbf{k} & 0 \\ 0 & 0 & 0 \end{pmatrix} \begin{pmatrix} \delta S^x_\mathbf{k} \\ \delta S^y_\mathbf{k} \\ \delta S^z_\mathbf{k} \end{pmatrix} \tag{2.27}$$

Finally, we end with the dispersion relation

$$\omega_\mathbf{k} = \left(J_0 - J_\mathbf{k}\right) \langle S \rangle \tag{2.28}$$

LSWT is usually taken as good approximation for temperatures $T < 0.75 T_C$ [106]. For FMs and collinear AFMs, the magnetisation in this range can be assumed to scale linearly with temperature. Beyond this point, spinwave-spinwave interactions become important leading to a breakdown in agreement between ASD and LSWT [106]. It is possible to derive the well-known equation for the spinwave dispersion for FMs by assuming nearest-neighbour coupling, $J$, with two neighbours along the $x$ direction with separation, $a$, at $T = 0\mathrm{K}$ ($\langle S \rangle = 1$). We can pull out the prefactor $\gamma/\mu_S$ which

we can assume was absorbed into the exchange constant in Eq. 2.22 to give

$$\begin{aligned}\omega_{k_x} = J_0 - J_{\mathbf{k}} &= 2\frac{J\gamma}{\mu_S} - \sum_{n.n}\frac{J\gamma}{\mu_S}e^{ik_x r} \\ &= 2\frac{J\gamma}{\mu_S} - \frac{J\gamma}{\mu_S}e^{ik_x a} - \frac{J\gamma}{\mu_S}e^{-ik_x a} \\ &= \frac{2J\gamma}{\mu_S}(1 - cos(k_x a))\end{aligned} \tag{2.29}$$

where $n.n$ represents a sum over the nearest neighbours. For materials with more than one atom per unit cell, such as ferrimagnets and antiferromagnets, the spinwave frequencies are given by the eigenvalues of the matrix [124]

$$\begin{bmatrix} \sum_n^N J_0^{ln} - J_{\mathbf{k}}^{ll} & -J_{\mathbf{k}}^{ln} \\ -J_{\mathbf{k}}^{ln\,*} & \sum_l^N J_0^{nl} - J_{\mathbf{k}}^{nn} \end{bmatrix} \tag{2.30}$$

where $N$ is the number of atoms per unit cell, $l, n$ are the atom indices, and $*$ denotes the complex conjugate.

### 2.5.2 Calculation of the Spin Waves Dispersion Within Atomistic Spin Dynamics

The dispersion relation can be calculated directly from atomistic spin dynamics via calculations of the dynamic structure factor [101]:

$$\mathcal{S}(\mathbf{k},\omega) = \frac{1}{N\sqrt{2\pi}}\sum_{\mathbf{r},\mathbf{r}'} \mathrm{e}^{\mathrm{i}\mathbf{k}\cdot(\mathbf{r}-\mathbf{r}')}\int_{-\infty}^{+\infty} \mathrm{e}^{\mathrm{i}\omega t} C\left(\mathbf{r}-\mathbf{r}',t\right)\mathrm{d}t \tag{2.31}$$

where $N$ is the number of terms in the summation and $C\left(\mathbf{r}-\mathbf{r}',t\right)$ is the correlation function, defined as

$$C\left(\mathbf{r}-\mathbf{r}',t\right) = \left\langle \mathbf{S}_{\mathbf{r}}(t)\mathbf{S}_{\mathbf{r}'}(0)\right\rangle - \left\langle \mathbf{S}_{\mathbf{r}}(t)\right\rangle\left\langle \mathbf{S}_{\mathbf{r}'}(0)\right\rangle \tag{2.32}$$

Computationally, the above is easily calculated by taking a discrete fast Fourier transform (FFT) in space and time of the spin lattice [106]

$$\mathcal{S}(\mathbf{k},\omega) = \mathrm{FT}_{(t)}\left[\mathcal{W}\left(\mathrm{FT}_{(\mathbf{r})}\left[\mathbf{S}(\mathbf{r},t)\right]\right)\right] \tag{2.33}$$

where $\mathcal{W}$ is usually the Hamming windowing function [125]

$$\mathcal{W}(t) = 0.54 - 0.46\cos\left(\frac{2\pi t}{\tau - 1}\right) \tag{2.34}$$

The calculations of dispersion relations in this thesis are on periodic lattices with periodic boundary conditions - ideal for spatial Fourier transforms. However, the stochastic dynamics in the time domain means the simulation may end with a truncation of the periodicity in time. The windowing function reduces the weights of the time series data points towards the edge of the simulation window, reducing spectral leakage. In cases where the spin-lattice is not periodic, the system size is doubled in size with spin values of 0 to prevent pollution from wrap-around data from the far ends.

# Chapter 3

# Multiscale Modelling of $Mn_2Au$: From *ab-initio* to Micromagnetics

*"And now," cried Max, "let the wild rumpus start!"*

– *MAURICE SENDAK*, Where the Wild Things Are.

## 3.1 Introduction

As mentioned in the introduction to this thesis, the main problem with AFMs is the ability to control, as well as read-out, the magnetisation dynamics because of the lack of net magnetisation. Two materials, $Mn_2Au$ and CuMnAs [65, 126–130] have been proposed for device applications because of the ability to control the magnetic state using electric fields. The induced torque as a result of the application of electrical currents, known as Néel spin-orbit torques (NSOT), is sufficient to induce Néel vector dynamics as a result of the strong spin-orbit coupling in these materials. Both materials have relatively high critical temperatures with experimental measurements placing the Néel temperature of $Mn_2Au$ between 1300 and 1600 K [131] and around 480 K for CuMnAs [132], making them ideal for room temperature applications. Experiments so far have not taken advantage of the intrinsically fast dynamics of AFMs with current-driven switching being attributed to domain wall processes [62, 65], rather than taking advantage of the THz frequency resonance mode. Of the two materials introduced here, The larger anisotropy and higher critical temperature make $Mn_2Au$ a more promising candidate for future applications.

In this chapter, we present a complete multiscale model of the AFM $Mn_2Au$. The multiscale model builds on from previously completed *ab-initio* calculations By S. Ruta and J. Jackson. Here, we calculate the thermal equilibrium properties using ASD and use the results as input into a macrospin AFM-LLB model. The transverse dynamics are presented in the context of antiferromagnetic Resonance (AFMR) with comparisons made to ASD and analytical approximations. We then introduce the longitudinal term in the AFM-LLB model and compare the dynamics from ASD and LLB simulations for step and transient temperature changes. Finally, as an example where both the longitudinal and transverse components of the AFM-LLB are important, we present a comparison for thermally induced domain wall motion induced by a temperature gradient along a thin film. The process of starting with first-principles calculations and ending with a description on micromagnetic length scales is known as multiscale modelling. This is the first study of its kind where both the transverse and longitudinal

processes of a collinear AFM has been accurately described within an LLB framework. The main results of this chapter are published in:

- Hirst, J., Atxitia, U., Ruta, S., Jackson, J., Petit, L., & Ostler, T. (2022). Temperature-dependent micromagnetic model of the antiferromagnet $Mn_2Au$: A multiscale approach. *Phys. Rev. B*, 106(9), 094402.

## 3.2 Atomistic Parameterisation

### 3.2.1 Exchange Constants and Magnetic Moment

The parameters for the atomistic model can be obtained via two methods. The first option is to reverse engineer the values from experimental observations. For ferromagnets, the critical temperature can easily be related to the exchange constant $J_{i,j}$ through a mean-field approximation [133]

$$J_{ij} = \frac{3k_B T_c}{\epsilon z} \tag{3.1}$$

where $k_B$ is the Boltzmann constant, $z$ is the number of nearest neighbours. The value $\epsilon$ is crystal structure dependent and is calculated using spin-wave theory. An extensive list of $\epsilon$ values can be found in Ref. [133]. The magnetic moment can be easily related to the saturation magnetisation, $M_s$ through the relation $\mu_s = M_s a^3/n$, where $a^3$ is the volume of the unit cell and $n$ is the number of atoms in the unit cell. As discussed in section 2.1, another option for the parameterisation of the microscopic constants is to use of *ab-initio* methods such as DFT. One method that goes beyond standard DFT approaches is the quasiparticle self-consistent GW (QSGW) approximation [134] which has been used previously to provide an accurate description of complex magnetic materials [135–137]. The "G" and "W" in the approximation represent the Green's function and screened Coulomb Interactions. A thorough description of the GW approximation can be found in Ref. [138]. The QSGW calculations of the magnetic moment, anisotropy and exchange constants were not performed as part of this thesis, but by collaborators under the scope of the overall project. The mathematical details of the QSGW method are not presented here, but in summary, the QSGW method calculates the electron density (as is the case with DFT) then creates a quasiparticle self-energy

using many-body perturbation theory which is iterated until it is minimised. This self-energy is calculated using the GW approximation. The main benefit to this method is that it is able to capture how the behaviour of an electron in the system is influenced by its own interactions with other electrons, which is usually underestimated in standard DFT [139]. In general, QSGW is more computationally demanding but is considered a more accurate and systematic method [134]. The *ab-initio* QSGW results for $Mn_2Au$ presented in this section were performed by S. Ruta and J. Jackson. The validation of the parameters, namely the calculation of the Néel temperature and spinwave dispersions were performed as part of this PhD. Simulation results for these quantities will be presented later in this chapter.

The calculations were performed using a full-potential linear muffin-tin orbital (FP-LMTO) method using the Questaal software package [140]. The structure used as the input in the calculations was taken from Ref. [131] with lattice constants $a = b = 3.30$ Å and $c = 8.537$ Å. The unit cell for $Mn_2Au$ can be found as an inset in Fig. 3.1 to aid with visualisation. To reduce computational workload while still accurately capturing accurate magnetisation dynamics and temperature-dependent properties. The first four sets of neighbouring exchange interactions are used. These are shown by red circles in Fig. 3.1. For the exchange constants $J_1, J_2$ & $J_3$ there are four interactions for each atomic site, for $J_4$ there is just one. The magnetic moment was determined to be $\mu_s = 3.87\mu_B$. Experiments by Barthem et al. obtain a value of $\sim 4\mu_B$ with theoretical work by Shick et al. [141] as well as Selzer et al. [142] calculating values of $\mu_s = 3.20\mu_B$ and $\mu_s = 3.74\mu_B$, respectively.

### 3.2.2 Anisotropy

The *ab-initio* calculations yield a strong negative uniaxial anisotropy constant along the $z$-direction of $d_z = 0.903$ meV, which, using the relation $H_a = \frac{2d_z}{\mu_s}$ equates to a field of 8 T. The Néel vector therefore sits in the $xy$-plane with no preferential direction within the $xy$-plane. In this chapter, an additional uniaxial anisotropy constant is included along the [100] direction with strength $d_x = 0.035$ meV as calculated by Shick et al.

| Constant | Value | Unit |
|---|---|---|
| Lattice constant, $a$ | 3.330 | Å |
| Lattice constant, $c$ | 8.537 | Å |
| Magnetic moment, $\mu_s$ | 3.8663 | $\mu_B$ |
| Exchange constant, $J_1$ | -5.3422 | meV |
| Exchange constant, $J_2$ | 0.6484 | meV |
| Exchange constant, $J_3$ | -0.6341 | meV |
| Exchange constant, $J_4$ | -6.8986 | meV |
| Sum of FM exchange, $J_{0,vv}$ | 2.5934 | meV |
| Sum of AFM exchange, $J_{0,v\kappa}$ | -30.8040 | meV |
| Uniaxial anisotropy in $z$ direction, $d_\parallel$ | -0.0663 | meV |
| Uniaxial strain anisotropy in $x$ direction, $d_\parallel^*$ | 0.0026 | meV |

**Table 3.1:** Parameters used in the atomistic model of $Mn_2Au$. The damping is varied in some sections and is therefore not included in the above table. The anisotropy constants used in this chapter differ from those in chapters 4 & 5.

[141] thus giving the Néel vector a single favoured orientation. It will be seen in chapters 4 and chapter 5 (which looks at reversal in $Mn_2Au$ and $Mn_2Au$/Py Bilayers) that a different, more careful treatment of the anisotropy is used. The main objective of this chapter is the verification of the AFM-LLB model, and a simple uniaxial anisotropy such that the system has a single preferential orientation makes the validation easier, especially when it comes to temperature-dependent domain wall dynamics. It is known that there exists a fourth-order anisotropy constant that keeps the Néel vector along one of 4 directions in the $xy$ easy-plane [142, 143] that approximately scales with the temperature as $\sim m^{10}$. This would make calculations of domain wall widths and velocities incredibly computationally expensive within the atomistic model at elevated temperatures due to the weakening of the anisotropy. We therefore opt to use a single strain uniaxial constant, $d_\parallel^*$ within easy-plane to for the proof of concept of the AFM-LLB model.

## 3.3 Spinwave Dispersion

The spinwave dispersion for bulk $Mn_2Au$ is shown in the top pane of Fig. 3.2. Atomistic Simulations were performed at four different temperatures of 0.1K (blue), 300K

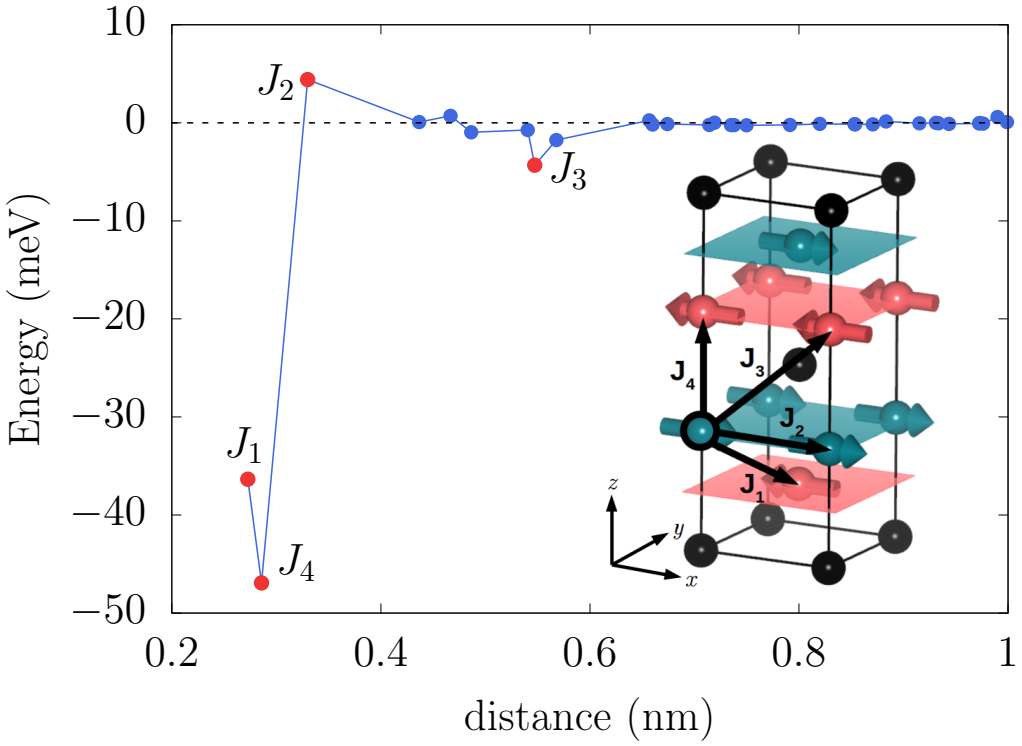


**Figure 3.1:** The exchange interaction strength as a function of distance with the $Mn_2Au$ unit cell shown as an inset. The exchange interactions used in this work are labelled $J_1$ to $J_4$. The exact values can be found in Table 3.1. The Au atoms are shown in black and the Mn sublattices/planes are shown in blue and pink.

(red), 600K (orange) and 900K (green). The methods for calculating the dispersion are outlined in Sec. 2.5.1 & 2.5.2. The bottom left panel in Fig. 3.2 shows the first Brillouin zone, with the path for the dispersion curve shown as a red line. The axes have been arbitrarily scaled to aid in visualisation of the path. the atomistic data, the points represent the highest amplitude frequency for each k-point. The data for each k-point is smoothed to prevent outliers from being identified as maximum values. The damping was set to a low value of $\lambda = 0.001$ to increase the lifetime of the spinwave modes. As expected, the agreement at close to 0 K is perfect. With increasing temperature, the LSWT underestimates the frequencies, particularly at the edge of the Brillouin zone due to spinwave-spinwave interactions. For the LSWT calculations, the temperature dependence is found by scaling the spinwave spectrum at 0K to the equilibrium magnetisation. This is equivalent to $\langle S \rangle$ in Eq. (2.28). Ideally, the spinwave spectrum would have been calculated for all the high symmetry points however compu-

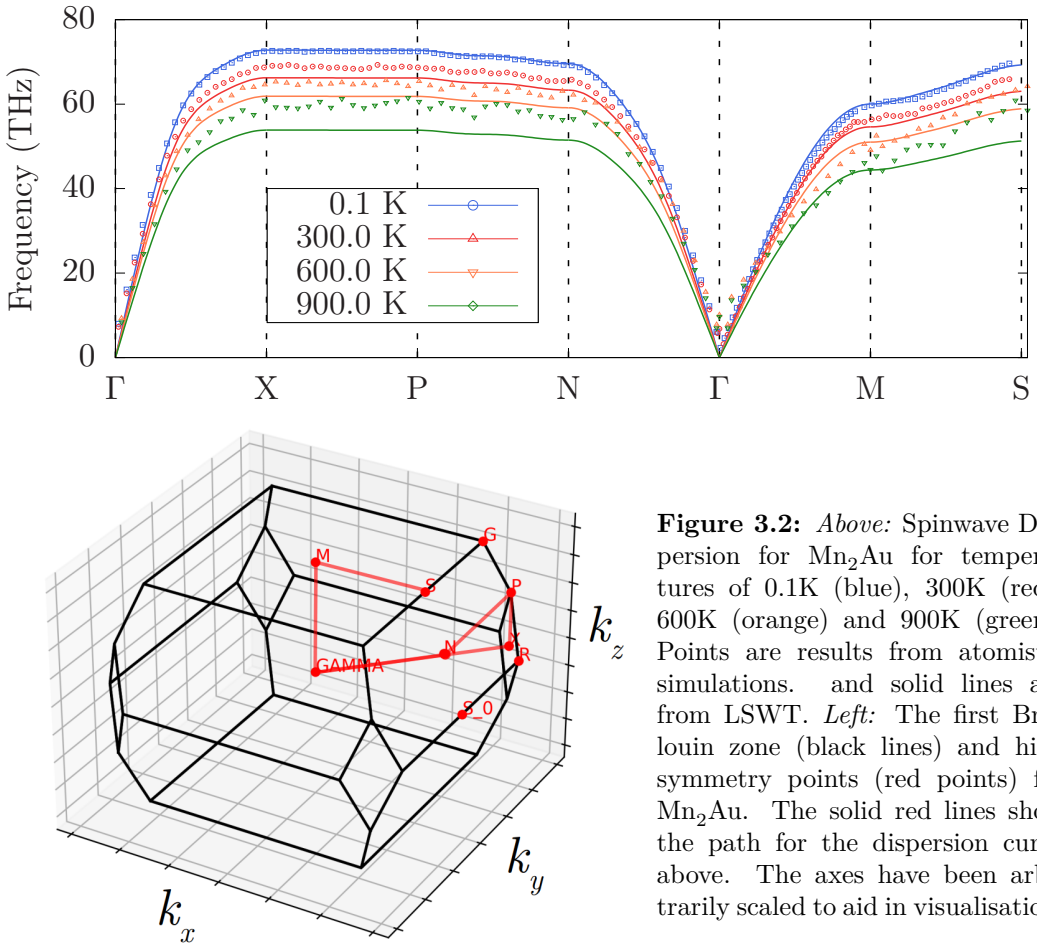


**Figure 3.2:** *Above:* Spinwave Dispersion for $Mn_2Au$ for temperatures of 0.1K (blue), 300K (red), 600K (orange) and 900K (green). Points are results from atomistic simulations. and solid lines are from LSWT. *Left:* The first Brillouin zone (black lines) and high symmetry points (red points) for $Mn_2Au$. The solid red lines show the path for the dispersion curve above. The axes have been arbitrarily scaled to aid in visualisation.

tationally this can be rather problematic. The transition from symmetry points where the incremental ratio in $\Delta k_x : \Delta k_y : \Delta k_z$ contains non-integer values means you cannot move exactly along the desired path leading to inaccurate dispersion curves. This can be alleviated to some degree by increasing the system size in the atomistic simulations but for some paths, this was not a feasible option. Regardless, LSWT and ASD show good agreement for the calculated paths. A comparison to experiment would have been key for the validation of the $J_{ij}$ values but at present, no data exists in the literature for this material.

## 3.4 Equilibrium Magnetisation and Susceptibility

The need to calculate the temperature-dependent properties is two-fold; firstly, for comparison to experimentally measured $T_N$. And secondly, to obtain profiles for the input

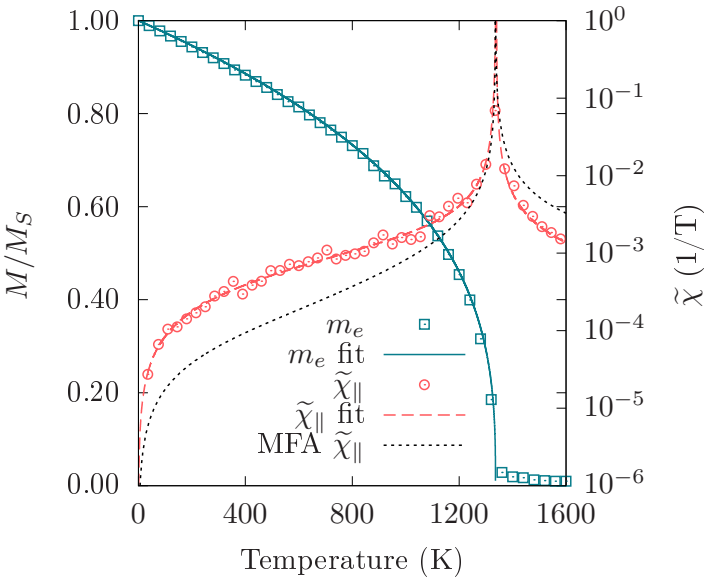


**Figure 3.3:** The sublattice magnetisation of $Mn_2Au$ as a function of temperature. The solid line is a fit to the expression $M/M_S = m_e(T) = (1 - T/T_N)^b$. The circular points show the longitudinal susceptibility, $\tilde{\chi}_\parallel(T)$, the fit function can be found in Eq. (3.4). The dotted line shows the longitudinal susceptibility as calculated using a mean-field approximation.

functions in the LLB model, namely the susceptibility, magnetisation and exchange stiffness. For the susceptibilities and magnetisation as a function of temperature (the exchange stiffness is presented in a later section), simulations were conducted with $30 \times 30 \times 30$ unit cells of $Mn_2Au$ with periodic boundary conditions. The damping parameter, $\lambda$, was set to 1.0 for both sublattices to allow for a faster equilibration. The magnetisation is shown by the empty squares in Fig. 3.3. The solid blue line shows a fit to the equation $M/M_S = m_e(T) = (1-T/T_N)^b$ with free fitting parameters $T_N$ and $b$. These provide an estimate for the critical temperature for an infinite bulk system. From the fit values of $T_N = 1335$ K and $b = 0.34$ are obtained. For an infinite system, the parameter $b$ approaches 1/3 in the Heisenberg model with frequency-independent white noise. A discussion of the scaling of $m(T)$ using different approaches can be found in Ref. [99].

The susceptibility is calculated in the atomistic model by measuring the fluctuations

of the magnetisation along a specific Cartesian direction

$$\tilde{\chi}_{\alpha}(T) = \frac{\mu_s N}{k_B T}\left(\langle S_{\alpha}^2\rangle - \langle S_{\alpha}\rangle^2\right) \tag{3.2}$$

where $\alpha = x, y, z$ is the Cartesian components of the magnetisation, $\langle ... \rangle$ denotes an average over all spins, and $k_B T$ is the thermal energy. Due to the strong uniaxial anisotropy constant $d_z$ the parallel anisotropy is taken as an average of the $x$ and $y$ components of the sublattice magnetisation. The parallel susceptibility is therefore given by the equation

$$\tilde{\chi}_{\parallel}(T) = \frac{\mu_s N}{2k_B T}\left(\langle S_x^2\rangle + \langle S_y^2\rangle - \langle S_x\rangle^2 - \langle S_y\rangle^2\right) \tag{3.3}$$

Because of the divergence at the critical temperature, alongside the magnetisation curve, can be a good way to calculate critical temperature. The parallel susceptibility is fitted to a high-order polynomial that is not derived from any kind of mean-field approximation but has been selected such that it diverges at the $T_N$ and captures the overall general trend well. Similar fitting processes have been used previously for multiscale models of both ferrimagnetic GdFeCo [97] and ferromagnetic FePt [107]. Because of the divergence, the fit parallel susceptibility is split below and above $T_N$. The piece-wise fit function is given by the equation

$$\tilde{\chi}_{\parallel}(T \lesssim T_N) = a_0 \frac{1}{T_N - T} + \sum_{i=1}^{8} a_i (T_N - T)^i \tag{3.4}$$

$$\tilde{\chi}_{\parallel}(T \gtrsim T_N) = b_0 \frac{1}{(1 - T/T_N)} + b_1 \frac{1}{(1 - T/T_N)^2} \tag{3.5}$$

where $a_i$ and $b_i$ are the free fitting parameters. A table of the values to the atomistically calculated susceptibility can be found in Tab. 3.2. The pink circles and solid pink line in Fig. 3.3 show the longitudinal susceptibility calculated from ASD and the fit using Eq. (3.4) and coefficients found in Tab. 3.2. Good agreement is observed between ASD and the fit for all simulated temperatures.

| Coefficient | Value |
|---|---|
| $a_0$ | $0.000301666637605849 \times 10^{0}$ |
| $a_1$ | $-3.49274821434772 \times 10^{-6}$ |
| $a_2$ | $1.41094494279237 \times 10^{-8}$ |
| $a_3$ | $-3.37215645540686 \times 10^{-11}$ |
| $a_4$ | $5.16808134953559 \times 10^{-14}$ |
| $a_5$ | $-5.04770001631655 \times 10^{-17}$ |
| $a_6$ | $3.02451608272015 \times 10^{-20}$ |
| $a_7$ | $-1.01229606567523 \times 10^{-23}$ |
| $a_8$ | $1.44928804153567 \times 10^{-27}$ |
| $b_0$ | $-0.000612249925645841 \times 10^{0}$ |
| $b_1$ | $6.10837120551714 \times 10^{-07}$ |

**Table 3.2:** Table of coefficients from the fitting of Eq. (3.4) to the longitudinal susceptibility calculated using atomistic spin dynamics.

## 3.5 Transverse Relaxation

To validate the transverse dynamics of the AFM-LLB, we use a form of the LLB equation, which neglects any changes in the magnetisation length and purely describes the transverse magnetisation dynamics:

$$\frac{d\mathbf{m}_\nu}{dt} = -\gamma \left[\mathbf{m}_\nu \times \mathbf{H}_{\text{eff},\nu}\right] - \gamma\alpha_\perp \frac{\left[\mathbf{m}_\nu \times \left[\mathbf{m}_\nu \times \mathbf{H}_{\text{eff},\nu}\right]\right]}{m_\nu^2} \tag{3.6}$$

where $\mathbf{m}_\nu$ is the macrospin magnetisation for sublattice $\nu$. As we are dealing with AFMs, the two sublattices will be denoted by subscripts $\nu$ and $\kappa$. For now, we are only considering a single macrospin with two sublattices. As with the LLG equation, there is a precessional and a damping-like term. The key differences in the above lie in the effective field, $\mathbf{H}_{\text{eff},\nu}$. The effective field in Eq. (3.6) for such a system with fixed magnetisation length, i.e., constant temperature, is given by

$$\mathbf{H}_{\text{eff},\nu} = \mathbf{B} + \mathbf{H}_{a,\nu} + \frac{J_{0,\nu\kappa}}{\mu}\Pi_\kappa \tag{3.7}$$

where $\mathbf{B}$ is the applied magnetic field, $\mathbf{H}_{a,\nu}$ is the anisotropy field, $J_{0,\upsilon\kappa}$ is the sum of the inter-lattice exchange (see Table 3.1), and $\Pi_\kappa$ is given by, $\Pi_\kappa = -\left[\mathbf{m}_\nu \times \left[\mathbf{m}_\nu \times \mathbf{m}_\kappa\right]\right]/m_\nu^2$

where $\mathbf{m}_\kappa$ is the magnetisation vector of the second sublattice. The anisotropy field in the macrospin model, $\mathbf{H}_{a,\nu}$, is defined as $\mathbf{H}_{a,\nu} = \frac{2K(T)}{M_S(T)}$ where the temperature dependence of the anisotropy constant is governed by Callen-Callen scaling for uniaxial second order anisotropy; $K(T) = K(0)m_e^3(T)$ [144].

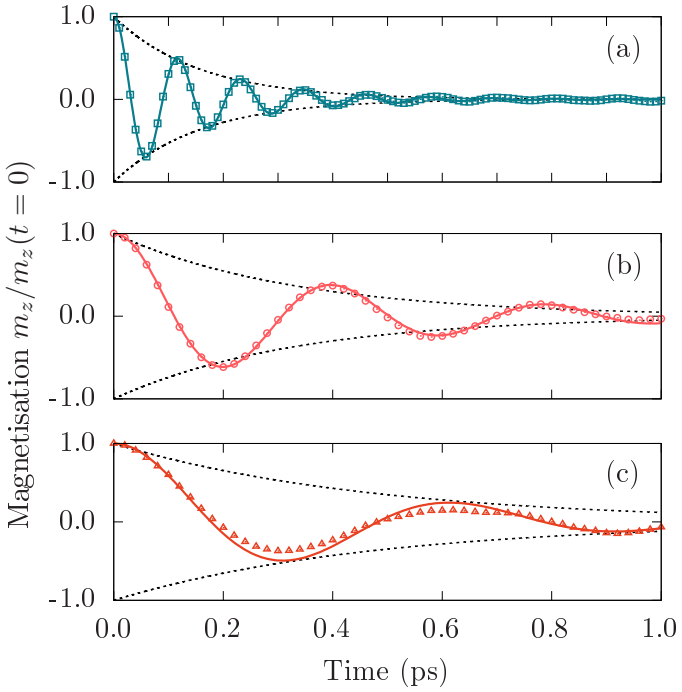


**Figure 3.4:** The $m_z$ motion following a rotation of both sublattices by 20 degrees out of the easy plane at (a) $T = 300$ K, (b) $T = 1000$ K and (c) $T = 1200$ K. Solid line are the AFM-LLB model and points are ASD. The dotted line shows the relaxation of the transverse dynamics. The relaxation time can be related to $\alpha_\perp$ through with Eq. (3.8).

Magnetic oscillations in AFMs have a resonance frequency in the THz range, orders of magnitude faster than the GHz range observed in ferromagnets. As a result of the complexity in current THz-signal generation methods [145–147], AFM oscillators have been proposed for use in adjustable room-temperature THz-frequency signal devices [56–58]. While attempts to experimentally measure the in-plane AFMR in $Mn_2Au$ driven by Néel spin-orbit torques have previously failed [148], it piqued the magnetism community's interest, highlighting the importance of not only measuring, but simulating the resonant frequency in AFMs. Since the AFMR essentially sets the speed limit of the AFM dynamics, calculating this quantity is highly relevant for the development of ultrafast memory applications. To calculate the AFMR, the system is initially set to

relax to its equilibrium magnetisation for a given input temperature. Once relaxed, all spins are rotated by 20 degrees out of the easy $xy$-plane inducing a torque and thereby exciting the AFMR mode. The transverse relaxation time, $\tau_\perp$, following the release of the spins after the rotation can be related to the effective field and transverse damping via

$$\tau_\perp = \frac{m_e}{\alpha_\perp \omega_{\text{ex}}} \tag{3.8}$$

where $\omega_{\text{ex}} = \gamma H_E = \gamma \frac{J_{0,\nu\kappa}}{\mu_s} m_e$. A comparison of the out-of-plane $m_z$ dynamics at temperatures of 300K, 1000K and 1200K for ASD and AFM-LLB with a value of $\lambda = 0.01$ can be seen in Fig. 3.4. The value of $\tau_\perp$ was found by fitting the atomistic sublattice magnetisation dynamics to the equation $m_z(t)/m_e = \cos(\omega_{\text{AFMR}} t)\exp(-t/\tau_\perp)$. The relaxation rate, $\exp(-t/\tau_\perp)$, is shown as dotted lines in Fig. 3.4, the solid lines are the AFM-LLB dynamics and the points are ASD. The AFMR frequency of the dynamics was extracted via Fast Fourier Transform (FFT) of $m_z$. The results of this frequency analysis can be found in Fig. 3.5 showing excellent agreement between the models and the analytical expression. The analytic expression for the AFMR, shown by the solid line in Fig. 3.5, is given by:

$$f = \frac{\gamma}{2\pi}\sqrt{H_A(H_A + 2H_E)} \tag{3.9}$$

Additional simulations following a rotation out of the $xy$-plane were conducted for damping parameters of $\lambda = 0.05$ (blue squares) & 0.001 (orange triangles), as shown in Fig. 3.6. The relaxation time for each damping value has been normalised to the value of $\tau_\perp$ at $T = 0$ K. The solid lines show the relaxation time as predicted by Eq. (3.8), the empty points show the results from ASD simulations and the solid blue circles show the relaxation time of AFM-LLB simulations with a damping of 0.01. The scaling of the relaxation time is identical for all damping values in the AFM-LLB model. In the atomistic simulations, it was observed that for the lowest value of $\lambda$, the relaxation time of the transverse dynamics decreased approaching $T_N$. With increased damping, the sublattices spend a greater amount of time out of equilibrium with one another and thus generate a larger exchange field. Further from equilibrium, a larger amount of

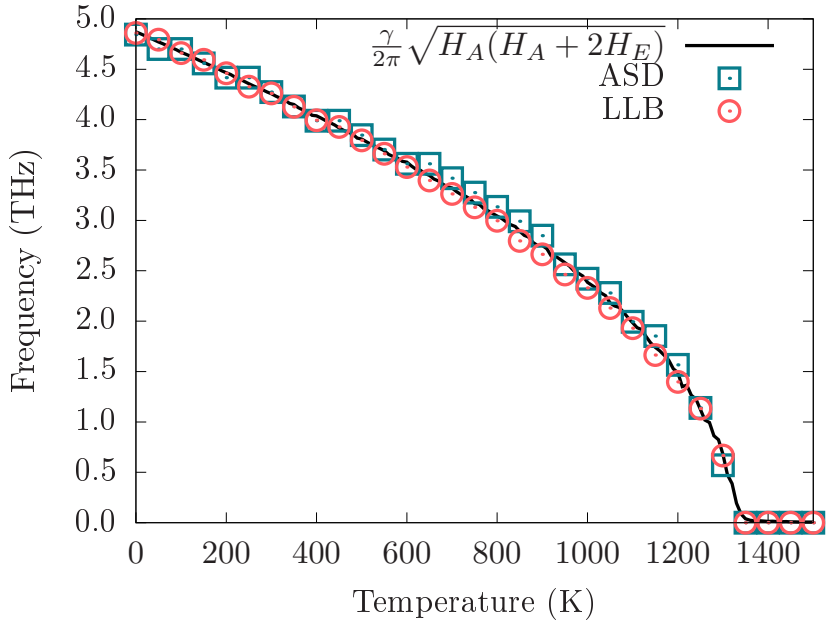


**Figure 3.5:** AFMR frequency of $Mn_2Au$. The solid line is the result from Eq. (3.9), square points are from ASD, and circular points are the LLB simulations respectively.

angular momentum can be transferred between sublattices leading to a faster transverse relaxation. The effect of increased angular momentum transfer is also the reason why the longitudinal dynamics in AFMs relax faster than ferromagnets [149]. This effect is naturally captured in the ASD model because of the exchange coupling at the atomic level between antiferromagnetically coupled spins, but is not taken into account in the AFM-LLB. The exact form of this damping dependence should be investigated as part of future work.

## 3.6 Longitudinal Relaxation

As mentioned in the introductory chapter, much effort in recent years has gone into the understanding of femtosecond laser-pulse induced ultrafast magnetisation dynamics in FM and FiMs while the mechanism behind demagnetisation on this timescale still being broadly under debate. The quenching of the magnetic order in AFMs is less known because of the difficulties in accessing the magnetic information experimentally but is likely to be studied more as interest continues to grow in this class of magnetic materials. To describe the quenching in $Mn_2Au$, we introduce a term in the LLB equation that

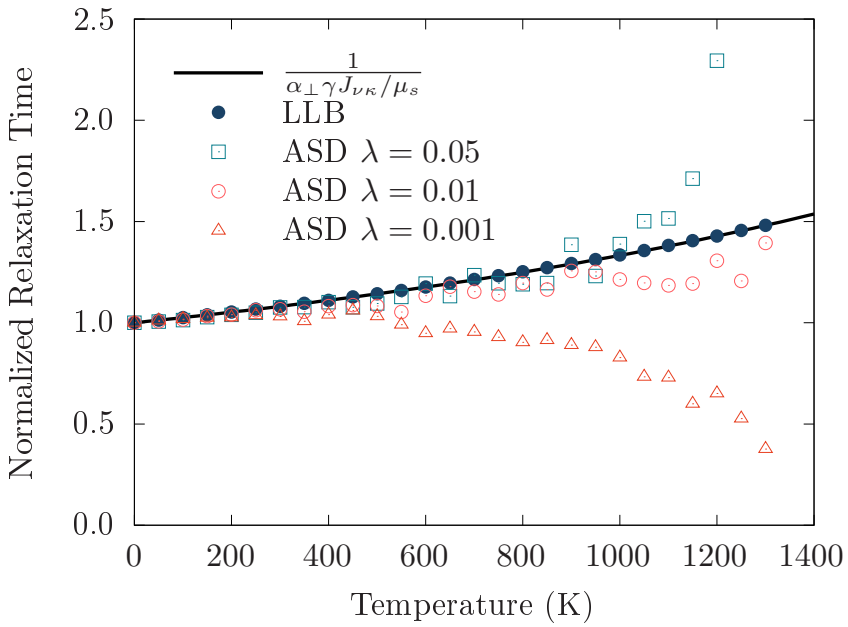


**Figure 3.6:** The transverse relaxation time, $\tau_\perp$ as function of temperature. Empty points represent ASD simulations with values of $\lambda = 0.05$ (square), 0.01 (circle) and 0.001 (triangles). Solid circles are the AFM-LLB model. The solid line is given by Eq. (3.8).

accounts for changes in the magnetisation length. Here we are only interested in the longitudinal dynamics – parallel to the magnetisation direction – and can therefore ignore the precessional and damping terms presented in the previous section

$$\frac{d\mathbf{m}_\nu}{dt} = \gamma \alpha_\parallel^{\mathrm{AF}} \frac{\left(\mathbf{m}_\nu \cdot \mathbf{H}_{\mathrm{eff},\nu}\right)}{m_\nu^2} \mathbf{m}_\nu \tag{3.10}$$

The effective field for a purely longitudinal relaxation (where one can ignore any external, anisotropy or inter-macrospin exchange fields) is given by

$$\mathbf{H}_{\mathrm{eff},\nu}^{\parallel} = \begin{cases} \frac{1}{2\tilde{\chi}_\parallel}\left(1 - \frac{m_\nu^2}{m_\mathrm{e}^2}\right)\mathbf{m}_\nu, & T \lesssim T_N \\ -\frac{1}{\tilde{\chi}_\parallel}\left(1 + \frac{3}{5}\frac{T_N}{T - T_N} m_\nu^2\right)\mathbf{m}_\nu, & T \gtrsim T_\mathrm{c} \end{cases} \tag{3.11}$$

where $\tilde{\chi}_\parallel$ is the reduced longitudinal susceptibility. In this work we opt to use the susceptibility taken from a MFA [150]. We find that the agreement in the longitudinal relaxation between ASD and LLB when using $\tilde{\chi}_\parallel$ taken from ASD simulations gave large discrepancies between the two models at lower temperatures while using $\tilde{\chi}_\parallel$ taken from a MFA gave excellent agreement for all temperatures. This problem has been

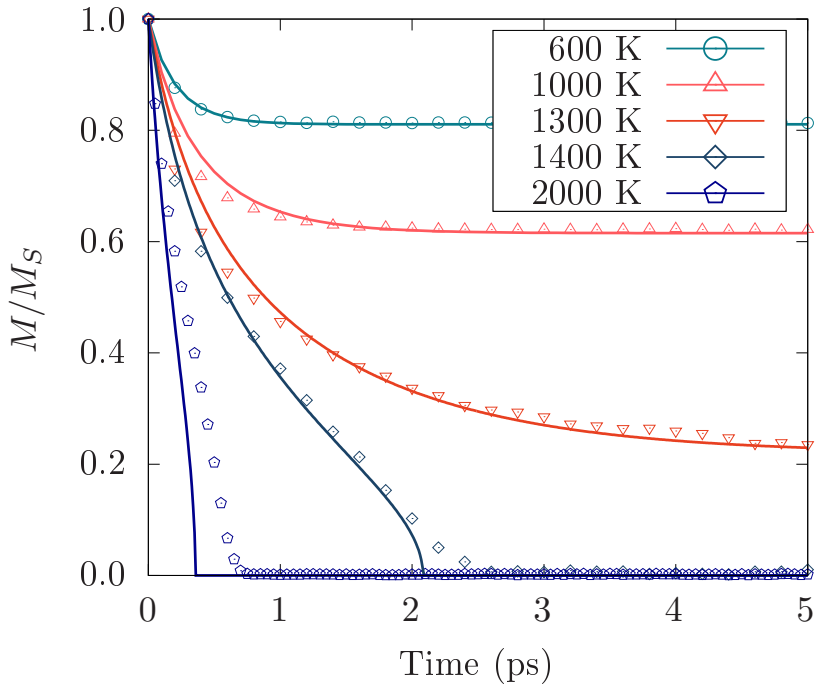


**Figure 3.7:** A comparison at five different temperatures between the AFM-LLB and the atomistic modelling. Symbols represent the atomistic spin dynamics results and the solid lines correspond to the AFM-LLB. No stochastic noise was present in the AFM-LLB simulations.

noted elsewhere - Vogler *et al.* mention that calculations of $\tilde{\chi}_{\parallel}$ only work for hard magnetic materials with strong uniaxial anisotropy [151] with similar problems having been identified in ferrimagnets [152]. The exact reason for the difference is unclear and should be the subject of future investigation. The method of calculating the MFA longitudinal susceptibility follows directly from [110]. Using the same value for the exchange constants in ASD and MFA approaches yields a higher critical temperature compared to the atomistic results ($T_N^{\mathrm{MFA}} > T_N^{\mathrm{ASD}}$). Therefore, we rescale the exchange constant to match the value for the Néel temperature extracted from Fig. 3.3. The process of using a scaled MFA susceptibility has been seen previously in atomistic modelling of GdFeCo [153]. Assuming that the macrospin magnetisation remains along single axis, $\mathbf{m}_\nu = [m_\nu, 0, 0]$, Eq. (3.10) simplifies to

$$\frac{dm_\nu}{dt} = \gamma \alpha_{\parallel}^{\mathrm{AF}} H_{\mathrm{eff},\nu}^{\parallel}. \tag{3.12}$$

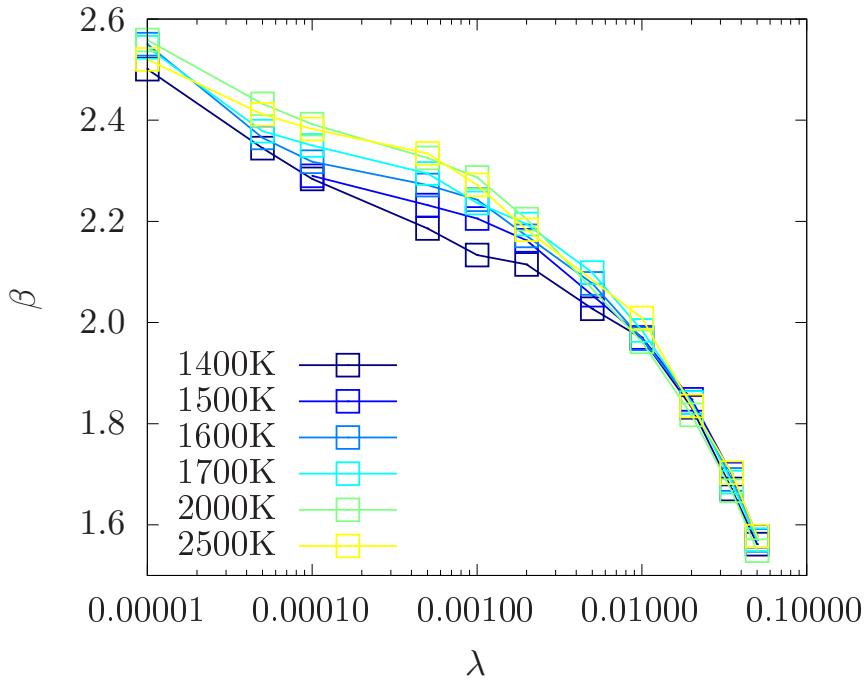


**Figure 3.8:** The damping dependence of $\beta$. The MFA LLB equation [133] is fitted to the longitudinal dynamics from atomistic simulations following a step change in temperature from $T = 0$ K to $T > T_N$. All other parameters in the LLB besides $\beta$ remain fixed.

Experimental works studying the ultrafast magnetic order dynamics in the FM and AFM phases of dysprosium (Dy) have shown that the AFM phase exhibits faster longitudinal dynamics than the FM phase [149] with the speed up being attributed to the exchange of angular momentum between sublattices. Dy is known to have FM order at lower temperatures but undergoes a phase transition to a helical AFM phase in the temperature range 85K to 178K [154] thus allowing for a direct comparison of FM and AFM dynamics in the same material. One of the key figures from this work can be found in Fig. 3.9. The symbols denote the normalised magnetic order parameter for the FM (blue) and AFM (orange) configurations, with the lines showing exponential fits to the data. It was found that following excitation from a 50 fs laser, the AFM order decreased with an exponential time constant of 290 fs followed by a slower 14 ps constant, compared to a single relaxation constant of 3.2 ps for the FM. They find the maximum rate of angular momentum transfer is over 5 times higher for AFM than FM order making quenching of AFM order more energy efficient.

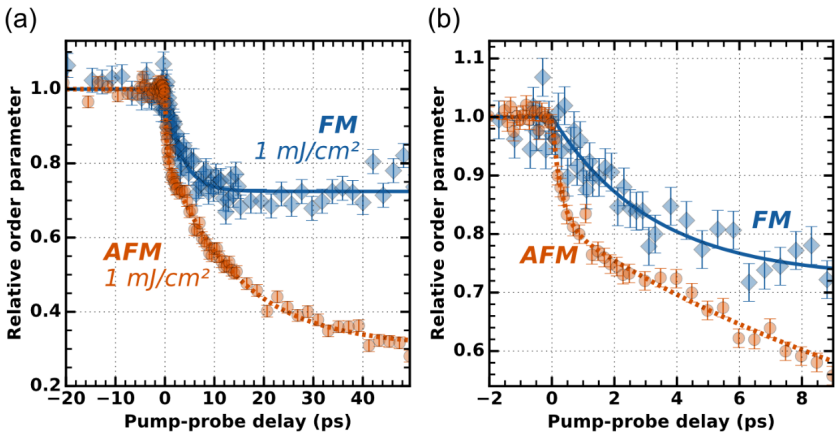


**Figure 3.9:** (a) Pump-probe delay scans in the FM (blue) and AFM (orange) phase for an absorbed laser fluence of 1 mJ/cm$^2$. The symbols denote the normalised magnetic order parameter; the lines denote exponential fits to the data. (b) The first 9 ps of the delay traces on an enlarged scale. Taken from Ref. [149].

For $Mn_2Au$, the absence of a FM phase makes such a comparison impossible. However, a recent theoretical work by Jakobs & Atxitia [155] has concluded that the speed up of the AFM dynamics comes from the exchange-enhancement of the effective damping parameter

$$\alpha_{\parallel}^{\mathrm{AF}} = \alpha_{\parallel}^{\mathrm{FM}} \left( 1 + \frac{2}{z\,|m_\nu|^{\beta}} \right) \tag{3.13}$$

where, $\alpha_{\parallel}^{\mathrm{FM}}$ is the ferromagnetic longitudinal damping parameter (where the relaxation is solely due to the dissipation of angular momentum to the heat bath) and is defined by

$$\alpha_{\parallel}^{\mathrm{FM}} = \lambda \frac{2T}{3T_N} \tag{3.14}$$

In Eq. (3.13), theory predicts that $z$ is the number of nearest neighbours antiferromagnetically coupled to a given spin. While for a simple cubic with only nearest neighbours this number is 6, for $Mn_2Au$ this would correspond to 5 (See inset in Fig. 3.1). Our simulations show that $z \approx 6.0$. The exponent $\beta$ in Eq. (3.13) is a phenomenological parameter, necessary for the description of high non-equilibrium situations where the temperature goes well above the critical temperature. While for small deviations from the equilibrium of the magnetic order parameter, $\beta = 1$, for larger deviations, for example when the temperature of the system changes from $T = 0$ K to $T = 2T_N$, the exponent takes a value of $\approx 2$. We also find that alongside the temperature dependence

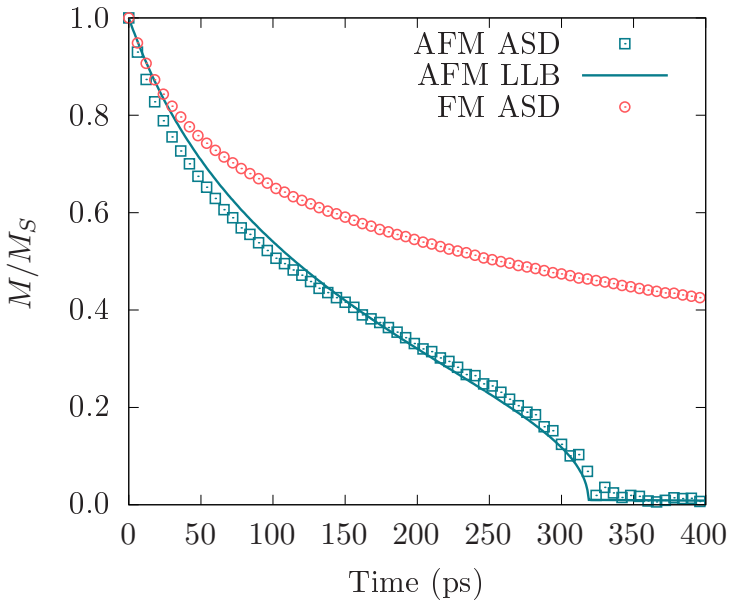


**Figure 3.10:** The longitudinal relaxation following a step change in temperature from 0 K to 1400 K. The Gilbert damping was set to 0.00005. Square points are from ASD simulations of the ground state AFM configuration of $mn_2Au$. Circular points are from ASD simulations representing an FM configuration of $Mn_2Au$ where the absolute values of $J_1$ to $J_4$ have been used. The solid line shows the AFM-LLB.

of the $\beta$ exponent, it also exhibits a damping dependence, which can be found in Fig. 3.8. As small deviations from equilibrium give $\beta = 1$, the damping dependence of $\beta$ is investigated by numerically fitting the mean-field form of the AFM-LLB equation following a large step change in temperature from $T = 0$ K to $T > T_N$ to the corresponding ASD simulations. For the fitting, we use a MFA form of the effective field that is not dependent on any atomistically derived parameters. Instead of using Eq. (3.11), the effective field is given by [111]

$$H^{\parallel}_{\text{eff},\nu} = \frac{(m_\nu - m_{0,\nu})}{\mu_s \beta L'(\xi_\nu)} \tag{3.15}$$

here $m_{0,\nu}$ is not the equilibrium magnetisation and is instead given by $m_{0,\nu} = L(\xi_\nu)$ where $L(\xi_\nu) = \coth(\xi_\nu) - 1/\xi_\nu$ is the Langevin function and $L'(\xi_\nu) = dL/d\xi_\nu$ with $\xi_\nu = \beta\mu_s H^{\text{MFA}}_\nu$ and $\beta = 1/k_B T$. The MFA field is defined as $H^{\text{MFA}}_\nu = 3k_B T_N m_\kappa$ [109]. Using the results of our determination of $\beta$ for a value of $\lambda = 0.01$ we have furthermore carried out simulations of the longitudinal dynamics after a temperature step (Fig. 3.7). In these temperature step simulations, we begin with a perfectly or-

dered AFM configuration of $Mn_2Au$ at $T = 0$ K, we then apply a temperature step and record the relaxation to the equilibrium magnetisation. Fig. 3.7 shows the longitudinal relaxation for 5 different temperatures (with $\lambda = 0.01$ for all simulations), the points are simulations using the stochastic LLG equation and the solid lines are from the LLB model. The agreement at lower temperatures is excellent. At temperatures well above $T_N$, finite size effects lead to a longer relaxation time in the atomistic model. It is also worth stressing that instantaneous step changes in temperature from 0 Kelvin to near $T_N$ are radical, and some disagreement would be expected. The reasonable damping value of $\lambda = 0.01$ has been chosen in accordance with previous atomistic modelling of $Mn_2Au$ [71, 156].

To highlight the importance of the $\beta$ exponent in Eq. (3.13), we performed ASD and LLB simulations with values for $\lambda = 0.00005$ for a step change to above the critical temperature, as shown in Fig. 3.10. We also include ASD results for an entirely ferromagnetic exchange to show the difference in the relaxation rates between FM and AFM. We find that relaxation dynamics in AFMs are defined by two distinct processes, (i) an exponential decay due to the dissipation of angular momentum to the heat-bath and (ii) a power-law decay due to the angular momentum exchange between the sublattices. While for the FM configuration of $Mn_2Au$, the relaxation dynamics are described by an exponential decay, for AFMs, the exponential decay only dominates for values of the order parameter $n > 1/3$. As the magnetic order reduces to small values, the rate of angular momentum dissipation remains constant, $(\mu_{\text{at}}/\gamma)\dot{n} \approx (2/3)\lambda k_B T/n^{\beta-1}$, leading to a power-law decay.

## 3.7 Two-Temperature Model Heating

Although simulations of a sudden step-like increase in temperature is easy to achieve, experimentally, this is not the case. A common approach to strong and rapid heating of the system is possible by applying, for example, a femtosecond laser pulse. In these scenarios the temperature of the system is difficult to determine, however, given semi-classical considerations [157] one can define the temperature of an electron and

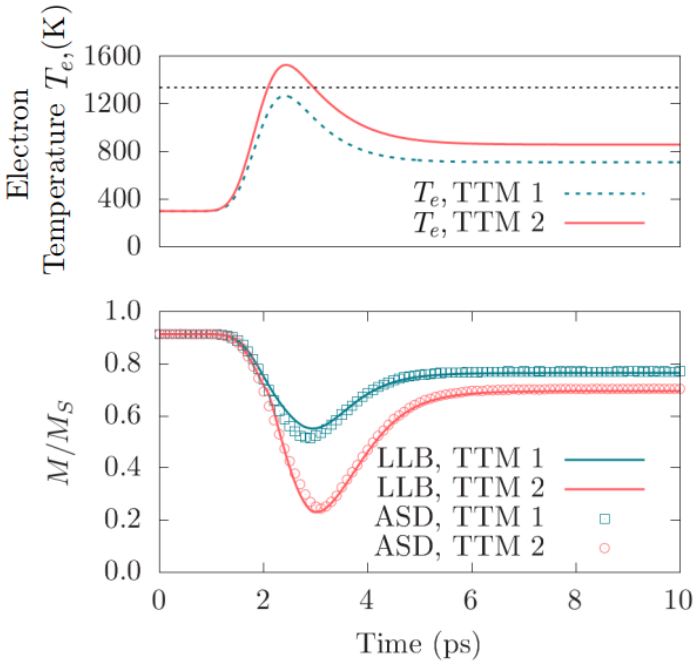


**Figure 3.11:** (Top) The electronic temperature, $T_e$, dynamics using a TTM for heating to below and above the critical temperature, $T_N$. Horizontal black dotted line shows the critical temperature. (Bottom) magnetisation dynamics from atomistic (Points) and LLB (Solid lines) following application of the laser. The spin temperature is coupled with the electron temperature. Blue and red markers/line correspond to heating to just below and just above $T_N$ respectively.

a phonon bath. A laser pulse will couple more strongly to the electron system giving large and rapid temperature increases, in hundreds of femtoseconds, to a temperature above $T_N$, however, the electron system also quickly cools downs on the ps timescale by transferring energy to the phonon system via electron-phonon coupling. The electronic temperature is calculated using a two-temperature model (TTM) [158]. The equations to describe the dynamics of the electron and phonon temperatures, $T_e$ and $T_p$ are given by the equations:

$$\begin{aligned} C_e \frac{\partial T_e(z,t)}{\partial t} &= G_{ep}\left(T_p(z,t) - T_e(z,t)\right) + P(z,t) + \frac{\partial}{\partial z}\kappa\frac{\partial T_e}{\partial z} \\ C_p \frac{\partial T_p(z,t)}{\partial t} &= G_{ep}\left(T_e(z,t) - T_p(z,t)\right) \end{aligned} \tag{3.16}$$

Where in the above, $C_e$ and $C_p$ are the electron and phonon heat capacities, $G_{ep}$ is the electron-phonon coupling, $P(z,t)$ is the absorbed laser power and $\kappa$ is the lateral heat transport. For the nm lengthscale systems under consideration in this section,

we assume uniform heating from the laser throughout the system such that $P(z,t)$ becomes $P(t)$ and $\kappa = 0$. Fig. 3.11 shows the longitudinal magnetisation dynamics for a transient change in temperature following heating from a laser pulse. We begin at $T = 300$ K then heat to just below and above $T_N$, shown in profiles TTM 1 and TTM 2 in Fig. 3.11. As well as capturing the demagnetisation, the AFM-LLB captures the remagnetisation process remarkably well in both heating cases.

## 3.8 Exchange Stiffness & Domain Walls

To be able to describe domain walls (DWs) within an LLB framework, we introduce a term into the LLB Hamiltonian that describes the exchange coupling between neighbouring macrospins, given by:

$$\mathbf{H}_{\text{ex}}^{v,i} = \frac{2A(T)}{d^2 M_S m_e^2} \sum_j \left(\mathbf{m}_{v,j} - \mathbf{m}_{v,i}\right) \tag{3.17}$$

Where $A(T)$ is the exchange stiffness, $d^2$ is the surface area connecting neighbouring macrospins, and $M_S$ is the saturation magnetisation. We should emphasise here that we use a different equation for the exchange coupling to Chen *et al.* [159]. They use an exchange term that sums over the opposite sublattice in the neighbouring macrospins. This term would be non-zero when sublattices in neighbouring macrospins are parallel, leading to a disagreement between LLB and ASD simulations of the AFMR.

Compared to the other input parameters in the LLB equation, the exchange stiffness, $A(T)$, is notably the most difficult to calculate. The simplest, but least rigorous, is to simply calculate the exchange stiffness at 0K using the $J_{ij}$'s and assume scaling within a mean field approximation. The zero temperature exchange stiffness $A(0)$ is given by [160]

$$A(0) = \frac{1}{V_0} \sum_{i,v} \left|J_{i,v}\right| a_{i,v}^2 \tag{3.18}$$

where $V_0$ is the unit cell volume, $v$ represents all the neighbours for site $i$ where $x$ or $y$ are non-zero as the domain wall forms in the $xy$-plane, and $a_v$ is the absolute distance

between site $i$ and site $v$. As we are interested in the domain walls along the ferromagnetic planes, we can exclude any $J_4$ interactions (See Fig. 3.1). In total, there are 12 interactions that contribute to $A(0)$. Using the values for $J_1$ to $J_3$ in Table 3.1 yields $A(T = 0\text{ K}) = 2.34 \times 10^{-11}$ J/m, which agrees well with calculations of the exchange stiffness through atomistic simulations of the DW width, as shown in Fig. 3.13. The exchange stiffness, $A(T)$ scales with $m_e^2$ within a MFA. Fig. 3.13 shows the exchange stiffness as a function of temperature with points representing atomistic simulation results, and the dotted line showing the scaling law $m_e^2$.

For the atomistic simulations of the domain wall width, we ensure the length of the system in the $x$-direction is much wider than the zero Kelvin domain wall width. The Mn sites at the left hand boundary of the slab remain fixed in an anti-parallel alignment to the spins at the right-hand boundary. The remainder of the spins are allowed to relax to form a domain wall profile. The system size dimensions in the ASD calculations is $1000 \times 10 \times 10$ unit cells, which gives a chain length of approximately 330 nm. For the LLB simulations, we use cell sizes of $3 \times 10 \times 10$ nm to ensure that we have a good resolution along the $x$-direction for an accurate calculation of the domain wall width while ensuring numerical stability with a large value of $d^2$ in the denomenator of Eq. (3.17) to ensure numerical stability of the inter-macrospin exchange field. The magnetisation is averaged over the $y$ and $z$ components for each $x$ value to The give a reduced magnetisation along the spin chain direction, $m(x)$. This is then fitted to a hyperbolic tangent function to find the domain wall width parameter:

$$m(x) = m_e \tanh\left(\frac{x-b}{\delta_0}\right) \tag{3.19}$$

where $b$ is the central position of the DW, and $\delta_0$ is the wall-width parameter. A comparison of the DW profile at $T$ =0 K can be found in Fig. 3.12. The width can be related to the wall width parameter through $\delta = \pi\delta_0$. We calculate $\delta(0) = 31.2$ nm from atomistic simulations and see good agreement between ASD and LLB in Fig. 3.12 for intermediate and high temperatures. The relation that links the DW width to the

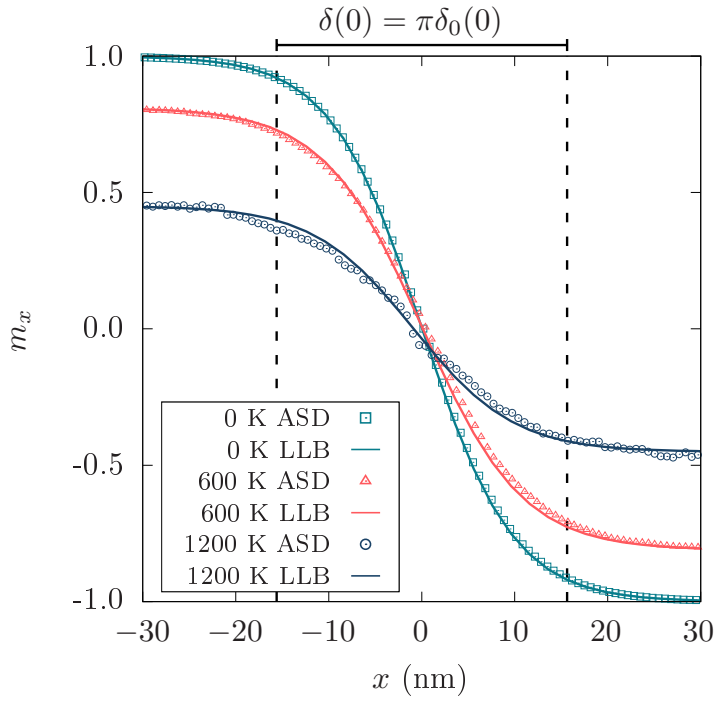


**Figure 3.12:** The domain wall width at 0 K, 600 K and 1200 K. Solid lines are from LLB simulations and points are from ASD. The Néel domain-wall width is given by $\delta(T) = \pi\delta_0(T)$. The dotted lines show the width of the domain wall at 0 K.

exchange stiffness is given by

$$\delta_0(T) = \sqrt{\frac{A(T)}{K(T)}} \tag{3.20}$$

where $K(T)$ is the anisotropy energy where again we use Callen-Callen scaling [144], $K(T) = Km_e^3(T)$.

## 3.9 Thermally Induced Domain Wall Motion

The manipulation of domain walls (DW) has been proposed for use in the next generation of logic and memory devices [161, 162]. The motion of the DWs can be modulated using spinwaves [163, 164], spin currents [165–167] or external magnetic fields [168, 169], for example. Another possibility is to drive DW motion by thermal gradients [170, 171]. Under thermal gradient, the motion of the domain wall is induced towards the hotter end of the nanowire due to a reduction in the free energy, $\Delta F(T)$. For large thermal gradients in ferromagnets, there is a precession of the internal magnetisation, which leads to a reduction in the domain wall velocity, known as the Walker breakdown [168].

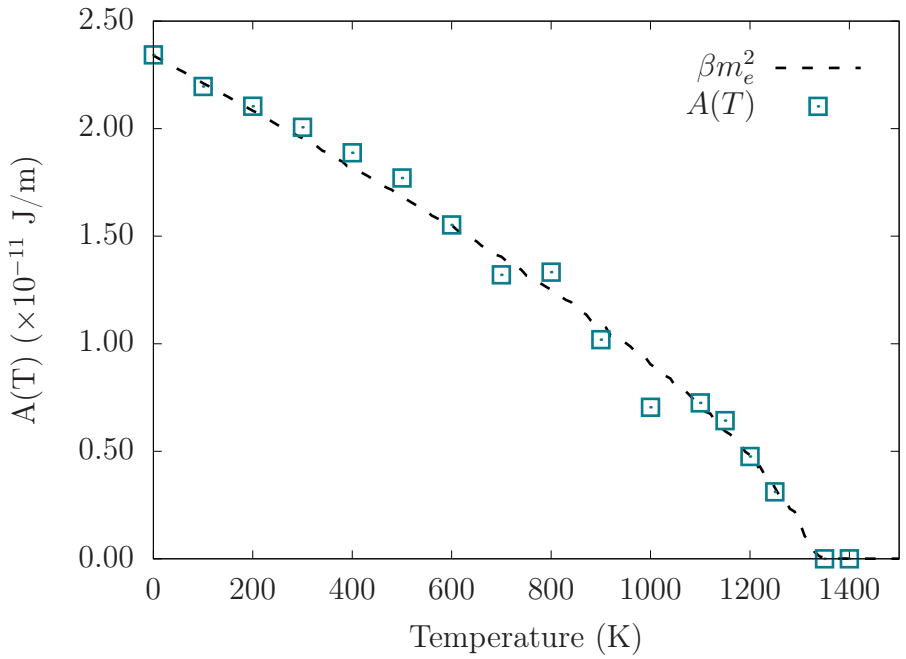


**Figure 3.13:** Exchange stiffness as a function of temperature. Points are from atomistic simulations of the domain wall width. Dotted line shows the proportionality to the equilibrium magnetisation with $A(0)$ taken from Eq. (3.18).

In previous ASD simulations of AFMs, it has been shown that there is no breakdown in the DW velocity due to the symmetry of the torques acting on the DW [172], meaning DWs in AFMs are able to reach higher speeds, and are only limited by the maximum magnon group velocity, $v_g$, $\delta_{\mathrm{DW}} = \delta_0\sqrt{1-\left(v_{\mathrm{DW}}/v_{\mathrm{g}}\right)^2}$ where $\delta_0$ is the DW width at rest.

Conventional micromagnetic methods have limitations in the modelling of thermally driven DWs, as they cannot account for the dynamic changes in the magnetisation length. It has been shown experimentally that ultrashort laser pulses can drive DW motion [171]. In these scenarios, heating and cooling will play a role, and the effects of this cannot be captured using an LLG-based micromagnetic model. This could be simulated using an atomistic approach, but the calculations are expensive and require large ensembles to reduce statistical noise. The LLB model overcomes these issues, making it an important tool for temperature-dependant calculations of topological structures such as domain-wall, spin-spirals and skyrmions. As an example of simulations that require both accurate descriptions of the longitudinal and transverse dynamics, we present a comparison of the DW motion under a thermal gradient using both atomistic

and AFM-LLB models and compare to previously derived analytical expressions for the DW velocity.

For the atomistic calculations of the DW velocity, we begin with a DW initialised at 0 Kelvin along the $x-$direction, we then apply a linear thermal gradient in the direction of the DW. It has been shown that the DW velocity induced by a thermal gradient in an AFM can be approximated by [173]

$$v_{\mathrm{DW}}^{\mathrm{LLB}} = \frac{2\gamma}{M_s \alpha_\perp} \frac{\partial T}{\partial z} \frac{\partial A}{\partial T} \tag{3.21}$$

As seen in previous analyses of domain walls [173, 172], the weak temperature dependence of $\alpha_\perp$ is neglected and the exchange stiffness is linearised to $dA/dT \approx A(0)/T_C$. Fig. 3.14 shows the domain wall velocity for $Mn_2Au$ in atomistic and LLB simulations due to a thermal gradient, showing good agreement with Eq. (3.21). The velocity is calculated by, once again, fitting the DW profile to Eq. (3.19) to find the centre of the domain wall, then tracking the movement of this central position in time. While the relation appears linear in Fig. 3.14, in reality, the velocity will reach a saturation point governed by the magnon group velocity [174]. In the atomistic modelling of thermally induced DW motion, Selzer et al [172] state that there is no acceleration phase, and the DW moves with constant velocity, which is what we observe in $Mn_2Au$ in both LLG and LLB simulations.

## 3.10 Summary

Using a multiscale approach, it has been demonstrated that antiferromagnets such as $Mn_2Au$ can be modelled micromagnetically on micrometre length scales using an AFM-LLB model. We started with parameters from previous work for the exchange, anisotropy and magnetic moment which were fed into an atomistic model of $Mn_2Au$. Then, we calculated the temperature-dependent parameters $m_e(T)$, $A(T)$, $\tilde{\chi}_\parallel(T)$ using atomistic spin dynamics before using these as input into the AFM-LLB.

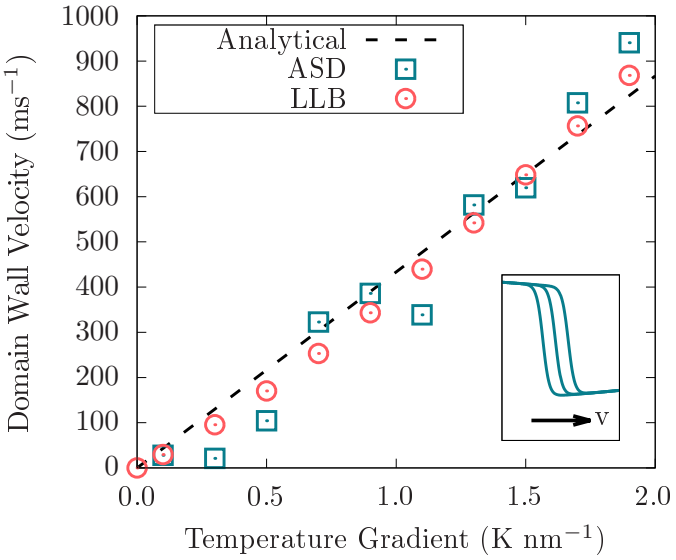


**Figure 3.14:** Domain Wall velocity as a function of the temperature gradient. $\lambda$ was set to 0.01 for the simulations. The solid line is given by Eq. (3.21). The inset shows an example of the domain wall at three different timesteps. The wall is moving from left to right in the figure.

To verify the dynamics described by the proposed LLB model for $Mn_2Au$, first, we presented consistent results between ASD, LLB and the Kittel relation for the antiferromagnetic resonance frequency. As well as serving as a validation of the transverse dynamics, we have revealed the first estimate of the in-plane AFMR frequency in $Mn_2Au$. The fact the resonant frequency sits within the THz range opens the possibility sub-ps switching and generation of THz electromagnetic signals at ambient temperatures. Second, we compared ASD simulations results to the AFM-LLB model for the longitudinal dynamics following step changes in temperature and laser pulse heating - both of which give excellent agreement between the models. Finally, we provided a comparison of the domain wall motion due to a thermal gradient as an example of how the LLB model for an AFM can be utilised on $\mu$m length and $\mu$s timescales - opening the door to micromagnetic simulations of AFM materials for use in realistic spintronic devices. While questions such as the damping dependence of the transverse relaxation time, and the poor agreement for the longitudinal relaxation between ASD and LLB with $\tilde{\chi}$ from ASD remain unanswered, the AFM-LLB opens the possibility for the description of laser-induced local thermal gradients on length-scales and the benchmark of other thermodynamic effects in collinear AFMs on micrometre length-scales.

$Mn_2Au$ has been chosen as an exemplar material for this study due to the recent interest it has drawn for spintronic applications. Its ability to generate staggered torques from electric field pulses, simple collinear structure, and high critical temperature makes it ideal for possible AFM switching. The multiscale process for AFMs could easily be applied to other For other collinear AFM, such as CuMnAs, where the calculation of the temperature-dependant functions $m_e(T)$, $A(T)$, $\tilde{\chi}_{\parallel}(T)$ would be a straightforward process and the present theory would be sufficient for a complete parameterisation using the AFM-LLB model. However, for materials with more intricate anisotropies, where the temperature dependence may need to be calculated using Monte-Carlo methods [175, 176], or AFM systems featuring more than two sublattices or non-collinear configurations, a thorough examination of AFM properties becomes necessary, along with an extension of the current theoretical framework.

# Chapter 4

# Simulations of Magnetisation Reversal in $Mn_2Au$

*This place I am hoping to get to is so marvellous that if I described it to you now you would go crazy with excitement. And then, if we failed to get there (which is very possible), you would die of disappointment. I don't want to raise your hopes too much, my darlings.*

– *ROALD DAHL*, Fantastic Mr. Fox.

## 4.1 Introduction

Computationally, it has already been shown that square staggered fields arising from current-driven NSOTs can lead to a reversal in $Mn_2Au$ with pulse durations of the order of a few picoseconds [142, 177, 72]. Experimentally, reports of switching in $Mn_2Au$ began in 2018 with Bodnar *et al.* [66] reporting reversal of the Néel vector following the application of an electric field with an efficient readout via large anisotropic magnetoresistance (AMR) of between 5% and 6%. In the same year, Meinhart *et al.* [65] also reported switching in epitaxial films of $Mn_2Au$ and, using a macroscopic model, explained the importance of Joule heating in the reorientation process. However, it was then suggested that these magnetoresistance measurements alone might not be sufficient to imply SOT switching. Chiang *et al.* [178] showed that when using current densities similar to those seen in the aforementioned experiments, similar resistive readings were generated with and, importantly, without the presence of AFM in the multiterminal devices, casting doubt on the previous results. Then conclusively in 2023, direct observations of SOT switching were observed in $Mn_2Au$ using X-ray magnetic linear dichroism - photoelectron emission microscopy (XMLD-PEEM) techniques by Reimers *et al.* [64] with only a small amount of heating (approximately 20 K) arising from the current pulse. The observed switching was not itself on picosecond timescales, and was the result of $\mu$s and ms current pulses, as shown in Fig. 4.1. Because of the timescales involved, the switching was attributed to domain wall motion rather than a coherent reorientation of the Néel vector.

More recently, Behovits *et al.* [179] have shown experimentally that ps timescale reversal is almost within reach. In their work, they use intense single-cycle THz pulses to excite magnetic dynamics in $Mn_2Au$ thin films and detect the response using time-resolved magneto-optic probing. The THz pumping is performed on as-grown and prealigned samples. In the prealigned case, the samples is subject to a huge magnetic field of approximately 60 T for 150 ms to ensure the Néel vector is aligned along the easy axis. In the prealigned sample, deflections of up to 30° were achieved at the maximum peak field of 600 kV/cm in free space, which reduced to 40 kV/cm (roughly 6% of the

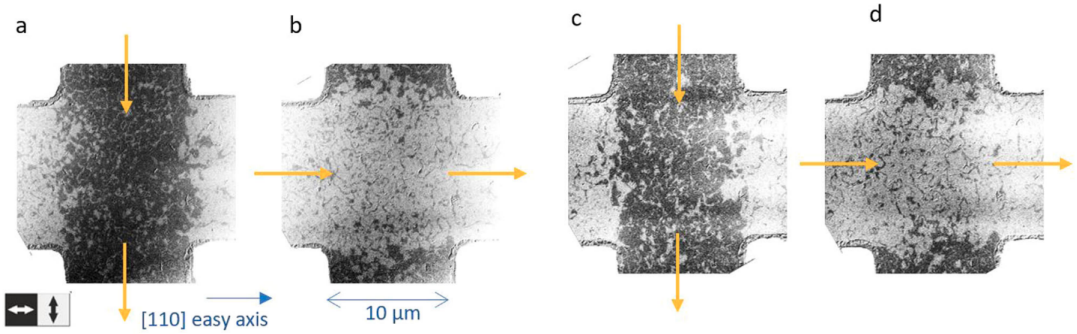


**Figure 4.1:** XMLD-PEEM images of the Néel vector reorientation for current pulses along different directions (yellow arrows). Dark and light regions show horizontal and vertical alignment of the Néel vector, respectively. Panels (a) and (b) show reversal after 100 pulses of 1ms length each with a current density of $2.6 \times 10^{11}$ A m$^{-2}$. Panels (c) and (d) show reversal after 1 bipolar pulse of 10 s length with a current density of $3.0 \times 10^{11}$ A m$^{-2}$. Image taken from Ref. [64].

free space value) inside the sample. By fitting the experimentally observed dynamics to a macrospin model, they predicted THz pulses with a peak field strength of around 120 kV/cm would be sufficient to generate 90° reversal. A direct comparison to the work in Ref. [179] will be presented later in this chapter.

In this study, we explore the possibility of achieving coherent reversal of $Mn_2Au$ utilising THz frequency pulses, while also examining the impact of transient heating during the switching process. So far, computational studies have only used square field pulses, while this is a good first approximation, experimental realisation of such a profile is challenging. Advances in the experimental generation of ultrashort THz pulses [180–183] and greater understanding of the mechanisms behind the control of magnetisation reversal of THz frequencies [184, 185] has opened the possibility for excitation and reversal of the Néel vector using sub-picosecond single and multi-cycle fields. Here, the effects of resonantly pumping $Mn_2Au$ using SOT fields are explored for varying pulse durations and static temperatures using ASD. The main results on THz switching in $Mn_2Au$ can be found in:

- Hirst, J., Ruta, S., Jackson, J. et al. Simulations of magnetization reversal in FM/AFM bilayers with THz frequency pulses. Scientific Reports **13**, 12270 (2023).

Recent studies have also shown that static temperature plays an important role in the reduction of the critical field [172] in AFMs, but little is also understood about the effect of transient heating. Using the AFM-LLB model introduced in the previous chapter, the effect of transiently heating the AFM using a TTM model while varying the relative application time of a staggered field is explored. To confirm the accuracy of the LLB model, comparisons to ASD are made.

## 4.2 The Heisenberg Hamiltonian

In the previous chapter, we employed a realistic value for the $d_z$ constant (which aligns favourably with other values reported in the literature [141, 142]) and an additional anisotropy constant, $d_{\parallel}^{*}$, derived from the calculations of Shick *et al.* [141] that can arise due to an induced strain. In experiments, it has been well documented that $Mn_2Au$ has two equivalent $\langle 110 \rangle$ easy axes in the (001)-plane [131, 186, 66, 64]. The reason for the exclusion of any cubic anisotropy constants that give rise to the $\langle 110 \rangle$ preferential orientations in the last chapter is that it has a very weak temperature scaling. The cubic anisotropy temperature dependence follows the Callen-Callen scaling with a $K_c(T) \sim m_e(T)^{10}$ dependence compared to $K_u(T) \sim m_e(T)^2$ for uniaxial terms. This would have meant the validation of the AFM-LLB, especially for the calculation of domain wall width/motion at elevated temperatures, a challenge. For the atomistic simulations, it would have required system sizes an order of magnitude larger to balance the increase in wall width and stochastic motion of the Néel vector. For accurate simulations of coherent magnetic switching (where the anisotropy constants define the energy barriers needed to be overcome to flip states), a more realistic treatment is needed. We opt to take anisotropies quoted in the work of Selzer et al. [142]. The Heisenberg Hamiltonian now reads:

$$\mathcal{H}_{\mathrm{Mn}} = \sum_{i \neq j} J_{ij}^{\mathrm{Mn}} \mathbf{S}_i \cdot \mathbf{S}_j - \sum_i d_z S_{i,z}^2 - \sum_i d_{zz} S_{i,z}^4 - \sum_i d_{xy} S_{i,x}^2 S_{i,y}^2 \tag{4.1}$$

with anisotropy constants $d_z = -1.19$ meV, $d_{zz} = -0.015$ meV and $d_{xy} = 0.04$ meV [142]. The exchange constants and magnetic moment used are the same as in the

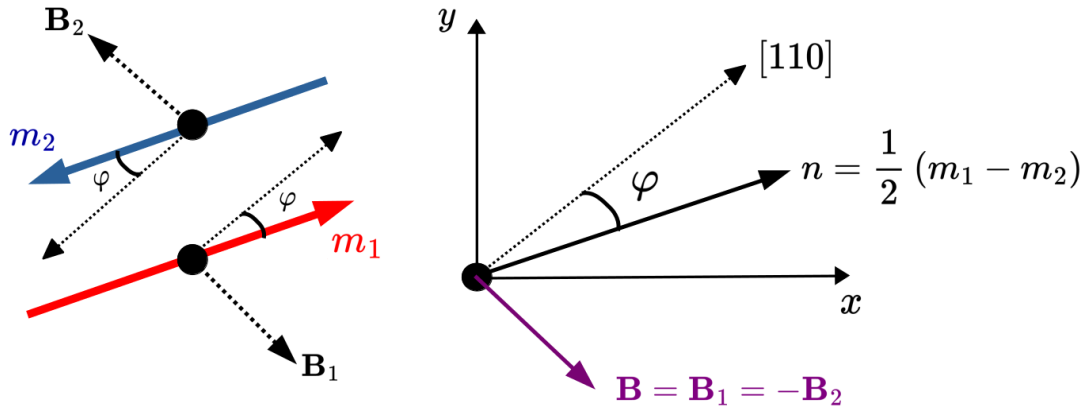


**Figure 4.2:** A schematic of the system. (Left) A top-down view of the two sublattices denoted by $\mathbf{m}_1$ and $\mathbf{m}_2$ coupled together by the exchange field $H_{\text{ex}}$ with anisotropy field $H_{\text{an}}$ keeping the macrospin aligned somewhat closely to the [110] and [$\bar{1}\bar{1}$0] directions for each respective sublattice. (Right) The Néel vector, $\mathbf{n}$, in the $xy$-plane rotated by angle $\varphi$ away from the easy [110] direction.

previous chapter. The damping is treated as a fixed with $\lambda = 0.01$ in accordance with previous atomistic modelling of $Mn_2Au$ [142, 177].

## 4.3 The Macrospin Equation of Motion

For the next couple of sections, we are interested in a coherent reorientation of the Néel vector for static temperatures. Under such scenarios, the Néel vector can be accurately described by a single macroscopic equation of motion [187, 188, 177]. This can then be compared to ASD simulations to ensure consistency between analytics and simulation. For $Mn_2Au$ assuming two collinear sublattices, $\mathbf{m}_1$ and $\mathbf{m}_2$, with easy anisotropy axes $\langle 110 \rangle$ subject to a field that is staggered for each sublattice, $\mathbf{B_1}$ at $\mathbf{m}_1$ and $\mathbf{B_2}$ at $\mathbf{m}_2$ with $\mathbf{B} = \mathbf{B_1} = -\mathbf{B_2}$ (see Fig. 4.2 for a schematic diagram) the implicit Landau-Lifshitz equation can be written as:

$$\begin{aligned}\dot{\mathbf{m}}_1 =& -\gamma\left(\mathbf{m}_1 \times \mathbf{H}_1\right) + \gamma\lambda\left(\mathbf{m}_1 \times \dot{\mathbf{m}}_1\right) \\ =& -\gamma H_{\text{ex}}\left(\mathbf{m}_1 \times \mathbf{m}_2\right) - \gamma H_{xy} m_{1,x} m_{1,y}^2 \left(\mathbf{m}_1 \times \hat{\mathbf{u}}_{xy}\right) - \gamma H_{xy} m_{1,x}^2 m_{1,y} \left(\mathbf{m}_1 \times \hat{\mathbf{u}}_{xy}\right) \\ & - \gamma H_z m_{1,z} \left(\mathbf{m}_1 \times \hat{\mathbf{z}}\right) + \gamma\left(\mathbf{m}_1 \times \mathbf{B}\right) + \lambda\left(\mathbf{m}_1 \times \dot{\mathbf{m}}_1\right)\end{aligned} \tag{4.2}$$

and for the second sublattice:

$$\begin{aligned}\dot{\mathbf{m}}_2 =& -\gamma\left(\mathbf{m}_2 \times \mathbf{H}_2\right) + \lambda\left(\mathbf{m}_2 \times \dot{\mathbf{m}}_2\right) \\ =&\gamma H_{\text{ex}}\left(\mathbf{m}_1 \times \mathbf{m}_2\right) - \gamma H_{xy} m_{2,x} m_{2,y}^2 \left(\mathbf{m}_2 \times \hat{\mathbf{u}}_{xy}\right) - \gamma H_{xy} m_{x,2}^2 m_{2,y} \left(\mathbf{m}_2 \times \hat{\mathbf{u}}_{xy}\right) \\ &- \gamma H_z m_{2,z}\left(\mathbf{m}_2 \times \hat{\mathbf{z}}\right) - \gamma\left(\mathbf{m}_2 \times \mathbf{B}\right) + \lambda\left(\mathbf{m}_2 \times \dot{\mathbf{m}}_2\right)\end{aligned} \tag{4.3}$$

where $\dot{\mathbf{m}}$ denotes the time derivative of the magnetisation. The field arising from the $d_{zz}$ anisotropy constant in Eq. (4.1) has been neglected as $|d_{zz}| << |d_z|$. The Néel vector can be defined as $\mathbf{n} = (\mathbf{m}_1 - \mathbf{m}_2)/2$ and the magnetisation as $\mathbf{m} = (\mathbf{m}_1 + \mathbf{m}_2)/2$. The dynamics can be written purely in terms of $\mathbf{n}$ and $\mathbf{m}$. Combining Eq. (4.2) and (4.3) gives:

$$\begin{aligned}\dot{\mathbf{m}} = \frac{1}{2}\left(\dot{\mathbf{m}}_1 + \dot{\mathbf{m}}_2\right) =&\gamma H_{xy}\hat{\mathbf{u}}_{xy} \times \left(m_x m_y^2 \mathbf{m} + n_x n_y^2 \mathbf{n}\right) + \gamma H_z \hat{\mathbf{z}} \times \left(m_z \mathbf{m} + n_z \mathbf{n}\right) \\ &+\gamma H_{xy}\hat{\mathbf{u}}_{xy} \times \left(m_x^2 m_y \mathbf{m} + n_x^2 n_y \mathbf{n}\right) + \gamma\left(\mathbf{n} \times \mathbf{B}\right) + \lambda\left(\mathbf{n} \times \dot{\mathbf{n}}\right)\end{aligned} \tag{4.4}$$

and in terms of the Néel vector:

$$\begin{aligned}\dot{\mathbf{n}} = \frac{1}{2}\left(\dot{\mathbf{m}}_1 - \dot{\mathbf{m}}_2\right) =&\gamma H_{xy}\hat{\mathbf{u}}_{xy} \times \left(m_x m_y^2 \mathbf{n} + n_x n_y^2 \mathbf{m}\right) + \gamma H_z \hat{\mathbf{z}} \times \left(m_z \mathbf{m} + n_z \mathbf{n}\right) \\ &+\gamma H_{xy}\hat{\mathbf{u}}_{xy} \times \left(m_x^2 m_y \mathbf{n} + n_x^2 n_y \mathbf{m}\right) + \gamma\left(\mathbf{m} \times \mathbf{B}\right) + 2\gamma H_{\text{ex}}\left(\mathbf{n} \times \mathbf{m}\right)\end{aligned} \tag{4.5}$$

Any terms containing $\lambda\mathbf{m} \times \dot{\mathbf{m}}$, $\lambda\mathbf{m} \times \mathbf{n}$ and $\lambda\mathbf{n} \times \dot{\mathbf{m}}$ have been neglected since $|m| << |n|$. The torque from the staggered field generates a small out-of-plane component that is equal for both sublattices, meaning that the system can be characterised by $\mathbf{m} = (0, 0, m_z)$ and $\mathbf{n} = (n_x, n_y, 0)$. Removing any $m_x$,$m_y$ or $l_z$ from the above and noting that $n_x^2 + n_y^2 = 1$ leaves us with

$$\begin{aligned}\dot{\mathbf{m}} =&\gamma H_{xy} n_x n_y \left(n_x + n_y\right)\left(\hat{\mathbf{u}}_{xy} \times \mathbf{n}\right) + \gamma\left(\mathbf{n} \times \mathbf{B}\right) + \lambda\left(\mathbf{n} \times \dot{\mathbf{n}}\right) \\ \dot{\mathbf{n}} =&\gamma H_{xy} n_x n_y \left(n_x + n_y\right)\left(\hat{\mathbf{u}}_{xy} \times \mathbf{m}\right) + 2\gamma H_{\text{ex}}\left(\mathbf{n} \times \mathbf{m}\right)\end{aligned} \tag{4.6}$$

any terms associated with the out-of-plane anisotropy field have been dropped because the fluctuations in $z$ are much smaller than those in the $xy$-plane because of the size, $H_z \sim 10$ T. We can also safely assume the exchange field is much larger than both

the anisotropy and applied fields. We can therefore ignore the first term in the second equation above. If we then take the cross product of $\mathbf{n}$ we have

$$\mathbf{m} = \frac{1}{2\gamma H_{\text{ex}}} \left(\mathbf{n} \times \dot{\mathbf{n}}\right) \tag{4.7}$$

Taking the derivative of the above and substituting the above into the first equation in Eq. (4.6) gives

$$\frac{1}{2\gamma H_{\text{ex}}} (\dot{\mathbf{n}} \times \ddot{\mathbf{n}}) = \gamma H_{xy} n_x n_y \left(n_x + n_y\right) \left(\hat{\mathbf{u}}_{xy} \times \mathbf{n}\right) + \lambda \left(\mathbf{n} \times \dot{\mathbf{n}}\right) + \gamma \left(\mathbf{n} \times \mathbf{B}\right) \tag{4.8}$$

which simplifies to

$$0 = \mathbf{n} \times \left(\dot{\mathbf{n}} - 2\gamma^2 H_{\text{ex}} H_{xy} n_x n_y \left(n_x + n_y\right) \hat{\mathbf{u}}_{xy} + 2H_{\text{ex}} \lambda \dot{\mathbf{n}} + \gamma \mathbf{B}\right) \tag{4.9}$$

it is possible to write the Néel vector in terms of the angle, $\varphi$, away from the [110] ($\hat{\mathbf{u}}_{xy}$) direction by substituting:

$$\begin{aligned} n_x &= \cos(\varphi) + \sin(\varphi) \\ n_y &= \cos(\varphi) - \sin(\varphi) \end{aligned} \tag{4.10}$$

substituting the above into Eq. (4.9), after some simplification (see Appendix B) the equation of motion becomes

$$0 = \ddot{\varphi} + 2\lambda\dot{\varphi} + \gamma^2 H_{\text{an}} H_{\text{ex}} \sin\left(4\varphi\right) + \gamma H_{\text{ex}} B \cos\left(\varphi\right) \tag{4.11}$$

In the above, it is assumed the applied field is acting perpendicular to the starting orientation to maximise the torque. The dynamics can be described by a micromagnetic model in terms of a single angle, $\varphi$. To be able to directly compare the simulations to experimental results, the above equation can be modified to include the conductivity, $\sigma_c$ (which can be taken from literature), and a coupling parameter, $\alpha_{\text{NSOT}}$. By fitting the atomistic simulation data to this equation, a value of the coupling parameter can be extracted and compared directly to experimentally obtained results. The final form

of the equation of motion is:

$$0 = \ddot{\varphi} + 2\lambda\dot{\varphi} + \gamma^2 H_{\text{an}} H_{\text{ex}} \sin(4\varphi) + \gamma H_{\text{ex}} \sigma_c \alpha_{\text{NSOT}} B \cos(\varphi) \tag{4.12}$$

where $\varphi_{\text{L}}$ is the angle of rotation in the easy plane, $B$ is the staggered field given in equation (4.14), $\lambda$ is the Gilbert damping constant, $H_{\text{an}}$ and $H_{\text{ex}}$ are the anisotropy and exchange fields respectively, $\sigma_c$ is the conductivity and $\alpha_{\text{NSOT}}$ is the torquance from the staggered field.

## 4.4 Switching From a Staggered Gaussian Field

In this section, sub-picosecond timescale Gaussian staggered fields are used to induce switching in $Mn_2Au$ in the absence of any thermal noise. In the simulations, both the strength and width of the Gaussian pulse are varied. The staggered field is modelled using the following equation:

$$B(t) = H \exp\left(-\frac{(t-t_0)^2}{2\sigma^2}\right) \tag{4.13}$$

The field is staggered for each sublattice meaning sublattice one, $m_1$, experiences field $B(t)$ while sublattice two, $m_2$, experiences field $-B(t)$. The field is applied in perpendicular directions in the $xy$-plane to that of the starting configuration. The switching phase diagram is calculated at $T = 0$ K and is shown in Fig. 4.3. The colours show different reorientation angles. The inset shows the critical field for pulse widths below 0.2 ps. The inset data has been smoothed to aid in the visualisation of the main trend. This figure shows that switching using sub-ps pulses with staggered field strengths of approximately 200 mT.

Similar shaped critical field curves can be found for switching diagrams presented in Ref. [72] where square fields were used instead of the Gaussian pulse used here. The strength of the critical field where it plateaus is smaller by an order of magnitude in Ref. [172], with switching at 0 K occurring for critical field strengths of 40 mT for

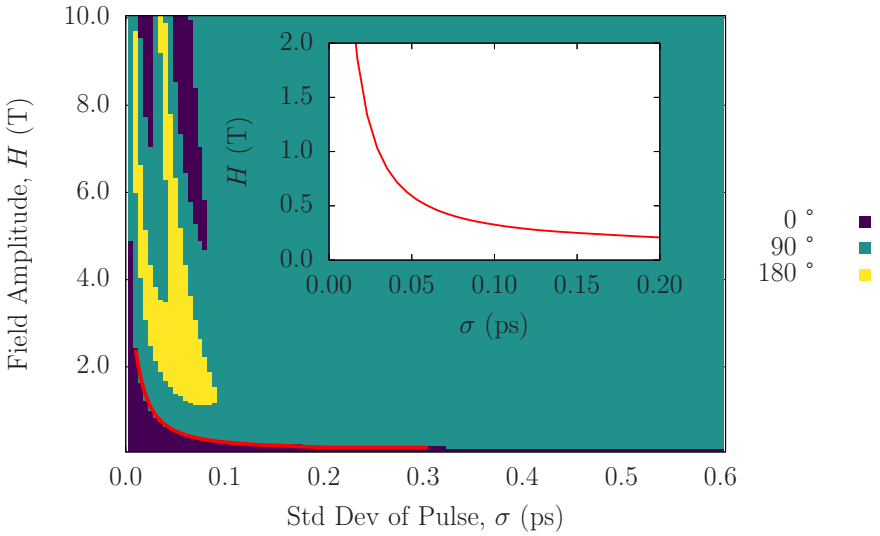


**Figure 4.3:** Switching phase diagram for pure $Mn_2Au$ following the application of a staggered Gaussian field. Turquoise and yellow regions show regions of 90° and 180° switching respectively. The inset shows a closer inspection of the critical field for field widths below 0.2 ps. The data in the inset has been smoothed.

similar pulse durations. The reason for this is a weaker Gilbert damping of $\lambda = 0.001$ being used in their study. There is no experimental evidence to suggest the damping for this material is that low. At present, the only experimental calculation of the damping can be found in Ref. [179] where a value of $\lambda = 0.008$ suggesting the critical fields calculated here are likely to coincide better if experimental observation of precessional switching are made. The reason for not selecting $\lambda = 0.008$ is simply that the experimental results of Behovits *et al.* [179] were presented to the community after the completion of the simulations in this thesis. Despite this, the values are close, and there is no reason to believe that the calculations presented in this chapter will differ greatly from the experimental measurements.

## 4.5 THz Pumping at In-plane Resonant Frequency

In this section, the effect of exciting $Mn_2Au$ close to the resonant frequency associated with the anisotropy field, $H_{xy}$, is explored (note this resonant frequency is not linked to the AFMR calculations in the previous chapter that were associated with the anisotropy

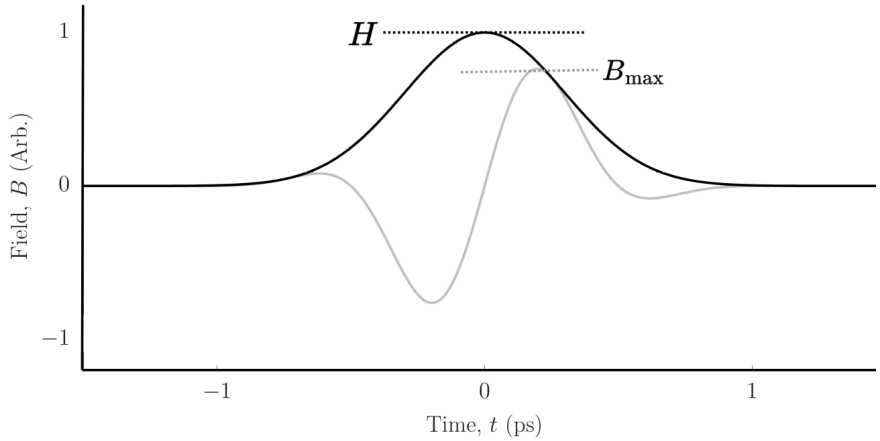


**Figure 4.4:** A schematic of the differences between the field profiles used in this and the previous section. When using a THz frequency, the maximum amplitude varies as a function of both $H$ and $\sigma$.

field from constant $d_z$). Here, we model the staggered field with the equation:

$$B(t) = H \exp\left(-\frac{(t-t_0)^2}{2\sigma^2}\right) \sin\left(2\pi f\,(t-t_0)\right) \tag{4.14}$$

where $\sigma$ is the standard deviation, $f$ is the frequency, $H$ is a scaling prefactor, and $t_0$ is the location of the central maximum of the pulse. In the atomistic simulations, the staggered field quantities subject to variation will be $\sigma$ and $H$. The relationship between $H$ and $\sigma$ means that for short pulse widths, the difference between $H$ and the maximum amplitude of the field, $B_{\text{max}}$, can differ greatly. For example, a $\sigma = 0.1$ ps pulse with $H = 10$ T yields a $B_{\text{max}} = 0.127$ T compared to an identical value of $H$ with $\sigma = 0.6$ ps yields $B_{\text{max}} = 8.45$ T. Because of this, references to the field for the remainder of this chapter will be in terms of $B_{\text{max}}$, rather than the varied quantity $H$. A schematic highlighting the differences between the constant $H$ and $B_{\text{max}}$ can be found in Fig. 4.4

We conducted atomistic simulations with a THz staggered field at temperatures of 0 and 300 K. For the 0 K case, the magnetisation dynamics are precessional and there is no thermal noise, meaning a single unit cell is sufficient. At room temperature, a system size of $70 \times 70 \times 70$ unit cells of $Mn_2Au$ is used, each consisting of 4 atoms yielding a total system size of 1,372,000 Mn atoms. Periodic boundary conditions are

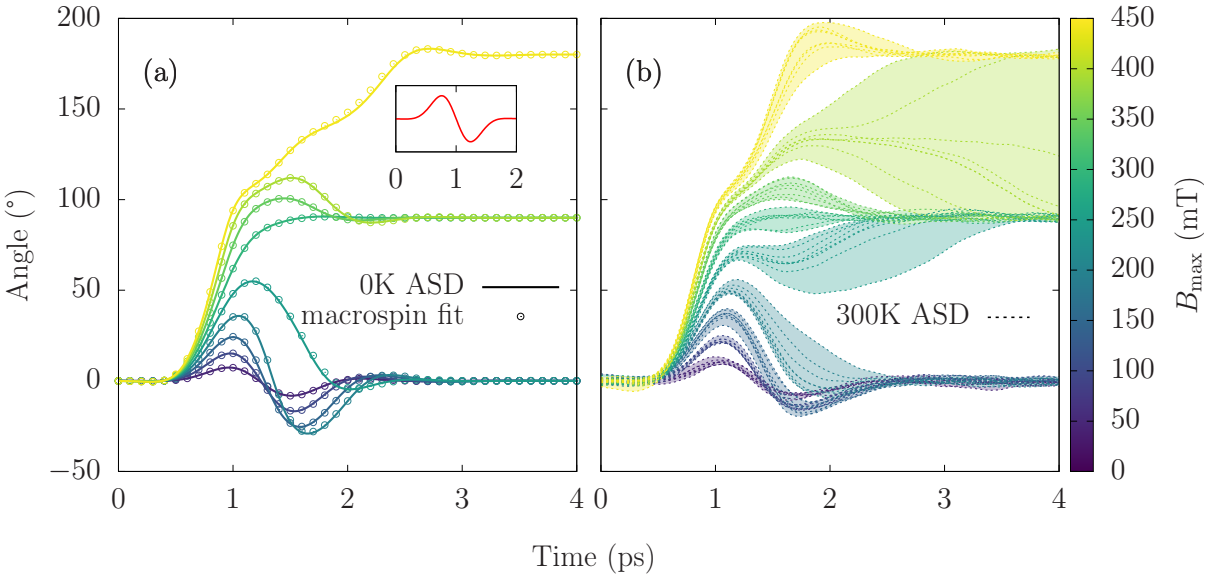


**Figure 4.5:** Magnetization reversal in $Mn_2Au$ for varying maximum field amplitudes, $B_{max}$, from approximately 50 to 450 mT at (a) $T = 0$ and (b) $T = 300$ K for a constant pulse width and frequency of $\sigma = 0.3$ ps and $f = 0.67$ THz. Inset in (a) shows the field profile between 0 and 1 ps or a $\sigma = 0.3$ ps. The dotted lines in (b) represent sublattice dynamics from individual simulations, the shaded area corresponds to the upper and lower bound for each field strength.

used at every surface. At 300 K, we simulated 9 values of $H$ in Eq. (4.14) varying from 80 to 720 mT in steps of 80 mT. A value of $H = 720$ mT for $\sigma = 0.3$ ps yields a maximum field amplitude of $B_{max} \approx 442$ mT. The standard deviation and frequency remain fixed in this instance at $\sigma = 0.3$ ps and $f = 0.67$ THz respectively. These values were selected following a visit to the Freie Universität Berlin in 2022 and discussions with experimentalists in the group of Tobias Kampfrath, particularly fellow PhD student Yannic Behovits. At this time, they were in the early stages of performing experimental measurements on THz electric field pumping of $Mn_2Au$. The parameters used for the field profile were chosen to be similar to those used in the experiments as it would allow for a good and simple future comparison. A figure comparing the field profile used in the atomistic simulations and that used in the experiments of Behovits *et al.* [179] can be found in Fig. 4.6. At the time of writing, only the preprint version is available.

Fig. 4.5 shows the Néel vector reorientation in the easy-plane following the THz pulse at 0 K (left pane) and 300 K (right pane). It is worth noting that the out-of-plane angle

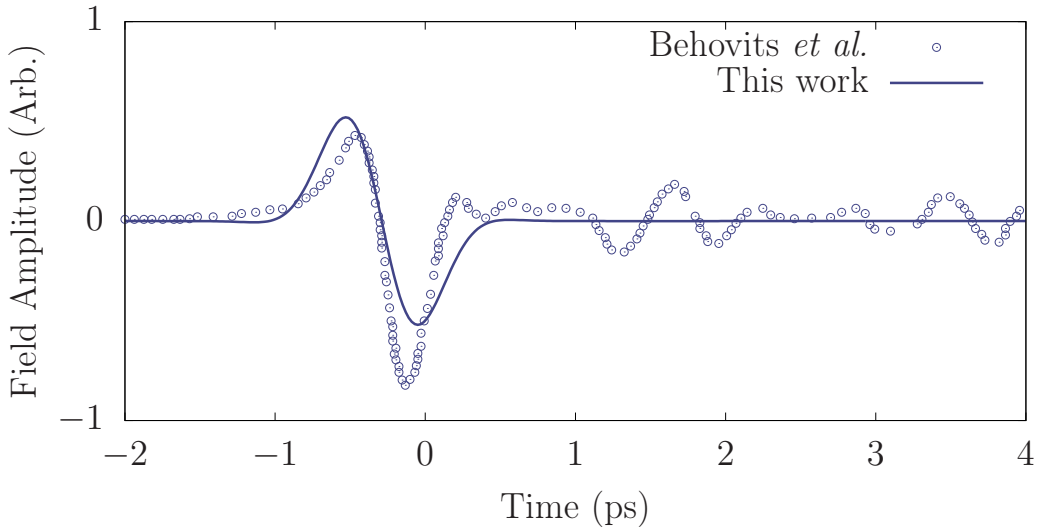


**Figure 4.6:** Comparison between the field profile used in the atomistic simulations and the experiments of Behovits *et al.* [179]. The experimental data has been extracted from Fig. 3d of their paper. The atomistic profile uses a frequency of $f = 0.67$ THz and a pulse with of $\sigma = 0.3$ ps.

remains close to zero through the entire process due to the large uniaxial easy-plane anisotropy constant $d_z$ in Eq. (4.1). The onset of 90° switching occurs $B_{\text{max}} = 294$ mT with 180° being observed at $B_{\text{max}} = 442$ mT for $T = 0$ K. For 300 K, the simulations were repeated 8 times for all field values to account for the stochastic thermal effects. The dotted lines show the results from individual simulations, and shaded area represents the upper and lower bound for each field value. Upon comparing both panes in Fig. 4.5, the first instance of reversal has reduced from $B_{\text{max}} = 294$ mT for 0 K, to $B_{\text{max}} = 245$ mT for 300 K due to the reduction in anisotropy field. In the room temperature simulations, the switching was deterministic; however, the path and final reorientation angle were not - as seen for a field amplitude of $B_{\text{max}} = 392$ mT, where both 90° and 180° switching occurred.

Experimentally, the only estimation of the size of the staggered torques comes from the work of Behovits *et al.* [179] where they state that they achieve a staggered field of $8 \pm 3$ mT per $10^7$ A cm$^{-2}$ driving current density. In the *ab-initio* works of Zelezny *et al.* [189], they calculate a staggered field of 1.98 mT $10^7$ A cm$^{-2}$. In Ref. [142], Electric fields of $10^7$ kV/cm yield staggered fields of about 76 mT, in their work they

do not provide an exact value for the conductivity but state a field of 100 kV/cm inside the sample would correspond to a current density of the order $10^6$ to $10^7$ A cm$^{-2}$. For the critical field values of 294 and 245 mT at 0 and 300K respectively (see Fig. 4.5) a current density within the sample of $\sim 10^8$ A cm$^{-2}$ would be required (assuming a linear scaling with the staggered field). Electric fields of this order can be achieved in experimental facilities [190–192].

For 0 K, it is possible to sample a large phase space of $B_{\text{max}}$ and $\sigma$ with little computational cost using a single unit cell in the absence of any stochastic effects. In Fig. 4.7 we present a switching phase diagram at $T = 0$K for a range of applied field amplitudes and pulse durations for a fixed frequency of 0.67 THz. The colour shows whether the system undergoes 90 or 180 degree switching (relative to the initial state) following a THz staggered pulse. The field and pulse duration required for Néel vector reversal increases for a multi-cycle signal because of the changing sign of the external field. For $\sigma \gtrsim 0.4$ ps, the switching window appears less structured, which is likely due to the transition from a single-cycle to a multi-cycle field with increasing $\sigma$. What is surprising is that pulses as short as 0.2 ps with sub-Tesla staggered fields can drive antiferromagnetic switching. The phase diagram is more complex than that seen previously for antiferromagnetic NiO [70] due to the use of an un-staggered square field profile with a single uniaxial anisotropy constant in that study.

## 4.6 THz Switching Using the AFM-LLB

Calculation of the phase diagram presented in Fig. 4.7 but instead using an AFM-LLB model yielded almost identical results. Of the 24,000 data points, only 131 (0.005%) ended with final orientations that differed from the atomistic approach. Phase diagrams for static temperatures of 0, 300, 600 and 900 K are shown in Fig. 4.9. What is most evident is the increase in the area where the final state shows no reorientation of the Néel vector. This is not to say that the system is responding weakly to the THz field with increasing temperature, but instead is the result of an increase in the number of cases where the Néel vector performs at least one full rotation in the easy plane.

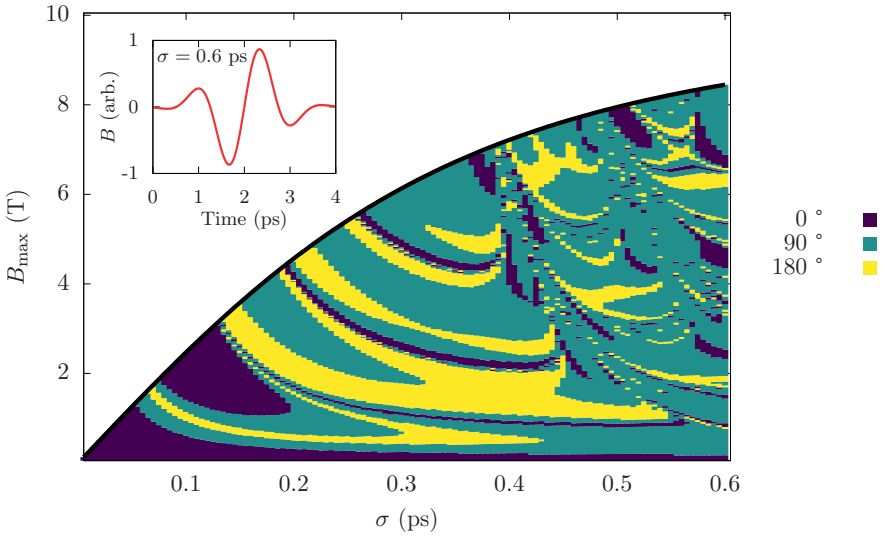


**Figure 4.7:** Switching phase diagram for pure $Mn_2Au$ following a THz pulse. Turquoise and yellow regions show regions of 90° and 180° switching respectively. Inset shows the field profile for the maximum pulse width of $\sigma = 0.6$ ps.

The time-dependent dynamics of the AFM-LLB are also compared against the finite temperature $T = 300$ K ASD simulations for a fixed with of $\sigma = 0.3$ ps presented in Fig 4.5. This comparison is shown in Fig 4.8. The dynamics agree remarkably well with all the AFM-LLB dynamics lying within the range of the ASD simulations.

These results highlight the suitability of using the AFM-LLB in simulations of magnetisation reversal. The combined total simulation time of the ASD dynamics shown in Fig. 4.8 was in excess of 30 hours using state-of-the-art Nvidia A100 Graphics cards, (costing somewhere in the region of £5,000). On the other hand, the AFM-LLB simulations took approximately 5 minutes using a single computing core of an i7-8700 CPU processor ($\approx$ £300), thus highlighting the huge reduction in computational workload when using an AFM-LLB model for precessional switching analysis.

## 4.7 Square Pulse Combined With Transient Two-Temperature Model Heating

It is well understood that increased temperature leads to reductions in the field required for switching. Recent work by Rama-Eiroa *et al.* [72] investigated the impact

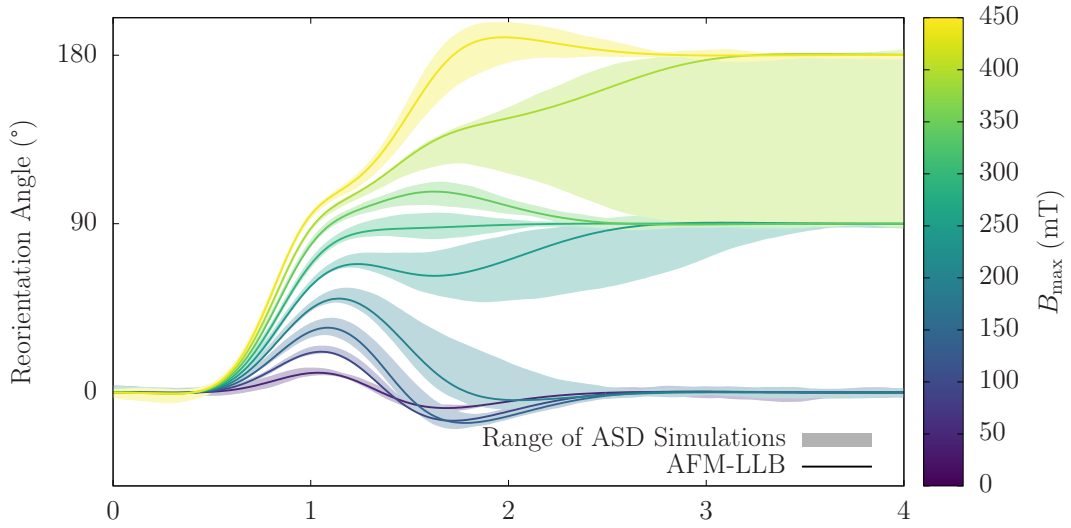


**Figure 4.8:** A comparison of the Néel vector dynamics at $T = 300$ K between ASD and AFM-LLB approaches. The shaded area shows the reorientation range across the 8 repeated ASD simulations. The solid lines are the AFM-LLB results. The colour bar shows varying maximum field amplitude, $B_{\max}$.

temperatures and durations of a square-pulse generated by a current-induced SOT had on reorientation of the Néel vector in $Mn_2Au$. In their model, they derive analytical expressions for the critical field required for switching and compare to atomistic simulations. The analytical expressions derived in their work are based on the same temperature dependence of the effective damping, anisotropy and exchange presented in chapter 3. The analytical expressions are derived for static temperature, and therefore their model cannot be used to derive strategies for reductions of the critical field as a result of laser heating. In this section, we explore the effects of transiently heating up $Mn_2Au$ using a two-temperature model in combination with a 0.5 ps staggered square pulse to induce reversal. Because of the temperature scaling of the cubic anisotropy ($K_{xy}(T) \propto M^{10}(T)$) combined with an already relatively low constant of $d_{xy} = 0.04$ meV means that atomistic simulations of reversal at temperatures close to the Néel temperature require exceptionally large system sizes. Therefore most of the simulations in this section will be completed using the LLB equation with ASD acting as a benchmark.

For the laser heating, a TTM approach is used as seen in previous chapters (see Eq. (3.16)). The parameters can be found in Tab. 4.1. Uniform heating is presumed

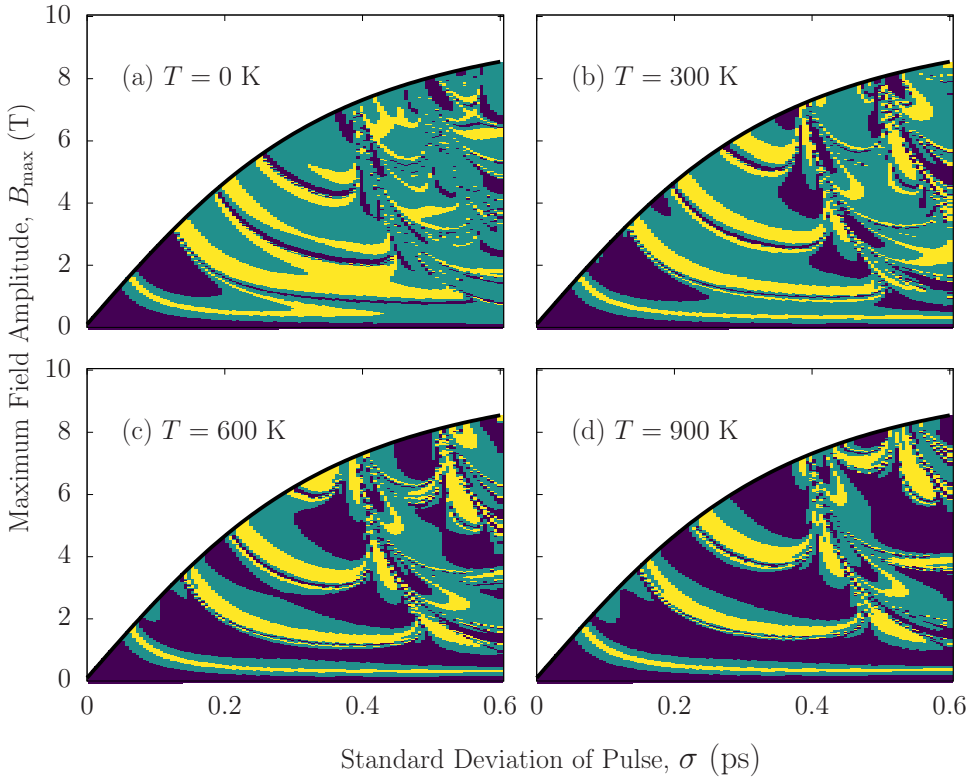


**Figure 4.9:** Magnetization reversal phase diagrams for $Mn_2Au$ using the AFM-LLB model. Panels are temperatures of (a) 0 K, (b) 300 K, (c) 600 K, and (d) 900 K.

throughout the system. The parameters should not be considered realistic values for this material as no comparison to literature can be found. They are however within a sensible range for other magnetic systems, with the focus here being on the the trends the magnetisation follows for dynamics changes in temperature, not necessarily to make exact quantitative predictions. The laser power is modelled with a Gaussian profile with respect to time with uniform heating presumed throughout the system. Fig. 4.10 shows the phonon, $T_p$ (dotted lines), and electron, $T_P$ (solid lines) for varying laser fluences. The shaded area shows the power profile and has been scaled arbitrarily to highlight the delay between the laser application and temperature increase. To ensure correct longitudinal dynamics in the LLB model, ASD simulations were conducted for the $P_0$ values presented in 4.10. The comparison between the AFM-LLB and ASD can be found in 4.11. Points and Solid lines are ASD and AFM-LLB models respectively. A larger disagreement is observed for the lower selected power values. The reason for this is that the maximum temperature for these fluences is extremely close

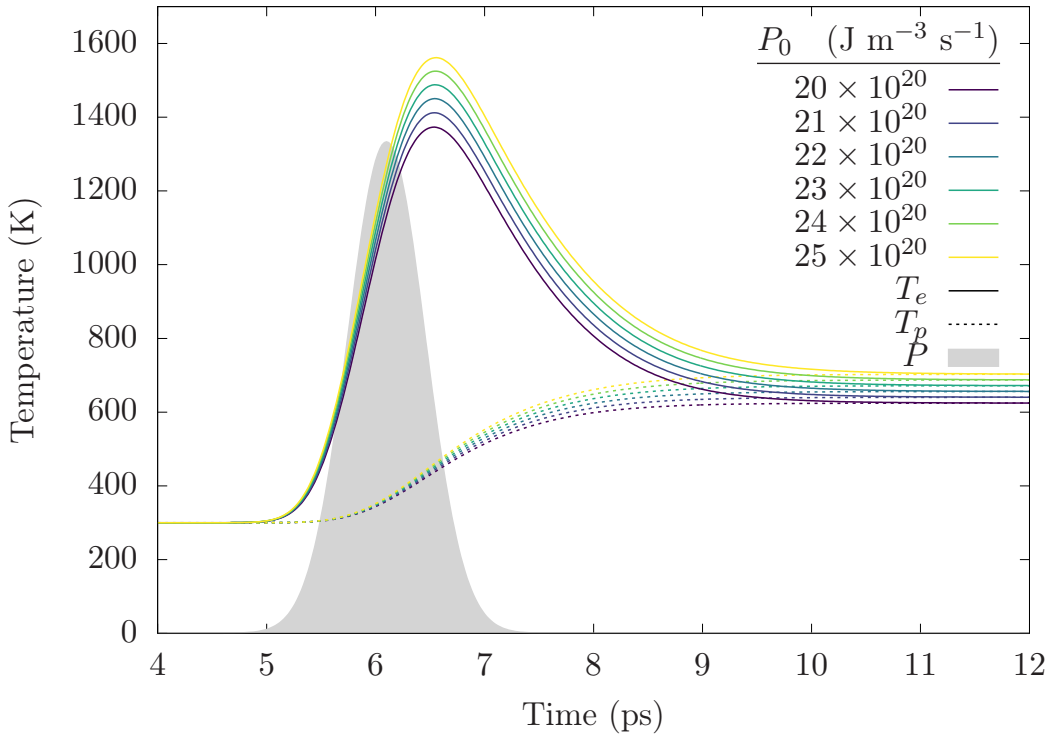


**Figure 4.10:** Eletron (solid lines) and phonon (dotted lines) temperature for varying laser fluence (colour). The shaded area shows the profile of the laser power and the delay between application of the laser and the resultant heating.

to that of the critical temperature, where the susceptibility diverges (see Fig. 3.3 for the susceptibility curve). Because the turning point is close to the critical temperature, the system spends a longer amount of time at close to the critical temperature than the simulations with higher fluence. The LLB model represents an infinite system in contrast to the ASD where finite size effects lead to shorter relaxation times close to the critical temperature. Occurrences of this effect can be found in multiscale modelling of ferromagnets, with notable examples found in Refs [193, 107].

| Physical Constant | Symbol | Value Used | Units |
|---|---|---|---|
| Electron specific heat coefficient ($\gamma_e$) | $C_e = \gamma_e T_e$ | $1 \times 10^3$ | J m$^{-3}$ K$^{-2}$ |
| Phonon specific heat | $C_p$ | $5 \times 10^6$ | J m$^{-3}$ K$^{-1}$ |
| Electron-phonon coupling | $G_{ep}$ | $1 \times 10^{17}$ | J m$^{-3}$ K$^{-1}$s$^{-1}$ |
| Laser pump temporal width | $\tau$ | 0.5 | ps |

**Table 4.1:** Table of parameters for the TTM heating.

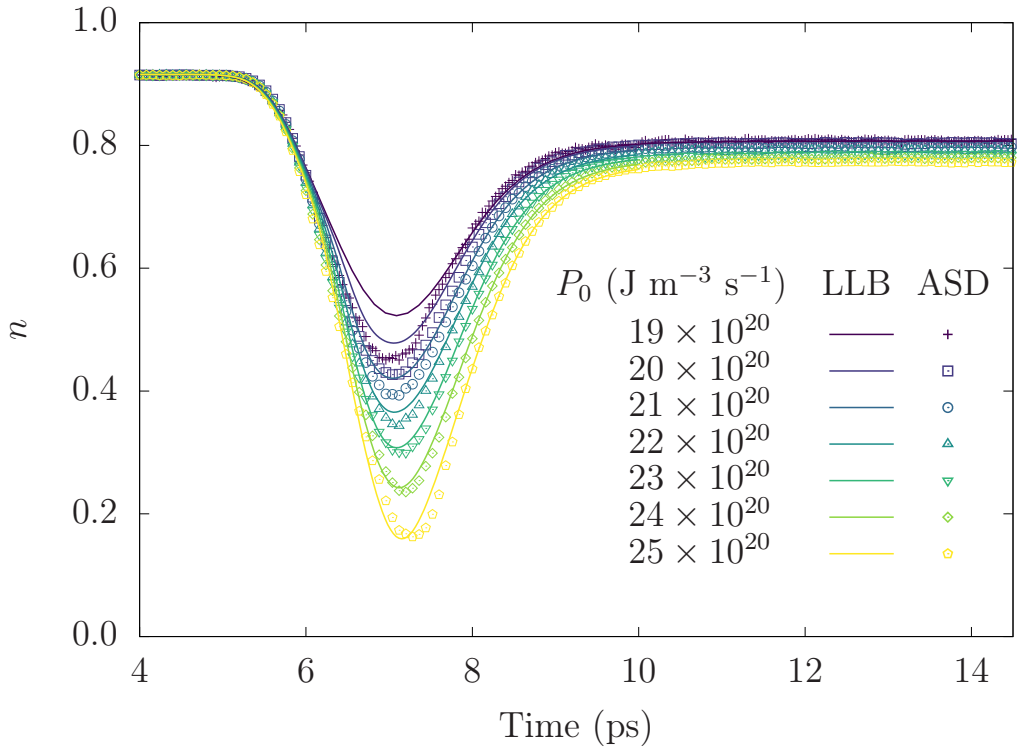


**Figure 4.11:** The longitudinal relaxation of the Néel vector for varying maximum laser fluence. Points are ASD and lines are LLB.

For the simulations combining a square pulse with TTM heating, the start time of the square pulse is varied while the laser timings remain fixed. The critical field is calculated as a function of delay for the previously shown laser fluences as shown in Fig. 4.12. The lines represent the critical field for switching. The areas below and above the critical field line represent regions of 0° and 90° reorientation in the $xy$-plane. The delay is defined as the difference between the start of the staggered field pulse and the point at which the laser is at maximum fluence. Between -2.0 and -1.5 ps delay, the staggered field has been applied too early for the heating to play any kind of role. This is followed by a reduction in the critical field for a delay of between -1.0 and -0.5 ps. For all simulated fluences, the reduction remains fairly constant, with a reduction from approximately 130 mT to 100 mT in this region, a drop of roughly 25%. Onwards from this point, there is an increase in the critical field with maximum divergence occurring when the staggered field is applied roughly 0.5 ps after the max fluence of the laser. For the larger fluences, drastic increases in the critical field are observed using the AFM-LLB, well over 70% for values of $P_0 = 24 \times 10^{20}$ J m$^{-3}$ s$^{-1}$ and $P_0 = 24 \times 10^{20}$ J m$^{-3}$ s$^{-1}$.

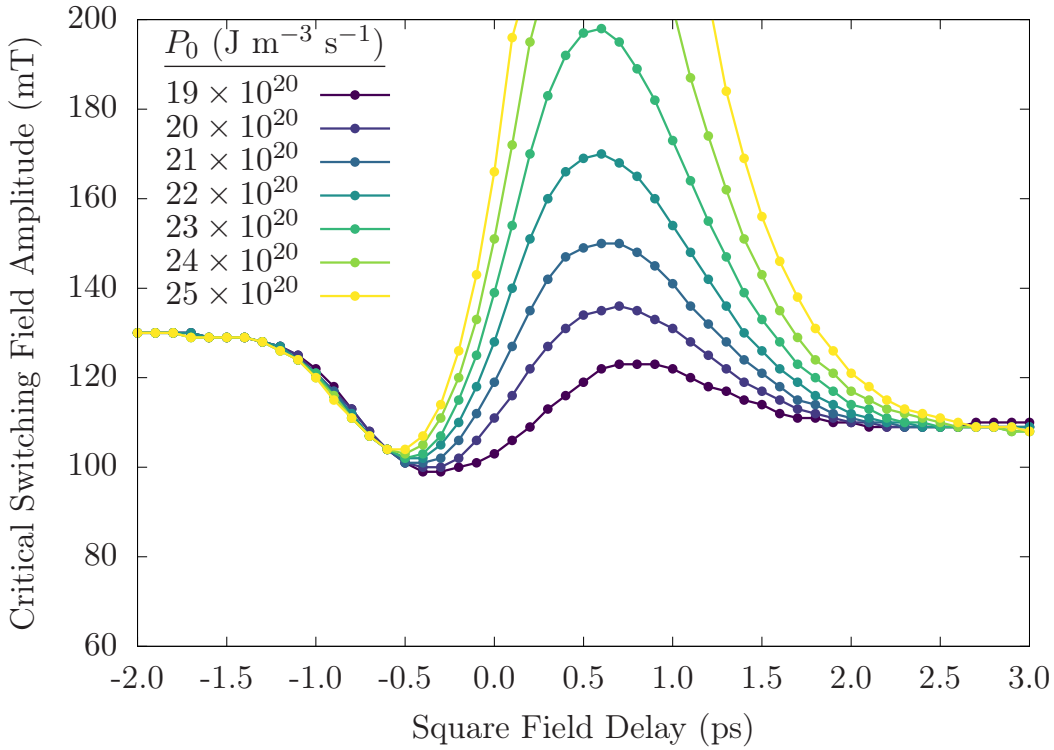


**Figure 4.12:** Critical field calculated from LLB simulations for varying maximum laser fluence. Below the lines, there is no switching. Above, there is 90 °reversal.

The reason for such a large increase in the critical field for larger fluences in the range between 0.5 and 1.0 ps rests with the fact that the switching field is being applied at the point in time when the spin system is at maximum demagnetisation following laser heating. For larger laser fluences, the greater the resulting demagnetisation. During this time, the spins are weakly correlated because of the thermal energy and the applied field to coherently reorientate the Néel vector must therefore be stronger to overcome increased thermal effects.

To confirm this result, ASD simulations are performed with a laser fluence of $P_0 = 2.4 \times 10^{21}$ J m$^{-3}$ s$^{-1}$ with a field amplitude of 150 mT for varying delays. ASD Simulations once again conducted with a system size of $70 \times 70 \times 70$ unit cells of $Mn_2Au$ with periodic boundary conditions at each surface. Simulations are repeated 12 times for each delay value to account for the thermal noise. The atomistic results overlayed on top of the LLB phase diagram can be found in the bottom pane of Fig. 4.13. The colour indicates the switching probability. The top pane shows the probability to further aid

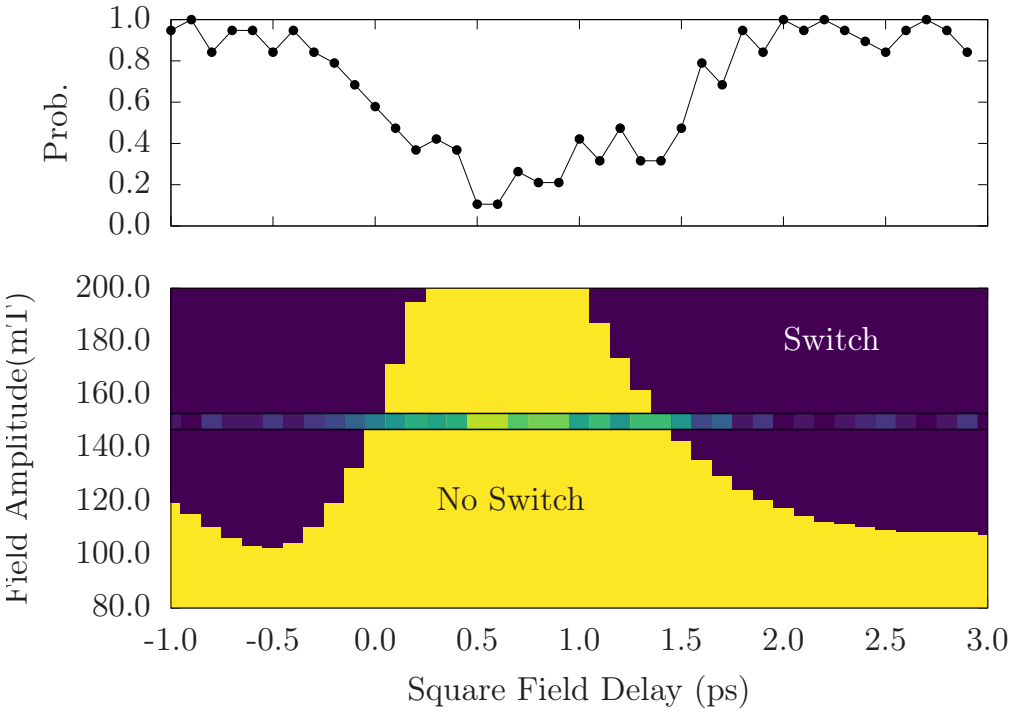


**Figure 4.13:** (Bottom) Phase diagram for a power of $P_0 = 25 \times 10^{20}$ J m$^{-3}$ s$^{-1}$. The line at 150 mT is from ASD rather than LLB. The simulations are repeated 12 times to account for the noise processes. Colour is the switching probability. As there is no noise in the LLB model, the switching is deterministic. (Top) Switching probability from the ASD simulations.

in visualisation. While the switching is not deterministic, there is a clear reduction in the probability that coincides with a region of no switching in the LLB phase diagram.

## 4.8 Summary

ASD and AFM-LLB simulations have been used in this chapter to simulate reversal following a sub-ps staggered Gaussian and THz field pulses. Experimentally, these fields would arise from a current pulses, and it has been shown that by pumping $Mn_2Au$ close to the in-plane resonant frequency, switching is achievable with fields of the order of 100s mT. Switching using square and Gaussian field profiles was shown to require much weaker fields compared to cyclic THz fields where the sign alternates. Ideally, square pulses would be used but experimental realisation of such profiles with sub-ps durations remains a challenge [179, 59]. It has been shown that THz pumping at room

temperature yields small reductions in the critical field, which agrees with previous finite temperature computational modelling of $Mn_2Au$ [72] following the application of square staggered fields. The AFM-LLB showed remarkable agreement at 0 K, with a fractional amount of simulations producing differing final reorientation states between ASD and AFM-LLB. Simulations using the AFM-LLB also show robust switching for a wide range of temperatures.

Although static temperatures serve as reliable indicators for overall trends in critical field reductions, for recording media applications it would likely require transient heating and cooling facilitated by a laser or near-field transducer to decrease the critical field and then restore its stability. It has been shown using the AFM-LLB that transient heating from a laser pulse can lead to reductions of up to 25% in the critical field. It is worth mentioning that only the impact of the field delay and laser power has been investigated. Further exploration using varied laser and applied field durations, staggered field profiles (THz, Gaussian) and damping could perhaps yield further reductions. The delay between heating and the application of a staggered field impacts the critical field heavily, with large increases in the critical field observed when the staggered field is applied at the point of maximum demagnetisation with drastic increases in the required critical field for 90° switching in $Mn_2Au$. ASD simulations agreed well with the AFM-LLB approach, however, the competition between the anisotropy and weak cubic anisotropy meant the switching was not deterministic when using an atomistic model. Larger system sizes would help eradicate this issue, but with this comes increased computational costs.

# Chapter 5

# Atomistic Simulations of $Mn_2Au$ and Permalloy Bilayers

***Mark:*** *Well, me and Dobby make a great team… Opposites attract!*

***Jez:*** *No they don't. Not really. That's just something scientists and people in horrible relationships say.*

– *MARK & JEZ*, Peep Show. Created by Jesse Armstrong and Sam Bain.

## 5.1 Introduction

The idea of coupling magnetic layers to alter the properties has been around for several decades now [194, 195], and has already found its way into HDD technology via the use of exchange spring media for perpendicular magnetic recording [196]. For high coercivity (often referred to as hard) magnets such as FePt, the fields generated by the write head cannot produce a strong enough field to induce switching of the grains [197]. By exchange coupling a strongly anisotropic layer to an additional weaker FM layer, the switching field can be reduced while still maintaining sufficient thermal stability. $Mn_2Au$ has a cubic anisotropy constant that is two orders of magnitude smaller than the uniaxial constant in FePt [87] thus nullifying the issue of having to use a large field to overcome the large anisotropy barrier. The main issue for AFMs is the readout of the Néel vector because of the alternating magnetic moments at the atomic level result in no net magnetisation, making detection of the magnetic order impossible using conventional GMR and TMR methods. Recently, it has been suggested that by coupling an FM layer to an AFM the FM spin dynamic frequencies can be enhanced, opening the possibility for faster switching in weakly anisotropic FM materials. The effect of an exchange coupling to reduce critical fields has been studied in interesting structures such as FePt/FeRh [198, 199], where FeRh undergoes a phase transition from AFM to FM with increasing temperature opening the possibility of using the FM phase to during the switching process, and the AFM phase to enhance thermal stability. Little is understood however about the ability to control switching dynamics when using an AFM configuration.

Recent work by Bommanaboyena *et al.* [200] investigated the effect of coupling $Mn_2Au$ to epitaxial thin films of Permalloy (Py) - a soft FM nickel-iron ($Ni_{80}Fe_{20}$) alloy with an intrinsically low anisotropy [201, 202]. In the atomistic modelling of Py vortices a cubic anisotropy constant of $3.355 \times 10^{-26}$ J is used, two orders of magnitudes smaller than the cubic anisotropy for $Mn_2Au$. What they found in the bilayer is the onset of a large exchange coupling between the FM and AFM layers with exact one-to-one imprinting of the AFM domain pattern on the FM Py. Fig. 5.1 shows the XMLD-PEEM and

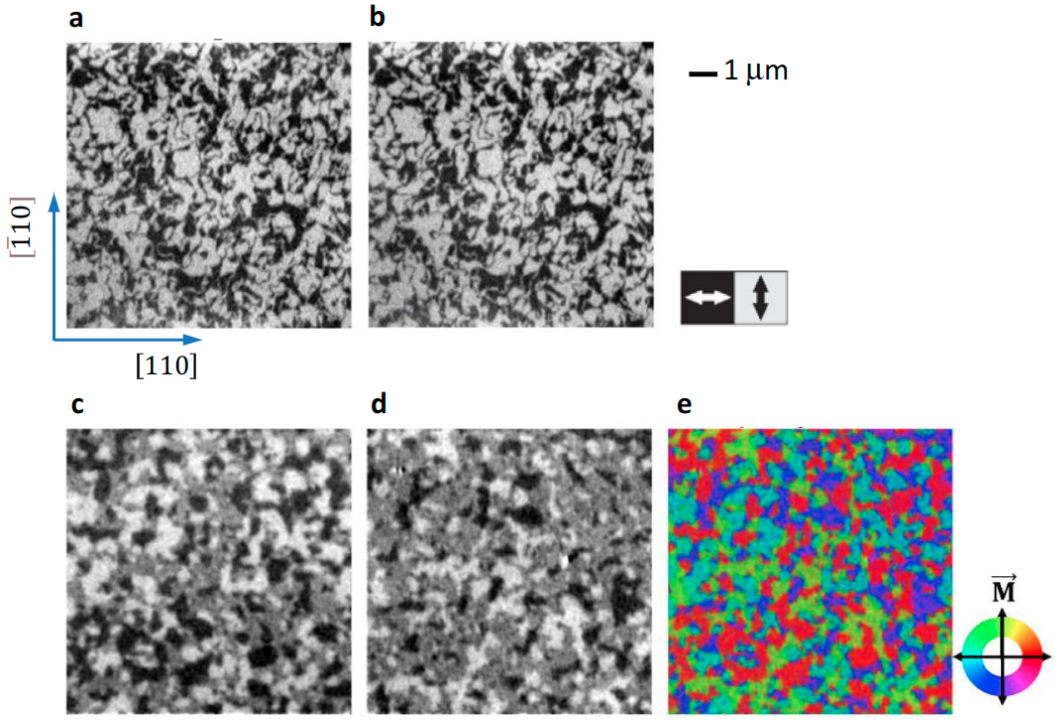


**Figure 5.1:** XMLD-PEEM images of as-grown $Mn_2Au$(40 nm)/Py(4 nm)/SiNx(2 nm). (a) Image of the $Mn_2Au$ AFM domains. (b) Image of the Py FM domains. Dark and light regions show the horizontal and vertical orientation of the magnetisation respectively. (c) scanning electron microscopy with polarisation analysis (SEMPA) image showing the x-component of the FM contrast. (d) SEMPA image of $y$-component of the FM contrast. Panel (e) is generated from panels (c) and (d) and shows the magnetisation of the Py domains is parallel to one of the 4 easy $\langle 110 \rangle$ directions. The field of view in each panel is 10 $\mu m^2$. Image taken from Ref. [200].

scanning electron microscopy with polarisation analysis (SEMPA) [203] images from their experiment. Panels (a) and (b) show the results of their XMLD-PEEM measurements on their as-grown sample of $Mn_2Au$(40 nm)/Py(4 nm)/$SiN_2$(2 nm). Panel (a) and (b) show the domain patterns of $Mn_2Au$ and Py, respectively. Upon comparing the two panels, it can be seen that the AFM domain pattern is perfectly imprinted on the FM layer with dark and light regions indicating horizontal and vertical orientation of the magnetisation respectively. Using SEMPA, they are able to indirectly obtain the exact orientation of the AFM domain structure. Panels (c) and (d) show the $x$ and $y$ components of the FM contrast. By combining these two plots into panel (e), they are able to reveal the exact direction of each FM domain and thus infer the orientation of each AFM domain. It is worth noting that they observe no exchange bias - the apparent shift of a hysteresis loop of an FM due to the interface coupling with an AFM

- and render it unattainable in this particular system. They attribute this to the high critical temperature of $Mn_2Au$ in relation to the comparatively low $T_C$ of Permalloy, 700 $\sim$ 800 K [204–206] preventing the creation of an exchange bias by field cooling methods [207, 208]. The strong FM coupling of the layers opens the possibility for the use of standard readout techniques to access the magnetic order, such as GMR or TMR. For an FM/AFM Bilayer to be a viable candidate for faster and more efficient memory applications, the extent to which the GHz dynamics slows down the switching speed needs to be properly understood.

In this chapter, we introduce an atomistic model of the $Mn_2Au$/Py bilayer and focus on two variable quantities in our simulations: (i) the thickness of the FM Py layer, and (ii) the strength of the exchange at the interface. Through Fourier analysis we explore how these variables affect the resonant frequency of the system and determine the temperature-dependent magnetisation and resonant frequencies. We analyse switching using a THz frequency pulse and present switching phase diagrams for a range of THz field strengths and widths. Simulations are conducted at static temperatures ranging from 0 to 600K to understand whether thermal effects play an important role in the switching process.

## 5.2 Atomistic System

For the bilayer system, we use lattice constants for $Mn_2Au$ with $a_{Mn_2Au} = 3.33$ Å and $c_{Mn_2Au} = 8.537$ Å. These are identical to those used in the atomistic model of $Mn_2Au$ in chapters 3 & 4. For the atomistic modelling, we assume the Py matches $a_{Mn_2Au}$ given a comparable experimental value of $a_{Py} = 3.55$ Å for bulk Permalloy [209]. The Py is stacked vertically on top of the $Mn_2Au$ in the (001) direction. This means only one of the AFM sublattices couples to the FM at the interface, preventing any frustration. We assume open boundary conditions at the top and bottom end of the chain and periodic boundaries on all others. A schematic of the chain close to the interface can be found in Fig. 5.2.

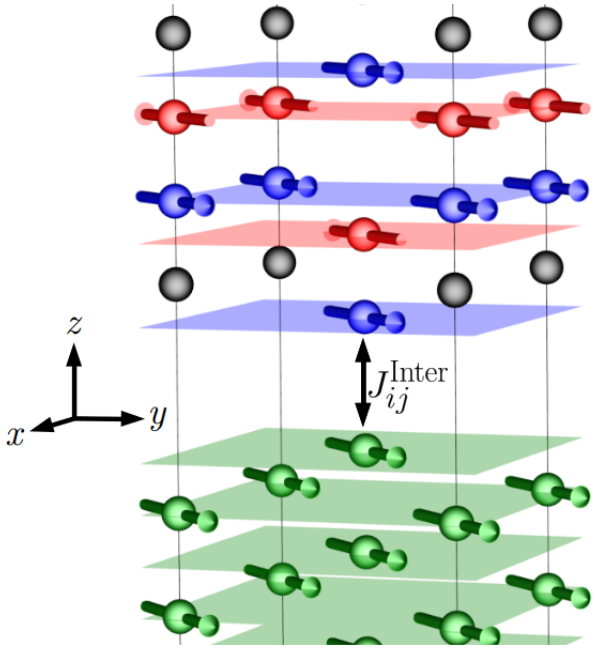


**Figure 5.2:** A snapshot of the system close to the interface. The Py atoms are shown in green, the Au in black, and the Mn sublattices in blue and red respectively. The Py and Mn is coupled ferromagnetically at the interface. Each axis has been scaled differently to aid in the visualisation.

The thickness of $Mn_2Au$ is fixed at 25 units cells along the vertical length of the system, which equates to roughly 21 nm. We chose to vary the thickness of Py using 6, 8, 10 and 20 unit cells. This corresponds to thin film thicknesses of approximately 2.13 nm, 2.84 nm, 3.55 nm and 7.1 nm respectively - similar thicknesses of Py were used in the $Mn_2Au$/Py bilayer experiments of Bommanaboyena *et al.* [200] where they vary the thickness of the FM layer between 2 and 10 nm.

At the interface, the exchange is treated as nearest-neighbour between Py and Mn atoms and is denoted by $J_{ij}^{\text{Inter}}$. In the simulations, the exchange coupling at the interface is varied from $0.5 \times 10^{-21}$ J ($\approx 15\%$ of the n.n $J_{ij}$ used for Py) to $5.0 \times 10^{-21}$ J. The interface coupling is chosen as a variable quantity in our simulations as it is possible to manipulate this experimentally by the insertion of a non-magnetic spacer between the FM and AFM [210] or doping at the FM/AFM interface. The second reason is that in the work of Bommanaboyena *et al.* [200] they do not provide an estimate for the exchange coupling, and therefore a range of values have been covered in the hope there is some crossover between experiments and simulation. For the bulk Py

atoms (those not at the bilayer interface), For simplicity, we use an average-moment model with nearest-neighbour exchange, totalling 12 interactions per Py site. Similar average moment models of The first term in the above can be found in Eq. (5.1). For the Permalloy, we use an average moment of $0.95\mu_B$ assuming a magnetic moment of $\mu_{\text{Ni}} = 0.62\mu_B$ and $\mu_{\text{Fe}} = 2.27$ with concentrations of 80% and 20% for Ni and Fe, respectively. We use nearest-neighbour exchange and exclude any anisotropy. The cubic anisotropy constant in bulk permalloy is four orders of magnitude smaller than $d_z$, and two orders smaller than $d_{xy}$ in $Mn_2Au$ and can therefore be safely ignored. For the 12 neighbouring interactions in Py, we use a value of $J_{ij}^{\text{Py}} = 3.01 \times 10^{-21}$ J which yields a Curie temperature $\approx 720$ K for a bulk system. For $Mn_2Au$, the exchange interactions, anisotropy and magnetic moment for $Mn_2Au$ are identical to those used in chapter 4. The atomistic Heisenberg Hamiltonian for the bilayer system reads

$$\mathcal{H}_{\text{Mn}} = \sum_{\text{Mn}} J_{ij}^{\text{Mn}} \mathbf{S}_i \cdot \mathbf{S}_j - \sum_{\text{Mn}} d_z S_{i,z}^2 - \sum_{\text{Mn}} d_{xy} S_{i,x}^2 S_{i,y}^2 + \sum_{\text{Py}} J_{ij}^{\text{Py}} \mathbf{S}_i \cdot \mathbf{S}_j + \sum_{\text{Inter}} J_{ij}^{\text{Inter}} \mathbf{S}_i \cdot \mathbf{S}_j \tag{5.1}$$

## 5.3 Frequency Scaling With Interface Exchange and Permalloy Thickness

The idea behind coupling the AFM to an FM is that you easily get access to the magnetic information while avoiding a significant slowdown in the magnetisation dynamics. Here we calculate the resonant frequency scaling at $T = 0$ K for varied interface exchange and Py thickness. As the simulations are performed at 0 K, an external stimulus is required to excite the dynamics. This is done by rotating the spins by 20° in the $xy$-plane away from the initial equilibrium position. The spins are then unpinned and the magnetisation dynamics are recorded for 50 ns with the damping value set to an unrealistically low value of 0.001 for both $Mn_2Au$ and Py to allow for a longer precessional motion. The resonant frequency is extracted via an FFT of the dynamics after an initial equilibration of 100 ps.

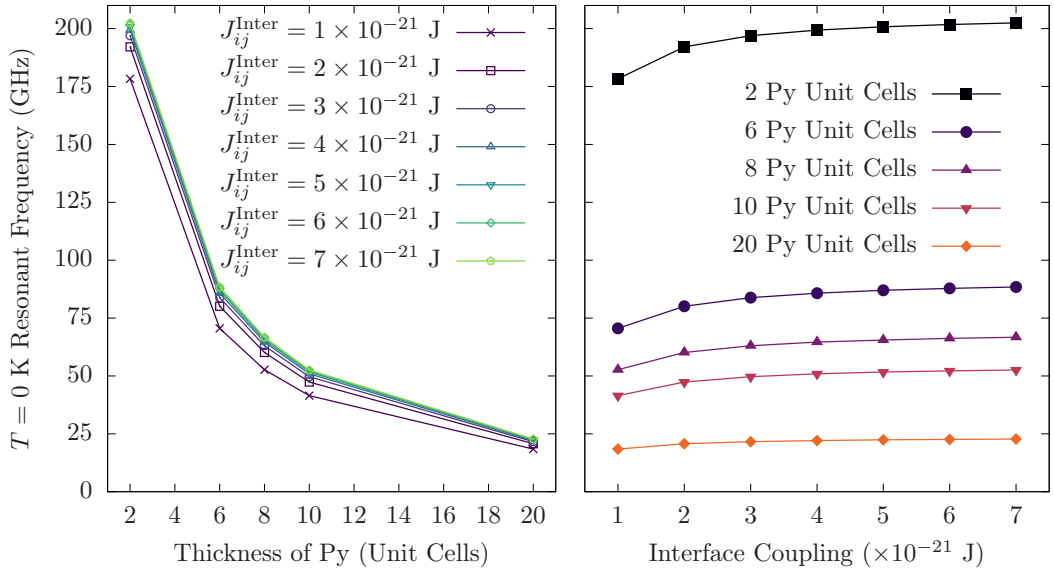


**Figure 5.3:** (Left) Frequency scaling with increasing Py thickness for varying interface exchange. (Right) Scaling with increasing interface exchange for varying Py thickness.

The frequency scaling with respect to increasing FM thickness is shown in the left pane of Fig. 5.3. As expected, a decrease in the resonant frequency is observed with increasing thickness of the FM layer as the GHz FM dynamics begin to dominate over the faster THz frequency AFM dynamics. An order of magnitude increase in the FM thickness from 2 to 20 unit cells leads to an approximately 8-fold decrease in the resonant frequency. On the right pane of Fig. 5.3 is the frequency scaling for increasing interface coupling for static FM thickness. Unlike with the Increasing FM thickness, the change in frequency is less drastic. A 7-fold increase in the interface exchange from $J_{ij}^{\text{Inter}} = 1 \times 10^{-21}$ J to $J_{ij}^{\text{Inter}} = 7 \times 10^{-21}$ J only yields an increase in the resonant frequency of between 1.1 and 1.4 depending on the Py thickness. For switching applications, it's therefore expected that a thinner FM would enable reversal for shorter field pulses with lower amplitudes while the interface exchange plays a less important role.

## 5.4 Temperature Dependence of the Magnetisation

Calculations of the magnetisation as a function of temperature are performed for two values of interface coupling, $0.5 \times 10^{-21}$ J and $5.0 \times 10^{-21}$ J with FM thicknesses of 6 and 20 unit cells. Simulations are performed for systems with 60 unit cell repetitions of the spin chain along the $x$ and $y$ directions. For the system with 6 unit cells of Py, there are 406,800 atomistic spins in total. For 20 Py unit cells, there is a total of 507,600. The number of Mn atoms remains fixed between both cases at 363,600 with 43,200 and 144,00 Py atoms for 6 and 20 unit cells, respectively. The damping is set to $\lambda = 1.0$ for both materials to achieve a faster relaxation in the longitudinal dynamics. The magnetisation is recorded for a total of 50 ps for each temperature value with the magnetisation averaged over the range from 10ps to 50ps. The magnetisation is recorded at increments of 50 K except in the regions 600K to 800K and 1300K to 1400K. In these regions, the temperature increment is dropped to 10K and 20K to more accurately capture the sudden drop in magnetisation close to the critical temperatures of Py and $Mn_2Au$. The critical temperature values for each thickness/interface exchange instance are determined by fitting the magnetisation curve to $m(T) = (1 - T/T_C)^{\beta}$, with $T_C$ and $\beta$ as free fitting parameters. This eliminates the need for visual determination of the critical temperature amidst the messy transition to a paramagnetic caused by the thin ferromagnetic layers and resulting finite size effects.

Fig. 5.4 shows the magnetisation curves for Py (top) and $Mn_2Au$ (bottom) for all four cases of interfacial exchange and Py length. The results show that for $Mn_2Au$, there is almost no distinguishing between cases with the introduction of Py to the system having no effect on the magnetisation curve. An identical $T_N$ is observed for the bilayer to that seen for bulk $Mn_2Au$ as shown already in Fig. 3.3 of Chapter 3. For the Py sublattice, there is a more clear distinction between cases, with the lowest $T_C$ being observed for bilayer containing 6 Py unit cells with an interface exchange of $0.5 \times 10^{-21}$ J and the highest $T_C$ for 20 Py unit cells with an interface exchange of $5.0 \times 10^{-21}$ J. The difference in critical temperatures between these two bilayer configurations is around 50 K. For 6 Unit cells, there is also a more noticeable tailing away of

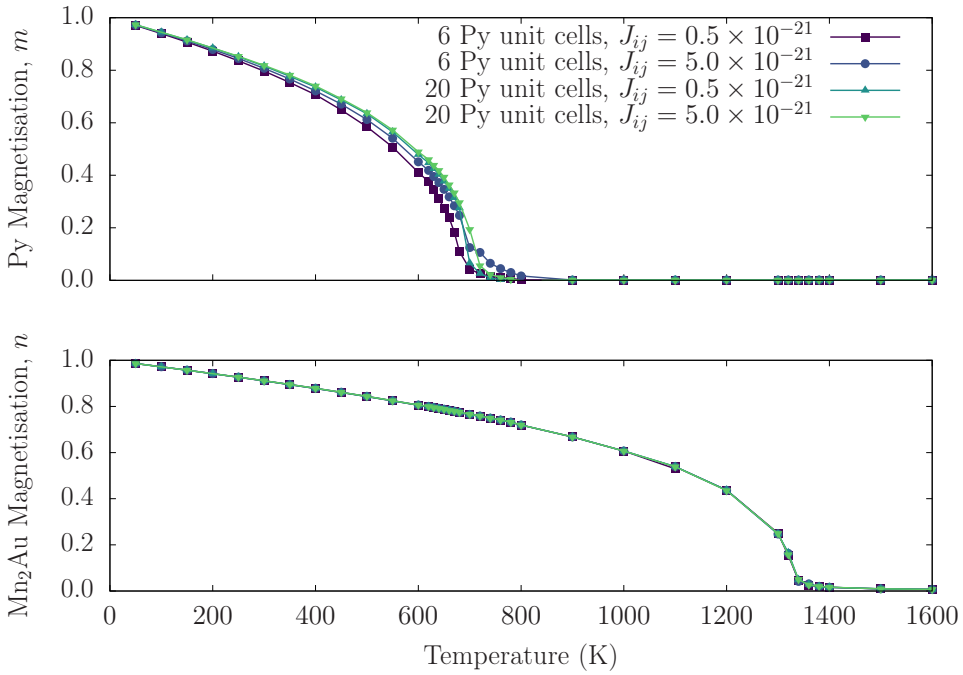


**Figure 5.4:** Temperature scaling of the magnetisation for Py (Top) and $Mn_2Au$ (Bottom) for interface coupling strengths of $0.5 \times 10^{-21}$ J and $5.0 \times 10^{-21}$ J with FM thicknesses of 6 and 20 unit cells.

the magnetisation close to $T_C$ due to the reduced number of Py atoms being summed to give the equilibrium magnetisation. This is a common occurrence in atomistic modelling with small system sizes, a good example of this effect can be found in Fig. 8 of Ref. [85]. These results show that the inclusion of Py with thicknesses as short as 5 unit cells means the system is still strongly magnetised at temperatures above 600K, making the $Mn_2Au$/Py system a good candidate for technological applications at room temperature.

## 5.5 Temperature Scaling of the Resonant Frequency

The temperature dependence of the resonant frequency has been calculated for the same combinations of interface exchange and Py thickness as seen in the previous section. In contrast to the $T = 0$K resonance calculations, where a spin canting was needed to excite the $n = 0$ resonance mode, it was found in the magnetisation dynamics calculations of the magnetisation that the resonance mode is sufficiently excited as a result of the transfer of angular momentum between the sublattices arising from the random

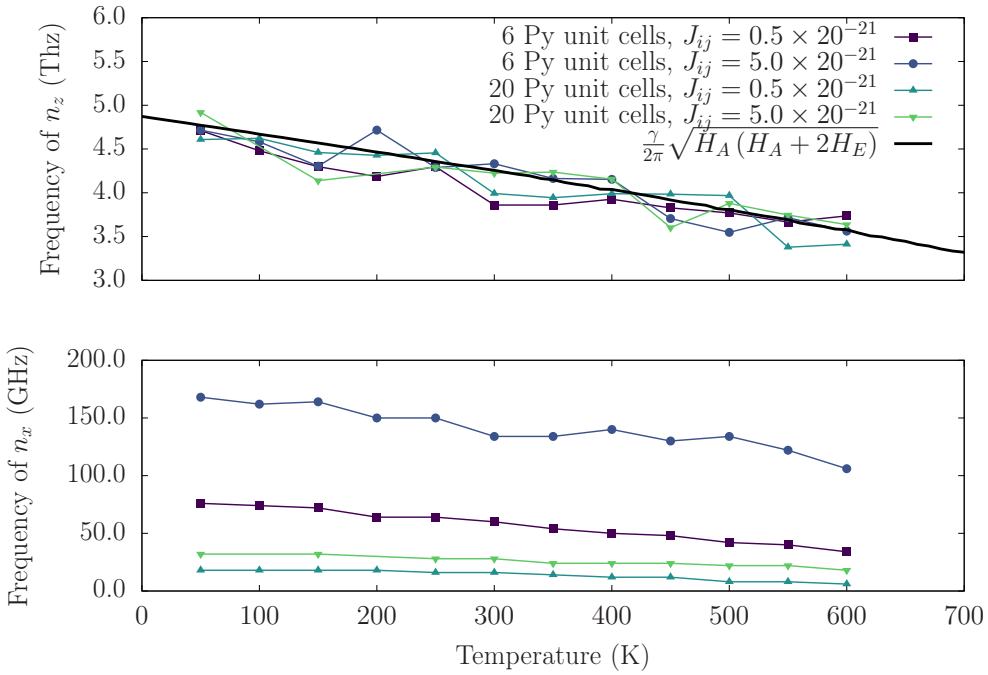


**Figure 5.5:** Temperature scaling of the in-plane (top) and out-of-plane (bottom) resonant frequencies for interface coupling strengths of $0.5\times10^{-21}$ J and $5.0\times10^{-21}$ J with FM thicknesses of 6 and 20 unit cells. Frequencies were extracted from the $x$ and $z$ components of the $Mn_2Au$ dynamics.

thermally induced spin fluctuations. Because of this, no spin canting or field need be applied to induce any kind of precessional motion in this section. The simulations are run for 500 ps to allow for a sufficient amount of cycles at resonance for each temperature step. The resonant frequency is then found via an FFT of the $Mn_2Au$ magnetisation dynamics over the range 100 ps to 500 ps. The initial equilibration window of 100 ps is once again used account allow for the longitudinal relaxation in the magnetisation for a given temperature. The resonant frequency of both the in-plane and out-of-plane dynamics can be found in Fig. 5.5. The top and bottom panes show the scaling of the in-plane and out-of-plane dynamics respectively. The resonant frequencies of the in-plane precession for the FM Py layer is in perfect agreement with $Mn_2Au$ after the initial equilibration period. For the out-of-plane dynamics, the common GHz frequency mode is observed in both FM and AFM layer while the AFM has an additional higher THz frequency mode arising from the large anisotropy constant $d_z$. The temperature dependence of the latter was calculated for bulk $Mn_2Au$ in chapter 3 (see Fig. 3.5). The solid black line in the bottom pane of Fig. 5.5 is the analytical approximation of

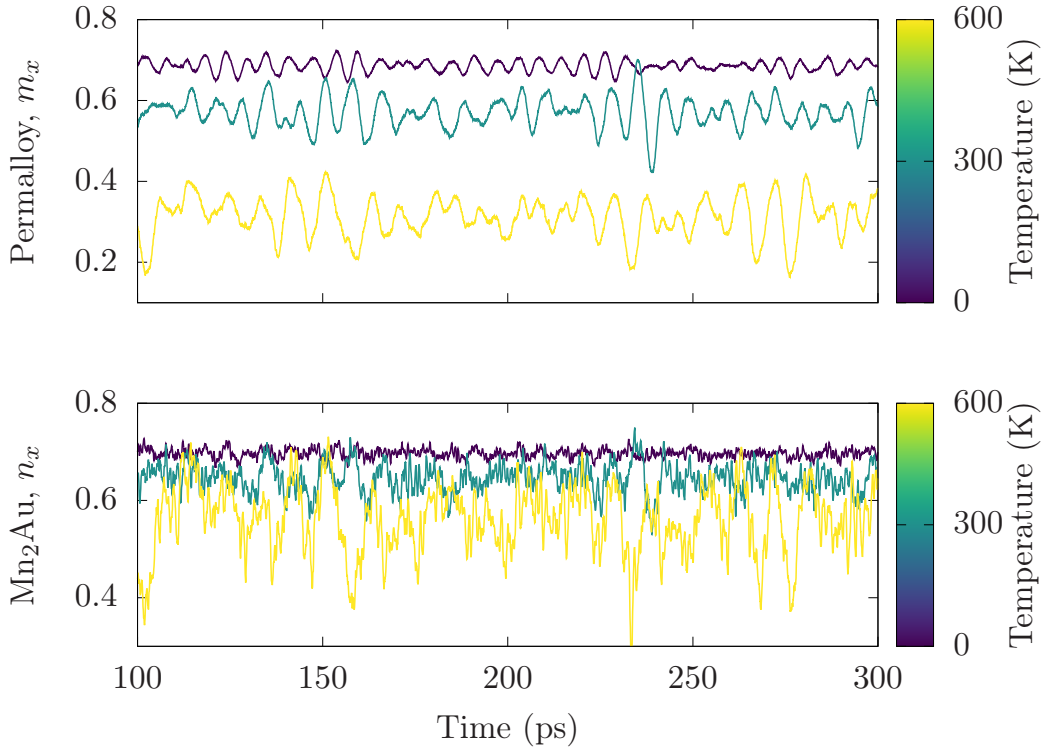


**Figure 5.6:** The ambient dynamics of the Bilayer system at temperatures of 50 K, 300 K and 600 K. (Top) $m_x$ dynamics for Py. (Bottom) $n_x$ dynamics for $Mn_2Au$. No external field has been applied to induce the precession.

the antiferromagnetic resonance given by Eq. (3.9). The inclusion of the Py layer has little impact on this resonant mode as shown by the overlap of all data points on the solid black line. Similar trends were observed for all cases of interface couplings and FM thicknesses with close agreement being observed with the analytical approximation.

An example of the $x$-components of the magnetisation dynamics for both Py and $Mn_2Au$ at the largest coupling strength of $5.0 \times 10^{-21}$ J with 6 units cells of Py for temperatures of 50, 300 and 600 K is shown in Fig. 5.6. The top and bottom panes show Py and $Mn_2Au$ dynamics, respectively. The common lower frequency mode is identifiable in both the FM and AFM dynamics, with it being more noticeable in the FM dynamics and less so in the AFM because of the much higher intrinsic THz frequency oscillations. Note the differing y-axis scale in Fig. 5.6, this has been used to account for the difference in magnetisation of the two materials for the respective temperatures.

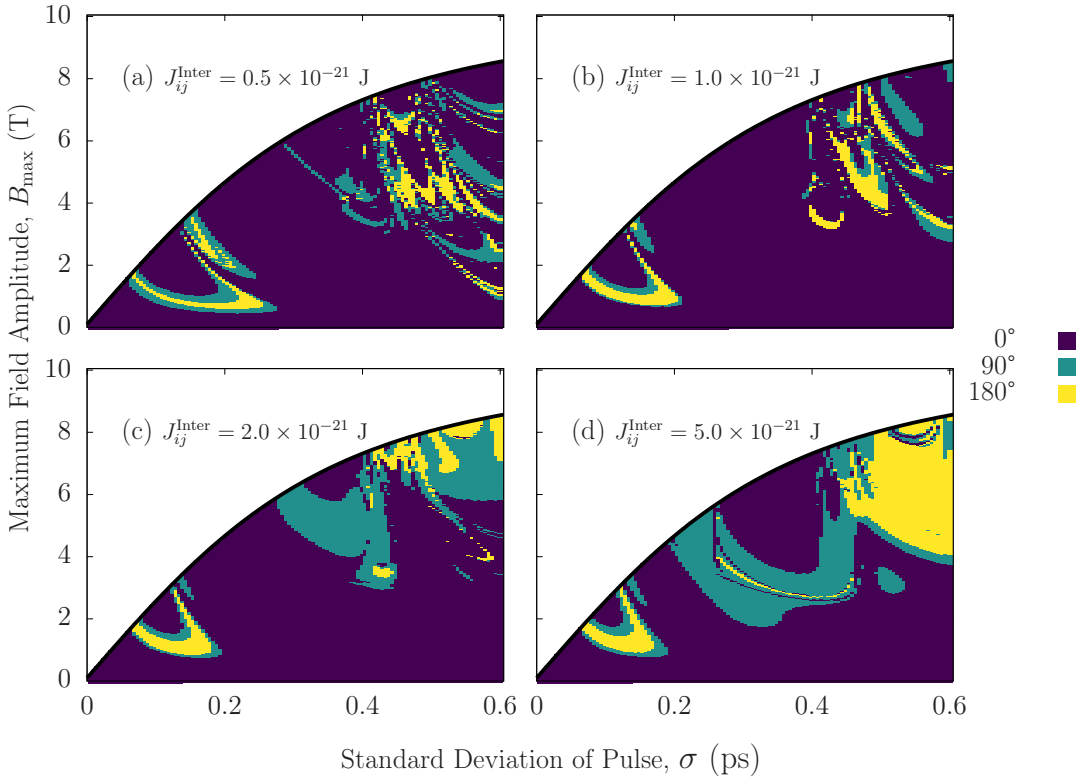


**Figure 5.7:** Magnetisation reversal using a THz pulse for a permalloy thickness of 6 unit cells for different coupling strengths between FM and AFM. (a) $0.5 \times 10^{-21}$ J, (b) $1.0 \times 10^{-21}$ J, (c) $2.0 \times 10^{-21}$ J, and (d) $5.0 \times 10^{-21}$ J. Turquoise and yellow are regions of 90° and 180° switching respectively.

## 5.6 Bilayer Switching

In this section, we present simulations of switching in the bilayer at 0K. Like with the switching in pure $Mn_2Au$ seen in chapter 4, we use a THz frequency field modelled using Eq. (4.14). The applied field is once again staggered for each Mn sublattice. An identical field to the sublattice containing the Mn atom at the interface is applied to the Py sublattice. Firstly, we consider the case of 6 unit cells of Py, and vary the strength of the coupling across the interface. Fig. 5.7 shows four different coupling strengths, namely 0.5, 1.0, 2.0 and $5.0 \times 10^{-21}$ J. For low $\sigma$, the phase diagram varies minimally in structure across an order of magnitude increase in the interface exchange. While this region remains similar, there is a significant change in the phase diagram for $\sigma \gtrsim 0.2$ which transitions from small and scattered switching windows

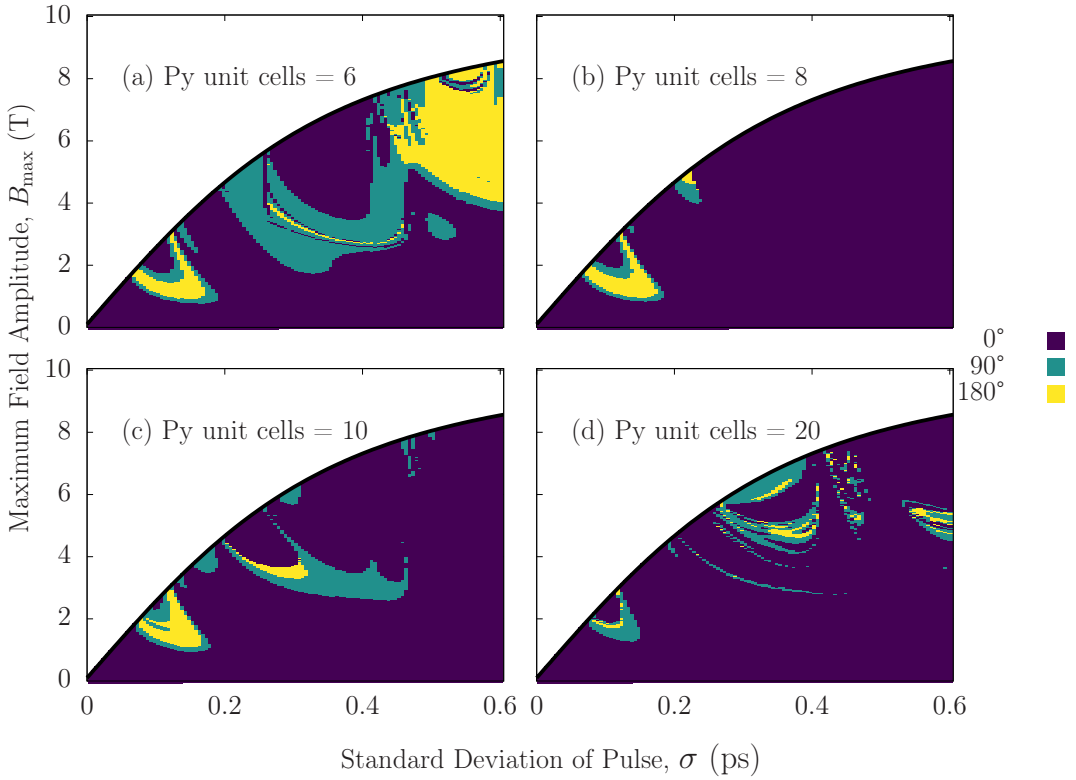


**Figure 5.8:** Magnetisation reversal using a THz pulse for an interface exchange of $5.0 \times 10^{-21}$ J with (a) 6, (b) 8, (c) 10 and (d) 20 unit cells of Py at T = 0 K. Turquoise and yellow are regions of 90° and 180° switching respectively.

to larger and more continuous regions of reversal. Simulations are also conducted for constant exchange coupling with varied Py thickness, we chose the largest value of $J_{ij}^{\text{Inter}} = 5.0 \times 10^{-21}$ J and varied the thickness from 6 to 20 unit cells. As was seen in Fig. 5.7, the phase diagram remains similar in shape for $\sigma \lesssim 0.2$, but there is a notable increase in the fields required for reversal in this region with almost no 180° reversal observed for the case of 20 Py unit cells. For $\sigma \gtrsim 0.2$, the change in the phase diagram as we transition from 6 to 20 unit cells is more disordered. In contrast to switching in pure $Mn_2Au$, there exist large bands in Figs 5.7 and Fig. 5.8 where no magnetisation reversal is observed, which suggests the FM is hindering the onset of switching.

To further reiterate this point, simulations were conducted where only the Mn sublattices were subject to an applied staggered field. Fig. 5.9 shows the change in the

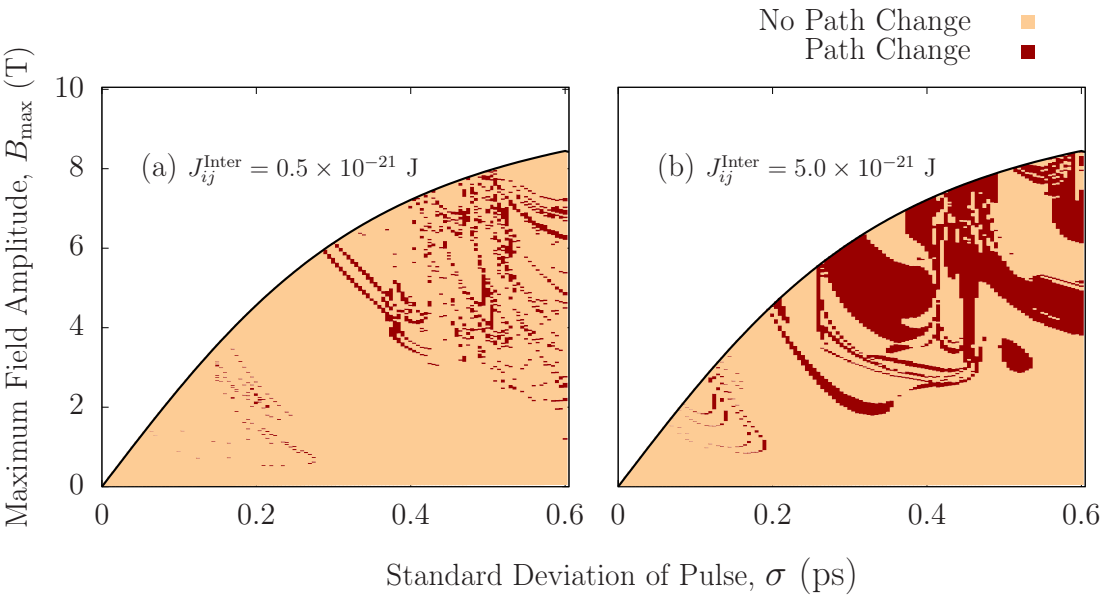


**Figure 5.9:** Changes in phase diagram from an excitation of both Mn and Py sublattices compared to an excitation of the Mn sublattices alone for coupling strengths of (a) $0.5 \times 10^{-21}$ J and (b) $5.0 \times 10^{-21}$ J. The lighter coloured areas show no change in switching between the two cases. Darker regions show regions where the final reorientation angle has changed.

phase diagram as a result of an excitation of the entire system compared to the case of excitation only in the AFM. For $\sigma \lesssim 0.2$ ps, changes are only observed at the boundary between two reorientation angles by, in most cases, a single shift in the field strength or pulse width increment. The AFM is therefore almost entirely responsible for the switching in this region. For larger pulse widths, the FM has an extended period of time to exhibit a response to the longer fields as highlighted by the significant changes in reorientation angle for $\sigma \gtrsim 0.3$.

## 5.7 Standing Spinwave Formation

Simulations at the lowest interface coupling of $J_{ij}^{\text{Inter}} = 0.5 \times 10^{-21}$ J with the thinnest FM film of 6 Py unit cells also revealed the formation of standing spinwaves in the FM layer. Fig. 5.10 shows the dynamics of every atomic layer at $T = 0$ K following the application of a THz field for coupling strengths of $J_{ij}^{\text{Inter}} = 0.5 \times 10^{-21}$ J and $J_{ij}^{\text{Inter}} = 5.0 \times 10^{-21}$ J. No switching occurs for either of these particular event. The THz pulse causes large deviations in the AFM for both exchange values, as shown by

the sharp contrast between blue and green regions around the 10 ps mark. In the case of the weaker coupling, the FM shows little response in the period between 10-11 ps, however, the exchange field at the interface is sufficient enough to create a standing spinwave at the $n = 1$ resonance mode in the FM layer. This is highlighted as an inset in the top pane (note the change in colour-axis scale to enhance the contrast between the standing spinwave maxima and minima). For the largest coupling value of $J_{ij}^{\text{Inter}} = 5.0 \times 10^{-21}$ (shown in the bottom pane of 5.10) the presence of any higher order standing waves is less evident with the AFM effectively pulling the FM on a similar trajectory. The $n = 0$ resonant mode can be seen clearly between 15 and 25 ps in both panes. There is no observed phase difference between the oscillations, with the FM and AFM layers oscillating in sync. The brighter contrast between maxima and minima in the FM Layer between 15 and 25 ps for both exchange values shows the FM oscillating at a greater amplitude than the AFM.

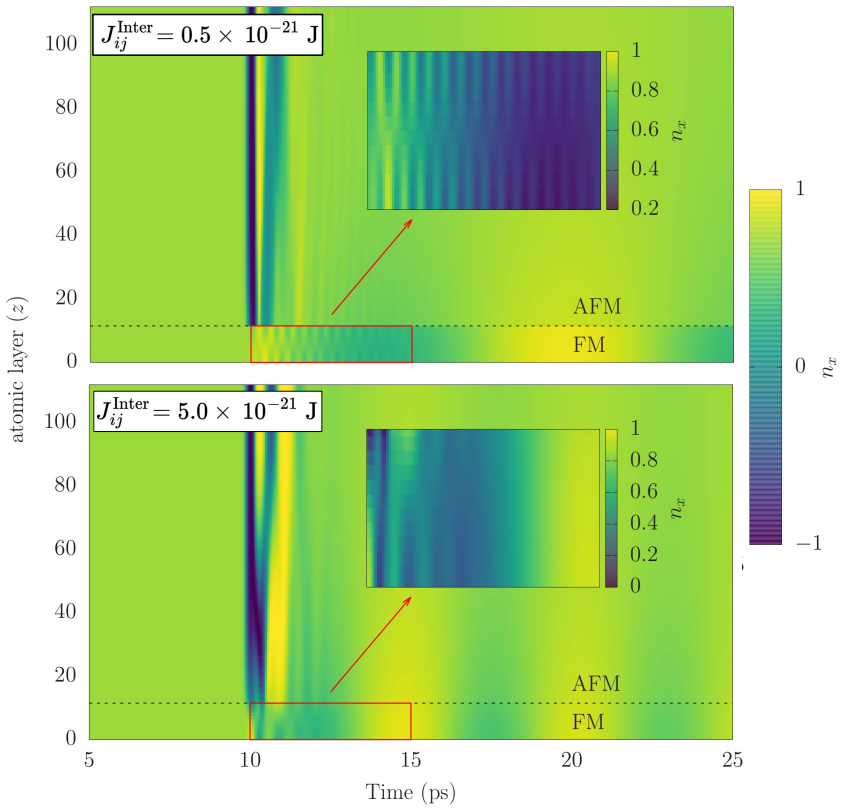


**Figure 5.10:** The dynamics for each atomic layer for an interface coupling of $J_{ij}^{\text{Inter}} = 0.5 \times 10^{-21}$ J and $J_{ij}^{\text{Inter}} = 5.0 \times 10^{-21}$ J for 6 unit cells of Py following the application of a THz field. The colour indicates the $n_x$ dynamics. Inset show the FM dynamics in the region shortly after the pulse. Note the change in colour bar axis in the insets to enhance the contrast.

## 5.8 Switching Simulations at Elevated Temperatures

It is well understood that elevated temperatures lead to a reduction in anisotropy fields [144, 211, 87]. Such heating is the key principle behind Heat Assisted Magnetic Recording (HAMR) [20–23]. Here, we conduct finite temperature simulations for the bilayer containing 6 unit cells of Py along the chain with an interface exchange of $0.5 \times 10^{-21}$ J, which shows the most favourable switching characteristics. Due to the increased computational cost of finite temperature ASD simulations a much smaller phase space is sampled. We conduct switching simulations in the ranges $0.1 \leq \sigma \leq 0.2$ ps and $0 \leq H \leq 6$ T (recall $H$ does not correspond to the maximum amplitude, $B_{\text{max}}$). This region captures the lower switching band that has been observed for all values of exchange and FM length. We use pulse width increments of $\Delta\sigma = 0.01$ ps and field

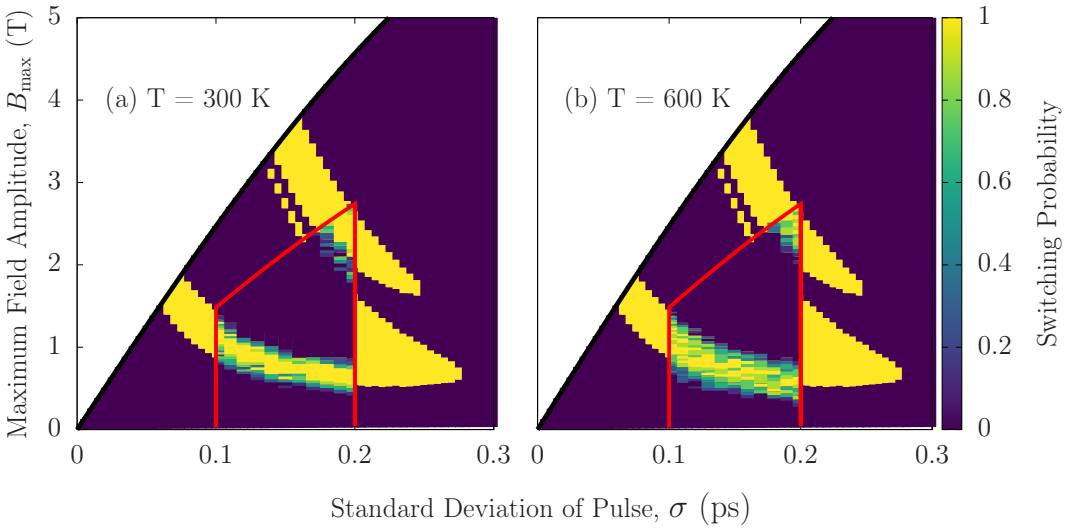


**Figure 5.11:** magnetisation reversal using a multicycle pulse for a Py thickness of 6 unit cells with a coupling strength of $0.5 \times 10^{-21}$ J. The area inside the red rectangle show results from finite temperature atomistic simulations. With (a) $T = 300$ K and (b) $T = 600$ K on the left and right respectively. The switching probability is averaged over 8 repeated simulations. The area outside the box is at 0 K. It is not possible to differentiate between 90° and 180° reversal in this figure.

increments of $\Delta H = 0.1$ T. Simulations are repeated 8 times at every value of $H$ and $\sigma$. Fig. 5.11 shows the switching probability for the temperatures of 300K (Left) and 600K (Right). The area inside the red box shows the finite temperature switching probability. The area outside the red box shows switching at 0 Kelvin. The switching is always deterministic, but has been included to highlight any changes in the switching band between 0K and the finite temperature results. It is not possible to differentiate between between 90° and 180° reversal in Fig. 5.11. What is shown is the probability of any switching event occurring. For elevated temperatures, a lowering and broadening of the switching band can be seen as we transition from 0K to 600 K. At 300 K, the equilibrium magnetisation is roughly 0.84 $M/M_S$ and 0.92 $M/M_S$ for the Py and $Mn_2Au$ sublattices respectively. At 600 K, it is approximately 0.42 $M/M_S$ and 0.81 $M/M_S$.

The reversal path for $Mn_2Au$ was found to be almost perfectly circular in the $xy$-plane for all temperatures because of the large negative uniaxial anisotropy constant $d_z$. The Py reversal path is also circular with no significant reduction in the magneti-

sation following the application of the field. Interestingly, the lack of any anisotropy in the FM layer allows for the precession of the Py sublattice out of the $xy$-plane which is not observed for the Mn sublattices. In other materials, it has been observed that there is a reduction in the magnetisation length during the reversal process which is known as linear reversal. FePt is one such material that transitions from a circular path to a linear path for static temperatures close to $T_C$ [212–214]. Linear reversal paths have been observed in atomistic simulations of the AFM NiO [215].

Fig. 5.12 shows the two most common reversal paths for an interface exchange of $0.5 \times 10^{-21}$ J with a Py thickness of 6 unit cells - the bilayer setup that shows the most favourable switching. Because of the highly circular precession in the $xy$-plane resulting from the strong uniaxial anisotropy $d_z$, the reversal pathways are derived from the dynamics of the Mn sublattices, making it simple to characterise the path in terms of a rotation about the $z$ axis. Panel (a) shows the dynamics corresponding to a 270° clockwise rotation of the Mn sublattices while panel (b) shows a reorientation after a clockwise rotation of 180°. In total, these two paths account for 51% of all the switching events at 300 K with panel (a) and panel (b) accounting for 29% and 22% of the switching events, respectively. There exist 8 other paths with occurrences of between 1% and 9% that account for the remaining 49% of switching events. If we characterise the reversal time as the time taken for the Mn sublattices to reach the final state, the average reversal time is $\sim 5$ ps and $\sim 9$ ps for panel (a) and (b) of Fig. 5.12, respectively.

While the switching events occur in only a few picoseconds, the system continues to oscillate at the resonant frequency for an extended period of time. The size of the oscillations after the removal of the applied field differs greatly in these two cases, with the 270° reorientation of $Mn_2Au$ case seeing much larger amplitudes. For the 270° scenario, the $Mn_2Au$ sublattice that is coupled ferromagnetically to the Py performs a 270° clockwise rotation, while the Py sublattice performs a 90° rotation anti-clockwise in the opposite direction. The AFM rotates incredibly quickly, with a full 270° rotation occurring on a sub-ps timescale. The slower dynamics of the FM mean it has little

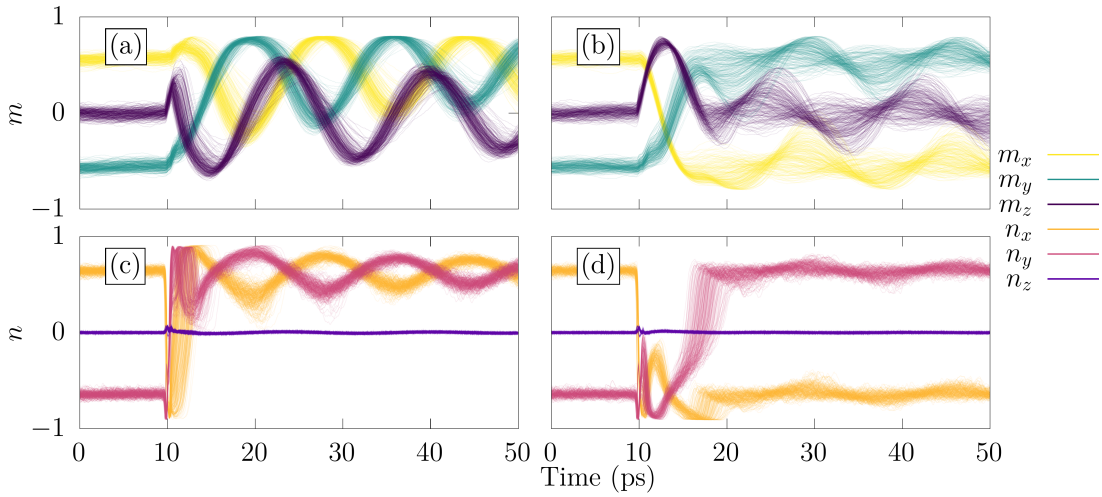


**Figure 5.12:** magnetisation dynamics at 300 K for the two most common reversal paths. (a) an anti-clockwise rotation of 270° in the $xy$-plane for the Mn sublattices and a clockwise rotation of 90° for the Py. (b) an anti-clockwise reorientation of 180° in the $xy$ plane for Mn sublattices and a rotation of 180°out of the $xy$ plane such that the Py sublattice is parallel to the $z$ axis roughly halfway through the switching process. These two paths account for 52% of all switching processes at 300 K.

time to react and by the time the AFM has reached the final angle, it is energetically favourable for the FM to rotate 90° in the opposite direction. In the 180° case, both $Mn_2Au$ and Py perform a clockwise 180° reorientation. The AFM quickly performs a 90 ° rotation, shown by the sudden change in the positive to negative at the 10 ps mark in the $n_x$ component in panel (d). The AFM then remains close to the 90 °reorientation angle for ≈ 2 ps around while the FM begins its response. This can be seen in the region between ≈ 12 and 14 ps in panel (b) of Fig. 5.12. The FM layer catches up and overshoots the 90° state. It is at this point the AFM and FM then rotate almost synchronously to the final reorientation angle of 180 °. This slower in-phase rotation of the AFM and the FM can be seen in the region from roughly 14 to 20 ps in panel (b) of Fig. 5.12.

## 5.9 Summary

The experimental observation of one-to-one imprinting of AFM domain structure onto an FM by Bommanaboyena *et al.* has opened the potential for AFM switching speeds

while still allowing access to the magnetic order parameter via the FM layer. Here we have replicated their system in an atomistic model with the Py stacked vertically on top of the $Mn_2Au$ with the lattice constants matched in the (001) direction. The exchange coupling at the interface is treated simply as a nearest-neighbour interaction between Mn and Py atoms, the strength of which is varied as a parameter in simulations. Additionally, the thickness of the Py layer is adjusted between 2 and 20 unit cells to explore its role in the magnetisation dynamics. The resonant frequencies of the coupled system were calculated for varying Py thicknesses and interfacial exchange strengths, with a reduction of around 90% from approximately 200 GHz to 20 GHz with an increase in thickness from 2 to 20 unit cells of Py. For an order of magnitude increase in the interfacial exchange, the increase in resonant frequency was only between 10% and 40% depending on the Py thickness. This result implies thinner FM films with stronger exchange coupling will allow faster switching for a given applied field. The temperature dependence of the magnetisation shows little variation with varying thickness and exchange parameters with a critical temperature decrease of 50 K observed between a system of 20 Py unit cells with an interface exchange of $J_{ij} = 5.0 \times 10^{-21}$ J compared against a system containing 6 Py unit cells with coupling $J_{ij} = 0.5 \times 10^{-21}$ J. Overall, the bilayer remains strongly magnetised well above room temperature. The temperature scaling of the resonant frequency revealed an expected decrease with rising temperatures. The common, lower GHz mode appears in both Py and $Mn_2Au$ dynamics, while the large anisotropy constant $d_z$ in $Mn_2Au$ generates an additional THz frequency mode observable only in the $z$-component of the AFM dynamics.

The phase diagrams presented in this chapter map out switching for different field amplitudes, pulse lengths, Py thicknesses and interfacial couplings. For weak coupling, the phase diagrams look quite similar for shorter pulse durations, even as the exchange interaction increases by an order of magnitude. Above a threshold of around 0.3 ps, much larger continuous areas of switching appear. Varying the Py thickness with a fixed, strong interfacial coupling still produces the most significant changes for short

pulse lengths. Comparisons made between exciting both the FM and the AFM versus just the AFM demonstrates that the antiferromagnet alone is responsible for reversal when pulse lengths are small. Interestingly, for weak coupling and thin Py films, the formation of standing spin waves can be seen in the FM layer for several ps following the THz pulse - opening the possibility for bilayer systems such as this to be used as generators in magnonic devices.

Finite temperature switching simulations at 300K and 600K show a slight lowering and broadening of the switching bands in the phase diagrams. The reversal is found to occur in just a few picoseconds, although oscillations at the natural resonant frequencies persist much longer. Different switching paths and timescales are observed for the two materials, with the AFM for example able to rotate 270° in under a picosecond while the ferromagnet lags behind and reaches its final state in a comparatively longer 10 ps timescale. The results presented here demonstrate the potential for staggered THz fields to reverse $Mn_2Au$/Py bilayers on ultrafast timescales with field amplitudes on the order of a few Tesla. Even with the addition of the ferromagnet, switching can primarily rely on excitations of the AFM as long as FM films are kept thin, typically a few unit cells, with sub-ps staggered fields.

# Chapter 6

# Spinwave Dynamics in AFM Thin Films and Multilayers With Combined FM and AFM Order

*OK, lovely people, let's go truffling in the forest of knowledge!*

– *STUART PIERCE*, The Thick of it. Created by Armando Iannucci.

## 6.1 Introduction

The emergence of thin magnetic materials in the range of several tens of nm present exciting possibilities for the future of information technologies. When patterned into discrete bits at these reduced dimensional scales, such materials may enable high-density magnetic data storage or novel approaches to information processing using spinwave based logic devices. Of particular interest are multilayered configurations, which exhibit quantised spinwave modes with frequencies in the THz range that depend on a range of parameters such as the layer thickness, interface coupling and magnetic moment. Unlike continuous spinwave spectra that emerge in bulk materials, these ultrathin layered structures support standing spinwave (SSW) modes at well-defined resonant frequencies. Being able to generate a wide range of signals in the THz range means it could become possible to selectively drive specific spinwave resonances within a multilayer of thin-film sample. As layer thicknesses continue to decrease, the separation between resonant mode frequencies increases, improving the precision with which distinct spin dynamics can be activated using tailored terahertz pulses. This is well highlighted in the well-known equation for spinwave resonance in ferromagnets

$$f(k) = \frac{\gamma}{2\pi}(H_A + Dk^2) \tag{6.1}$$

with wavevector $k = \pi n/d$ with $d$ being the thickness of the thin film. $D$ in the above is the spinwave stiffness, which can be related to the exchange constants with the equation [216–218]

$$D = \sum_j \frac{2\mu_B}{3\mu_j} J_{0j} R_{0j}^2 \tag{6.2}$$

where $\mu_j$ is the magnetic moment of atom $j$ and $R_{0j}$ is the corresponding inter-atomic distance. For $k = 0$ in Eq. (6.1), we are left with the standard ferromagnetic resonance mode. As the layer thickness decreases, the frequency spacing between adjacent resonance modes widens making thinner films more suitable for selective THz pumping. In the work of Razdolski *et al.* [219] in 2017, ultrashort spin-current pulses were used to drive non-uniform spin dynamics in 14 nm thin films of Fe. In their experiments,

they detect excitation of the first 5 standing spin-wave (SSW) modes, with the largest response amplitude observed for the $n = \frac{k_n d}{\pi} = 1$ resonance mode, where $k$ is the wave vector and $d$ is the thickness of the film. Fig. 6.1 shows some of the key results from their work. The top panel shows the magnetisation dynamics as measured by MOKE with the resonance of the $n = 1$ mode being most easily observable oscillation. The $n = 0$ mode can just be made out in the transverse component (green points/lines) of the MOKE Rotation curve. The Bottom pane shows the Fourier spectrum (blue line) of the MOKE measured dynamics with the peak frequencies (red circles) with the largest amplitude for the $n = 1$ mode, in agreement with the top pane. They observe peaks in the frequency amplitude up to the $n = 4$ mode. The solid red lines shows the spinwave dispersion curve as calculated using Eq. (6.1). This was the first study that looked at using spin current pulses to excite high-frequency spin waves above the $n = 0$ mode and marked an important step towards using higher modes for THz magnonics and switching on ultrafast timescales in FM thin films.

The Spinwave dynamics in AFMs, without factoring in thin film structures, is less documented in the literature due to challenges associated with accessing the magnetic information. The first demonstration of spinwave control came in 2011 by Kampfrath *et al.* [59] who uses single-cycle THz pulses to coherently excite the $f_0$ resonance mode in samples of NiO, as shown in Fig. 6.2. To detect the response in the magnetisation, they used an 8 fs optical probe pulse to measure the time-dependent dynamics via the Faraday effect, which causes a rotation of the probe polarisation. This study was the first demonstration of coherent control of the spinwaves, promising new methods for investigations of spin dynamics in AFMs. It was later shown by Hortensius *et al.* [121] that it is possible to measure spinwave propagation in AFMs using optical pumping for a broadband wavepacket of short-wavelength coherent spinwaves, not just the $k = 0$ mode that was seen in the experiments of Ref. [59]. They achieve this through the optical excitation of intense charge-transfer (CT) electronic transitions in $DyFeO_3$, unlike Ref. [59], which instead of electronic transitions, relied on the Faraday effect to induce the spinwave dynamics. The excitation resulting from the optical pulse leads to

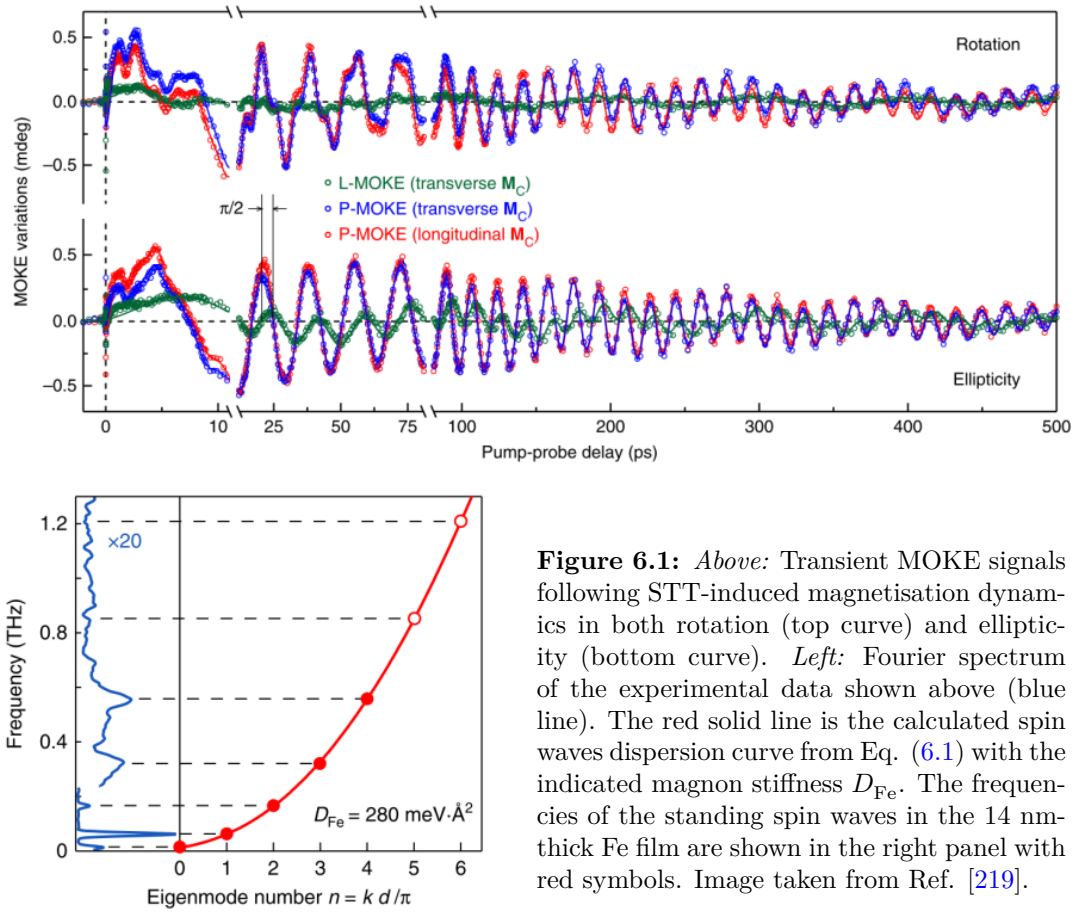


**Figure 6.1:** *Above:* Transient MOKE signals following STT-induced magnetisation dynamics in both rotation (top curve) and ellipticity (bottom curve). *Left:* Fourier spectrum of the experimental data shown above (blue line). The red solid line is the calculated spin waves dispersion curve from Eq. (6.1) with the indicated magnon stiffness $D_{\mathrm{Fe}}$. The frequencies of the standing spin waves in the 14 nm-thick Fe film are shown in the right panel with red symbols. Image taken from Ref. [219].

a non-uniform spin perturbation that is distributed among spinwave modes at different $k$ values. They find the amplitude, $A_k$, of the excitation can be approximated by the expression $A_k \approx I_0/(1+(k\delta)^2)$, where $I_0$ is the intensity, and $\delta$ is the penetration depth. By adjusting the energy of the pump pulse, and consequently altering the depth of penetration, they have the ability to control the excitation strength corresponding to various values of $k$. The approach outlined in this study introduced a new means of controlling the THz spinwave dynamics in AFMs. While both these studies involved system sizes on the order of $\sim$ 100s nm, they were the first to detect and excite spinwaves at the $n = 0$ mode and above, paving the way for ultrafast methods of controlling spinwave propagation and dynamics in AFM materials.

The ability to control and excite resonant frequencies above the fundamental mode by altering the thicknesses of thin film and multilayer structures opens new routes for

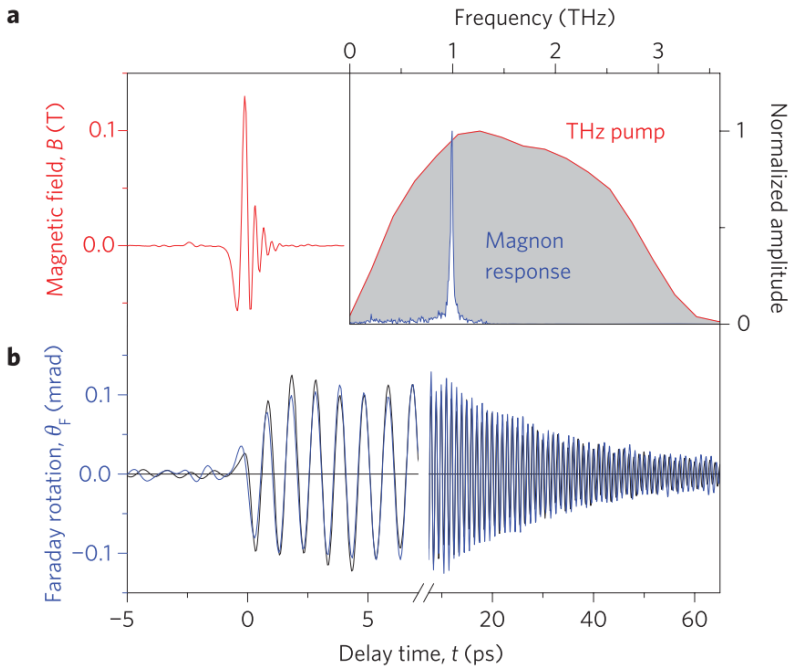


**Figure 6.2:** (a) The applied field pulse as a function of time, $B(t)$. (b) The observed Faraday rotation as detected by a 8 fs optical probe pulse. Inset shows the amplitude spectrum of the THz field in (a) and the magnetisation dynamics shown in (b). Image taken from Ref. [59].

switching. Here, we asses the potential to utilise resonant THz excitation of spinwaves in multilayered and AFM thin films to achieve magnetic switching. The chapter is broken down in the following way: firstly, we look at the creation of SSWs in multilayers of combined FM and AFM order and the effects different magnetic properties have on the frequencies of the standing and travelling modes using LSWT. We then look at the impact of applying a circularly polarised field at close to resonance and the effect this has on the amplitude of the modes. We then show atomistic simulations of switching in the multilayer for different variations of the applied magnetic field sublattice staggering, i.e. varying whether the field if positive or negative for each sublattice, to determine the most efficient switching route. Finally, we finish the chapter with an investigation of switching in a single thin AFM film. The frequencies of the SSW modes are determined via thermal excitations of the system. We then pump the system using a THz circularly polarised fields and apply a sub-ps staggered square pulse to understand whether excitations at higher order resonant modes can lead to a more energy-efficient reversal mechanism. This chapter is very much an exploratory piece of

work with ASD and LSWT calculations being performed on simplified multilayer models of multilayers and AFM thin films, where the physical parameters including the magnetic moment and exchange constants have been systematically varied. It is not as conclusive in its findings as in previous chapters, but it is hoped it lays the groundwork for further theoretical and experimental work on THz excitations in multilayer and thin film heterostructures.

## 6.2 Observation of Standing Spinwaves in Multilayer Structures with Combined FM and AFM Order

We begin this chapter with an introduction to the multilayer system used as part of this work. It consists of two materials which, initially, will be those of Fe and Co. Because the values will be varied in later sections, we shall simply refer to them as materials A and B and avoid attributing the parameters to any specific material. A table of the values used in this section can be found in Tab. 6.1. For this investigation, two configurations of material B will be considered: (i) a standard nearest-neighbour FM and (ii) a planar AFM with AFM coupling along the $x$-direction of the spin chain and FM coupling along $y$ and $z$. In all cases, the number of atoms in material A, $N_A$ and material B, $N_B$, are kept equal. Additionally, the number in each material is always fixed at an odd number. For the planar AFM configuration of B, an odd number of atoms ensures that there is a ferromagnetic interaction at either interface with material A. This prevents frustration and the formation of any helical structures. A schematic of the system can be found in Fig. 6.3. The quantities that have been systematically varied in this multilayer structure are the ground state configuration of material B, the length of the system with the constraint of $N_A = N_B$, and the magnitude of the magnetic moment and exchange coupling for material B. There are other parameters, such as the unit cell sizes with $N_A \neq N_B$, AFM interfacial coupling, the relative anisotropy strengths, and AFM ground states of both materials that could be explored as part of future work.

| parameter/material | A | B | units |
|---|---|---|---|
| $\mu_s$ | 2.22 | 1.72 | $\mu_b$ |
| $J_{AA,BB}$ | $7.05 \times 10^{-21}$ | $-6.064 \times 10^{-21}$ | J |
| $J_{AB}$ | $6.557 \times 10^{-21}$ | $6.557 \times 10^{-21}$ | J |
| $d_z$ | $5.65 \times 10^{-25}$ | $6.69 \times 10^{-25}$ | J |

**Table 6.1:** Parameters for multi-layer calculation. The system is simple cubic. Material B will be simulated as planar-AFM(XY) and FM. For the FM case, the absolute value, $|J_{BB}|$, will be used.

It is well understood that SSWs form in thin magnetic films but little is known about the presence of standing modes in layered structures with combined order. In this section, we calculate the dispersion curve using ASD and LSWT for varying numbers of atoms in the unit cell for different ground state configurations of material $B$. We chose three cases with $N_A = N_B = 3, 5, 9$ which corresponds to a unit cell containing 6, 10 and 18 atoms, respectively. In the atomistic simulations, the temperature is set to $T = 1$ K to sufficiently excite the spinwave modes. The damping is set to $\lambda = 0.0001$ to enhance the lifetime of the modes before they dissipate. The simulations are run for a total of 1 ns. Most of this is the equilibration of the system because of exceptionally low damping. The dispersion is calculated using the spin configurations for the final 50 ps of the simulation. For a short equilibration time or large damping value, there is an increased number of artefacts in the final data and a broadening of the modes, making distinguishing between individual modes difficult. The spin moments are initialised along the $z$-direction ($-z$ for the AFM sublattice of material B) in alignment with the field arising from the relatively small anisotropy constants for each material. In the atomistic modelling, the spinwave dispersion is calculated using Eq. (2.33) with the transverse component, $S_\perp = S_x^2 + S_y^2$, being used as input into the spatial FFT. The corresponding LSWT calculations were completed in collaboration with S. Ruta.

A comparison between the spinwave dispersions of FM and AFM configurations of material B for unit cells with $N_A = N_B = 3, 5, 9$ can be found in Fig. 6.4. The left and right columns show the dispersion relation for the FM and AFM configurations

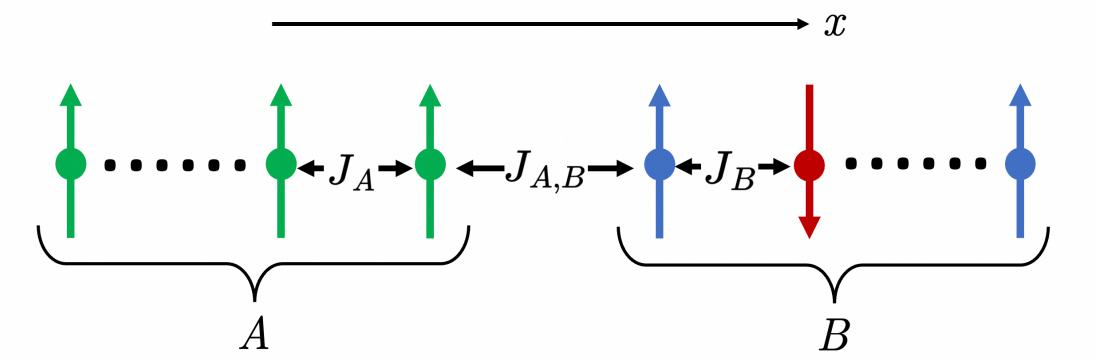


**Figure 6.3:** A schematic of the atomistic multilayer system. Two materials A and B with different magnetic moments and exchange constants. A full table of parameters is given in Tab. 6.1. They are coupled with exchange energy $J_{A,B}$. There is always an equal and odd number of atoms in materials A and B so that there is no frustration at one of the interfaces. Periodic and ferromagnetic coupling is always assumed in the $y$ and $z$ directions.

respectively. The dispersion relation is calculated up the centre of the 6th, 10th and 18th Brillouin zone for the system. Upon inspection of Fig. 6.4, it is clear that the combination of AFM and FM order introduces flat standing modes into the system. For the case of $N_A = N_B = 3$, a standing mode can be seen at around 15 THz for an AFM configuration in material B, while in the FM case, no standing modes are observed. For $N_A = N_B = 5$ two distinct standing modes can be seen at 10 and close to 20 THz. For the final case of $N_A = N_B = 9$, there exists a total of 9 standing modes between 0 and 40 THz. While no standing modes are present for the smallest unit cell size, what can be observed is a flattening of the highest order modes for increasing unit cell size, with the two highest frequency modes being completely stationary for the system with $N_A = N_B = 9$.

The calculations show that combining FM and AFM configurations into a layered structure can lead to the formation of standing modes at frequencies more easily accessible for experiments compared to standing modes for FM/FM coupled layers, where the formation of low amplitude standing modes occurs at the high frequencies. The ability of the AFM to pin and stabilise standing waves, owing to its intrinsic exchange field, opens an additional route for switching in addition to conventional switching that makes use of the $f_0$ mode.

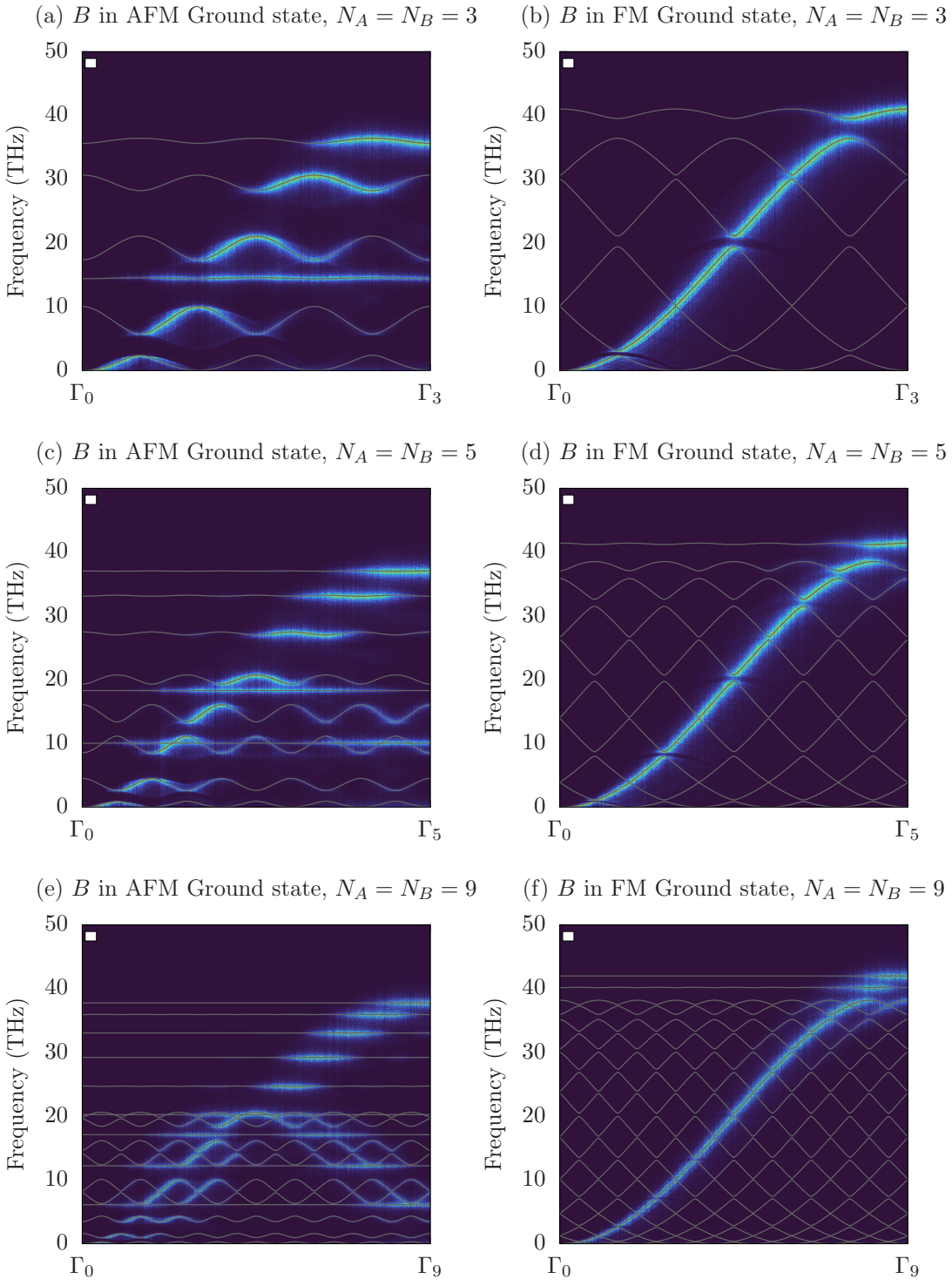


**Figure 6.4:** Spinwave spectrum comparison for FM (column 1) and AFM (column 2) configurations of material B for $N_A = N_B = 3$ (row 1), $N_A = N_B = 5$ (row 2) and $N_A = N_B = 9$ (row 3).

## 6.3 Variation of the Magnetic Moment and Interface Coupling

We also investigate the effect of varying the magnetic moment and interface coupling on the spinwave modes using LSWT. Firstly we consider the case of varying the magnetic moment of material $B$, while maintaining a constant interface coupling at $J_{AB} = 6.557 \times 10^{-21}$ J. For the system featuring $N_A = N_B = 5$ with periodic boundary conditions along the spin chain direction, we systematically adjusted the magnetic moment from $1.0\mu_B$ to $4.0\mu_B$ in $0.1\mu_B$ increments. The frequencies of each mode are monitored at the centre of the first Brillouin zone, $\Gamma$, as the magnetic moment of material $B$ is increased. The results are shown in Fig. 6.5, with the two standing modes visible in Figure 6.4(c) shown as dotted lines in Fig. 6.5.

During this magnetic moment range from 1 to 5 $\mu_B$, we observe a general trend of a reduction in frequency for all modes, however a more pronounced reduction in frequency is observed for standing modes compared to the travelling modes. Looking at the standing modes more specifically, the higher of the two standing modes (green dotted line) sees a 80% frequency reduction, while the lower standing mode (blue dotted line) decreases by 82%. In contrast to the most significant frequency reduction of 68% for a travelling mode across the same magnetic moment range. The modes also appear to tend towards an equilibrium value, with the two highest modes approaching steady state values of 35.5 THz and 29.3 THz, respectively.

While not depicted in this figure, the three highest frequency spinwave modes initially behaved as travelling modes for lower magnetic moment values. However, as the magnetic moment increased, these modes exhibited a flattening trend. The transition from travelling to standing modes can be attributed to the fact that with increasing magnetic moment of material $B$, the less susceptible the system is to high frequency magnetic fluctuations as depicted in the schematic diagram in Fig. 6.6. The figure shows the dispersion relation for an FM (blue) and the corresponding AFM dispersion (darkest

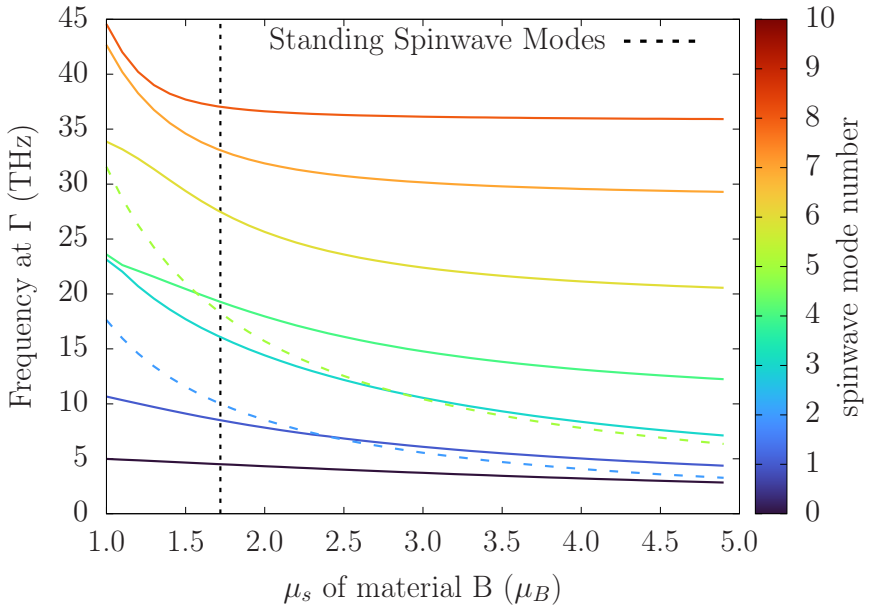


**Figure 6.5:** Frequency at the centre of the Brillouin zone, Γ, for the multilayer system with $N_A = N_B = 5$ as a function of the magnetic moment of material $B$. Coloured dotted lines show the SSW modes. The vertical dotted line shows the moment strength used in the spinwave dispersions shown in panel (c) of Fig. 6.4.

shade of red) for identical magnetic moments and exchange constant magnitude. As the magnetic moment increases in the AFM (shown by increasing transparency in red), the dispersion relation reduces in amplitude, meaning the spinwaves that propagate into the AFM from the FM at frequencies greater than the maximum amplitude are not supported by the system and the AFM begins to as a fixed boundary - thus enabling the formation of standing modes. It is reasonable to assume that this flattening of higher frequency modes would also occur for lower modes with further increases in the magnetic moment of material $B$.

LSWT calculations were also performed for varied interfacial exchange. The value of $J_{AB}$ is varied as a percentage of the mean of the intra-sublattice exchange constants, $(J_{AA} + J_{BB})/2$, from 0% to 200% in increments of 2%. Fig. 6.7 shows the results of the LSWT calculations. The general trend for all modes is an increased frequency for larger coupling, however the rates differ greatly, with the largest increases seen for the two higher frequency modes at 0% coupling. There exists sharp discontinuities at interface couplings of roughly 5% and 55% $(J_{AA} + J_{BB})/2$ where two modes intersect.

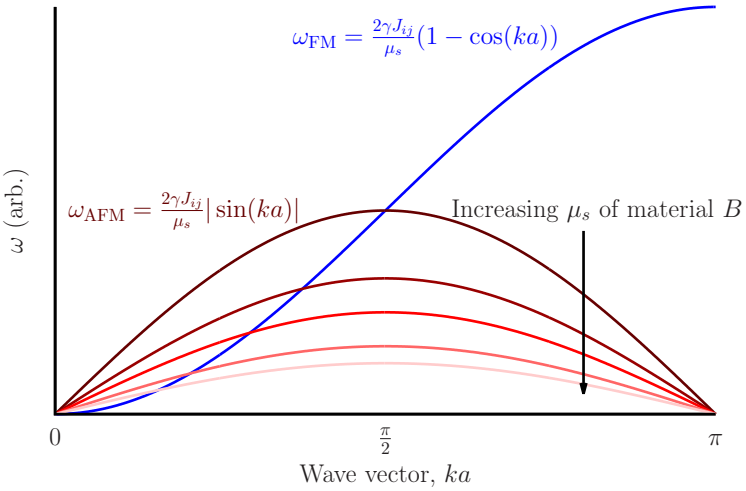


**Figure 6.6:** Spinwave dispersion for an FM (blue) and AFM (darkest shade of red) for identical magnetic moments and exchange constant magnitude. Increasing the magnetic moment reduces the amplitude of the spinwave dispersion (shown by the increasing transparency of AFM curve). High frequency modes that are present in the FM cannot be sustained by the AFM in the multilayer system.

In this region, the rate of increase in frequency is passed between spinwave modes, with the lower mode that was originally increasing at a faster rate suddenly slowing, while the higher increases in frequency sharply after the point of intersection.

### 6.3.1 Excitation of the Spinwave Modes

In this section, we look at the excitation of SSW modes using a linearly polarised sinusoidal field. The aim here is not to achieve switching, but to understand how the amplitude of the modes scales with varied applied field strength. The ASD simulations are performed for the system with $N_A = N_B = 9$ with periodic boundary conditions with a single unit cell at $T = 0$K. A staggered field is applied along a perpendicular direction to the initial magnetisation orientation. The applied field takes the form $B = (\pm B_0 \sin(2\pi f t), 0, 0)$ with the sign of the prefactor $B_0$ depending on whether the sublattice is spin-up or spin-down. The ASD simulations are run with an applied field for a considerable duration by atomistic modelling standards, with a total simulation time of 5 ns. The spinwave amplitudes at $k = 0$ are determined over the final 0.1 ns of the simulation. A figure of the amplitude scaling for applied field strength in the range 10 mT to 100 mT can be found in Fig. 6.8. The two curves are for different

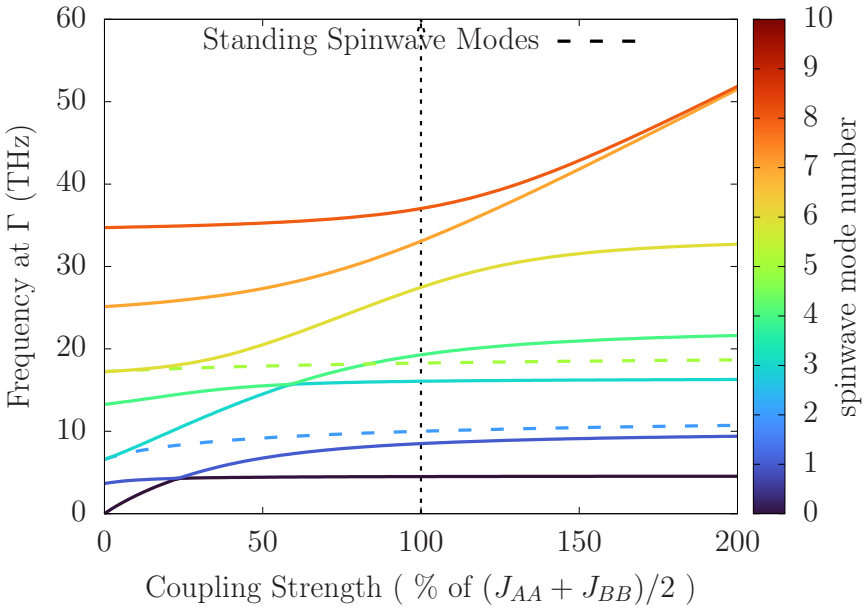


**Figure 6.7:** Frequency at the centre of the Brillouin zone, Γ, for the multilayer system with $N_A = N_B = 5$ as a function of coupling strength. The coupling strength is given as a percentage of the mean value $(J_{AA} + J_{BB})/2$. Coloured dotted lines show the SSW modes. The vertical dotted line shows the coupling strength used in the spinwave dispersions shown in panel (c) of Fig. 6.4.

pumping frequencies of 6.2 THz, which is closer to the lowest standing mode visible for this system in Fig. 6.4, and 8.0 THz, which is approximately the frequency of the next highest travelling mode. The data points show the amplitudes at Γ as calculated using ASD, with the amplitudes being normalised to the lower of the two curves. The solid lines show the scaling with the amplitude $\propto B_0^2/\lambda^2$ normalised to the amplitude at the lowest field strength of $B_0 = 10$ mT for each frequency.

While not for layered structures, similar amplitude scaling with the applied field squared has been noted in the literature for FM materials. In the work by Ostler *et al.* [112], they derive an analytical expression, using the LLB formalism, for the absorbed power in temperature-dependent simulations of FM resonance, which can be used to determine physical properties such as damping and anisotropy. The derived equation is verified against numerical LLB simulations for single and multi-macrospin systems of FePt with good agreement being observed between stochastic finite temperature LLB simulations and theory.

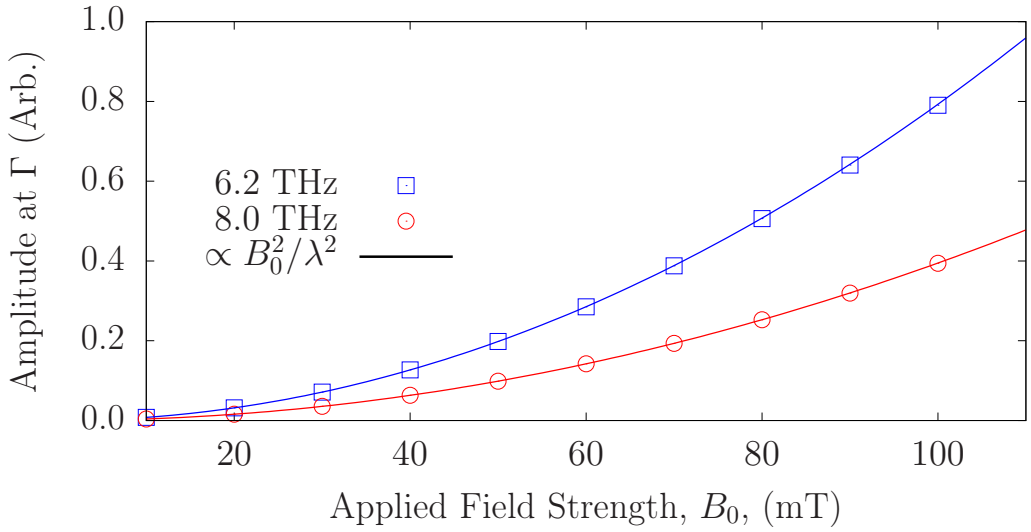


**Figure 6.8:** Amplitude scaling for varied applied field strengths, $B_0$, for pumping at spinwave modes with frequencies of 6.2THz and 8.0THz at the centre of the Brillouin zone. Amplitudes have been normalised to the value for frequency of 8.0THz at the lowest value of $B_0$. Points show amplitudes calculated from ASD, solid lines show the scaling being proportional to $B_0^2/\lambda^2$.

### 6.3.2 Switching Using a Square Pulse

As with the previous section, the focus here is on the multilayer system with 18 atoms in the unit cell and $N_A = N_B = 9$ with an AFM configuration of material B. Generally, we are interested in the easiest switching possible (i.e lower field strength for the shortest field duration). Throughout this thesis, we have emphasised the effectiveness of applying an oppositely signed staggered to each sublattice in AFM systems, as this generates a maximal torque. Conversely, for ferromagnetic (FM) systems, a uniformly applied field is the optimal choice. In this section, we explore the feasibility of switching in the multilayer system using standard square pulses while varying the sublattice staggering. As we are considering AFM order, which reacts weakly to uniform external fields due to the intrinsic inter-sublattice exchange, a uniform field may yield an insignificant response in the magnetisation dynamics. Here we explore how field staggering affects the ease of switching in multilayers with combined FM/AFM order. The sign of the field on each sublattice will be denoted by either -1, 0, or 1, corresponding to a negative field, no field, or a positive field, respectively. For instance, a field ordering of 0, 1, -1 implies the absence of a field on sublattice 1 (material A) and a staggered field on sublattices 2 and 3 (representing the spin-up and spin-down

sublattices of material B). A list of the field orderings used in this section is provided below:

- 1,1,1: Uniformly applied field on every sublattice
- 1,0,0: Only material A is subject to an applied field.
- 0,1,1: Only material B is subject to an applied field. The field is identical for both sublattices.
- 0,1,-1: Only material B is subject to an applied field. The field is staggered on each sublattice.
- 1,1,-1: Material A and B both receive an applied field. The field is staggered on material B.

In experimental settings, the most straightforward approach would be to uniformly apply a field across the entire system, while selectively exciting specific layers would present a greater challenge. For example in previous chapters, the use of electric fields to generate staggered NSOTs in AFMs has drawn much interest for switching in AFMs alone. Whether this can be extended to systems with ultrathin repeated layers remains an open question. Despite the current experimental constraints in generating such fields, it is important to understand which ordering results in easier switching, and it is hoped the results presented in this section serve as a preliminary insight to future experiments and theoretical work in multilayer switching.

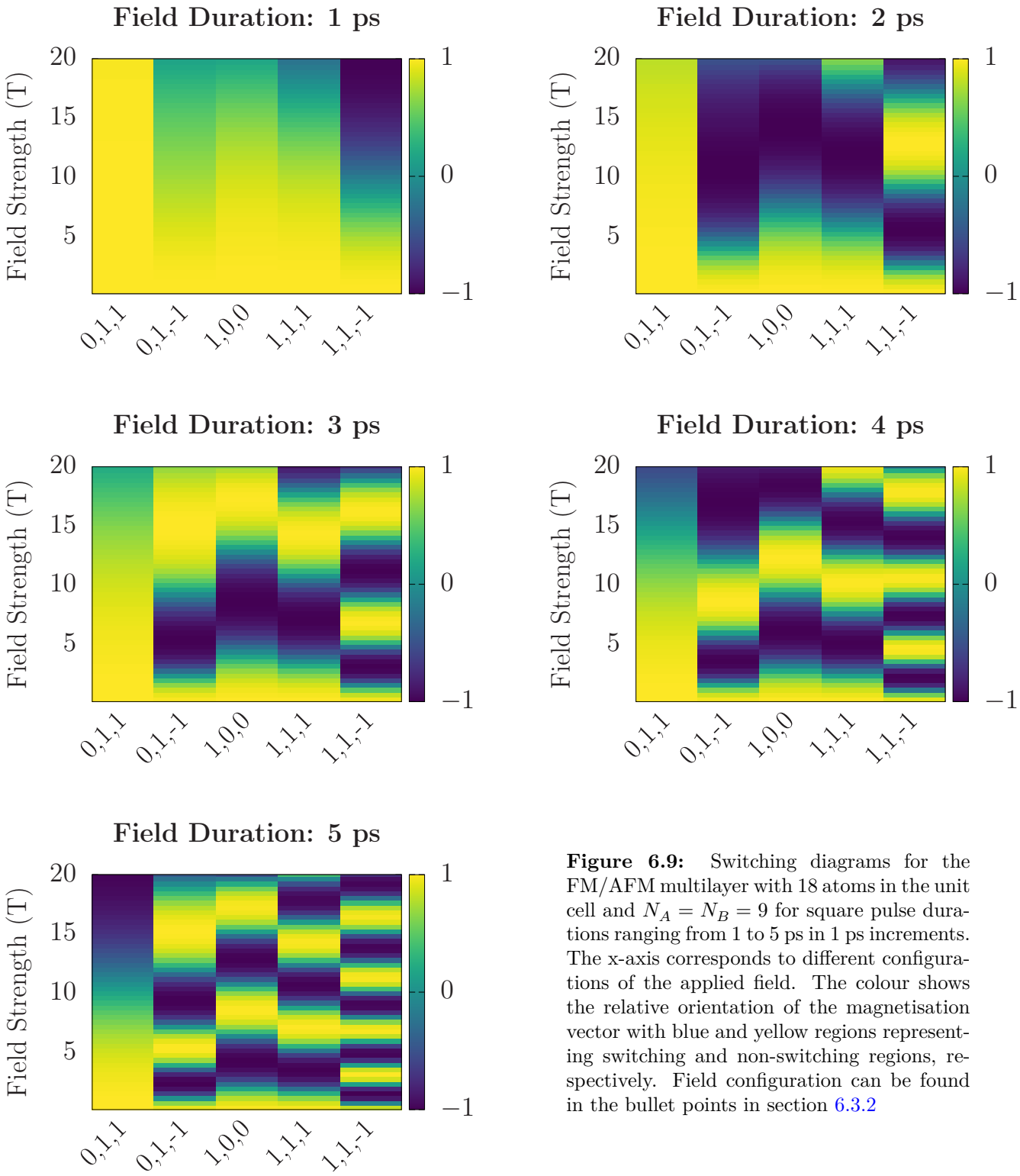


**Figure 6.9:** Switching diagrams for the FM/AFM multilayer with 18 atoms in the unit cell and $N_A = N_B = 9$ for square pulse durations ranging from 1 to 5 ps in 1 ps increments. The x-axis corresponds to different configurations of the applied field. The colour shows the relative orientation of the magnetisation vector with blue and yellow regions representing switching and non-switching regions, respectively. Field configuration can be found in the bullet points in section 6.3.2

For the switching simulations, we use field durations ranging from 1 to 5 ps in 1 ps increments. Simulations are performed at 0 K and run for 1 ns with a timestep of 0.1 fs. The magnetisation state at the end of the simulation is then used to determine if the system has switched or not. Fig. 6.9 shows the results for the five different field durations. The colour shows whether the system has switched (blue) or not (yellow) for different field ordering as a function of increasing field strength. The lowest strength switching for all field durations is seen for a staggered field on the AFM with the FM material receiving the same field as the positively coupled AFM sublattice (1,1,-1). This is then followed by a staggered field on just the AFM (0,1,-1) then a uniform field applied to all sublattices (1,1,1) before a field on the FM alone, and finally a uniform field on just the AFM (0,1,1). The smooth colour gradient that is most notable for the shortest field duration of 1 ps is due to the magnetisation having not relaxed fully to its final state. Ideally, the simulations would have been run for several ns to allow for a full relaxation. Had this been the case, the gradient would have been replaced by sharp sudden contrasts between yellow and blue regions.

## 6.4 Spinwave Mediated Switching in AFM Thin Films

This section explores the possibility of switching AFMs at higher resonance modes using a combination of staggered THz and square fields. Here we use a toy model with material constants that are not based on any physical system. We use a simple cubic planar antiferromagnet, where the spins are coupled antiferromagnetically along the $a$ axis, and ferromagnetically along the $b$ and $c$ axis. We use a magnetic moment of $\mu_s = 4.0\mu_B$, a positive uniaxial anisotropy constant of $d_z = 6.69 \times 10^{-23}$ and a nearest-neighbour exchange constant of $J_{ij} = 6.064 \times 10^{-21}$. The spin-chain consists of 20 atomic spins, with open boundary conditions along the $a$ axis and periodic boundary conditions in all other directions. To be able to pump the material at the SSW modes, the standing modes are found by performing atomistic simulations at finite temperature and taking a Fourier transform of the spins at the open boundary of the spin chain. The ASD simulations are performed at a temperature of $T = 10^{-5}$ K with a damping of $\lambda = 0.001$. Magnetisation dynamics are recorded for a period of 800 ps with a

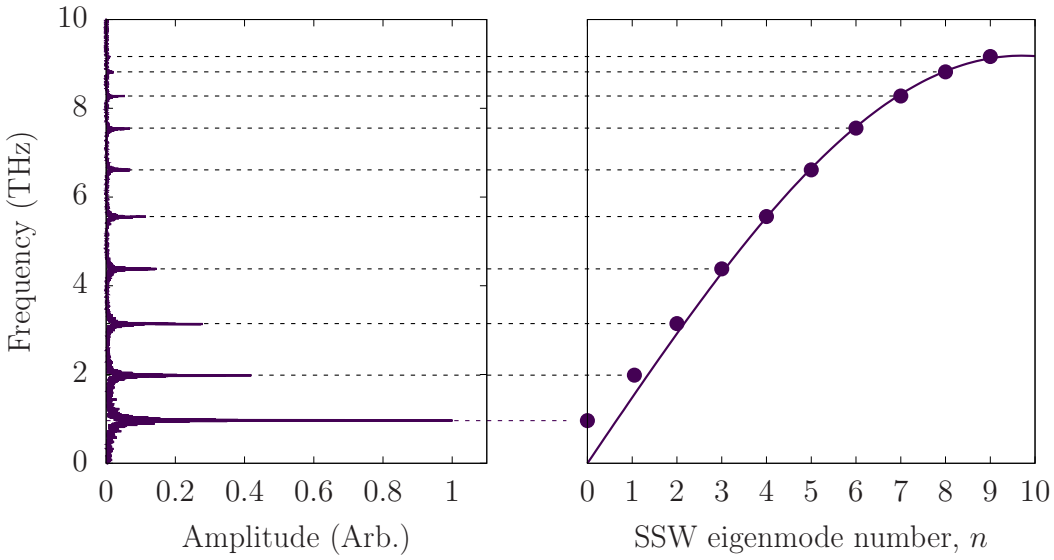


**Figure 6.10:** Observed SSW modes in the AFM thin film when subject to a thermal excitation at $T = 10^{-5}$ K. (Left) normalised amplitude of the resonant modes. (Right). Circles are extracted peaks from left panel. The solid line show the fitted dispersion curve.

timestep of $\Delta t = 0.01$ fs. A figure of the Fourier transform the $x$-component of the magnetisation dynamics for the spins at the open boundary of the spin chain can be found in Fig. 6.10. In the left pane, the spinwave amplitudes have been normalised to the largest value. On the right, the peaks have been extracted from the data in the left-hand pane and plotted as a function of the resonant mode number $n$. This is shown in the solid circles. The solid line shows a plot of the well-known equation for the spinwave dispersion relation in AFMs [6]

$$f = \frac{J_{ij}\gamma}{\pi\mu_s}\sin(kn) \tag{6.3}$$

where $J_{ij}$ and $mu_s$ are values used in the atomistic simulations with $k = 20/\pi$. The reason for the disagreement at eigenmode values $n = 1, 2$ is because the non-zero anisotropy gives rise to a resonance mode at $n = 0$ ($\omega_0 \approx \sqrt{H_A H_E}$). While difficult to see in Fig. 6.10 due to the small system size, the dispersion relation at low values of $k$ takes a quadratic form which arises as a result of the anisotropy in the material, this effect has been seen in experimental observations of spinwave dispersions in AFMs [121]. It is also well documented in the literature for FM materials [6, 220–222].

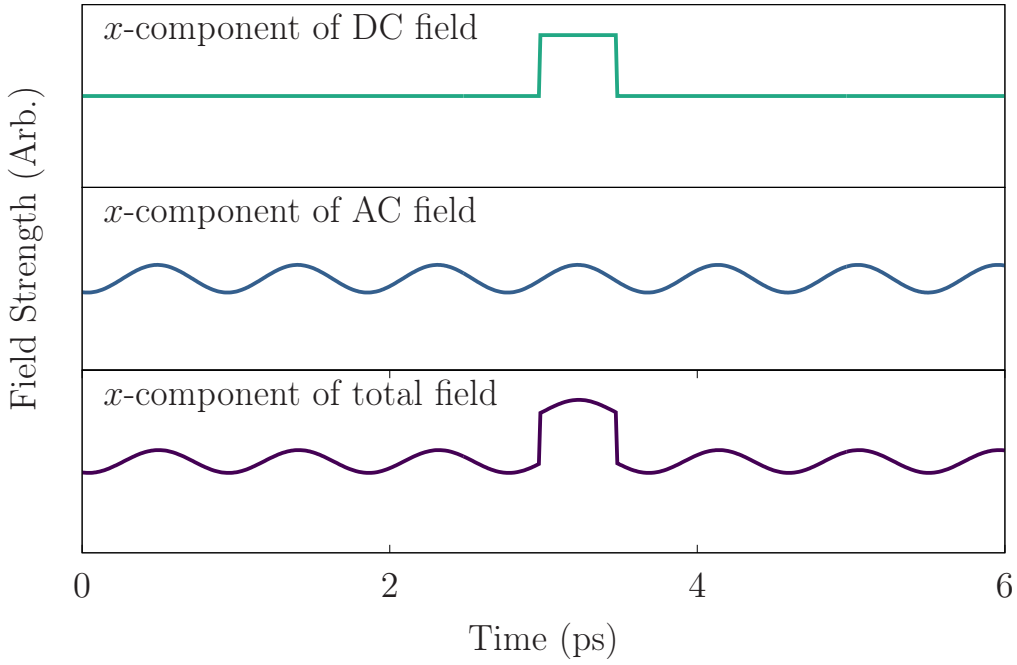


**Figure 6.11:** The $x$-components of the DC (top), AC (middle) and overall (bottom) field experienced by one of the sublattices. The DC field is centralised to a maximum in the AC field. The field amplitudes are arbitrary and have been enhanced to help with the visualisation.

Having calculated the SSW modes for the system, the attention now turns to understanding whether easier switching can be achieved via an excitation at different resonant modes. To excite the mode, a circularly polarised sinusoidal field is applied continually throughout the simulation. The field is staggered for each sublattice but is equal in magnitude for every atomic spin. After an initial equilibration window, a second square staggered field is applied to induce switching. These will be referred to as the AC and DC field components going forward. The width of the DC field remains fixed at 0.5 ps and is centralised to a maximum in the $x$-component of the AC field, after an initial equilibration period. An example of the fields and their relative timings can be found in Fig. 6.11. The top, middle and bottom panes show snapshots of the $x$-component of the AC field, DC field, and the sum of the two. The reason for the centralisation of the DC field peak around an AC field maxima is that in simulations where the DC field was applied at a fixed timepoint, irrespective of the AC field frequency, large shifts in the critical field were observed as a function of DC field position

when pumping close to a resonant mode. Therefore it was decided to fix the midpoint of the DC pulse to a maximum in the AC field.

In the switching simulations, we calculate critical fields for three different damping values and AC field strengths. The switching simulations are once again conducted at $T = 10^{-5}$ K. Initial simulations at $T = 0$ K resulted in all spins aligning along a single direction when exposed to AC fields with frequencies far above the system's resonant frequency. To prevent this spin pinning, a small amount of thermal energy is introduced so that random thermal motions disrupt any alignment. Critical field curves are calculated for three different damping values of $\lambda = 0.005, 0.01, 0.05$ and 0.1. This range is consistent with many physical systems. We also vary the amplitude of the staggered AC field, $H_{AC}$. The values simulated are $H_{AC} = 10$, 100, 200 and 500 mT. The simulations are run for a total of 2 ns with an initial period of 1 ns where the system is only subject to the AC field to allow for the formation of the standing modes. The DC field is then applied around the next maxima in the AC field after 1 ns has elapsed.

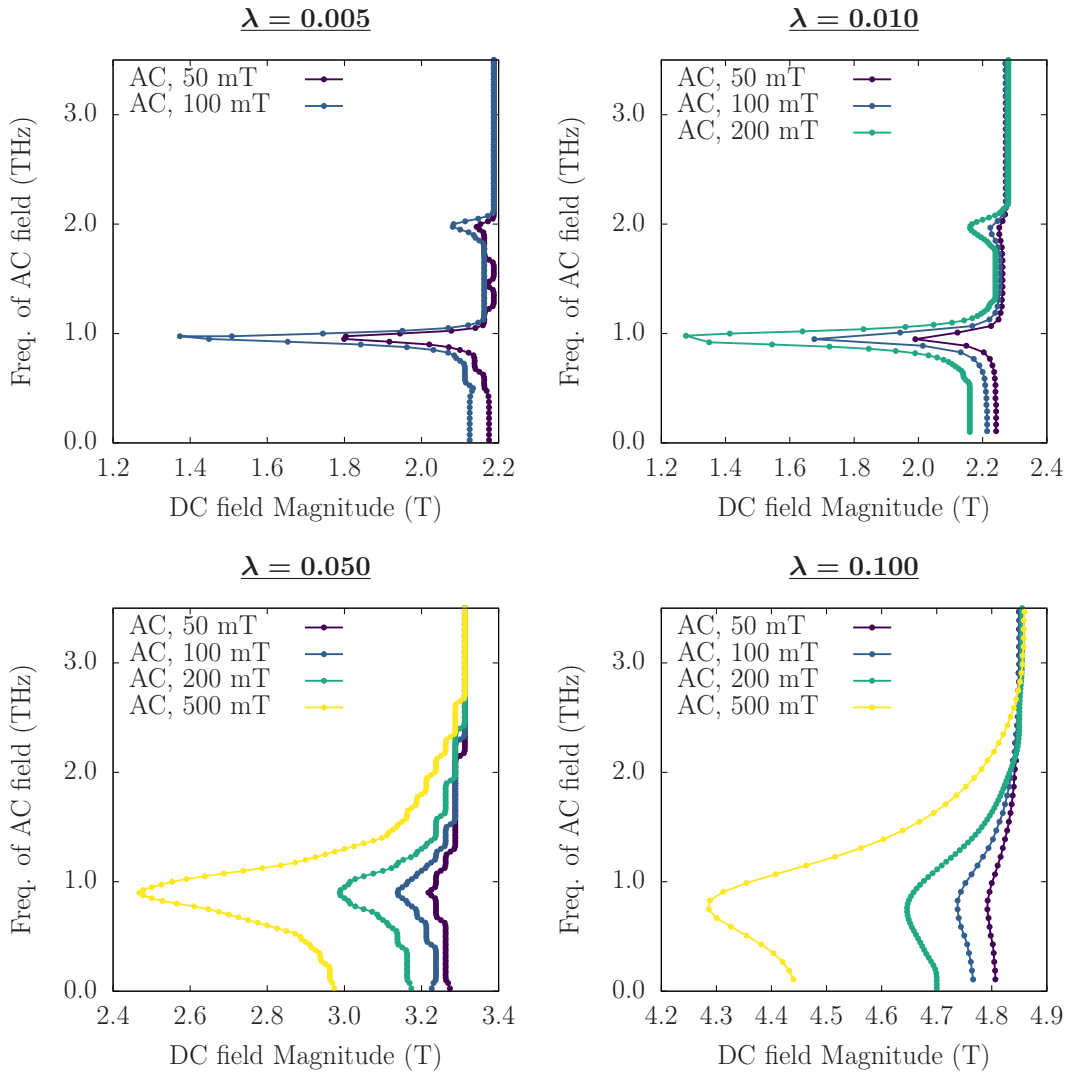


**Figure 6.12:** The critical field for four damping values of 0.005 (top left),0.01 (top right),0.05 (bottom left) and 0.1 (bottom right). Coloured lines show different AC field magnitudes.

The DC critical field lines for the AFM thin film subject to a constant AC and 0.5 ps staggered square pulse can be found in Fig. 6.12. The lines represent the contour from which the system goes from non-switching (left of the line) to switching (right of the line). What is most evident is a clear reduction in the DC field magnitude at roughly 1 THz for all damping values. This frequency corresponds to the $n = 0$ mode, as already seen in Fig. 6.10. The reduction in the critical field as a percentage of the baseline value is greatest for the lower damping values. Interestingly, the excitation close to the $n = 1$ mode at roughly 2 THz leads to a visible reduction in the critical field for damping values of 0.005 and 0.01 although much smaller than seen for $n = 0$.

No reduction in the critical field was seen for the $n = 2$ mode at approximately 3 THz. The omission of the highest AC strength of 500 mT for both these values is that the field was sufficiently strong enough in relation to the weak damping that it kept the magnetisation fixed in the $xy$-plane following the application of the DC pulse. Nonetheless, the ability to use coherent excitations to excite spinwave dynamics has been shown to reduce critical fields required for switching.

## 6.5 Summary

There are almost limitless ways of combining different magnetic materials with different spacer layers, and thicknesses grown on different seed layers to promote different structures. How the layers are structured will ultimately determine the frequencies of the resulting SSW modes. The main aim of this chapter was to better understand the effect of varying layer thickness, coupling, and magnetic moment, and how these parameters affect the spinwave resonance frequencies; and the possibility of exciting non-linear modes or inducing switching. SSW modes in FM/AFM layered materials arise in the $< 10$ THz range due to the alternating magnetic order of the multilayer. The number of modes, as well as the frequency spacing between said modes, increases for thinner layers. The thicknesses can therefore be used as a tool to tune the resonant modes of the system to a desired frequency that can be probed experimentally using THz fields.

Using LSWT, it was found that increasing the magnetic moment of the AFM layer leads to a flattening of the higher frequency spin wave branches, transitioning them to SSW modes. Stronger interfacial exchange coupling between the FM and AFM was found to increase the SSW frequencies overall, with more significant increases observed for the higher order modes. Driving the multilayer at particular SSW resonant frequencies using a circularly polarised AC magnetic field was shown to increase the amplitude at $k = 0$, scaling with the square of the driving field. For the atomistic simulations of switching in the multilayer using a square pulse of varied width, it was found that the staggering of the field on each sublattice heavily impacts the ease of switching. It

was found that switching also occurs for lower fields for all simulated pulse durations when the AFM receives a staggered field, while the FM layer receives the same field polarisation as the ferromagnetically aligned AFM sublattice. Whether it is possible to generate fields similar to this experimentally remains an open question.

In an AFM film, it was shown that a lowering of the switching field occurred when using an AC field pumping at the resonance frequency of the $n = 0$ in combination with a staggered DC pulse for all simulated damping values. For pumping at the $n = 1$ mode, a reduction in switching field was only observed for the lower simulated values of 0.01 and 0.005. No reduction in switching field was observed for the $n = 2$ mode or above. Regardless, the results highlights the potential for resonant spin wave excitation to reduce switching fields in AFM nanostructures. The ability to selectively excite resonant spin wave modes using tailored THz frequency magnetic fields and harnessing the increased amplitude resonant excitations could potentially reduce the switching fields in AFM thin films, which holds promise for future AFM spintronic applications. While this chapter is very much an initial theoretical exploration, it paves the way for further investigations into ultrafast switching in AFM nanostructures using THz spin wave engineering at higher frequency spinwave modes.

# Chapter 7

# Conclusion

*Don't adventures ever have an end? I suppose not. Someone else always has to carry on the story.*

– *J.R.R TOLKIEN,* The Fellowship of the Ring.

The continuous global move towards cloud-based storage and computing requires new solutions to fulfil rising data storage requirements. Traditional magnetic storage systems use FMs in HDDs, where the constraints of GHz-range resonance modes impose limitations on data reversal speed to ns timescales. This thesis looked at the potential of using the AFM $Mn_2Au$ for future data storage applications. The main results of this thesis focused on the development of new multiscale computational models of $Mn_2Au$ and the simulation of magnetisation reversal in both a bulk system, as well as systems with combined FM and AFM order. It has been demonstrated that ps timescale reversal is achievable in $Mn_2Au$ through the generation of Neel spin-orbit torques (NSOT) from the application of electric fields. It was shown that sub-tesla internal magnetic field strengths are required for reversal. Coupling of $Mn_2Au$ to a soft FM has shown the potential for reversal times in the tens of ps, while offering straightforward magnetic order readout. The ability to achieve ps speed data reversal with field magnitudes equal to current HDD technology opens the door to massive efficiency gains, possibly exceeding existing storage technology by several orders of magnitude. In this final chapter, the main conclusions are emphasised with respect to each chapter before ending with a section on possible paths to follow on from the work presented in this thesis.

*Multiscale Modelling of $Mn_2Au$*

The work presented in this chapter demonstrates a powerful multiscale modelling approach for antiferromagnetic materials like $Mn_2Au$. By combining first-principles calculations, atomistic spin dynamics simulations, and an adapted Landau-Lifshitz-Bloch formulation, the model was shown to accurately describe both transverse and longitudinal magnetisation dynamics from atomic to micromagnetic length scales. Notably, the approach captures ultrafast laser-induced demagnetisation processes and dynamics of thermally driven topological spin structures such as domain walls - overcoming key limitations of conventional micromagnetic techniques. While an extension of the theory would be required for more complex non-collinear antiferromagnets, the framework provided in this chapter is an important foundation for realistic simulations of antifer-

romagnetic spintronic devices and exploration of novel physical phenomena arising from the unique THz dynamics of these materials. Overall, this multiscale antiferromagnetic LLB approach enables new microscopic insights and exploration of cutting-edge applications in antiferromagnetic spintronics.

*Simulations of Magnetisation Reversal in $Mn_2Au$*

The work presented in this chapter of the thesis explores strategies for magnetisation reversal in the antiferromagnet $Mn_2Au$ using atomistic spin dynamics and the AFM-LLB. By applying staggered THz frequency pulses, 90° and 180° switching is demonstrated with fields under 500 mT. Resonant pumping close to the in-plane anisotropy field frequency reduces the required field further. Transient laser heating is also shown to reduce the critical switching field, with the relative timing between the heating from the laser pulse and the staggered field pulse playing a crucial role in the critical field size. Delaying the field until peak demagnetisation leads to large increases in the required reversal field. The adapted LLB approach shows excellent agreement with computationally demanding atomistic simulations for the precessional dynamics, enabling efficient modelling of temperature effects. Overall, the work provides important insights into ultrafast reversal processes in $Mn_2Au$ using experimentally feasible THz fields. It also demonstrates the power of extending micromagnetic techniques to antiferromagnetic systems, enabling device-relevant simulations of these technologically promising materials.

*Atomistic Simulations of $Mn_2Au$ and Permalloy Bilayers*

This chapter employs atomistic spin dynamics to explore magnetisation reversal in $Mn_2Au$/Permalloy bilayers using THz frequency staggered magnetic field pulses. An initial investigation is carried out investigating the effects of varying the ferromagnetic Permalloy thickness and interfacial exchange coupling strength on the temperature-dependent magnetisation and resonant dynamics. It is shown that thinner Permalloy

films enable faster and easier THz switching, while an order of magnitude increase in the interface exchange has little impact on switching with pulse durations $\lesssim 0.2$ ps. It was also shown that pumping the FM as well as the AFM makes very little difference to the switching phase diagram with these pulse durations. The switching was found to be consistent at 300K and 600K with elevated temperatures facilitating a small decrease ($\sim$ 100s mT) in the required reversal fields, with complex precessional dynamics arising from the competing FM and AFM layers. Overall, the results demonstrate the potential for ultrafast reversal mediated by the AFM, despite the coupling to an FM. With careful parameter tuning, switching on few-picosecond timescales is shown to be feasible. The atomistic approach provides insights into the rich microscopic dynamics at play in these exchange-coupled bilayers, highlighting the role of the AFM in driving rapid precessional switching relevant for possible future memory applications.

*Spinwave Dynamics in AFM Thin Films and Multliayers With Combined FM and AFM Order*

This chapter explores the potential for ultrafast switching in AFM thin films and multilayers by harnessing resonant spinwave excitations. Using a combination of ASD simulations and LSWT calculations, it was verified that SSW modes emerge in bulk multilayers with alternating FM and AFM layers. Varying the layer thicknesses and magnetic properties tunes the resonant frequencies that can then be selectively driven using tailored THz fields. Exciting spinwave dynamics at specific resonant frequencies is shown to increase excitation amplitudes and reduce the critical switching fields compared to off-resonant pumping. While exploratory, this work highlights new routes for energy-efficient antiferromagnetic switching by engineering the spinwave spectrum of magnetic heterostructures and coupling spin dynamics to tailored THz fields.

## 7.1 Future Work

The multiscale modelling of $Mn_2Au$ was the first of its kind that linked together computational work from *ab-initio* to micromagnetic length and timescales however an open question remains regarding the temperature-dependent forms of the transverse damping. It was found that there was a damping dependence on the transverse relaxation time in the atomistic model that is not captured in the LLB formalism. For $Mn_2Au$, experimental measurements indicate a damping factor of $\lambda = 0.008$ [179], which is close to the value of $\lambda = 0.01$ predominantly used throughout this thesis. Fortunately, the $\lambda = 0.01$ value showed the closest alignment with the analytical expression of the relaxation time but to provide a precise depiction for systems with considerably lower damping, a comprehensive examination of the dependence of relaxation time on damping is imperative.

The study of AFMs in the *ab-initio* and atomistic regime is already an extensive area of research whereas an LLB model for AFMs opens a wide range of possibilities for future work. One such possibility is the extension to the multilayer systems that were studied in later chapters. The FM LLB has already been extended to account for positively exchange-coupled magnetic grains like those found in HDD media [151]. It remains an open question whether exchange coupled systems, such as the $Mn_2Au$/Py bilayer presented in chapter 5, can be computationally modelled using the AFM-LLB. A development such as this would allow for much faster simulations with calculations of the phase diagrams shown in chapter 5 using a fractional amount of resources compared to an atomistic model. This would be especially prevalent for the finite temperature simulations, which required large system sizes and many repetitions to account for the thermal noise.

Regarding the bilayer switching simulations, there exists several parameters that were not explored as part of this work. An exploration of the switching dynamics for varied damping and AFM thickness may be a useful course of action for finding further

reductions in the field strengths and durations required for reversal. In our atomistic model, Py was modelled using an average moment. It would perhaps prove beneficial to model Py more accurately using a disordered alloy. Increasing the number of sublattices may alter the switching behaviour, and a systematic investigation into varying concentrations and distribution of both Ni and Fe in the system could yield interesting results. To add to this, a full parameterisation of the interfacial exchange based using DFT methods

The multilayer dynamics of the toy systems presented in chapter 6 were very much an exploratory investigation and had no basis on any physical system. An obvious extension is a full parameterisation of a repeated multilayer structure containing FM and AFM materials using *ab initio* techniques. While a system of Py and $Mn_2Au$ was only explored as a bilayer system in chapter 6, it could be extended as a repeated multilayer structure due to close matching of the lattice constants. Another FM that could work well for the same reason is Fe, a magnetic material that has been explored extensively. Electrical currents are known to generate SOTs in metallic AFMs, but experimentally being able to excite FM and AFM sublattices in a multilayered structure remains an unanswered question.

The standing spinwave-mediated switching in the thin AFM film that was shown in this chapter is an interesting result, it is the first simulated work of how excitations at resonant modes above the fundamental $n = 0$ mode can lead to reductions in the critical field. While most of this thesis has investigated dynamics in AFM materials, it is unknown whether this result can be replicated in FM thin films. In principle, excitations of standing spinwaves in thin FM films would, experimentally, be much easier as it does not require any kind of staggered field.

# Appendix A

# The Connection Between the Landau-Lifshitz and Landau-Lifshitz-Gilbert Equations

For isotropic damping, it can be shown that the LL and LLG equations take identical forms. Starting by taking the cross product of the LLG equation (Eq. (2.5)) with the magnetisation

$$\mathbf{M} \times \frac{\partial \mathbf{M}}{\partial t} = -\gamma \mathbf{M} \times (\mathbf{M} \times \mathbf{H}) + \frac{\lambda}{M} \mathbf{M} \times \left( \mathbf{M} \times \frac{\partial \mathbf{M}}{\partial t} \right) \tag{A.1}$$

Using the vector calculus identity $\mathbf{A} \times (\mathbf{B} \times \mathbf{C}) = \mathbf{B}(\mathbf{A} \cdot \mathbf{C}) - \mathbf{C}(\mathbf{A} \cdot \mathbf{B})$. The above becomes

$$\mathbf{M} \times \frac{\partial \mathbf{M}}{\partial t} = -\gamma \mathbf{M} \times (\mathbf{M} \times \mathbf{H}) + \frac{\lambda}{M} \left( \mathbf{M} \left( \mathbf{M} \cdot \frac{\partial \mathbf{M}}{\partial t} \right) - \frac{\partial \mathbf{M}}{\partial t} (\mathbf{M} \cdot \mathbf{M}) \right) \tag{A.2}$$

Since $M$ has fixed length, any changes in the direction of $M$ are orthogonal (perpendicular) to $M$ itself, i.e., $\mathbf{M} \cdot \frac{\partial \mathbf{M}}{\partial t} = 0$, the equation of motion simplifies to

$$\begin{aligned} \mathbf{M} \times \frac{\partial \mathbf{M}}{\partial t} &= -\gamma \mathbf{M} \times (\mathbf{M} \times \mathbf{H}) - \frac{\lambda}{M} \left( \frac{\partial \mathbf{M}}{\partial t} (\mathbf{M} \cdot \mathbf{M}) \right) \\ &= -\gamma \mathbf{M} \times (\mathbf{M} \times \mathbf{H}) - \lambda M \frac{\partial \mathbf{M}}{\partial t} \end{aligned} \tag{A.3}$$

If we now substitute the above back into the original LLG equation (Eq. (2.5)) we get

$$\begin{aligned} \frac{\partial \mathbf{M}}{\partial t} &= -\gamma (\mathbf{M} \times \mathbf{H}) - \frac{\lambda}{M} \left( \gamma \mathbf{M} \times (\mathbf{M} \times \mathbf{H}) + \lambda M \frac{\partial \mathbf{M}}{\partial t} \right) \\ &= -\gamma (\mathbf{M} \times \mathbf{H}) - \frac{\lambda \gamma}{M} \mathbf{M} \times (\mathbf{M} \times \mathbf{H}) - \lambda^2 \frac{\partial \mathbf{M}}{\partial t} \end{aligned} \tag{A.4}$$

Taking all the $\frac{\partial \mathbf{M}}{\partial t}$ onto the LHS and collecting the like terms

$$\frac{\partial \mathbf{M}}{\partial t} + \lambda^2 \frac{\partial \mathbf{M}}{\partial t} = -\gamma (\mathbf{M} \times \mathbf{H}) - \frac{\lambda \gamma}{M} \mathbf{M} \times (\mathbf{M} \times \mathbf{H}) \tag{A.5}$$

$$(1 + \lambda^2) \frac{\partial \mathbf{M}}{\partial t} = -\gamma (\mathbf{M} \times \mathbf{H}) - \frac{\lambda \gamma}{M} \mathbf{M} \times (\mathbf{M} \times \mathbf{H}) \tag{A.6}$$

$$\frac{\partial \mathbf{M}}{\partial t} = -\frac{\gamma}{(1 + \lambda^2)} (\mathbf{M} \times \mathbf{H}) - \frac{\lambda \gamma}{(1 + \lambda^2) M} \mathbf{M} \times (\mathbf{M} \times \mathbf{H}) \tag{A.7}$$

Setting $\gamma' = \lambda / (1 + \lambda^2)$, and $\alpha = \lambda / (1 + \lambda^2)$ the above reduces down to

$$\frac{\partial \mathbf{M}}{\partial t} = -\gamma' (\mathbf{M} \times \mathbf{H}) - \frac{\alpha \gamma}{M} \mathbf{M} \times (\mathbf{M} \times \mathbf{H}) \tag{A.8}$$

which is in an identical form to the LL equation except with a modified damping parameter and gyromagnetic ratio. In general, the Gilbert form is preferred in atomistic and micromagnetic because of the shortcomings it addresses with the standard LL equation [84, 223].

# Appendix B

# Simplification of the AFM Macrospin Equation

The equation of motion for the neel vector for the in-plane dynamics in Eq. (4.9) is given by

$$0 = \mathbf{n} \times \left(\dot{\mathbf{n}} - 2H_{\text{ex}}H_{xy}n_x n_y \left(n_x + n_y\right)\hat{\mathbf{u}}_{xy} + 2H_{\text{ex}}\lambda\dot{\mathbf{n}} + \gamma\mathbf{B}\right) \tag{B.1}$$

where $\hat{\mathbf{u}}_{xy} = \hat{\mathbf{x}} + \hat{\mathbf{y}}$. To be able to describe the dynamics in terms of a single angle, $\varphi$, away from the [110] orientation, the following substitution is made

$$\begin{aligned} n_x &= \cos(\varphi) + \sin(\varphi) \\ n_y &= \cos(\varphi) - \sin(\varphi) \end{aligned} \tag{B.2}$$

Using the chain rule, the first derivative of the above with respect to time is

$$\begin{aligned} \dot{n}_x &= -\sin(\varphi)\dot{\varphi} + \cos(\varphi)\dot{\varphi} \\ \dot{n}_y &= -\sin(\varphi)\dot{\varphi} - \cos(\varphi)\dot{\varphi} \end{aligned} \tag{B.3}$$

and the second derivative

$$n_x = -\cos(\varphi)\dot{\varphi}^2 - \sin(\varphi)\ddot{\varphi} - \sin(\varphi)\dot{\varphi}^2 + \cos(\varphi)\cdot\ddot{\varphi} \tag{B.4}$$

$$n_y = -\cos(\varphi)\dot{\varphi}^2 - \sin(\varphi)\ddot{\varphi} + \sin(\varphi)\dot{\varphi}^2 - \cos(\varphi)\cdot\ddot{\varphi} \tag{B.5}$$

Looking initially at the first term in Eq. (B.1), we have:

$$\mathbf{n}\times\ddot{\mathbf{n}} = \begin{pmatrix} \cos(\varphi)+\sin(\varphi) \\ \cos(\varphi)-\sin(\varphi) \\ 0 \end{pmatrix} \times \begin{pmatrix} -\cos(\varphi)\dot{\varphi}^2 - \sin(\varphi)\ddot{\varphi} - \sin(\varphi)\dot{\varphi}^2 + \cos(\varphi)\cdot\ddot{\varphi} \\ -\cos(\varphi)\dot{\varphi}^2 - \sin(\varphi)\ddot{\varphi} + \sin(\varphi)\dot{\varphi}^2 - \cos(\varphi)\cdot\ddot{\varphi} \\ 0 \end{pmatrix} \tag{B.6}$$

Expanding out the cross product:

$$\begin{aligned} \mathbf{n}\times\ddot{\mathbf{n}} = &\left(\cos(\varphi)+\sin(\varphi)\right)\left(-\cos(\varphi)\dot{\varphi}^2 - \sin(\varphi)\ddot{\varphi} + \sin(\varphi)\dot{\varphi}^2 - \cos(\varphi)\cdot\ddot{\varphi}\right) \\ &-\left(\cos(\varphi)-\sin(\varphi)\right)\left(-\cos(\varphi)\dot{\varphi}^2 - \sin(\varphi)\ddot{\varphi} - \sin(\varphi)\dot{\varphi}^2 + \cos(\varphi)\cdot\ddot{\varphi}\right) \end{aligned} \tag{B.7}$$

after expanding out the brackets and cancelling some terms:

$$\begin{aligned} \mathbf{n}\times\ddot{\mathbf{n}} = &-\cancel{\cos^2(\varphi)\dot{\varphi}^2} - \cancel{\cos(\varphi)\sin(\varphi)\ddot{\varphi}} + \cancel{\sin(\varphi)\cos(\varphi)\dot{\varphi}^2} - \cos^2(\varphi)\ddot{\varphi} \\ &-\cancel{\sin(\varphi)\cos(\varphi)\dot{\varphi}^2} - \sin^2(\varphi)\ddot{\varphi} + \cancel{\sin^2(\varphi)\dot{\varphi}^2} - \cancel{\sin(\varphi)\cos(\varphi)\ddot{\varphi}} \\ &+\cancel{\cos^2(\varphi)\dot{\varphi}^2} + \cancel{\cos(\varphi)\sin(\varphi)\ddot{\varphi}} + \cancel{\cos(\varphi)\sin(\varphi)\dot{\varphi}^2} - \cos^2(\varphi)\ddot{\varphi} \\ &-\cancel{\sin(\varphi)\cos(\varphi)\dot{\varphi}^2} - \sin^2(\varphi)\ddot{\varphi} - \cancel{\sin(\varphi)\dot{\varphi}^2} + \cancel{\sin(\varphi)\cos(\varphi)\ddot{\varphi}} \end{aligned} \tag{B.8}$$

which leaves us with

$$\begin{aligned} \mathbf{n}\times\ddot{\mathbf{n}} &= -2\sin^2(\varphi)\ddot{\varphi} - 2\cos^2(\varphi)\ddot{\varphi} \\ &= -2\ddot{\varphi}(\sin^2(\varphi)\ddot{\varphi} + \cos^2(\varphi)) \\ &= -2\ddot{\varphi} \end{aligned} \tag{B.9}$$

As required. Now returning to Eq. (B.1) and repeating the process with the second term:

$$= \begin{pmatrix} n_x \\ n_y \\ 0 \end{pmatrix} \times \begin{pmatrix} 2H_{\text{ex}}H_{xy}n_xn_y\left(n_x+n_y\right) \\ 2H_{\text{ex}}H_{xy}n_xn_y\left(n_x+n_y\right) \\ 0 \end{pmatrix} \tag{B.10}$$

substituting in $n_x$ and $n_y$ in terms of the angle $\varphi$:

$$= 2H_{\text{ex}}H_{xy}\begin{pmatrix}\cos(\varphi)+\sin(\varphi)\\ \cos(\varphi)-\sin(\varphi)\\ 0\end{pmatrix}\times\begin{pmatrix}2\cos(\varphi)\left(\cos(\varphi)+\sin(\varphi)\right)\left(\cos(\varphi)-\sin(\varphi)\right)\\ 2\cos(\varphi)\left(\cos(\varphi)+\sin(\varphi)\right)\left(\cos(\varphi)-\sin(\varphi)\right)\\ 0\end{pmatrix} \tag{B.11}$$

expanding out the brackets on the right-hand vector and simplifying:

$$= 2H_{\text{ex}}H_{xy}\begin{pmatrix}\cos(\varphi)+\sin(\varphi)\\ \cos(\varphi)-\sin(\varphi)\\ 0\end{pmatrix}\times\begin{pmatrix}2\cos(\varphi)\left(\cos^2(\varphi)-\sin^2(\varphi)\right)\\ 2\cos(\varphi)\left(\cos^2(\varphi)-\sin^2(\varphi)\right)\\ 0\end{pmatrix} \tag{B.12}$$

$$= 2H_{\text{ex}}H_{xy}\begin{pmatrix}\cos(\varphi)+\sin(\varphi)\\ \cos(\varphi)-\sin(\varphi)\\ 0\end{pmatrix}\times\begin{pmatrix}2\cos(\varphi)\cos(2\varphi)\\ 2\cos(\varphi)\cos(2\varphi)\\ 0\end{pmatrix} \tag{B.13}$$

$$= 4H_{\text{ex}}H_{xy}\cos(\varphi)\cos(2\varphi)\left(\cos(\varphi)+\sin(\varphi)-\cos(\varphi)+\sin(\varphi)\right) \tag{B.14}$$

$$= 4H_{\text{ex}}H_{xy}\cos(\varphi)\cos(2\varphi)\sin(\varphi) \tag{B.15}$$

$$= 2H_{\text{ex}}H_{xy}\cos(2\varphi)\sin(2\varphi) \tag{B.16}$$

$$= 2H_{\text{ex}}H_{xy}\sin(4\varphi) \tag{B.17}$$

As required. For the third term in Eq. (B.1), we have:

$$\mathbf{n}\times 2H_{\text{ex}}\lambda\dot{\mathbf{n}} = 2H_{\text{ex}}\lambda\begin{pmatrix}\cos(\varphi)+\sin(\varphi)\\ \cos(\varphi)-\sin(\varphi)\\ 0\end{pmatrix}\times\begin{pmatrix}-\sin(\varphi)\dot{\varphi}+\cos(\varphi)\dot{\varphi}\\ -\sin(\varphi)\dot{\varphi}-\cos(\varphi)\dot{\varphi}\\ 0\end{pmatrix} \tag{B.18}$$

expanding out the cross product, cancelling and simplifying terms:

$$\begin{aligned}=&2H_{\text{ex}}\lambda(\,(\cos(\varphi)+\sin(\varphi))\,(-\sin(\varphi)\dot{\varphi}-\cos(\varphi)\dot{\varphi})\\&-(\cos(\varphi)-\sin(\varphi))\,(-\sin(\varphi)\dot{\varphi}+\cos(\varphi)\dot{\varphi})\,)\end{aligned}\tag{B.19}$$

$$\begin{aligned}=&2H_{\text{ex}}\lambda(\,-2\cos(\varphi)\sin(\varphi)\dot{\varphi}-\sin^2(\varphi)\dot{\varphi}\\&-\cos^2(\varphi)\dot{\varphi}-\cos^2(\varphi)\dot{\varphi}+2\cos(\varphi)\sin(\varphi)\dot{\varphi}-\sin^2(\varphi))\end{aligned}\tag{B.20}$$

$$=2H_{\text{ex}}\lambda(\,-\sin^2(\varphi)\dot{\varphi}-\cos^2(\varphi)\dot{\varphi}-\cos^2(\varphi)\dot{\varphi}-\sin^2(\varphi))\tag{B.21}$$

$$=-4H_{\text{ex}}\lambda\dot{\varphi}(\,\cos^2(\varphi)+\sin^2(\varphi))\tag{B.22}$$

$$=-4H_{\text{ex}}\lambda\dot{\varphi}\tag{B.23}$$

Finally, we arrive at the final term:

$$\mathbf{n}\times\gamma\mathbf{B}=\begin{pmatrix}\cos(\varphi)+\sin(\varphi)\\\cos(\varphi)-\sin(\varphi)\\0\end{pmatrix}\times\begin{pmatrix}B_x\\B_y\\0\end{pmatrix}\tag{B.24}$$

$$=(\,\cos(\varphi)+\sin(\varphi))B_y-(\,\cos(\varphi)-\sin(\varphi))B_x\tag{B.25}$$

If we assume that the field acts perpendicular to the neel vector, $[\bar{1}\bar{1}0]$, with equal magnitude for each cartesian component (i.e $-B_x=+B_y=B$) to maximise the torque the above simplifies to:

$$=-(\,\cos(\varphi)+\sin(\varphi))B-(\,\cos(\varphi)-\sin(\varphi))B\tag{B.26}$$

$$=-2B\cos(\varphi)\tag{B.27}$$

Therefore the full equation of motion in its simplified form can be written as a combination of Eqs. (B.9), (B.17), (B.23) and (B.27):

$$\begin{aligned} 0 =& -2\ddot{\varphi} - 2\gamma^2 H_{\mathrm{ex}} H_{xy} \sin(4\varphi) - 4H_{\mathrm{ex}}\lambda\dot{\varphi} - 2B\cos(\varphi) \\ 0 =& \ddot{\varphi} + \gamma^2 H_{\mathrm{ex}} H_{xy} \sin(4\varphi) + 2H_{\mathrm{ex}}\lambda\dot{\varphi} + B\cos(\varphi) \end{aligned} \tag{B.28}$$

# References


[1] seagate.com, "BarraCuda Hard Drives | Seagate US." https://www.seagate.com/gb/en/products/hard-drives/barracuda-hard-drive/, 2023. [Accessed 20-08-2023].

[2] IEA, "Data centres and data transmission networks – analysis." https://www.iea.org/reports/data-centres-and-data-transmission-networks. [Accessed August 2022].

[3] B. Odom, D. Hanneke, B. D'Urso, and G. Gabrielse, "New measurement of the electron magnetic moment using a one-electron quantum cyclotron," *Phys. Rev. Lett.*, vol. 97, p. 030801, Jul 2006.

[4] S. Blundell, *Magnetism in condensed matter*. OUP Oxford, 2001.

[5] R. Skomski, *Simple Models of Magnetism*. Oxford University Press, 01 2008.

[6] J. M. Coey, *Magnetism and magnetic materials*. Cambridge university press, 2010.

[7] T. Ruijgrok, "On the theory of ferromagnetism," *Physica*, vol. 28, no. 9, pp. 877–892, 1962.

[8] A. Aharoni, *Introduction to the Theory of Ferromagnetism*, vol. 109. Clarendon Press, 2000.

[9] A. Meo, *Atomistic model of magnetisation dynamics and equilibrium properties of magnetic tunnel junctions*. PhD thesis, University of York, 2018.

[10] M. Ellis, *Simulations of magnetic reversal properties in granular recording media*. PhD thesis, University of York, 2015.

[11] S. I. Ruta, *Study of interaction effects in magnetic granular systems for recording media application*. PhD thesis, University of York, 2017.

[12] S. Piramanayagam, "Perpendicular recording media for hard disk drives," *Journal of Applied Physics*, vol. 102, no. 1, 2007.

[13] D. Weller, O. Mosendz, G. Parker, S. Pisana, and T. S. Santos, "L10 fe p t x–y media for heat-assisted magnetic recording," *physica status solidi (a)*, vol. 210, no. 7, pp. 1245–1260, 2013.

[14] W. Digital, "Leadership in hdd." https://investor.wdc.com/static-files/a8478f23-401e-4008-8d05-8bb6cf238886, 2022. [Accessed 29-01-2024].

[15] E. A. Dobisz, Z. Z. Bandic, T.-W. Wu, and T. Albrecht, "Patterned media: Nanofabrication challenges of future disk drives," *Proceedings of the IEEE*, vol. 96, no. 11, pp. 1836–1846, 2008.

[16] C. Kittel, "On the theory of ferromagnetic resonance absorption," *Phys. Rev.*, vol. 73, pp. 155–161, Jan 1948.

[17] L. Néel, "Théorie du traînage magnétique des ferromagnétiques en grains fins avec application aux terres cuites," in *Annales de géophysique*, vol. 5, pp. 99–136, 1949.

[18] R. F. L. Evans, R. W. Chantrell, U. Nowak, A. Lyberatos, and H.-J. Richter, "Thermally induced error: Density limit for magnetic data storage," *Applied Physics Letters*, vol. 100, p. 102402, 03 2012.

[19] M. H. Kryder, E. C. Gage, T. W. McDaniel, W. A. Challener, R. E. Rottmayer, G. Ju, Y.-T. Hsia, and M. F. Erden, "Heat assisted magnetic recording," *Proceedings of the IEEE*, vol. 96, no. 11, pp. 1810–1835, 2008.

[20] R. E. MacDonald and J. W. Beck, "Magneto-optical recording," *Journal of Applied Physics*, vol. 40, pp. 1429–1435, 1969.

[21] R. Rottmayer, S. Batra, D. Buechel, W. Challener, J. Hohlfeld, Y. Kubota, L. Li, B. Lu, C. Mihalcea, K. Mountfield, K. Pelhos, C. Peng, T. Rausch, M. Seigler, D. Weller, and X.-M. Yang, "Heat-assisted magnetic recording," *IEEE Transactions on Magnetics*, vol. 42, no. 10, pp. 2417–2421, 2006.

[22] A. Meo, W. Pantasri, W. Daeng-am, S. E. Rannala, S. I. Ruta, R. W. Chantrell, P. Chureemart, and J. Chureemart, "Magnetization dynamics of granular heat-assisted magnetic recording media by means of a multiscale model," *Phys. Rev. B*, vol. 102, p. 174419, Nov 2020.

[23] L. Pan and D. B. Bogy, "Heat-assisted magnetic recording," *Nature Photonics*, vol. 3, pp. 189–190, Apr 2009.

[24] W.-H. Hsu and R. Victora, "Heat-assisted magnetic recording — micromagnetic modeling of recording media and areal density: A review," *Journal of Magnetism and Magnetic Materials*, vol. 563, p. 169973, 2022.

[25] W. Challener, C. Peng, A. Itagi, D. Karns, W. Peng, Y. Peng, X. Yang, X. Zhu, N. Gokemeijer, Y.-T. Hsia, *et al.*, "Heat-assisted magnetic recording by a near-field transducer with efficient optical energy transfer," *Nature photonics*, vol. 3, no. 4, pp. 220–224, 2009.

[26] N. Kazantseva, D. Hinzke, U. Nowak, R. W. Chantrell, U. Atxitia, and O. Chubykalo-Fesenko, "Towards multiscale modeling of magnetic materials: Simulations of fept," *Phys. Rev. B*, vol. 77, p. 184428, May 2008.

[27] D. Weller, G. Parker, O. Mosendz, A. Lyberatos, D. Mitin, N. Y. Safonova, and M. Albrecht, "Fept heat assisted magnetic recording media," *Journal of Vacuum Science & Technology B*, vol. 34, no. 6, 2016.

[28] seagate.com, "Heat assisted magnetic recording (hamr) the next generation of enterprise hard drive capacity.." https://www.seagate.com/gb/en/innovation/hamr/, 2023. [Accessed 24-08-2023].

[29] "Seagate's Breakthrough 30TB+ Hard Drives Ramp Volume, Marking an Inflection Point in the Storage Industry | Seagate US — seagate.com." https://www.seagate.com/gb/en/news/news-archive/seagates-breakthrough-30tb-plus-hard-drives-ramp-volume-marking-an-inflection-point-in-the- Jan 2024. [Accessed 29-01-2024].

[30] E. Beaurepaire, J.-C. Merle, A. Daunois, and J.-Y. Bigot, "Ultrafast spin dynamics in ferromagnetic nickel," *Phys. Rev. Lett.*, vol. 76, pp. 4250–4253, May 1996.

[31] T. Kampfrath, R. G. Ulbrich, F. Leuenberger, M. Münzenberg, B. Sass, and W. Felsch, "Ultrafast magneto-optical response of iron thin films," *Physical Review B*, vol. 65, no. 10, p. 104429, 2002.

[32] H. Kronmüller, "Handbook of magnetism and advanced magnetic materials," *(No Title)*, vol. 1, 2007.

[33] B. Koopmans, F. Dalla Longa, D. Steiauf, M. Fähnle, T. Roth, M. Cinchetti, and M. Aeschlimann, "Explaining the paradoxical diversity of ultrafast laser-induced demagnetization," *Nature materials*, vol. 9, no. 3, pp. 259–265, 2010.

[34] V. Shokeen, M. Sanchez Piaia, J.-Y. Bigot, T. Müller, P. Elliott, J. K. Dewhurst, S. Sharma, and E. K. U. Gross, "Spin flips versus spin transport in nonthermal electrons excited by ultrashort optical pulses in transition metals," *Phys. Rev. Lett.*, vol. 119, p. 107203, Sep 2017.

[35] W. Töws and G. M. Pastor, "Many-body theory of ultrafast demagnetization and angular momentum transfer in ferromagnetic transition metals," *Phys. Rev. Lett.*, vol. 115, p. 217204, Nov 2015.

[36] M. Battiato, K. Carva, and P. M. Oppeneer, "Superdiffusive spin transport as a mechanism of ultrafast demagnetization," *Physical Review Letters*, vol. 105, no. 2, pp. 1–4, 2010.

[37] C. Dornes, Y. Acremann, M. Savoini, M. Kubli, M. J. Neugebauer, E. Abreu, L. Huber, G. Lantz, C. A. Vaz, H. Lemke, E. M. Bothschafter, M. Porer, V. Esposito, L. Rettig, M. Buzzi, A. Alberca, Y. W. Windsor, P. Beaud, U. Staub, D. Zhu, S. Song, J. M. Glownia, and S. L. Johnson, "The ultrafast Einstein–de Haas effect," *Nature*, vol. 565, no. 7738, pp. 209–212, 2019.

[38] C. D. Stanciu, F. Hansteen, A. V. Kimel, A. Kirilyuk, A. Tsukamoto, A. Itoh, and T. Rasing, "All-optical magnetic recording with circularly polarized light," *Physical Review Letters*, vol. 99, no. 4, pp. 1–4, 2007.

[39] I. Radu, K. Vahaplar, C. Stamm, T. Kachel, N. Pontius, H. A. Dürr, T. A. Ostler, J. Barker, R. F. Evans, R. W. Chantrell, A. Tsukamoto, A. Itoh, A. Kirilyuk, T. Rasing, and A. V. Kimel, "Transient ferromagnetic-like state mediating ultrafast reversal of antiferromagnetically coupled spins," *Nature*, vol. 472, pp. 205–209, 4 2011.

[40] T. A. Ostler, J. Barker, R. F. Evans, R. W. Chantrell, U. Atxitia, O. Chubykalo-Fesenko, S. El Moussaoui, L. Le Guyader, E. Mengotti, L. J. Heyderman, F. Nolting, A. Tsukamoto, A. Itoh, D. Afanasiev, B. A. Ivanov, A. M. Kalashnikova, K. Vahaplar, J. Mentink, A. Kirilyuk, T. Rasing, and A. V. Kimel, "Ultrafast heating as a sufficient stimulus for magnetization reversal in a ferrimagnet," *Nature Communications*, vol. 3, 2012.

[41] D. P. Gweha Nyoma, M. Vergès, M. Hehn, D. Lacour, J. Hohlfeld, S. van Dijken, G. Malinowski, S. Mangin, and F. Montaigne, "Size effect on single pulse all-optical helicity-independent switching in gdfeco disk arrays," *Applied Physics Letters*, vol. 123, no. 5, 2023.

[42] S. Mangin, M. Gottwald, C. Lambert, D. Steil, V. Uhlíř, L. Pang, M. Hehn, S. Alebrand, M. Cinchetti, G. Malinowski, *et al.*, "Engineered materials for all-optical helicity-dependent magnetic switching," *Nature materials*, vol. 13, no. 3, pp. 286–292, 2014.

[43] G. Kichin, M. Hehn, J. Gorchon, G. Malinowski, J. Hohlfeld, and S. Mangin, "From multiple- to single-pulse all-optical helicity-dependent switching in ferromagnetic Co/Pt multilayers," *Phys. Rev. Appl.*, vol. 12, p. 024019, Aug 2019.

[44] M. L. M. Lalieu, M. J. G. Peeters, S. R. R. Haenen, R. Lavrijsen, and B. Koopmans, "Deterministic all-optical switching of synthetic ferrimagnets using single femtosecond laser pulses," *Phys. Rev. B*, vol. 96, p. 220411, Dec 2017.

[45] L. Avilés-Félix, A. Olivier, G. Li, C. S. Davies, L. Álvaro-Gómez, M. Rubio-Roy, S. Auffret, A. Kirilyuk, A. V. Kimel, T. Rasing, L. D. Buda-Prejbeanu, R. C. Sousa, B. Dieny, and I. L. Prejbeanu, "Single-shot all-optical switching of magnetization in tb/co multilayer-based electrodes," *Scientific Reports*, vol. 10, p. 5211, Mar 2020.

[46] C. Banerjee, N. Teichert, K. E. Siewierska, Z. Gercsi, G. Y. Atcheson, P. Stamenov, K. Rode, J. M. Coey, and J. Besbas, "Single pulse all-optical toggle switching of magnetization without gadolinium in the ferrimagnet mn2ruxga," *Nature Communications*, vol. 11, pp. 1–6, 2020.

[47] J. Gorchon, C.-H. Lambert, Y. Yang, A. Pattabi, R. B. Wilson, S. Salahuddin, and J. Bokor, "Single shot ultrafast all optical magnetization switching of ferromagnetic Co/Pt multilayers," *Applied Physics Letters*, vol. 111, p. 042401, 07 2017.

[48] J. Igarashi, W. Zhang, Q. Remy, E. Díaz, J.-X. Lin, J. Hohlfeld, M. Hehn, S. Mangin, J. Gorchon, and G. Malinowski, "Optically induced ultrafast magnetization switching in ferromagnetic spin valves," *Nature Materials*, 3 2023.

[49] N. Louis, "The Nobel Prize in Physics 1970."

[50] M. N. Baibich, J. M. Broto, A. Fert, F. N. Van Dau, F. Petroff, P. Etienne, G. Creuzet, A. Friederich, and J. Chazelas, "Giant magnetoresistance of (001)fe/(001)cr magnetic superlattices," *Phys. Rev. Lett.*, vol. 61, pp. 2472–2475, Nov 1988.

[51] G. Binasch, P. Grünberg, F. Saurenbach, and W. Zinn, "Enhanced magnetoresistance in layered magnetic structures with antiferromagnetic interlayer exchange," *Phys. Rev. B*, vol. 39, pp. 4828–4830, Mar 1989.

[52] B. Dieny, V. S. Speriosu, S. S. P. Parkin, B. A. Gurney, D. R. Wilhoit, and D. Mauri, "Giant magnetoresistive in soft ferromagnetic multilayers," *Phys. Rev. B*, vol. 43, pp. 1297–1300, Jan 1991.

[53] B.-Y. Jiang, K. Zhang, T. Machita, W. Chen, and M. Dovek, "Tunneling magnetoresistive devices as read heads in hard disk drives," *Journal of Magnetism and Magnetic Materials*, vol. 571, p. 170546, 2023.

[54] A. Meo, R. Chepulskyy, D. Apalkov, R. W. Chantrell, and R. F. L. Evans, "Atomistic investigation of the temperature and size dependence of the energy barrier of CoFeB/MgO nanodots," *Journal of Applied Physics*, vol. 128, p. 073905, 08 2020.

[55] F. Keffer and C. Kittel, "Theory of antiferromagnetic resonance," *Physical Review*, vol. 85, no. 2, pp. 329–337, 1952.

[56] J. Checinski, M. Frankowski, and T. Stobiecki, "Antiferromagnetic nano-oscillator in external magnetic fields," *Phys. Rev. B*, vol. 96, p. 174438, Nov 2017.

[57] R. Cheng, D. Xiao, and A. Brataas, "Terahertz antiferromagnetic spin hall nano-oscillator," *Phys. Rev. Lett.*, vol. 116, p. 207603, May 2016.

[58] R. Khymyn, I. Lisenkov, V. Tiberkevich, B. A. Ivanov, and A. Slavin, "Antiferromagnetic THz-frequency Josephson-like Oscillator Driven by Spin Current," *Scientific Reports*, vol. 7, no. January, pp. 1–10, 2017.

[59] T. Kampfrath, A. Sell, G. Klatt, A. Pashkin, S. Mährlein, T. Dekorsy, M. Wolf, M. Fiebig, A. Leitenstorfer, and R. Huber, "Coherent terahertz control of antiferromagnetic spin waves," *Nature Photonics*, vol. 5, pp. 31–34, Jan 2011.

[60] A. Barman, G. Gubbiotti, S. Ladak, A. O. Adeyeye, M. Krawczyk, J. Grafe, C. Adelmann, S. Cotofana, A. Naeemi, V. I. Vasyuchka, B. Hillebrands, S. A. Nikitov, H. Yu, D. Grundler, A. V. Sadovnikov, A. A. Grachev, S. E. Sheshukova, J. Y. Duquesne, M. Marangolo, G. Csaba, W. Porod, V. E. Demidov, S. Urazhdin, S. O. Demokritov, E. Albisetti, D. Petti, R. Bertacco, H. Schultheiss, V. V. Kruglyak, V. D. Poimanov, S. Sahoo, J. Sinha, H. Yang, M. Münzenberg, T. Moriyama, S. Mizukami, P. Landeros, R. A. Gallardo, G. Carlotti, J. V. Kim, R. L. Stamps, R. E. Camley, B. Rana, Y. Otani, W. Yu, T. Yu, G. E. Bauer, C. Back, G. S. Uhrig, O. V. Dobrovolskiy, B. Budinska, H. Qin, S. V. Dijken, A. V. Chumak, A. Khitun, D. E. Nikonov, I. A. Young, B. W. Zingsem, and M. Winklhofer, "The 2021 magnonics roadmap," *Journal of Physics Condensed Matter*, vol. 33, 10 2021.

[61] P. Wadley and K. Edmonds, "Spin switching in antiferromagnets using néel-order spin-orbit torques," *Chinese Physics B*, vol. 27, no. 10, p. 107201, 2018.

[62] P. Wadley, B. Howells, J. Železný, C. Andrews, V. Hills, R. P. Campion, V. Novák, K. Olejník, F. Maccherozzi, S. S. Dhesi, S. Y. Martin, T. Wagner, J. Wunderlich, F. Freimuth, Y. Mokrousov, J. Kuneš, J. S. Chauhan, M. J. Grzybowski, A. W. Rushforth, K. Edmond, B. L. Gallagher, and T. Jungwirth, "Spintronics: Electrical switching of an antiferromagnet," *Science*, vol. 351, pp. 587–590, 2016.

[63] J. Železný, H. Gao, K. Výborný, J. Zemen, J. Mašek, A. Manchon, J. Wunderlich, J. Sinova, and T. Jungwirth, "Relativistic néel-order fields induced by electrical current in antiferromagnets," *Phys. Rev. Lett.*, vol. 113, p. 157201, Oct 2014.

[64] S. Reimers, Y. Lytvynenko, Y. R. Niu, E. Golias, B. Sarpi, L. S. Veiga, T. Denneulin, A. Kovács, R. E. Dunin-Borkowski, J. Bläßer, M. Kläui, and M. Jourdan, "Current-driven writing process in antiferromagnetic mn2au for memory applications," *Nature Communications*, vol. 14, 12 2023.

[65] M. Meinert, D. Graulich, and T. Matalla-Wagner, "Electrical switching of antiferromagnetic $mn_2Au$ and the role of thermal activation," *Phys. Rev. Applied*, vol. 9, p. 064040, Jun 2018.

[66] S. Y. Bodnar, L. Šmejkal, I. Turek, T. Jungwirth, O. Gomonay, J. Sinova, A. A. Sapozhnik, H. J. Elmers, M. Klaüi, and M. Jourdan, "Writing and reading antiferromagnetic Mn2Au by Neél spin-orbit torques and large anisotropic magnetoresistance," *Nature Communications*, vol. 9, no. 1, pp. 1–7, 2018.

[67] X. Z. Chen, R. Zarzuela, J. Zhang, C. Song, X. F. Zhou, G. Y. Shi, F. Li, H. A. Zhou, W. J. Jiang, F. Pan, and Y. Tserkovnyak, "Antidamping-torque-induced switching in biaxial antiferromagnetic insulators," *Phys. Rev. Lett.*, vol. 120, p. 207204, May 2018.

[68] F. L. A. Machado, P. R. T. Ribeiro, J. Holanda, R. L. Rodríguez-Suárez, A. Azevedo, and S. M. Rezende, "Spin-flop transition in the easy-plane antiferromagnet nickel oxide," *Phys. Rev. B*, vol. 95, p. 104418, Mar 2017.

[69] A. A. Sapozhnik, M. Filianina, S. Y. Bodnar, A. Lamirand, M.-A. Mawass, Y. Skourski, H. J. Elmers, H. Zabel, M. Kläui, and M. Jourdan, "Direct imaging of antiferromagnetic domains in mn 2 au manipulated by high magnetic fields," *Physical Review B*, vol. 97, p. 134429, 2018.

[70] S. Wienholdt, D. Hinzke, and U. Nowak, "Thz switching of antiferromagnets and ferrimagnets," *Phys. Rev. Lett.*, vol. 108, p. 247207, Jun 2012.

[71] S. Selzer, L. Salemi, A. Deák, E. Simon, L. Szunyogh, P. M. Oppeneer, and U. Nowak, "Current-induced switching of antiferromagnetic order in $mn_2Au$ from first principles," *Phys. Rev. B*, vol. 105, p. 174416, May 2022.

[72] R. Rama-Eiroa, R. M. Otxoa, and U. Atxitia, "Temperature-dependent critical spin-orbit field for orthogonal switching in antiferromagnets," *Applied Physics Letters*, vol. 121, 9 2022.

[73] P. Hohenberg and W. Kohn, "Inhomogeneous electron gas," *Phys. Rev.*, vol. 136, pp. B864–B871, Nov 1964.

[74] P. Giannozzi, S. Baroni, N. Bonini, M. Calandra, R. Car, C. Cavazzoni, D. Ceresoli, G. L. Chiarotti, M. Cococcioni, I. Dabo, A. D. Corso, S. de Gironcoli, S. Fabris, G. Fratesi, R. Gebauer, U. Gerstmann, C. Gougoussis, A. Kokalj, M. Lazzeri, L. Martin-Samos, N. Marzari, F. Mauri, R. Mazzarello, S. Paolini, A. Pasquarello, L. Paulatto, C. Sbraccia, S. Scandolo, G. Sclauzero, A. P. Seitsonen, A. Smogunov, P. Umari, and R. M. Wentzcovitch, "QUANTUM ESPRESSO: a modular and open-source software project for quantum simulations of materials," *Journal of Physics: Condensed Matter*, vol. 21, p. 395502, sep 2009.

[75] H. Ebert, D. Ködderitzsch, and J. Minár, "Calculating condensed matter properties using the KKR-green's function method—recent developments and applications," *Reports on Progress in Physics*, vol. 74, p. 096501, aug 2011.

[76] G. Kresse and D. Joubert, "From ultrasoft pseudopotentials to the projector augmented-wave method," *Phys. Rev. B*, vol. 59, pp. 1758–1775, Jan 1999.

[77] A. Vansteenkiste, J. Leliaert, M. Dvornik, M. Helsen, F. Garcia-Sanchez, and B. Van Waeyenberge, "The design and verification of mumax3," *AIP Advances*, vol. 4, no. 10, p. 107133, 2014.

[78] M. J. Donahue and D. G. Porter, "Oommf user's guideversion 1.0. (national institute of standards and technology, gaithersburg, md, 1999)," 1999.

[79] E. Ising, "Beitrag zur theorie des ferromagnetismus," *Zeitschrift für Physik*, vol. 31, no. 1, pp. 253–258, 1925.

[80] L. Onsager, "Crystal statistics. i. a two-dimensional model with an order-disorder transition," *Physical Review*, vol. 65, no. 3-4, p. 117, 1944.

[81] N. Metropolis, A. W. Rosenbluth, M. N. Rosenbluth, A. H. Teller, and E. Teller, "Equation of State Calculations by Fast Computing Machines," *The Journal of Chemical Physics*, vol. 21, pp. 1087–1092, 12 2004.

[82] W. Sucksmith, R. R. Pearce, and A. M. Tyndall, "The paramagnetism of the ferromagnetic elements," *Proceedings of the Royal Society of London. Series A. Mathematical and Physical Sciences*, vol. 167, no. 929, pp. 189–204, 1938.

[83] L. D. Landau and E. Lifshitz, "On the theory of the dispersion of magnetic permeability in ferromagnetic bodies," *Phys. Z. Sowjet.*, vol. 8, p. 153, 1935.

[84] T. Gilbert, "A phenomenological theory of damping in ferromagnetic materials," *IEEE Transactions on Magnetics*, vol. 40, no. 6, pp. 3443–3449, 2004.

[85] R. F. Evans, W. J. Fan, P. Chureemart, T. A. Ostler, M. O. Ellis, and R. W. Chantrell, "Atomistic spin model simulations of magnetic nanomaterials," *Journal of Physics: Condensed Matter*, vol. 26, no. 10, p. 103202, 2014.

[86] J. A. F. Roldan, *Micromagnetism of Cylindrical Nanowires with Compositional & Geometric Modulations*. PhD thesis, Universidad Autonoma de Madrid, 2019.

[87] O. N. Mryasov, U. Nowak, K. Y. Guslienko, and R. W. Chantrell, "Temperature-dependent magnetic properties of fept: Effective spin hamiltonian model," *Europhysics Letters*, vol. 69, pp. 805–811, 2005.

[88] I. Dzyaloshinsky, "A thermodynamic theory of "weak" ferromagnetism of antiferromagnetics," *Journal of physics and chemistry of solids*, vol. 4, no. 4, pp. 241–255, 1958.

[89] V. Mazurenko, Y. O. Kvashnin, A. Lichtenstein, and M. Katsnelson, "A dmi guide to magnets micro-world," *Journal of Experimental and Theoretical Physics*, vol. 132, pp. 506–516, 2021.

[90] A. Fert, N. Reyren, and V. Cros, "Magnetic skyrmions: advances in physics and potential applications," *Nature Reviews Materials*, vol. 2, no. 7, pp. 1–15, 2017.

[91] M. Bode, M. Heide, K. Von Bergmann, P. Ferriani, S. Heinze, G. Bihlmayer, A. Kubetzka, O. Pietzsch, S. Blügel, and R. Wiesendanger, "Chiral magnetic order at surfaces driven by inversion asymmetry," *nature*, vol. 447, no. 7141, pp. 190–193, 2007.

[92] P. Milde, D. Köhler, J. Seidel, L. Eng, A. Bauer, A. Chacon, J. Kindervater, S. Mühlbauer, C. Pfleiderer, S. Buhrandt, *et al.*, "Unwinding of a skyrmion lattice by magnetic monopoles," *Science*, vol. 340, no. 6136, pp. 1076–1080, 2013.

[93] T. Moriya, "Anisotropic superexchange interaction and weak ferromagnetism," *Phys. Rev.*, vol. 120, pp. 91–98, Oct 1960.

[94] A. Fert, "Magnetic and transport properties of metallic multilayers," in *Materials science forum*, vol. 59, pp. 439–480, Trans Tech Publ, 1990.

[95] J. A. Brock, M. D. Kitcher, P. Vallobra, R. Medapalli, M. P. Li, M. De Graef, G. A. Riley, H. T. Nembach, S. Mangin, V. Sokalski, *et al.*, "Dynamic symmetry breaking in chiral magnetic systems," *Advanced Materials*, vol. 33, no. 39, p. 2101524, 2021.

[96] W. F. Brown, "Thermal fluctuations of a single-domain particle," *Phys. Rev.*, vol. 130, pp. 1677–1686, Jun 1963.

[97] T. Ostler, *Computer Simulations of Ultrafast Magnetisation Reversal*. PhD thesis, University of York, 2012.

[98] U. Atxitia, O. Chubykalo-Fesenko, R. W. Chantrell, U. Nowak, and A. Rebei, "Ultrafast spin dynamics: The effect of colored noise," *Phys. Rev. Lett.*, vol. 102, p. 057203, Feb 2009.

[99] J. Barker and G. E. W. Bauer, "Semiquantum thermodynamics of complex ferrimagnets," *Phys. Rev. B*, vol. 100, p. 140401, Oct 2019.

[100] P.-W. Ma, C. H. Woo, and S. L. Dudarev, "Large-scale simulation of the spin-lattice dynamics in ferromagnetic iron," *Phys. Rev. B*, vol. 78, p. 024434, Jul 2008.

[101] B. Skubic, J. Hellsvik, L. Nordström, and O. Eriksson, "A method for atomistic spin dynamics simulations: Implementation and examples," *Journal of Physics Condensed Matter*, vol. 20, 2008.

[102] U. Nowak, "Classical spin models," Dec. 2007.

[103] G. P. Müller, M. Hoffmann, C. Dißelkamp, D. Schürhoff, S. Mavros, M. Sallermann, N. S. Kiselev, H. Jónsson, and S. Blügel, "Spirit: Multifunctional framework for atomistic spin simulations," *Phys. Rev. B*, vol. 99, p. 224414, Jun 2019.

[104] P. Depondt and F. Mertens, "Spin dynamics simulations of two-dimensional clusters with heisenberg and dipole–dipole interactions," *Journal of Physics: Condensed Matter*, vol. 21, no. 33, p. 336005, 2009.

[105] J. Mentink, M. Tretyakov, A. Fasolino, M. Katsnelson, and T. Rasing, "Stable and fast semi-implicit integration of the stochastic landau–lifshitz equation," *Journal of Physics: Condensed Matter*, vol. 22, no. 17, p. 176001, 2010.

[106] J. Barker, *Atomistic Models of Magnetic Systems with Combined Ferromagnetic and Antiferromagnetic Order*. PhD thesis, 2013.

[107] N. Kazantseva, *Dynamic Response of the Magnetisation to Picosecond Heat Pulses*. PhD thesis, University of York, 2008.

[108] W. H. Press, *Numerical recipes in C : the art of scientific computing*. Cambridge University Press, 1992.

[109] D. A. Garanin, "Fokker-planck and landau-lifshitz-bloch equations for classical ferromagnets," *Phys. Rev. B*, vol. 55, pp. 3050–3057, Feb 1997.

[110] U. Atxitia, D. Hinzke, and U. Nowak, "Fundamentals and applications of the Landau-Lifshitz-Bloch equation," *Journal of Physics D: Applied Physics*, vol. 50, no. 3, 2017.

[111] U. Atxitia, P. Nieves, and O. Chubykalo-Fesenko, "Landau-lifshitz-bloch equation for ferrimagnetic materials," *Phys. Rev. B*, vol. 86, p. 104414, Sep 2012.

[112] T. A. Ostler, M. O. A. Ellis, D. Hinzke, and U. Nowak, "Temperature-dependent ferromagnetic resonance via the landau-lifshitz-bloch equation: Application to fept," *Phys. Rev. B*, vol. 90, p. 094402, Sep 2014.

[113] D. Hinzke, U. Atxitia, K. Carva, P. Nieves, O. Chubykalo-Fesenko, P. M. Oppeneer, and U. Nowak, "Multiscale modeling of ultrafast element-specific magnetization dynamics of ferromagnetic alloys," *Phys. Rev. B*, vol. 92, p. 054412, Aug 2015.

[114] X. Lu, X. Zou, D. Hinzke, T. Liu, Y. Wang, T. Cheng, J. Wu, T. A. Ostler, J. Cai, U. Nowak, R. W. Chantrell, Y. Zhai, and Y. Xu, "Roles of heating and helicity in ultrafast all-optical magnetization switching in TbFeCo," *Applied Physics Letters*, vol. 113, p. 032405, 07 2018.

[115] D. D. Stancil and A. Prabhakar, *Spin waves: Theory and applications*. Springer.

[116] R. S. Fishman, J. A. Fernandez-Baca, and T. Rõõm, *Spin-wave theory and its applications to neutron scattering and THz spectroscopy*. Morgan & Claypool Publishers, 2018.

[117] R. J. Elliott and R. Lowde, "The inelastic scattering of neutrons by magnetic spin waves," *Proceedings of the Royal Society of London. Series A. Mathematical and Physical Sciences*, vol. 230, no. 1180, pp. 46–73, 1955.

[118] J. Goedkoop and T. Riste, "Neutron diffraction study of antiferromagnetic spin waves in $\alpha$-ferric oxide," *Nature*, vol. 185, no. 4711, pp. 450–452, 1960.

[119] B. Lenk, H. Ulrichs, F. Garbs, and M. Münzenberg, "The building blocks of magnonics," *Physics Reports*, vol. 507, no. 4-5, pp. 107–136, 2011.

[120] V. Kruglyak and R. Hicken, "Magnonics: Experiment to prove the concept," *Journal of Magnetism and Magnetic Materials*, vol. 306, no. 2, pp. 191–194, 2006.

[121] J. R. Hortensius, D. Afanasiev, M. Matthiesen, R. Leenders, R. Citro, A. V. Kimel, R. V. Mikhaylovskiy, B. A. Ivanov, and A. D. Caviglia, "Coherent spin-wave transport in an antiferromagnet," *Nature Physics*, vol. 17, pp. 1001–1006, sep 2021.

[122] S. Toth and B. Lake, "Linear spin wave theory for single-q incommensurate magnetic structures," *Journal of Physics: Condensed Matter*, vol. 27, p. 166002, mar 2015.

[123] S. Petit and F. Damay, "Spinwave, a software dedicated to spin wave simulations," *Neutron News*, vol. 27, no. 4, pp. 27–28, 2016.

[124] C. Etz, L. Bergqvist, A. Bergman, A. Taroni, and O. Eriksson, "Atomistic spin dynamics and surface magnons," *Journal of Physics: Condensed Matter*, vol. 27, no. 24, p. 243202, 2015.

[125] R. B. Blackman and J. W. Tukey, "The measurement of power spectra from the point of view of communications engineering — part i," *Bell System Technical Journal*, vol. 37, no. 1, pp. 185–282, 1958.

[126] X. Chen, S. Shi, G. Shi, X. Fan, C. Song, X. Zhou, H. Bai, L. Liao, Y. Zhou, H. Zhang, A. Li, Y. Chen, X. Han, S. Jiang, Z. Zhu, H. Wu, X. Wang, D. Xue, H. Yang, and F. Pan, "Observation of the antiferromagnetic spin hall effect," *Nature Materials*, vol. 20, pp. 800–804, Jun 2021.

[127] V. Grigorev, M. Filianina, S. Y. Bodnar, S. Sobolev, N. Bhattacharjee, S. Bommanaboyena, Y. Lytvynenko, Y. Skourski, D. Fuchs, M. Kläui, M. Jourdan, and J. Demsar, "Optical readout of the néel vector in the metallic antiferromagnet $mn_2Au$," *Phys. Rev. Applied*, vol. 16, p. 014037, Jul 2021.

[128] F. Máca, J. Mašek, O. Stelmakhovych, X. Martí, H. Reichlová, K. Uhlířová, P. Beran, P. Wadley, V. Novák, and T. Jungwirth, "Room-temperature antiferromagnetism in cumnas," *Journal of Magnetism and Magnetic Materials*, vol. 324, no. 8, pp. 1606–1612, 2012.

[129] K. Olejník, V. Schuler, X. Marti, V. Novák, Z. Kašpar, P. Wadley, R. P. Campion, K. W. Edmonds, B. L. Gallagher, J. Garces, M. Baumgartner, P. Gambardella, and T. Jungwirth, "Antiferromagnetic cumnas multi-level memory cell with microelectronic compatibility," *Nature Communications*, vol. 8, p. 15434, May 2017.

[130] M. J. Grzybowski, P. Wadley, K. W. Edmonds, R. Beardsley, V. Hills, R. P. Campion, B. L. Gallagher, J. S. Chauhan, V. Novak, T. Jungwirth, F. Maccherozzi, and S. S. Dhesi, "Imaging current-induced switching of antiferromagnetic domains in cumnas," *Phys. Rev. Lett.*, vol. 118, p. 057701, Jan 2017.

[131] V. M. Barthem, C. V. Colin, H. Mayaffre, M. H. Julien, and D. Givord, "Revealing the properties of Mn 2 Au for antiferromagnetic spintronics," *Nature Communications*, vol. 4, 2013.

[132] P. Wadley, V. Hills, M. R. Shahedkhah, K. W. Edmonds, R. P. Campion, V. Novák, B. Ouladdiaf, D. Khalyavin, S. Langridge, V. Saidl, P. Nemec, A. W. Rushforth, B. L. Gallagher, S. S. Dhesi, F. Maccherozzi, J. Železný, and T. Jungwirth, "Antiferromagnetic structure in tetragonal cumnas thin films," *Scientific Reports*, vol. 5, p. 17079, Nov 2015.

[133] D. A. Garanin, "Self-consistent gaussian approximation for classical spin systems: Thermodynamics," *Phys. Rev. B*, vol. 53, pp. 11593–11605, May 1996.

[134] M. van Schilfgaarde, T. Kotani, and S. Faleev, "Quasiparticle self-consistent *gw* theory," *Phys. Rev. Lett.*, vol. 96, p. 226402, Jun 2006.

[135] L. Sponza, P. Pisanti, A. Vishina, D. Pashov, C. Weber, M. van Schilfgaarde, S. Acharya, J. Vidal, and G. Kotliar, "Self-energies in itinerant magnets: A focus on fe and ni," *Phys. Rev. B*, vol. 95, p. 041112, Jan 2017.

[136] J. Barker, D. Pashov, and J. Jackson, "Electronic structure and finite temperature magnetism of yttrium iron garnet," *Electronic Structure*, vol. 2, p. 044002, feb 2021.

[137] T. Kotani and M. van Schilfgaarde, "Spin wave dispersion based on the quasiparticle self-consistent gw method: Nio, mno and -mnas," *Journal of Physics: Condensed Matter*, vol. 20, p. 295214, jul 2008.

[138] L. Reining, "The gw approximation: content, successes and limitations," *Wiley Interdisciplinary Reviews: Computational Molecular Science*, vol. 8, no. 3, p. e1344, 2018.

[139] T. Kotani, M. van Schilfgaarde, S. V. Faleev, and A. Chantis, "Quasiparticle self-consistent gw method: a short summary," *Journal of Physics: Condensed Matter*, vol. 19, no. 36, p. 365236, 2007.

[140] D. Pashov, S. Acharya, W. R. Lambrecht, J. Jackson, K. D. Belashchenko, A. Chantis, F. Jamet, and M. van Schilfgaarde, "Questaal: A package of electronic structure methods based on the linear muffin-tin orbital technique," *Computer Physics Communications*, vol. 249, p. 107065, 2020.

[141] A. B. Shick, S. Khmelevskyi, O. N. Mryasov, J. Wunderlich, and T. Jungwirth, "Spin-orbit coupling induced anisotropy effects in bimetallic antiferromagnets: A route towards antiferromagnetic spintronics," *Phys. Rev. B*, vol. 81, p. 212409, Jun 2010.

[142] S. Selzer, L. Salemi, A. Deák, E. Simon, L. Szunyogh, P. M. Oppeneer, and U. Nowak, "Current-induced switching of antiferromagnetic order in $mn_2Au$ from first principles," *Phys. Rev. B*, vol. 105, p. 174416, May 2022.

[143] M. Arana, F. Estrada, D. S. Maior, J. B. S. Mendes, L. E. Fernandez-Outon, W. A. A. Macedo, V. M. T. S. Barthem, D. Givord, A. Azevedo, and S. M. Rezende, "Observation of magnons in Mn2Au films by inelastic Brillouin and Raman light scattering," *Applied Physics Letters*, vol. 111, 11 2017. 192409.

[144] H. Callen and E. Callen, "The present status of the temperature dependence of magnetocrystalline anisotropy, and the l(l+1)2 power law," *Journal of Physics and Chemistry of Solids*, vol. 27, no. 8, pp. 1271–1285, 1966.

[145] L. Ozyuzer, A. E. Koshelev, C. Kurter, N. Gopalsami, Q. Li, M. Tachiki, K. Kadowaki, T. Yamamoto, H. Minami, H. Yamaguchi, T. Tachiki, K. E. Gray, W.-K. Kwok, and U. Welp, "Emission of coherent thz radiation from superconductors," *Science*, vol. 318, no. 5854, pp. 1291–1293, 2007.

[146] H.-W. Hübers, "Towards thz integrated photonics," *Nature Photonics*, vol. 4, pp. 503–504, Aug 2010.

[147] E. A. Nanni, W. R. Huang, K.-H. Hong, K. Ravi, A. Fallahi, G. Moriena, R. J. Dwayne Miller, and F. X. Kärtner, "Terahertz-driven linear electron acceleration," *Nature Communications*, vol. 6, p. 8486, Oct 2015.

[148] N. Bhattacharjee, A. A. Sapozhnik, S. Y. Bodnar, V. Y. Grigorev, S. Y. Agustsson, J. Cao, D. Dominko, M. Obergfell, O. Gomonay, J. Sinova, M. Kläui, H.-J. Elmers, M. Jourdan, and J. Demsar, "Retraction: Néel spin-orbit torque driven antiferromagnetic resonance in $mn_2Au$ probed by time-domain thz spectroscopy [phys. rev. lett. 120, 237201 (2018)]," *Phys. Rev. Lett.*, vol. 124, p. 039901(E), Jan 2020.

[149] N. Thielemann-Kühn, D. Schick, N. Pontius, C. Trabant, R. Mitzner, K. Holldack, H. Zabel, A. Föhlisch, and C. Schüßler-Langeheine, "Ultrafast and energy-efficient quenching of spin order: Antiferromagnetism beats ferromagnetism," *Phys. Rev. Lett.*, vol. 119, p. 197202, Nov 2017.

[150] U. Atxitia, O. Chubykalo-Fesenko, N. Kazantseva, D. Hinzke, U. Nowak, and R. W. Chantrell, "Micromagnetic modeling of laser-induced magnetization dynamics using the Landau-Lifshitz-Bloch equation," *Applied Physics Letters*, vol. 91, no. 23, pp. 1–3, 2007.

[151] C. Vogler, C. Abert, F. Bruckner, and D. Suess, "Landau-lifshitz-bloch equation for exchange-coupled grains," *Phys. Rev. B*, vol. 90, p. 214431, Dec 2014.

[152] C. Vogler, C. Abert, F. Bruckner, and D. Suess, "Stochastic ferrimagnetic landau-lifshitz-bloch equation for finite magnetic structures," *Phys. Rev. B*, vol. 100, p. 054401, Aug 2019.

[153] T. A. Ostler, R. F. L. Evans, R. W. Chantrell, U. Atxitia, O. Chubykalo-Fesenko, I. Radu, R. Abrudan, F. Radu, A. Tsukamoto, A. Itoh, A. Kirilyuk, T. Rasing, and A. Kimel, "Crystallographically amorphous ferrimagnetic alloys: Comparing a localized atomistic spin model with experiments," *Phys. Rev. B*, vol. 84, p. 024407, Jul 2011.

[154] D. R. Behrendt, S. Legvold, and F. H. Spedding, "Magnetic properties of dysprosium single crystals," *Phys. Rev.*, vol. 109, pp. 1544–1547, Mar 1958.

[155] F. Jakobs and U. Atxitia, "Exchange-enhancement of the ultrafast magnetic order dynamics in antiferromagnets," 2022.

[156] P. E. Roy, R. M. Otxoa, and J. Wunderlich, "Robust picosecond writing of a layered antiferromagnet by staggered spin-orbit fields," *Phys. Rev. B*, vol. 94, p. 014439, Jul 2016.

[157] J. Chen, D. Tzou, and J. Beraun, "A semiclassical two-temperature model for ultrafast laser heating," *International Journal of Heat and Mass Transfer*, vol. 49, pp. 307–316, jan 2006.

[158] M. Kaganov, I. Lifshits, and L. Tanatarov, "Relaxation between electrons and the crystalline lattice," *Soviet Physics, JETP*, vol. 31, 01 1957.

[159] Z. Y. Chen, Z. R. Yan, M. H. Qin, and J.-M. Liu, "Landau-lifshitz-bloch equation for domain wall motion in antiferromagnets," *Phys. Rev. B*, vol. 99, p. 214436, Jun 2019.

[160] U. Atxitia, D. Hinzke, O. Chubykalo-Fesenko, U. Nowak, H. Kachkachi, O. N. Mryasov, R. F. Evans, and R. W. Chantrell, "Multiscale modeling of magnetic materials: Temperature dependence of the exchange stiffness," *Phys. Rev. B*, vol. 82, p. 134440, Oct 2010.

[161] D. A. Allwood, G. Xiong, C. C. Faulkner, D. Atkinson, D. Petit, and R. P. Cowburn, "Magnetic domain-wall logic," *Science*, vol. 309, no. 5741, pp. 1688–1692, 2005.

[162] S. S. P. Parkin, M. Hayashi, and L. Thomas, "Magnetic domain-wall racetrack memory," *Science*, vol. 320, no. 5873, pp. 190–194, 2008.

[163] D.-S. Han, S.-K. Kim, J.-Y. Lee, S. J. Hermsdoerfer, H. Schultheiss, B. Leven, and B. Hillebrands, "Magnetic domain-wall motion by propagating spin waves," *Applied Physics Letters*, vol. 94, no. 11, p. 112502, 2009.

[164] J.-S. Kim, M. Stärk, M. Kläui, J. Yoon, C.-Y. You, L. Lopez-Diaz, and E. Martinez, "Interaction between propagating spin waves and domain walls on a ferromagnetic nanowire," *Phys. Rev. B*, vol. 85, p. 174428, May 2012.

[165] D. Hinzke and U. Nowak, "Domain wall motion by the magnonic spin seebeck effect," *Phys. Rev. Lett.*, vol. 107, p. 027205, Jul 2011.

[166] C. Schieback, D. Hinzke, M. Kläui, U. Nowak, and P. Nielaba, "Temperature dependence of the current-induced domain wall motion from a modified landau-lifshitz-bloch equation," *Phys. Rev. B*, vol. 80, p. 214403, Dec 2009.

[167] K. M. D. Hals, Y. Tserkovnyak, and A. Brataas, "Phenomenology of current-induced dynamics in antiferromagnets," *Phys. Rev. Lett.*, vol. 106, p. 107206, Mar 2011.

[168] N. L. Schryer and L. R. Walker, "The motion of 180° domain walls in uniform dc magnetic fields," *Journal of Applied Physics*, vol. 45, no. 12, pp. 5406–5421, 1974.

[169] J. Shibata, G. Tatara, and H. Kohno, "A brief review of field- and current-driven domain-wall motion," *Journal of Physics D: Applied Physics*, vol. 44, no. 38, 2011.

[170] W. Jiang, P. Upadhyaya, Y. Fan, J. Zhao, M. Wang, L.-T. Chang, M. Lang, K. L. Wong, M. Lewis, Y.-T. Lin, J. Tang, S. Cherepov, X. Zhou, Y. Tserkovnyak, R. N. Schwartz, and K. L. Wang, "Direct imaging of thermally driven domain wall motion in magnetic insulators," *Phys. Rev. Lett.*, vol. 110, p. 177202, Apr 2013.

[171] Y. A. Shokr, O. Sandig, M. Erkovan, B. Zhang, M. Bernien, A. A. Ünal, F. Kronast, U. Parlak, J. Vogel, and W. Kuch, "Steering of magnetic domain walls by single ultrashort laser pulses," *Phys. Rev. B*, vol. 99, p. 214404, Jun 2019.

[172] S. Selzer, U. Atxitia, U. Ritzmann, D. Hinzke, and U. Nowak, "Inertia-free thermally driven domain-wall motion in antiferromagnets," *Phys. Rev. Lett.*, vol. 117, p. 107201, Aug 2016.

[173] F. Schlickeiser, U. Ritzmann, D. Hinzke, and U. Nowak, "Role of entropy in domain wall motion in thermal gradients," *Phys. Rev. Lett.*, vol. 113, p. 097201, Aug 2014.

[174] O. Gomonay, T. Jungwirth, and J. Sinova, "High antiferromagnetic domain wall velocity induced by néel spin-orbit torques," *Phys. Rev. Lett.*, vol. 117, p. 017202, Jun 2016.

[175] R. F. L. Evans, L. Rózsa, S. Jenkins, and U. Atxitia, "Temperature scaling of two-ion anisotropy in pure and mixed anisotropy systems," *Phys. Rev. B*, vol. 102, p. 020412, Jul 2020.

[176] Q. Gong, M. Yi, R. F. L. Evans, B.-X. Xu, and O. Gutfleisch, "Calculating temperature-dependent properties of $nd_2fe_{14}B$ permanent magnets by atomistic spin model simulations," *Phys. Rev. B*, vol. 99, p. 214409, Jun 2019.

[177] P. E. Roy, R. M. Otxoa, and J. Wunderlich, "Robust picosecond writing of a layered antiferromagnet by staggered spin-orbit fields," *Phys. Rev. B*, vol. 94, p. 014439, Jul 2016.

[178] C. C. Chiang, S. Y. Huang, D. Qu, P. H. Wu, and C. L. Chien, "Absence of evidence of electrical switching of the antiferromagnetic néel vector," *Phys. Rev. Lett.*, vol. 123, p. 227203, Nov 2019.

[179] Y. Behovits, A. L. Chekhov, S. Y. Bodnar, O. Gueckstock, S. Reimers, T. S. Seifert, M. Wolf, O. Gomonay, M. Kläui, M. Jourdan, and T. Kampfrath, "Nonlinear terahertz néel spin-orbit torques in antiferromagnetic $mn_2au$," 2023.

[180] F. Blanchard, L. Razzari, H.-C. Bandulet, G. Sharma, R. Morandotti, J.-C. Kieffer, T. Ozaki, M. Reid, H. F. Tiedje, H. K. Haugen, and F. A. Hegmann, "Generation of 1.5 $\mu$j single-cycle terahertz pulses by optical rectification from a large aperture znte crystal," *Opt. Express*, vol. 15, pp. 13212–13220, Oct 2007.

[181] K.-L. Yeh, M. C. Hoffmann, J. Hebling, and K. A. Nelson, "Generation of 10 $\mu$j ultrashort terahertz pulses by optical rectification," *Applied Physics Letters*, vol. 90, no. 17, p. 171121, 2007.

[182] T. Kampfrath, A. Sell, G. Klatt, A. Pashkin, S. Mährlein, T. Dekorsy, M. Wolf, M. Fiebig, A. Leitenstorfer, and R. Huber, "Coherent terahertz control of antiferromagnetic spin waves," *Nature Photonics*, vol. 5, pp. 31–34, 1 2011.

[183] J. A. Fülöp, S. Tzortzakis, and T. Kampfrath, "Laser-driven strong-field terahertz sources," *Advanced Optical Materials*, vol. 8, no. 3, p. 1900681, 2020.

[184] S. Ruan, X. Lin, H. Chen, B. Song, Y. Dai, X. Yan, Z. Jin, G. Ma, and J. Yao, "Terahertz probe of nonequilibrium carrier dynamics and ultrafast photocurrents in the topological insulator Sb2Te3," *Applied Physics Letters*, vol. 118, 01 2021. 011102.

[185] D. Xiong, Y. Jiang, K. Shi, A. Du, Y. Yao, Z. Guo, D. Zhu, K. Cao, S. Peng, W. Cai, D. Zhu, and W. Zhao, "Antiferromagnetic spintronics: An overview and outlook," *Fundamental Research*, vol. 2, no. 4, pp. 522–534, 2022.

[186] M. Jourdan, H. Bräuning, A. Sapozhnik, H. J. Elmers, H. Zabel, and M. Kläui, "Epitaxial mn2au thin films for antiferromagnetic spintronics," *Journal of Physics D: Applied Physics*, vol. 48, 2015.

[187] R. Cheng, M. W. Daniels, J.-G. Zhu, and D. Xiao, "Ultrafast switching of antiferromagnets via spin-transfer torque," *Phys. Rev. B*, vol. 91, p. 064423, Feb 2015.

[188] O. Gomonay, T. Jungwirth, and J. Sinova, "Narrow-band tunable terahertz detector in antiferromagnets via staggered-field and antidamping torques," *Physical Review B*, vol. 98, pp. 1–8, 2018.

[189] J. Železný, H. Gao, A. Manchon, F. Freimuth, Y. Mokrousov, J. Zemen, J. Mašek, J. Sinova, and T. Jungwirth, "Spin-orbit torques in locally and globally noncentrosymmetric crystals: Antiferromagnets and ferromagnets," *Phys. Rev. B*, vol. 95, p. 014403, Jan 2017.

[190] R. Rouzegar, A. Chekhov, Y. Behovits, B. Serrano, M. Syskaki, C. Lambert, D. Engel, U. Martens, M. Münzenberg, M. Wolf, G. Jakob, M. Kläui, T. Seifert, and T. Kampfrath, "Broadband spintronic terahertz source with peak electric fields exceeding 1.5 mv/cm," *Phys. Rev. Appl.*, vol. 19, p. 034018, Mar 2023.

[191] C. Bull, S. M. Hewett, R. Ji, C.-H. Lin, T. Thomson, D. M. Graham, and P. W. Nutter, "Spintronic terahertz emitters: Status and prospects from a materials perspective," *APL Materials*, vol. 9, 09 2021. 090701.

[192] T. S. Seifert, L. Cheng, Z. Wei, T. Kampfrath, and J. Qi, "Spintronic sources of ultrashort terahertz electromagnetic pulses," *Applied Physics Letters*, vol. 120, 05 2022. 180401.

[193] O. Chubykalo-Fesenko, U. Nowak, R. W. Chantrell, and D. Garanin, "Dynamic approach for micromagnetics close to the curie temperature," *Phys. Rev. B*, vol. 74, p. 094436, Sep 2006.

[194] E. F. Kneller and R. Hawig, "The exchange-spring magnet: a new material principle for permanent magnets," *IEEE Transactions on Magnetics*, vol. 27, no. 4, pp. 3588–3560, 1991.

[195] E. E. Fullerton, J. Jiang, and S. Bader, "Hard/soft magnetic heterostructures: model exchange-spring magnets," *Journal of Magnetism and Magnetic Materials*, vol. 200, no. 1-3, pp. 392–404, 1999.

[196] D. Suess, T. Schrefl, S. Fähler, M. Kirschner, G. Hrkac, F. Dorfbauer, and J. Fidler, "Exchange spring media for perpendicular recording," *Applied Physics Letters*, vol. 87, no. 1, 2005.

[197] D. Suess, J. Lee, J. Fidler, and T. Schrefl, "Exchange-coupled perpendicular media," *Journal of Magnetism and Magnetic Materials*, vol. 321, no. 6, pp. 545–554, 2009.

[198] F. Garcia-Sanchez, O. Chubykalo-Fesenko, O. Mryasov, R. Chantrell, and K. Y. Guslienko, "Exchange spring structures and coercivity reduction in fept/ ferh bilayers: A comparison of multiscale and micromagnetic calculations," *Applied Physics Letters*, vol. 87, no. 12, 2005.

[199] J.-U. Thiele, S. Maat, J. L. Robertson, and E. E. Fullerton, "Magnetic and structural properties of fept-ferh exchange spring films for thermally assisted magnetic recording media," *IEEE transactions on magnetics*, vol. 40, no. 4, pp. 2537–2542, 2004.

[200] S. P. Bommanaboyena, D. Backes, L. S. Veiga, S. S. Dhesi, Y. R. Niu, B. Sarpi, T. Denneulin, A. Kovács, T. Mashoff, O. Gomonay, J. Sinova, K. Everschor-Sitte, D. Schönke, R. M. Reeve, M. Kläui, H. J. Elmers, and M. Jourdan, "Readout of an antiferromagnetic spintronics system by strong exchange coupling of Mn2Au and Permalloy," *Nature Communications*, vol. 12, no. 1, pp. 1–7, 2021.

[201] L. Yin, D. Wei, N. Lei, L. Zhou, C. Tian, G. Dong, X. Jin, L. Guo, Q. Jia, and R. Wu, "Magnetocrystalline anisotropy in permalloy revisited," *Physical review letters*, vol. 97, no. 6, p. 067203, 2006.

[202] D. Meilak, S. Jenkins, R. Pond, and R. F. Evans, "Massively parallel atomistic simulation of ultrafast thermal spin dynamics of a permalloy vortex," *arXiv preprint arXiv:1908.08885*, 2019.

[203] H. P. Oepen, G. Steierl, and J. Kirschner, "Scanning electron microscope with polarization analysis: Micromagnetic structures in ultrathin films," *Journal of Vacuum Science & Technology B: Microelectronics and Nanometer Structures Processing, Measurement, and Phenomena*, vol. 20, pp. 2535–2538, 12 2002.

[204] R. J. Wakelin and E. L. Yates, "A study of the order-disorder transformation in iron-nickel alloys in the region feni3," *Proceedings of the Physical Society. Section B*, vol. 66, p. 221, mar 1953.

[205] C. S. Tian, D. Qian, D. Wu, R. H. He, Y. Z. Wu, W. X. Tang, L. F. Yin, Y. S. Shi, G. S. Dong, X. F. Jin, X. M. Jiang, F. Q. Liu, H. J. Qian, K. Sun, L. M. Wang, G. Rossi, Z. Q. Qiu, and J. Shi, "Body-centered-cubic ni and its magnetic properties," *Phys. Rev. Lett.*, vol. 94, p. 137210, Apr 2005.

[206] P. Yu, X. F. Jin, J. Kudrnovský, D. S. Wang, and P. Bruno, "Curie temperatures of fcc and bcc nickel and permalloy: Supercell and green's function methods," *Phys. Rev. B*, vol. 77, p. 054431, Feb 2008.

[207] A. A. Sapozhnik, M. Jourdan, H. Zabel, M. Kläui, and H.-J. Elmers, "Exchange bias in epitaxial mn2au (0 0 1)/fe (0 0 1) bilayers," *Journal of Physics D: Applied Physics*, vol. 52, p. 465003, sep 2019.

[208] A. K. Nayak, M. Nicklas, S. Chadov, C. Shekhar, Y. Skourski, J. Winterlik, and C. Felser, "Large zero-field cooled exchange-bias in bulk $mn_2PtGa$," *Phys. Rev. Lett.*, vol. 110, p. 127204, Mar 2013.

[209] H. Stremme, "Lattice parameter and ferromagnetic properties of f.c.c. ni-fe invar alloys," *Physics Letters A*, vol. 46, no. 2, pp. 126–128, 1973.

[210] R. Cuadrado, L. Oroszlány, L. Szunyogh, G. Hrac, R. Chantrell, and T. Ostler, "A multiscale model of the effect of ir thickness on the static and dynamic properties of fe/ir/fe films," *Scientific Reports*, vol. 8, p. 3879, 2018.

[211] R. F. L. Evans, L. Rózsa, S. Jenkins, and U. Atxitia, "Temperature scaling of two-ion anisotropy in pure and mixed anisotropy systems," *Phys. Rev. B*, vol. 102, p. 020412, Jul 2020.

[212] N. Kazantseva, D. Hinzke, R. W. Chantrell, and U. Nowak, "Linear and elliptical magnetization reversal close to the curie temperature," *Europhysics Letters*, vol. 86, no. 2, p. 27006, 2009.

[213] M. Ellis and R. Chantrell, "Switching times of nanoscale fept: Finite size effects on the linear reversal mechanism," *Applied Physics Letters*, vol. 106, no. 16, 2015.

[214] J. Barker, R. F. L. Evans, R. W. Chantrell, D. Hinzke, and U. Nowak, "Atomistic spin model simulation of magnetic reversal modes near the curie point," *Applied Physics Letters*, vol. 97, no. 19, 2010.

[215] T. Dannegger, M. Berritta, K. Carva, S. Selzer, U. Ritzmann, P. M. Oppeneer, and U. Nowak, "Ultrafast coherent all-optical switching of an antiferromagnet with the inverse Faraday effect," 2021.

[216] A. I. Liechtenstein, M. Katsnelson, V. Antropov, and V. Gubanov, "Local spin density functional approach to the theory of exchange interactions in ferromagnetic metals and alloys," *Journal of Magnetism and Magnetic Materials*, vol. 67, no. 1, pp. 65–74, 1987.

[217] M. Pajda, J. Kudrnovskỳ, I. Turek, V. Drchal, and P. Bruno, "Ab initio calculations of exchange interactions, spin-wave stiffness constants, and curie temperatures of fe, co, and ni," *Physical Review B*, vol. 64, no. 17, p. 174402, 2001.

[218] O. Šipr, S. Mankovsky, and H. Ebert, "Spin wave stiffness and exchange stiffness of doped permalloy via ab initio calculations," *Physical Review B*, vol. 100, no. 2, pp. 1–11, 2019.

[219] I. Razdolski, A. Alekhin, N. Ilin, J. P. Meyburg, V. Roddatis, D. DIesing, U. Bovensiepen, and A. Melnikov, "Nanoscale interface confinement of ultrafast spin transfer torque driving non-uniform spin dynamics," *Nature Communications*, vol. 8, pp. 6–10, 2017.

[220] C. Kittel and P. McEuen, *Introduction to solid state physics*. John Wiley & Sons, 2018.

[221] S. M. Rezende, R. L. Rodríguez-Suárez, and A. Azevedo, "Diffusive magnonic spin transport in antiferromagnetic insulators," *Phys. Rev. B*, vol. 93, p. 054412, Feb 2016.

[222] M. J. Hurben and C. E. Patton, "Theory of two magnon scattering microwave relaxation and ferromagnetic resonance linewidth in magnetic thin films," *Journal of Applied Physics*, vol. 83, pp. 4344–4365, 04 1998.

[223] O. Eriksson, A. Bergman, L. Bergqvist, and J. Hellsvik, *Atomistic spin dynamics: foundations and applications*. Oxford university press, 2017.